Crystal Growth and Mineral Replacement Reactions in Biomimetic and Biological Calciumcarbonate and Calciumphosphate Composites

vorgelegt von

Martina Greiner

München, 23.7.2019

~ Für Mama und Papa ~

Abstract

Biological hard tissues are composites of minerals and biopolymers. This thesis combines investigations on carbonate and phosphate biominerals, their replacement and thermal reaction kinetics, and biomimetic synthesis experiments. In order to gain a deeper understanding about carbonate and phosphate biological hard tissues, biomimetic crystal growth experiments using hydrogel as organic growth matrix were performed.

Apatite (AP) crystallites were grown in double-diffusion systems in agarose and gelatin matrices with high and low solid contents.. A low solid content using the same hydrogel results in a lower gel strength compared to a high solid content. The protein amelotin (AMTN) which promotes AP mineralization and regulates the enamel AP microstructure in teeth was added to some of the experiments to investigate its influence on the AP-hydrogel composites. The aggregates were analysed by X-ray Powder Diffraction (XRPD) with quantitative Rietveld refinement and Scanning Electron Microscopy (SEM). Summarized, all AP crystal aggregates which were grown with AMTN gave larger crystallites than the crystallites grown in experiments without AMTN, except for agarose 2 wt%.

However, the characterization of AP composites is rather complicated due to their nanocrystalline size. Therefore, the carbonate-agar aggregates were grown in order to transfer the newly acquired knowledge about carbonate composites to phosphate composites. Carbonate composites grown with two different solute concentrations in agar hydrogel with different solid contents (light/ dense gels) by counter-diffusion were investigated. High reagent solution concentrations give rise to high supersaturation and high growth rates. Both parameters alone or combined influence the characteristics of the carbonate agar composite. The calcite co-orientation and diverse misorientations within the composites were analysed by Electron Backscatter Diffraction (EBSD) measurements. High reagent solution concentrations combined with a light gel form *single crystal composites* and *mosaic crystal composites* in dense gels. *Single crystal composites* also form in low reagent solutions when combined with a light gel; in a dense gel the aggregate is a *co-oriented polycrystal composite*. The gel-mineral interlinkage and the gel fabric were visualized by etching and decalcification procedures and imaged by SEM. The amount of gel incorporated into the mineral increases with gel density. The gel accumulates regionally in the composites when the growth rate is low; the gel is homogeneously distributed for high growth rates. In general, the amount of incorporated gel and the calcite orientation are mainly determined by the agar gel solid

content and the reagent solution concentration influences the pattern of gel distribution inside the composites.

Structural and chemical variations in calcium phosphate biominerals were investigated by analysing 65 archaeological animal and human bone finds. Mammal bone primarily consists of the mineral component bioapatite (carbonated AP) and a collagen organic matrix. Deviations between crystallographic parameters were found. Those can be primarily ascribed to different species, type of bone and crystal age rather than to archaeological age. Furthermore, the decomposition of fresh bone under acidic conditions was studied. At pH values below 5 the calcium phosphate phase brushite is stable. However, even after eight weeks stored under acidic conditions, analysis by XRPD did not reveal any brushite being formed.

Moreover, structural and chemical changes of biological phosphates in consequence of heat-treatment were investigated by carrying out heating experiments on fresh bone. The results can also be applied to determine the incineration temperatures of archaeological bone finds. The heat-induced changes in bone were analysed by combining several methods such as quantitative XRPD, Fourier Transform Infrared Spectroscopy (FTIR), and Infrared-coupled Thermogravimetric Analysis (TGA-FTIR). There are no or only minor amounts of hydroxyl-ions in original bone mineral. However, thermal treatment induced an increase of hydroxyl groups in the apatite lattice accompanied by a depletion of water and reduction of carbonate contents during heating. At temperatures from 700 °C onwards after 30 minutes of heating, a considerable crystallite growth and recrystallization reaction from bioapatite (carbonated AP) to hydroxyapatite occurred. This transformation reaction mainly sets in after the organic matrix compounds and their residues have been combusted enabling the AP grains to get into direct contact. When heated above 800 °C the mineral buchwaldite ($CaNaPO_4$) is formed from the Na component within the bone mineral.

Furthermore, the reaction kinetics of biological aragonite composites to AP were investigated. Bioaragonitic hard materials depicting diverse specific microstructures were partially and fully converted into AP by dissolution-reprecipitation in an aqueous medium after time spans between four and 14 days. The used samples were two bivalves, *Hyriopsis cumingii* and *Arctica islandica,* the cephalopod *Sepia officinalis* and *Porites* sp. a warm water coral whose hard materials show different porosities and biopolymer contents. Conversion rates were quite different for the investigated biominerals even though all of them consist of biological aragonite of similar crystallite size. Conversion rates strongly depend on the feasibility of the

reaction fluid to access aragonite crystallites. When aragonite is dissolved and apatite is precipitated, porosity is generated which facilitates the infiltration of the reaction fluid and gives rise to large surface areas for the dissolution of aragonite crystallites and conversion to AP. Moreover, conversion rates are influenced by the biopolymer content of the biominerals and their feasibility to be decomposed.

The cuttlebone *Sepia officinalis* was fully converted into AP, the least conversion is observed for the nacreous shell portion of the bivalve *Hyriopsis cumingii* (<1 wt% apatite after 14 days). The acicular microstructure of the coral *Porites* sp. (38 wt% apatite after 14 days) and the prismatic microstructure of *H. cumingii* (26 wt% apatite after 14 days) allow considerable conversion of aragonite to apatite. Compared to those, the cross-lamellar microstructure of *Arctica islandica* is more resistant to phase conversion, as it depicts only 11-18 wt% apatite after   14   days.

Zusammenfassung

Biologische Hartgewebe sind Komposite aus Mineralen und Biopolymeren, sogenannte Biominerale. Diese Doktorarbeit kombiniert Untersuchungen an Biomineralen, deren thermisches Verhalten und deren biomimetische Syntheseexperimente. Um ein besseres Verständnis über biologische Hartgewebe aus Karbonat und Phosphat zu erlangen, wurden biomimetische Kristallzüchtungsexperimente mit Hydrogelen als organische Wachstumsmatrix durchgeführt.

Apatit (AP) Kristallite wurden in einem „double-diffusion" System in Agarose- und Gelatine-Matrizen mit hohem und niedrigem Feststoffanteil gezüchtet. Ein niedriger Feststoffanteil verglichen mit einem hohen Feststoffanteil resultiert in einer niedrigeren Gelstärke bei gleichem Hydrogel. Das Protein Amelotin (AMTN), welches AP Mineralisation fördert und die Mikrostruktur von AP in Zahnschmelz reguliert, wurde den Experimenten beigefügt, um seinen Einfluss auf die AP-Hydrogel Komposite zu untersuchen. Die Aggregate wurden mittels Röntgenpulverdiffraktometrie (XRPD) mit quantitativer Rietveld-Verfeinerung und Rasterelektronenmikroskopie analysiert. Zusammengefasst waren mit Ausnahme des Experiments mit 2 Gew. % Agarose alle AP-Kristallaggregate, welche mit AMTN gezüchtet wurden, größer als die Kristallite, welche in Experimenten ohne AMTN gezüchtet wurden.

Die Charakterisierung von AP-haltigen Kompositen ist aufgrund ihrer nanokristallinen Größe sehr aufwendig. Daher wurden Karbonat-Agar-Aggregate gezüchtet, um das neu erlangte Wissen über Karbonat-Komposite auf Phosphat-Komposite zu übertragen. Es wurden Karbonat-Komposite untersucht, welche jeweils mit zwei verschiedenen Lösungskonzentrationen in Hydrogelen mit zwei unterschiedlichen Feststoffanteilen (schwaches Gel/starkes Gel) mit der Gegendiffusionsmethode gezüchtet wurden. Eine hohe Konzentration der Reagenzlösung führt zu hoher Übersättigung und hohen Wachstumsraten. Beide Parameter einzeln oder kombiniert beeinflussen die Charakteristika der Karbonat-Agar-Komposite. Die Kalzit-Koorientierung und verschiedene Arten seiner Misorientierung im Komposit wurden mit der Elektronen-Rückstreu-Beugungs-Methode (EBSD) analysiert. Bei hohen Lösungskonzentrationen kombiniert mit einem schwachen Gel werden *Einkristallkomposite* gebildet, kombiniert mit einem starken Gel werden *Mosaik-Kristall-Komposite* gebildet. *Einkristallkomposite* werden auch bei niedrigen Lösungskonzentrationen kombiniert mit einem schwachen Gel gebildet; in starken Gelen werden koorientierte *Polykristallkomposite* gebildet. Die Gel-Mineral Vernetzung und die Gelstruktur wurden durch Ätz- und Dekalzifizierungsverfahren sichtbar gemacht und mit einem

Rasterelektronenmikroskop untersucht. Der Einbau des Gels in das Mineral nimmt mit der Geldichte zu. Das Gel akkumuliert lokal in den Kompositen, wenn die Wachstumsrate gering ist. Grundsätzlich wird die Menge des eingebauten Gels und die Kalzit-Orientierung hauptsächlich vom Agar-Feststoffanteil bestimmt; die Konzentration der Reagenzlösungen beeinflusst das Muster der Gelverbreitung im Komposit.

Strukturelle und chemische Variationen von Calcium-Phosphat-Biomineralen wurden untersucht, indem 65 archäologische tierische und menschliche Knochenfunde analysiert wurden. Säugetierknochen bestehen hauptsächlich aus der Mineralkomponente Karbonat-Apatit (sog. Bioapatit) und einer Kollagenmatrix. Es wurden unterschiedliche kristallographische Parameter des Bioapatits festgestellt. Diese Unterschiede treten hauptsächlich aufgrund verschiedener Spezies, Art der Knochen und Alter der Kristalle auf, weniger aufgrund des archäologischen Alters. Des Weiteren wurde die Zersetzung von frischem Knochen unter sauren Bedingungen untersucht. Bei pH-Werten unter 5 ist die Calcium-Phosphat-Phase Brushit stabil. Allerdings wurde im Knochen, der acht Wochen sauren Bedingungen ausgesetzt war, mittels XRPD keine Brushitbildung nachgewiesen.

Ferner wurden strukturelle und chemische Veränderungen in biologischen Phosphaten als Folge von Wärmebehandlung mittels Heizexperimenten an frischen Knochen untersucht. Die Ergebnisse können auch angewendet werden, um die Verbrennungstemperaturen von archäologischen Knochenfunden zu bestimmen. Die hitzebedingten Veränderungen in Knochen wurden durch eine Kombination von mehreren Methoden untersucht, wie beispielsweise quantitative XRPD, Fourier Transform Infrarot Spektroskopie (FTIR) und thermogravimetrische Analyse gekoppelt mit FTIR. In ursprünglichem Knochenmineral gibt es keine, oder nur wenig Hydroxylionen. Wärmebehandlung rief einen Anstieg von Hydroxylgruppen im Apatit-Gitter hervor, einhergehend mit einer Abreicherung an Wasser und einer Reduktion des Karbonatgehalts während des Heizens. Nach 30 Minuten Heizen bei Temperaturen ab 700 °C erfolgt ein bemerkenswertes Kristallwachstum und eine Umwandlungsreaktion von Bioapatit zu Hydroxylapatit findet statt. Diese Umwandlung setzt hauptsächlich ein, sobald die organischen Matrixkomponenten und deren Rückstände verbrannt sind, was einen direkten Kontakt der AP-Körner zueinander ermöglicht. Bei Heizen über einer Temperatur von 800 °C bildet sich das Mineral Buchwaldit ($CaNaPO_4$) aus der Natrium-Komponente im Knochenmineral.

Darüber hinaus wurde die Reaktionskinetik von biologischen Aragonit-Kompositen zu AP untersucht. Aus biologischem Aragonit bestehende Hartgewebe mit diversen speziellen

Mikrostrukturen wurden in einer wässrigen Lösung teilweise oder vollständig nach vier bis 14 Tagen durch Auflösung-Repräzipitation in AP umgewandelt. Die verwendeten Proben waren zwei Bivalven (*Hyriopsis cumingii* und *Arctica islandica*), der Kopffüßer (*Sepia officinalis*) und eine Warmwasserkoralle (*Porites* sp.). Das Hartmaterial der genannten Proben weist unterschiedliche Porositäten und Biopolymergehalte auf. Die Umwandlungsraten waren sehr unterschiedlich für die untersuchten Biominerale, obwohl es sich bei allen um biologischen Aragonit ähnlicher Kristallitgröße handelte. Die Umwandlungsraten hängen stark davon ab, ob es für das Reaktionsfluid möglich ist, Zugang zu den Aragonitkristallen zu bekommen. Wenn Aragonit aufgelöst und AP präzipitiert wird, wird eine Porosität generiert, welche die Infiltration des Reaktionsfluids fördert und eine größere Oberfläche schafft für die Auflösung von Aragonitkristallen und deren Umwandlung zu AP. Des Weiteren sind die Umwandlungsraten vom Biopolymer-Gehalt des Biominerals und dessen Zersetzungsverhalten beeinflusst. Die Schale von *Sepia officinalis* wurde vollständig in AP umgewandelt, die geringste Umwandlung zeigte der Perlmutt-Schalenteil der Bivalve *Hyriopsis cumingii* (< 1 Gew. % AP nach 14 Tagen). Die kreuz-lamellare Struktur von *Arctica islandica* weist nach 14 Tagen 11-18 Gew. % AP auf. Damit verglichen zeigen die nadelige Mikrostruktur der Koralle *Porites* sp. (38 Gew. % AP nach 14 Tagen) und die prismatische Mikrostruktur von *H. cumingii* (26 Gew. % AP nach 14 Tagen) eine weiter fortgeschrittene Umwandlung von Aragonit zu AP.

List of Abbreviations

ACC   amorphous calcium carbonate

AFM   atomic force microscopy

AMGN   amelogenin

AMTN   amelotin

AP   apatite

ATP   adenosine triphosphate

CI   crystallinity index

DNA   deoxyribonucleic acid

EBSD   electron backscatter diffraction

FE-SEM   field emission-scanning electron microscopy

FTIR   Fourier-transform infrared spectroscopy

HR-TEM   high resolution transmission electron spectroscopy

IRSF   infrared splitting factor

MUD   multiple of uniform distribution

OCP   octacalcium phosphate

RNA   ribonucleic acid

SAXS   small-angle X-ray scattering

SEM   scanning electron microscopy

SS-NMR   solid state nuclear magnetic resonance

TEM   transmission electron microscopy

TGA   thermogravimetric analysis

XRPD   X-ray powder diffraction

Table of Contents

1. Introduction

This thesis focuses on carbonate and phosphate biominerals and biomimetic hard tissues. Biominerals are composites of biopolymers and minerals which are formed by organisms through biological crystallization ("biomineralization"). The investigation of crystallization and recrystallization processes in biomimetic systems enhances the understanding of the natural formation of biological hard tissues. The scientific results presented in this thesis aim to expand the current knowledge on biomimetic and biological hard tissues.

1.1 Biomineralization and Biological Hard Tissues

The term biomineralization defines the processes by which organisms form minerals. Until today 64 different minerals are known to be formed by both, prokaryotes and eukaryotes (Knoll 2003, Weiner & Dove 2003). The basic processes of biomineralization are described in two different concepts: "Biologically induced mineralization" (Lowenstam 1981) and "biologically controlled mineralization" (Mann 1983). Biologically induced mineralization can occur e.g. by cations which are released by the cell, the introduction of metabolic end-products or by the formation of a charged surface e.g. a cell wall. This process is uncommon among animals and is predominant among the monera, fungi and protista (Lowenstam & Weiner 1989). Biologically controlled mineralization is categorized as either an extra-, inter-, or intracellular process (Lowenstam & Weiner 1989). The mineralization is biologically controlled when the nucleation, growth and morphology of the deposited mineral is directed by cells (Weiner & Dove 2003). Here, a material with specific biological functions and structures is formed, e.g. bones, teeth, or shells. The mechanisms of the extracellular mineralization process have been highly discussed by e.g. Weiner & Addadi et al. (2011) and Simonet Roda et al. (2019) but they end up in controversial models.

About 50% of the known biogenic minerals contain calcium as a major component, which is a consequence of organisms developing the ability to manipulate this ion very early in the evolution of life. However, silica, iron oxides, metal sulfides, sulfates and oxalate biominerals comprise the other half of the known biominerals (Lowenstam & Weiner 1989).

The produced biominerals are usually adapted to specific functional purposes such as biomechanics (e.g. protection or mobility), gravity receptors (e.g. fish, mammals) or to sense the Earth's magnetic field (magnetotactic bacteria) (Mann 2001).

1.1.1 Carbonate Phases in Biological Hard Tissues

One of the most abundant geologic and biogenic minerals on Earth is calcium carbonate (Lippmann 1973, Lowenstam & Weiner 1989). Calcium carbonate has various known polymorphs – diverse amorphous forms (amorphous calcium carbonate, ACC), calcium carbonate monohydrate, calcium carbonate hexahydrate (mineral name: ikaite), the recently discovered calcium carbonate hemihydrate (Zou et al. 2019), and three anhydrous polymorphs: calcite, aragonite and vaterite. Monohydrocalcite and the stable forms of ACC contain one water molecule per calcium carbonate. ACC and the anhydrous polymorphs are known to be formed biologically (Pauly 1963, Cartwright et al. 2012). As calcite is the thermodynamically most stable carbonate polymorph under ambient conditions, calcite is the most abundant phase among all calcium carbonate phases (Plummer & Busenberg 1982). Table 1.1-1 summarizes calcium carbonate phases in biominerals in some organisms. Among other purposes, calcium carbonate fulfils mainly structural functions e.g. to stiffen and strengthen the biological tissue (Addadi et al. 2003). The calcite lattice can incorporate Mg^{2+} ions, e.g. in sea urchin teeth up to concentrations of 45 mol% (Ma & Qi 2010). Calcite and aragonite are used as gravity sensors in land and sea animals (e.g. *otoliths* or *otoconia* in the inner ear) and are usually the preferred minerals for shells in molluscs. Many types of seashell contain both phases, however the minerals are spatially separated in different parts of the shell. The least thermodynamically stable phase of the three crystalline calcium carbonate polymorphs is vaterite. In aqueous solution, it transforms quickly to calcite or aragonite and occurs e.g. in *ascidians* (sea squirts) as structural support or to deter predators (Mann 2001).

Table 1.1-1 Calcium carbonate biominerals modified after Mann 2001.

Mineral	Formula	Organism
Calcite	$CaCO_3$	Coccolithophores
		Foraminifera
		Trilobites
		Molluscs
		Crustaceans
		Birds
		Mammals
Mg-calcite	$(Mg,Ca)CO_3$	Octocorals
		Echinoderms
Aragonite	$CaCO_3$	Scleractinian corals
		Molluscs
		Gastropods
		Cephalopods
		Fish
Vaterite	$CaCO_3$	Gastropods
		Ascidians
Amorphous	$CaCO_3 \cdot nH_2O$	Crustaceans
		Plants

1.1.2 Calcium Phosphate Biominerals

As well as calcium carbonates, calcium phosphates show ideal characteristics such as high lattice energies and low solubilities, and are therefore thermodynamically stable in biological environments (Mann 2001). Most phosphate biominerals are produced by controlled mineralization, except struvite and brushite (Weiner & Dove 2003). Biologic calcium phosphate is found as amorphous phase used for phosphate storage and it is the mineral component of skeletons in brachiopods of the subphylum linguliformea, and in vertebrates and some extinct clades (see also Table 1.1-2). The apatite (AP) crystal lattice is highly flexible towards the incorporation of ions such as carbonate, magnesium, sodium, water or fluoride (Montel et al. 1981, Elliott 1994, Wilson et al. 1999, Elliott 2002, Pan & Fleet 2002). The enhanced solubility of biogenic AP compared to non-biological apatite is essential when constant remodelling is required, as it is the case for vertebrates (Currey 2002, Weiner & Dove 2003). Biological AP (also bioapatite, carbonated apatite) is the most abundantly produced phosphate mineral and the mineral component of dentin and enamel in teeth and in bones. Here, the mineral provides physical properties which are necessary for the

functionality of the tissue such as mechanical grinding (teeth) and structural support (bone) (Pasteris et al. 2008). Moreover, the presence of carbonate in the biological apatite increases its solubility and reactivity which are essential properties for re- and demineralization of bone and teeth (Shimoda et al. 1990, Dorozhkin 2007). Other phosphate minerals mentioned in the context of biomineralization besides apatite are: octacalcium phosphate (OCP) $Ca_8H_2(PO_4)_6$, whitlockite $Ca_{18}H_2(Mg,Fe^{2+})_2 (PO_4)_{14}$, struvite $Mg(NH_4)(PO_4) \cdot 6H_2O$, monetite $CaHPO_4$, brushite $CaHPO_4 \cdot 2H_2O$, amorphous calcium phosphate, and vivianite $Fe_3(PO_4)_2 \cdot 8 H_2O$ (Lowenstam & Weiner 1989, Weiner & Dove 2003).

Table 1.1-2. Calcium phosphate biominerals modified after Mann 2001.

Mineral	Formula	Organism
(Carbonated) apatite	$(Ca, Sr, Mg, Na, H_2O, [\ ])_{10} (PO_4, HPO_4, CO_3P_2O_7)_6 (OH, F, Cl, H_2O, O, [\ ])_2$	Vertebrates Mammals Fish
Octacalcium phosphate	$Ca_8H_2(PO_4)_6$	Vertebrates
Amorphous	variable	Chitons Gastropods Bivalves Mammals Mammals

1.1.3 Bone Apatite: Chemical Composition and Structure

Among vertebrates, the most broadly mineralized material is bone (Lowenstam & Weiner 1989). Bone is a composite material which is constituted of carbonated AP (bioapatite) nanocrystals, mainly type I collagen microfibrils, non-collageneous proteins and water (Lim 1975, Weiner et al. 1999, Fratzl et al. 2004, Olszta et al. 2007).
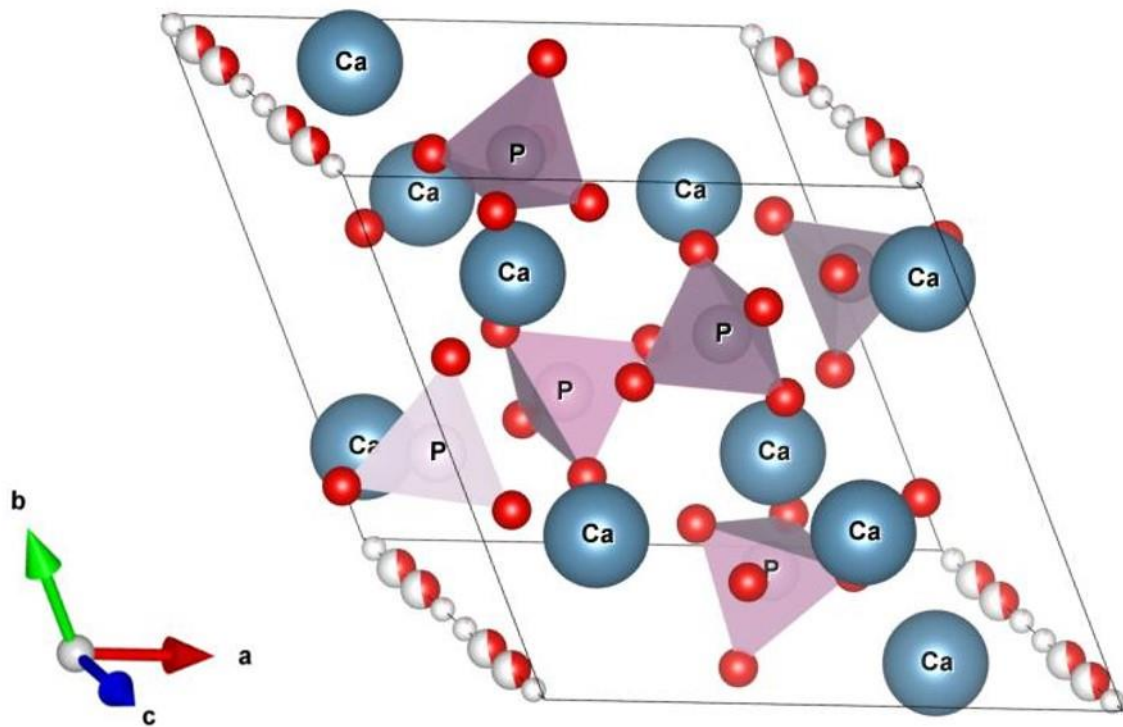
Figure 1.1-1. Crystal structure of hexagonal hydroxyapatite after Wilson et al. (1999) visualized with the program VESTA 3 (Momma & Izumi 2011). In bioapatite, the $(PO_4)^{3-}$ is exchanged by $(CO_3)^{2-}$ and $(HPO_4)^{2-}$and the OH$^-$ ions (channel sites along *c*) undergo substitution by $(CO_3)^{2-}$, H_2O and other ions. The Ca-sites can be occupied by e.g. Na$^+$, Sr^{2+} and by vacancies.

Bone formation is an "organic matrix-mediated" mineralization process. First, collagen is synthesized by osteoblasts, extruded from the cell and self-assembles in the extracellular space (Lowenstam 1981, Mann 2001) The bone structure is complex and hierarchically organized (Figure 1.1-2) which provides stiffness and compressive strength (e.g. Rho et al. 1998, Weiner et al. 1999, Reznikov et al. 2014, Schwarcz et al. 2014, Wegst et al. 2014). Bone is a chemical reservoir for phosphorous which is present in numerous biomolecules such as collagen, deoxyribonucleic acid (DNA), ribonucleic acid (RNA), and essential for the formation of adenosine triphosphate (ATP) (Pasteris et al. 2008). The mineral to collagen ratio in bone differs among species, type of bone and changes over lifetime. It has major control on the material properties of bone (e.g. ultimate strength, stiffness and toughness), the

higher the mineral to collagen ratio, the stronger but more brittle the bone appears (Pasteris et al. 2008).

In comparison to stoichiometric hydroxyapatite (Figure 1.1-1) $Ca_5(PO_4)_3(OH)$, the chemical composition of biological AP (bioapatite) is more complex: $(Ca, Mg, Na, vacancy)_5 (PO_4, HPO_4, CO_3)_3 (CO_3, H_2O, OH, F, Cl$ etc.) (Montel et al. 1981, Elliott 1994, Wilson et al. 1999, Elliott 2002, Pan & Fleet 2002). In bone mineral, two ionic substitution mechanisms exist: (1) the direct displacement of 2 OH^- by CO_3^{2-} in the OH^- site (A-type substitution) and (2) the replacement of PO_4^{3-} tetrahedra by CO_3^{2-} (B-type substitution) (LeGeros et al. 1969, Rey et al. 1990, Wopenka & Pasteris 2005, Yi et al. 2013). The resulting charge balance is compensated by depleting hydroxyl and calcium ions in the mineral and by creating vacancies (LeGeros 1981). Pasteris et al. (2012) showed by Raman spectroscopy that the hydroxyl ion concentration correlates inversely with the carbonate concentration and that the hydroxyl depletion in bone is mainly a result of B-type substitution. The crystallographic structure of bioapatite is generally accepted as hexagonal (space group $P6_3/m$) (Fleet 2015), however, some authors (Ikoma et al. 1999, Tonegawa et al. 2010) describe well-crystalline hydroxyapatite with a monoclinic symmetry (space group $P2_1/c$).

Transmission electron microscopy (TEM) and Small-angle X-ray scattering (SAXS) studies (Kim et al. 1995, Burger et al. 2008) and atomic force microscopy (AFM) studies (Eppell et al. 2001, Tong et al. 2003) showed that apatite crystallites in bone are nano-sized platelets elongated at their *c*-axis and are oriented parallel with the collagen fibre direction (Figure 1.1-2f, g). Published values for their dimensions vary, however platelet sizes reported by Palmer et al. (2008) using TEM analysis are (30-50) x (20-25) x (1.5-4) nm³; by measuring the extent of X-ray diffraction peak broadening, crystallites with a needle-like shape and sizes from 5-18 nm were reported (e.g. Stuhler 1938, Piga et al. 2013, Schmahl et al. 2017, Greiner et al. 2018a; 2019). Moreover, crystallite size also depends on the crystal age (initial formation until maturation of the crystallite) which makes it even more complicated to describe bone crystal dimensions (Glimcher 2006).

Recently, the existence of a hydrated layer on the apatite crystal surface containing HPO_4^{2-} ions was discussed and referred to "non-apatitic domains" (Rey et al. 2014). This was investigated using spectroscopic methods such as Fourier transform infrared spectroscopy (FTIR) on bone crystals (Cazalbou et al. 2004, 2005) and solid state nuclear magnetic resonance (SS-NMR) on biomimetic apatites (Sfihi & Rey 2002, Wang et al. 2012). Consistent data obtained from those studies support the hypothesis of existing non-apatitic

environments of CO_3^{2-} and HPO_4^{2-}. Studies on wet nanocrystalline apatites using FTIR and SS-NMR combined revealed that the surface hydrated layers are structured and that the surface composition is easily altered by fast, reversible ionic exchange which leaves the AP domains unchanged (Eichert et al. 2004; 2005) However, this hydrated layer seems rather fragile and appeared as amorphous-like domains in dried samples observed by high resolution transmission electron spectroscopy (HR-TEM) (Bertinetti et al. 2009).
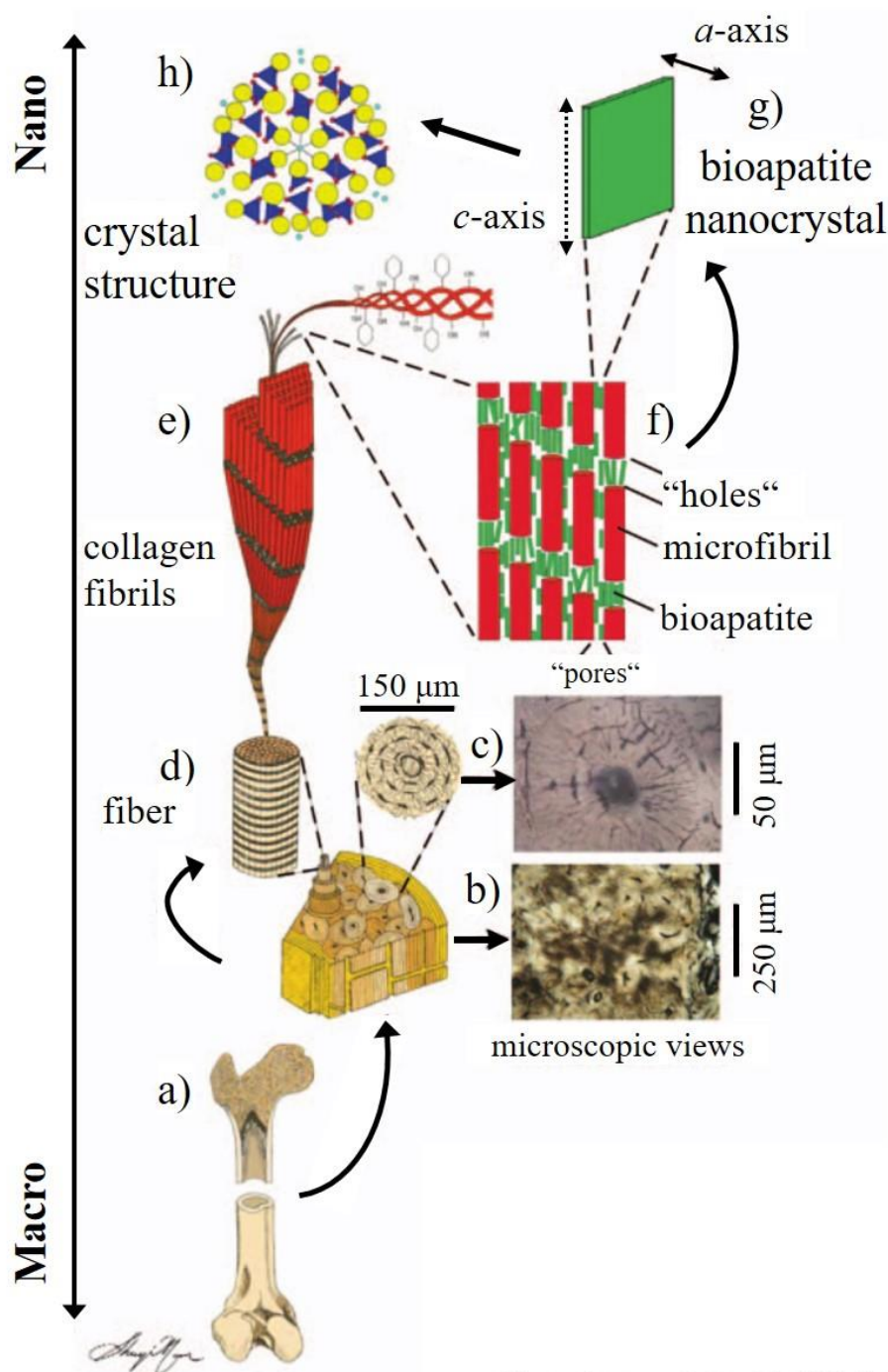
Figure 1.1-2. The hierarchical levels of the cortical bone structure modified after Pasteris et al. (2008), sketches show: a) Long bone (e.g. a femur) depicting porous cancellous bone (ends) and dense cortical bone (shaft); b) Cross-sectional slice of cortical bone which consists mostly of cylindrical osteons; c) osteon which consists of a central vascular cavity ("Haversian canal") surrounded by channels formed by lamellae; d) collagen fiber consisting of hundreds of fibrils; e) collagen fibril, the smallest building unit of the organic component in bone. Five collagen molecules form a microfibril; f) microfibrils are bundled to fibrils (e); f) collagen microfibrils ~300 nm long and ~4 nm thick; g) bioapatite crystallite which depicts a platelet shape with only 2-3 unit cells thickness; h) atomic structure of hexagonal apatite viewed down the *c*-axis, for further details refer to Figure 1.1-1.

1.2 Biological and Biomimetic Composites

In contrast to geological minerals, most biological minerals are composites whose inorganic units are separated by organic materials (Weiner & Dove 2003). The organic fraction usually is termed "organic matrix". The intercrystalline organic matrix is a continuous sheet like structure which subdivides the space where mineralization occurs (Lowenstam & Weiner 1989). In addition, there is an intracrystalline organic matrix incorporated inside the crystals (Griesshaber et al. 2013, Maier et al. 2014). In general, the organic matrix is a structural framework of hydrophobic macromolecules (proteins and/or polysaccharides) and water-soluble acidic macromolecules (in many cases glycoproteins) which appear to act as a nucleation surface for biomineralization (Mann 2001). Major organic framework macromolecules found in mineralized hard tissues of organisms are e.g. collagen type I in bone and dentin (chordata), complexes of chitin and protein (mollusca, arthropoda, brachiopoda, ectoprocta, annelida) or cellulose (plant silica) (Lowenstam & Weiner 1989, Mann 2001).

The network constructed by the organic matrix and the biological mineral exhibits specific functions required by the organism (e.g. protection, movement, cutting and grinding) which forms it. Compared to inorganic minerals, mineral-biopolymer composites display enhanced mechanical properties such as strength, hardness and toughness (e.g. Mann 2001, Currey et al. 2001, Goetz et al. 2011). To name an example, nacreous aragonite (mother-of-pearl) exhibits a brick wall-like microstructure of platelet-shaped aragonite tablets between sheets of a protein-polysaccharide organic matrix. Moreover, the tablet crystal is substructured by the matrix network (Griesshaber et al. 2013).

1.2.1 Crystal Growth Concepts

A crystal is a solid phase with a regular atomic structure characterized by periodicity and anisotropy (Sunagawa 2005). Crystal growth from a solution requires the continual addition of ions to the crystal's surface and their subsequent incorporation into lattice sites (Mann 2001). Depending on growth conditions, the same crystal species can show different external forms (polyhedral, skeletal or dendritic). When there is no change in orientation throughout a crystal, the structure is referred to as a single crystal even though it may contain various defects of lattice order. An agglomeration of single crystals with different orientations is termed a polycrystalline aggregate (Sunagawa 2005). When a crystal shows an internal orientational spread which is delimited to slightly misoriented subunits tilted relative to each

other by a small angle, it is referred to as mosaic crystal (Darwin 1922, Hull 1975, Wuttke 2014). Small angle grain boundaries are arrays of dislocations with more or less regular spacing D. For the purpose of this thesis, the upper limit of a "small" angle was arbitrarily defined (Greiner et al. 2018b) as the case when the spacing D drops below 10 times the length of the Burgers vector of the dislocations ($\tan\alpha= 0.1 \rightarrow \alpha= 5.7°$), such that the disturbed structures around the dislocations overlap and the boundary becomes an incoherent large angle boundary (Hull 1975).

Thermodynamically, crystal growth or crystallization is a first-order phase transition where a regular structure develops out of a disordered and irregular state. When a driving force causes a system to depart from its equilibrium conditions towards supersaturation (or supercooling in single-component systems), a nucleus of a crystal can be formed and begin to grow. In a state where neither temperature nor the concentration changes in a system, neither growth nor dissolution of a crystal can occur (De Yoreo & Vekilov 2003, Sunagawa 2005).

The classical theory of nucleation is based on the work of Gibbs (1928) and is based on the condensation of a vapour to a liquid but it may be extended to the crystallization from melts and solutions (Mullin 2001). According to the classical crystal growth concept, particles smaller or larger than a critical radius r_c (see Figure 1.2.-1), are formed in the system. Subcritical clusters usually dissociate again after their formation, some of them may grow larger than the critical size by thermal activation. The process up to the point where the particles reach the critical size is called the nucleation stage. When they exceed the critical size and grow larger, this process is called the growth stage. The driving force for phase transformation at constant pressure is the change of the Gibbs free energy (ΔG). The change in free energy during precipitation depends on the size of the nucleus which is usually approximated to be spherical for simplicity (Kashchiev 2000, Mullin 2001).

The free energy of the nucleus or protonucleus is

$$\Delta G = \Delta G_S + \Delta G_v = 4\,\pi\,r^2\,\gamma + \frac{4}{3}\,\pi\,r^3\,\Delta G_v \text{ (Eq. 1.2-1)}$$

where r is the radius of the nucleus, ΔG_S is the surface free energy, ΔG_v is the volume free energy change of the transformation and γ the specific interfacial energy (i.e. between the supersaturated solution and the developing crystalline surface. ΔG_v is negative if the phase to form is thermodynamically stable, while the second term of the sum is positive. For small nuclei, the energy contribution for the formation of the nucleus surface predominates, but is

10

overbalanced by the energy contribution correlated to the formation of the nucleus volume once r_c is reached. Hence, the newly formed crystalline lattice structure can either grow or re-dissolve, but result in the decrease of the free energy of the particle (Mullin 2001, Sangwal 2007).
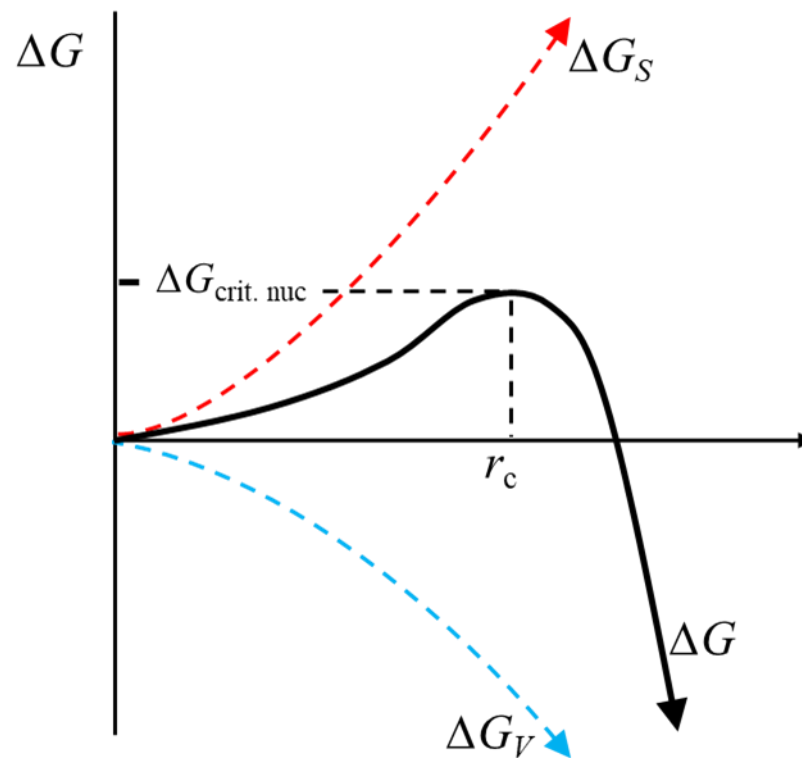
Figure 1.2-1. Change in Gibbs free energy ΔG as a function of the nucleus radius formed in a supersaturated medium.

Nucleation can be classified as "spontaneous or homogeneous nucleation" which needs no intervention by other factors to take place and "heterogeneous nucleaction" which occurs due to the presence of foreign particles, an impurity or due to the presence of a surface wall of a vessel. The latter requires significantly less driving force.

After the nucleation stage is complete, the growth stage commences at the expense of a much smaller energy than that necessary for nucleation (Sunagawa 2005). When an atom arrives at a crystal surface, it is able to migrate on the surface before it becomes integrated into the crystal lattice (Chernov 1984). A new layer is created by attachment of further atoms/ ions to active sites on the surface until the surface is completed (layer-by-layer growth mode). Those active sites can be kinks, steps and terraces (Figure 1.2-2). Here, the kink site is favoured as

the attachment energy of the growth unit to the crystal site decreases from terrace to kink site (Sunagawa 2005, Sangwal 2007).
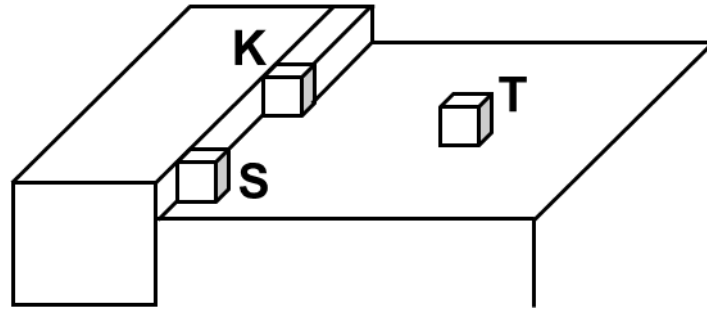
Figure 1.2-2. Cubic lattice model with different positions for the attachment of growth units according to Kossel (1927) and Stranski (1928) illustrating three growth sites T: Terrace site with one neighbour, S: Step site with two neighbours, K: Kink with three out of six (for bulk atoms) nearest neighbours. Modified after Sangwal 2007.

In general, there are four different growth mechanisms in the classical model of crystal growth which depend on the anatomical rough- or smoothness of the interface:

1) the adhesive type growth mechanism which predominates at high supersaturations

2) the two-dimensional nucleation growth mechanism which occurs at intermediate supersaturations

3) the spiral growth mechanism, which is expected only on smooth interfaces and predominates at low supersaturations

According to the thermodynamic model of classical crystallization, crystals are assumed to grow from primary building blocks (atoms, ions, molecules) which coalesce to form clusters or disintegrate again. However, this classical crystallization model is challenged by numerous crystallization processes summarized by Meldrum & Cölfen (2008) where the classical model cannot be applied. Those processes can be interpreted in the framework of a second, "non-classical" pathway of crystallization which especially applies to systems far from equilibrium. According to the "non-classical crystallization" theory, intermediary clusters or phase separation to liquid precursors form in parallel and act as primary building blocks (see Figure 1.2-3). Crystallization occurs via amorphous intermediates involving temporary amorphous building blocks that can undergo mesoscopic transformations. The nanoparticles self-organize to oriented aggregates, and finally arrange to a highly ordered superstructure (mesostructure) (Niederberger & Cölfen 2006).
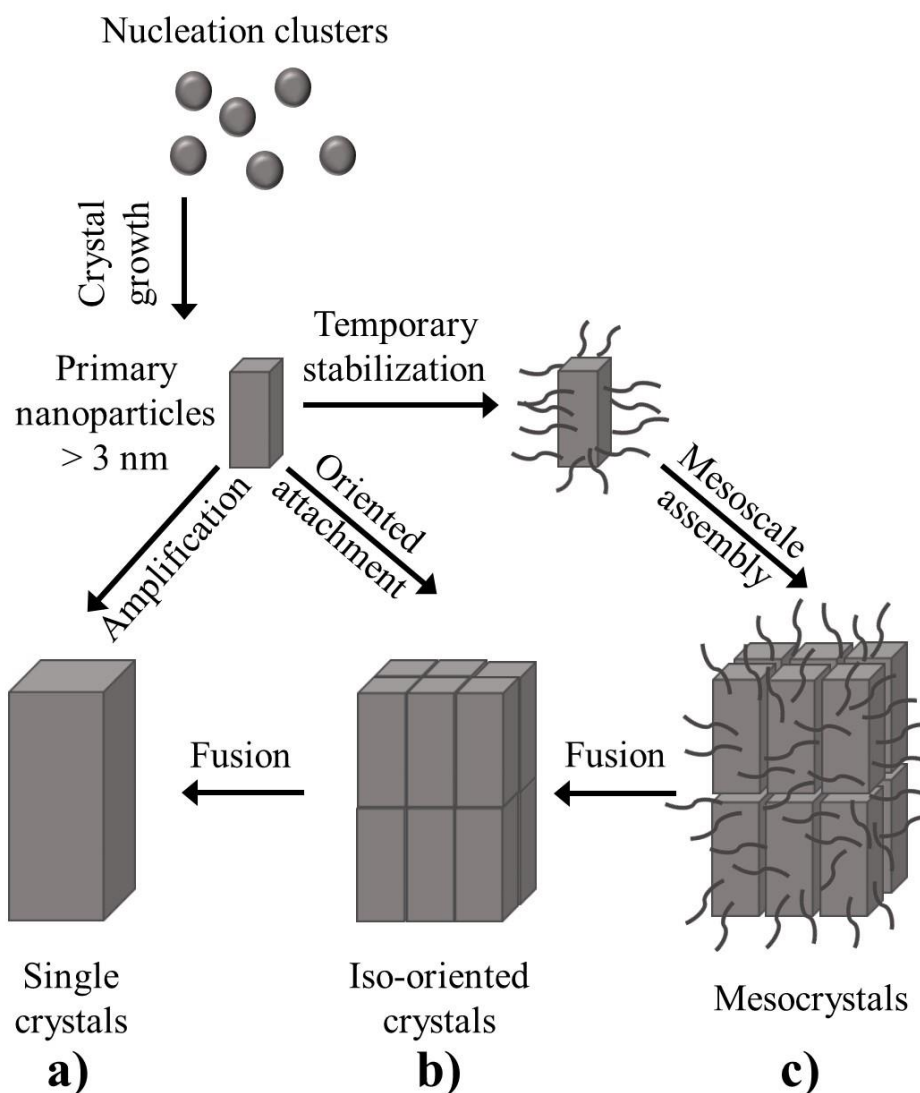
Figure 1.2-3. Schematic illustration of classical and non-classical crystallization pathways modified after Cölfen and Antonietti (2005a;b): a) classical crystallization where nucleation clusters form and grow until they reach r_c growing to a primary nanoparticle which is amplified to a single crystal; b) the primary nanoparticles arrange and form an iso-oriented crystal where the nanocrystalline building units can crystallographically lock in and form a single crystal by fusing; c) the primary nanoparticles are covered by additives (e.g. a polymer), undergo a mesoscale assembly and form a mesocrystal.

Nanoparticle-mediated non-classical crystallization can be relevant for biological systems, as crystallization is thought to be practically independent of ion products or molecular solubility and might occur without osmotic pressure or pH change in the crystallization medium (Niederberger & Cölfen 2006). According to Niederberger & Cölfen 2006, the precursor particles can be formed independently at different locations and can be stored and transported to the site where the crystallization occurs so that precipitation effects (pH changes or elevated ion concentrations) do not affect this site. Crystallization under kinetic control can

occur at high supersaturation conditions promoting a fast particle nucleation which often involves an initial amorphous phase that can be highly susceptible to rapid phase transformation. As well, additives such as specific ions or molecules in the crystallization medium can lead to the predominance of the kinetic control (Meldrum & Cölfen 2008).

1.2.2 Hydrogels as Organic Matrices for Biomimetic Composites

Hydrogels show features which are quite similar to those of biological organic matrices. They are excellent models of the extracellular matrix microenvironment and are therefore highly suitable for mimicking biomineralization processes (e.g. Estroff et al. 2004, Asenath-Smith et al. 2012, Nindiyasari et al. 2014a,b; 2015 and references therein). For that purpose, hydrogels such as gelatin, agar, agarose, silica, polyacrylamide are popular materials as they show characteristics of organic matrices in biominerals (Dorvee et al. 2012 and references therein)

Recent studies on biomimetic mineralization have shown that crystals grown in hydrogels incorporate the gel matrix during growth and can therefore be described as mineral-gel composites (e.g. Li et al. 2009; 2011, Nindiyasari et al. 2014a,b; 2015, Greiner et al. 2018b). The growth rate of the crystal (which is related to the supersaturation) and the gel strength influence the amount of gel incorporated into the crystal. During growth, the crystal applies pressure against the hydrogel matrix. When the hydrogel is weak and the growth rate is slow, the hydrogel is pushed away by the crystal and only minor amounts of gel accumulate inside the crystal. In contrast, a strong hydrogel can resist the crystallization pressure which leads to a larger amount of hydrogel incorporated into the crystal (Li & Estroff 2009, Asenath-Smith et al. 2012). A strong hydrogel combined with a slow growth rate significantly lowers the crystal co-orientation within the aggregate. The distribution pattern of gel within the aggregate is mainly determined by the growth rate, e.g. slow growth rates in a strong gel result in oscillations or local accumulations of the gel within the composite (Greiner et al. 2018b).

1.3 Replacement Reactions

Replacement reactions play a significant role in numerous large-scale geological processes such as metamorphism, weathering, and metasomatism. Replacement reactions are processes which result from solid-fluid-interactions at rock or mineral grain surfaces. Moreover, mineral replacement is the fundamental process of Earth's rock cycle. In the Earth's crust and on the surface, most of the mineral assemblages are influenced by fluid-solid interactions. Replacement reactions are processes which result from solid-fluid-interactions at rock or mineral grain surfaces. If minerals get into contact with a fluid which is out of equilibrium, re-equilibration takes place to reduce the free energy of the system (Putnis & Putnis 2007, Putnis 2009, Ruíz-Agudo et al. 2014, Altree-Williams et al. 2015).

In natural environments, replacement reactions also occur during fossilisation and diagenetic overprint and under moderate hydrothermal conditions. Here, for example biogenic aragonite and (magnesian) calcite is replaced by inorganic calcite, magnesite is substituted by aragonite, or calcium sulphate minerals such as anhydrite and gypsum are replaced by calcium carbonate polymorphs (carbonation) (Freyer & Voigt 2003, Casella et al. 2017; 2018a;b;c and references therein). To name more examples, buried bone remains are subject to diagenetic processes which can alter their chemical composition and structure such as the loss of organic matter (mainly collagen) and/or ionic and isotopic exchange of the bone mineral with the surrounding fluids and sediments (Hedges 2002, Tütken 2003). Here, the buried remains can undergo recrystallization processes. It is assumed that crystallographic parameters such as lattice parameters and crystallite size of the apatite crystallites in bone correlate with archaeological age. Smaller crystallites are dissolved and subsequently recrystallize to larger, more thermodynamically stable crystals (Nielsen-Marsh et al. 2000, Hedges 2002). Moreover, the bioapatite in bone can get dissolved and secondary minerals such as inorganic hydroxyapatite or calcite may form (Schmahl et al. 2017). Under certain conditions, e.g. when the remains are buried in a sarcophagus or in shaft graves, the destruction of the corps by microorganisms leads to an acid milieu. Here, the bone apatite is turned into brushite which is the more stable calcium phosphate phase in acid media (Herrmann & Newesely 1982). Furthermore, the bone apatite chemical composition and structure changes in consequence of heat treatment. The cremation of human remains was a common funeral rite for many cultures e.g. the Romans (Grupe et al. 2015), therefore investigations on archaeological cremated bone finds are challenged by the heat-induced changes in bone. When heated at 700 °C and higher

temperatures, the bioapatite recrystallizes and significant crystallite growth sets in (Greiner et al. 2019).

Replacement reactions are also applied to produce biomaterials which are highly relevant for biomedical devices and tissue engineering. The biomaterial is used to improve or to restore the normal biological function of the damaged tissue. Due to their biologic nature, skeletons of marine organisms are biodegradable, biocompatible and osteoconductive, which stimulates osteogenesis, giving them high potential for medical applications. To name an example, natural corals have been used for more than ten years as bone substitute due to their similar pore structure to that of human bone (Maxwell et al. 2005, Lalzawmliana et al. 2019). The so called replamineform process is a technique for the fabrication of porous bone replacement materials. Here, the microstructure of marine invertebrates is used as template and their carbonate skeleton is converted to apatite by hydrothermal treatment (White et al. 1972, Roy & Linnehan 1974, Damien & Revell 2004).

1.3.1 The Dissolution-Reprecipitation Mechanism

Dissolution and precipitation are the fundamental driving mechanisms for re-equilibration reactions when a fluid phase is present. First, the parent mineral gets dissolved due to contact with an unsaturated fluid which causes supersaturation of a thermodynamically more stable phase at interfacial layers. Eventually, the product phase nucleates and grows at the parent mineral's surface controlled by the local supersaturation occurring at the interface of the replacement reaction. The dissolution rate of the primary mineral phase and the precipitation of the secondary minerals phase are coupled; therefore, the mechanism of mineral replacement reactions can be described as "coupled dissolution-reprecipitation reaction". Hereby the dissolution of the parent mineral is the rate-limiting process to the precipitation rate of the product mineral phase. The replacement of the parent mineral by another can result in the formation of pseudomorphs of the parent phase whose external shape and volume is preserved (Putnis 2002, Putnis & Putnis 2007, Putnis 2009, Ruíz-Agudo et al. 2014). Two of the main characteristics of pseudomorphic replacement reactions are the preservation of the external dimensions and the development of porosity. The molar volume and the solubility of the secondary phase are lower than for the parent phase, this is compensated by the formation of numerous pores and/or cracks. The generation of porosity enables the fluid to react with the parent mineral interface (Fernández-Díaz et al. 2009, Xia et al. 2009a; b). The formed

porosity allows continuous access of the fluid to the reaction front and eventually the complete replacement of the parent phase by the product phase (Pedrosa et al. 2016).

1.4 Author Contributions and Thematic Overview of Scientific Works

This thesis is the detailed report of the author's Ph.D. research work on crystal growth and mineral replacement reactions in biomimetic and biological calcium carbonate and calcium phosphate composites.

Three chapters in the Results and Discussion section of this thesis are scientific research manuscripts which were published as journal articles (chapters 2.2, 2.5 and 2.6). Martina Greiner is the principal author of those three published manuscripts:

Chapter 2.2 was published in Crystal Growth and Design. Martina Greiner and Florian Weitzel performed the experiments; M.G., Erika Griesshaber, Lurdes Fernández-Díaz and Sabino Veintemillas-Verdaguer analysed the data; Andreas Ziegler and Xiaofei Yin contributed to biochemical preparation, X.Y., E.G., L.F.-D., M.G., W.W.S. and S.V.-V. contributed to the discussion. L.F.-D., E.G. and M.G. wrote the paper. W.W.S. was the scientific supervisor.

Chapter 2.5 was published in Journal of Archaeological Science: Reports. Katrin Mayer, Balazs Kocsis and Martina Greiner conceived and designed the experiments; M.G. and K.M. performed the experiments; M.G., Alejandro Rodríguez-Navarro and Mario F. Heinig analysed the data; Anita Toncala, B.K. and Andrea Göhring contributed to sample preparation and sample logistics; M.G., A.R.-N., A.T., A.G., Gisela Grupe and Wolfgang W. Schmahl contributed to the discussion; M.G. wrote the paper. W.W.S. and G.G. were the scientific supervisors.

Chapter 2.6 was published in Minerals. Lurdes Fernández-Díaz, Sabino Veintemillas-Verdaguer and Martina Greiner conceived and designed the experiments; M.G. performed the experiments; M.G. and Erika Griesshaber and Moritz N. Zenkert analysed the data; Andreas Ziegler and Xiaofei Yin contributed to biochemical preparation, S.V.-V. contributed to the discussion. Wolfgang W. Schmahl and S.V.-V. read the final version of the manuscript; L.F.-D., E.G. and M.G. wrote the paper.

Chapter 2.3 is a verification report written by Martina Greiner in the framework of the DFG research group FOR 1670. M.G. and Moritz N. Zenkert analysed the data; Simon Trixl collected and identified the samples; Ferdinand M. Neuberger, Andrea Grigat and Anita

Toncala contributed to sample preparation and sample logistics; M.G. and Wolfgang W. Schmahl contributed to the discussion; W.W.S. and Joris Peters were the scientific supervisors; M.G. wrote the paper.

Chapters 2.1 and 2.2 of this thesis focus on the crystallization of apatite and calcium carbonate in hydrogel biomimetic counter-diffusion (double-diffusion) systems. Chapters 2.3 and 2.5 of this thesis focus on the structural and chemical variations of bone mineral and compositional and structural changes of bone in consequence of heat-treatment. Chapter 2.4 of this thesis is a short study on the decomposition of bovine bone under acidic conditions and investigates a possible phase transformation from bioapatite to brushite and/or monetite. Chapter 2.6 focuses on the dissolution-reprecipitation mechanism and reaction kinetics of biological aragonite with different microstructures substituted by apatite.

2. Results and Discussion

2.1 Biomimetic Apatite-Hydrogel Composites

2.1.1 Introduction

The mineralization of dentine and bone is controlled by an organic matrix which contains about 90 wt% collagenous proteins. In contrast, the enamel extracellular matrix mainly consists of non-collagenous proteins (enamelins and amelogenins) (Goldberg et al. 1995, Elliott 2002). The protein amelotin (AMTN) has been recently discovered and influences directly the biomineralization process during dental enamel formation. It promotes apatite (AP) mineralization and regulates the enamel AP microstructure (Abbarin et al. 2015). The biomineralization process can be mimicked by a double-diffusion experimental setup (u-tube columns) with two reservoirs of two reagent solutions separated from each other by hydrogel (e.g. Kniep & Busch 1996, Busch et al. 1999, Asenath-Smith et al. 2012, Wang et al. 2015). Aggregates which are formed in hydrogels incorporate the gel matrix, therefore those aggregates are mineral-polymer composites (e.g. Li & Estroff 2007; 2009, Li et al. 2011, Asenath-Smith et al. 2012, Greiner et al. 2018b).

With this short study we aim to investigate the influence of the protein AMTN on the crystallization of AP composites in hydrogel matrices. The crystal aggregates are characterized by X-ray Powder Diffraction (XRPD), Rietveld refinement (Rietveld 1969) and imaged by scanning electron microscopy (SEM).

2.1.2 Materials and Methods

Crystallization experiments were carried out at room temperature using a double-diffusion column system of 95 mm in length and 9 mm in diameter consisting of a horizontal and two vertical branches. The horizontal branch was filled with agarose or gelatin hydrogel while the vertical branches were filled with 5 ml of reagent aqueous solutions: Gelatin from porcine skin (300 g bloom, Sigma Aldrich) and Agarose (type I-A, low EEO, Sigma Aldrich) were prepared by dissolving gelatin/ agarose in 1M Tris(hydroxymethyl)aminomethane (Trizma base, $\geq 99.9\%$, Sigma Aldrich) and hydrochloric acid (HCl, HACH) buffer solution that was heated up to 60 °C (gelatin) and 80 °C (agarose) and adjusted to pH 7.2. Two different gelatin concentrations (2.5 wt% and 10 wt%) and two different agarose concentrations (0.5 wt% and 2 wt%) were prepared.

For details about the AMTN protein expression the reader can refer to Abbarin et al. 2015. 140 µg freeze-dried AMTN was dissolved in 1.4 ml Milli-Q water. 14 µl of 5 % w/v sodium azide solution NaN$_3$) was added to the AMTN-solution and mixed thoroughly to avoid bacterial or fungal growth. Control columns without AMTN were prepared for comparison.

Hydrogels were poured into the horizontal branch and 0.1 ml of the AMTN- NaN$_3$ solution was injected into the hydrogel with a syringe. The hydrogels were kept at room temperature for gelation and left for 24 hours to settle. Aqueous reagent solutions were prepared using the Tris-HCl buffer solution and adjusted to pH 7.2: 0.6 M Diammoniumhydrogenphosphate (BioUltra, $\geq$ 99.0%, Sigma Aldrich) and 1 M calcium chloride (BioXtra, $\geq$ 99.0%, Sigma Aldrich). Reagent solutions were poured into the vertical branches of the column. All solutions were prepared using high purity deionized (Milli-Q) water (18.2 MΩ). Aggregates were extracted after six weeks by dissolving the gel in hot water. The precipitate was filtered through a 0.2 µm pore-sized membrane, and the aggregates were washed three times with hot Milli-Q water and air-dried at room temperature.

X-ray diffractograms were measured on a General Electric 3003 powder diffractometer in Bragg-Brentano reflection geometry. Cu-K$_{\alpha1}$ radiation was selected with a focusing monochromator in the primary beam. An exposure time of 500s on a 1D-Meteor detector was chosen, which resulted in a data collection time of 2.5 hours for a diffractogram from 10-110° 2θ.

The instrumental resolution function was experimentally determined with a NIST LaB$_6$ standard. For data evaluation and Rietveld refinement (Rietveld 1969) we applied the FULLPROF code (Rodríguez-Carvajal 1993, Rodríguez-Carvajal & Roisnel 2004) and chose a hexagonal symmetry model (Wilson et al. 2004) for refinement.

For full profile analysis, we applied the Thompson-Cox-Hastings method for convolution of instrumental resolution (as determined with a NIST LaB$_6$ standard) with anisotropic size and isotropic microstrain broadening (Thompson et al. 1987).

2.1.3 Results and Discussion

X-ray diffractograms of all aggregates harvested from the double-diffusion experiments only show reflections which can be assigned to apatite, no formation of further calcium phosphate phases could be observed.

Table 2.1-1. Overview of all experimental conditions conducted in this study, the crystalline phase identified by XRPD, and crystallite sizes calculated by Rietveld refinement. The estimated standard deviation for crystallite sizes is 5 %.

hydrogel and conc. [wt%]	AMTN conc. [mg/ml]	phase	crystallite size in a direction [Å]	crystallite size in c direction [Å]
gelatin 2.5	-	AP	92	447
gelatin 2.5	0.1	AP	95	500
gelatin 10	-	AP	89	420
gelatin 10	0.1	AP	146	777
agarose 0.5	-	AP	113	472
agarose 0.5	0.1	AP	129	579
agarose 2	-	AP	150	601
agarose 2	0.1	AP	118	489

Exemplary Rietveld refinements of apatite aggregates grown in 10 wt% gelatin are shown in Figure 2.1-1. The diffractogram of the aggregates grown with AMTN in Figure 2.1-1a shows sharper diffraction peaks than the diffractogram of the aggregates grown without AMTN in Figure 2.1-1b, especially the 211, 112 and 030 reflections from 31-33.5° 2 Theta. According to the refinements, crystallite size for apatites grown with AMTN is 777 Å in c- and 146 Å in a-direction; for apatites grown without AMTN the crystallite size is 420 Å in c- and 89 Å in a-direction (Table 2.1-1). However, for lighter gelatin concentrations (2.5 wt%) we can only observe slightly larger crystallite sizes for the aggregates grown with AMTN (Table 2.1-1). AP crystallites grown in light agarose hydrogel (0.5 wt%) display slightly larger crystallite sizes when AMTN is added to the experiment (Table 2.1-1). In comparison, we observe the opposite phenomenon for denser agarose gel (2 wt%) where apatite crystallites are smaller when AMTN is added (Table 2.1-1).
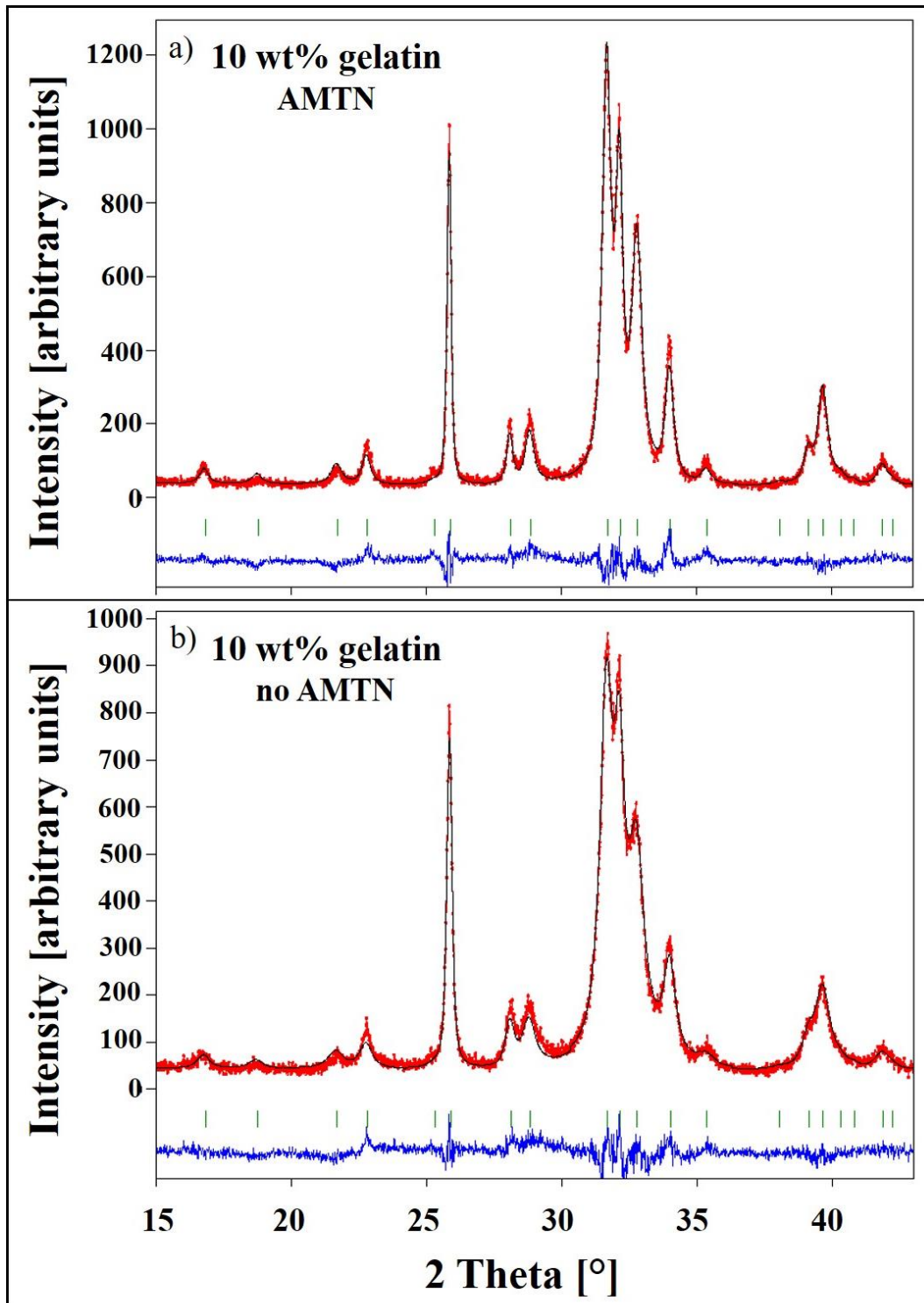
Figure 2.1-1. Rietveld refinement (15-42° 2θ) of **a)** apatite aggregates grown in 10 wt% gelatin with 0.1 mg/ml AMTN **b)** apatite aggregates grown in 10 wt% gelatin without AMTN. Red dots: observed data points; black line: calculated XRD profile; bottom blue line: difference of observed and calculated data; green vertical bars: positions of diffraction peaks of apatite.

SEM imaging is rather difficult due to the nano-size of the apatite crystal aggregates, however crystallites grown in 0.5 wt% agarose without AMTN are shown in Figure 2.1-2.
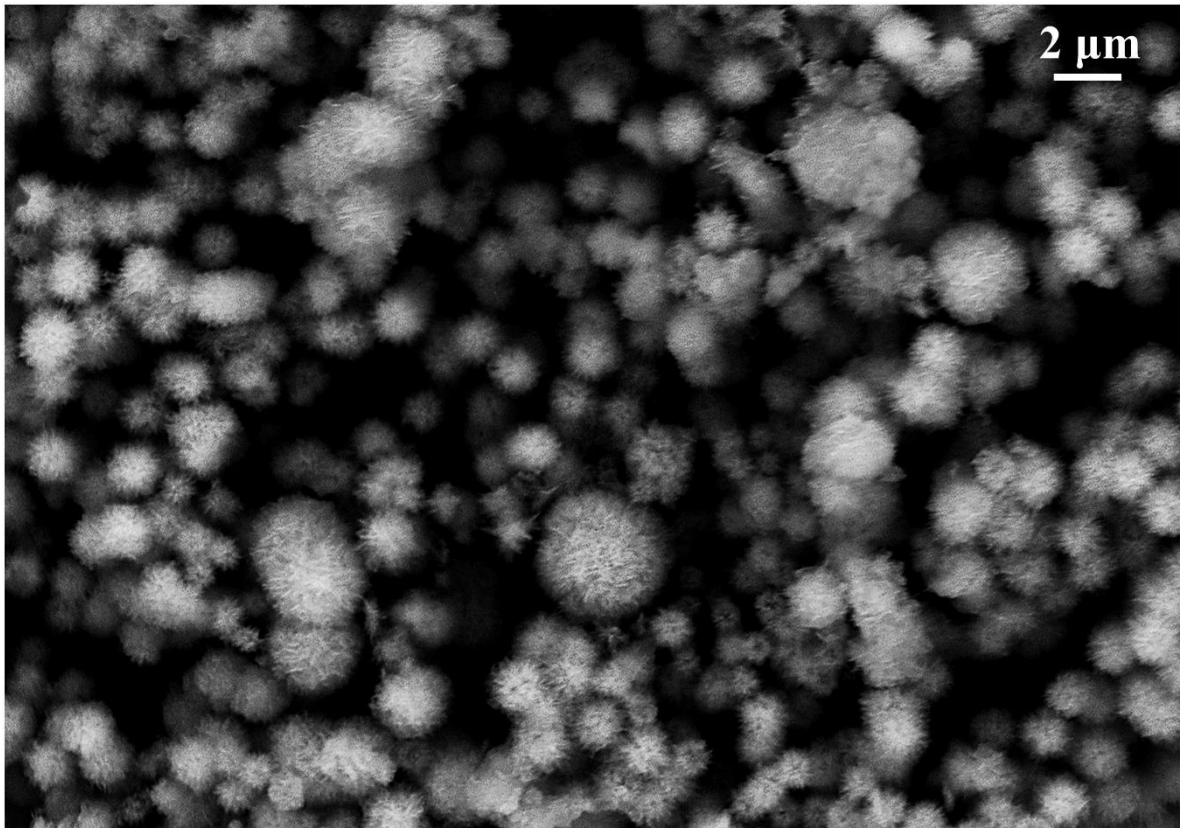
Figure 2.1-2. BSE-SEM image of mineral precipitates (AP) grown in 0.5 wt% agarose (no AMTN).

In conclusion, all apatite crystal aggregates which were grown with AMTN gave larger crystallites than the crystallites grown without AMTN, except the experiment with agarose 2 wt%. However, experiments need to be repeated to ensure reproducibility of the obtained results. In addition, TEM (transmission electron microscope) imaging will give further information about the morphology of the nanocrystalline apatites. Moreover, further studies on the influence of different AMTN concentrations on apatite crystal growth need to be conducted.

2.2 The Combined Influence of Reagent Concentrations and Agar Hydrogel Strength on the Formation of Biomimetic Hydrogel-Calcite Composites

Martina Greiner[1], Xiaofei Yin[1], Lurdes Fernández-Díaz[2,3], Erika Griesshaber[1], Florian Weitzel[1], Andreas Ziegler[4], Sabino Veintemillas-Verdaguer[5], and Wolfgang W. Schmahl[1]

1 Department für Geo-und Umweltwissenschaften, Ludwig-Maximilians-Universität, 80333 Munich, Germany

2 Departamento de Cristalografía y Mineralogía, Universidad Complutense de Madrid, 28040 Madrid, Spain

3 Instituto de Geociencias (UCM, CSIC), Ciudad Universitaria, 28040 Madrid, Spain

4 Central Facility for Electron Microscopy, University of Ulm, 89081 Ulm, Germany

5 Instituto de Ciencia de Materiales de Madrid, (ICMM, CSIC), 28049 Madrid, Spain

2.2.1 Abstract

We report results of CaCO$_3$ crystallization experiments by counter diffusion in agar gel with two different solid contents (0.5 and 2 wt%) and two solute concentrations (0.1 M CaCl$_2$, 0.1 M Na$_2$CO$_3$; 0.5 M CaCl$_2$, 0.5 M Na$_2$CO$_3$). Solute concentration and hydrogel strength influence the characteristics of the gel/mineral composite formation.

High reagent solution concentrations give rise to high supersaturation and high growth rates. When combined with a light gel, *single crystal composites* form; in a dense gel the aggregates are *mosaic crystal composites*. Low reagent solution concentrations result in low supersaturation and low growth rates; when combined with a light gel, *single crystal composites* form; in a dense gel, the precipitate is a *co-oriented polycrystal composite*.

Gel occlusion within the mineral increases with gel density. Gel distribution inside the mineral is homogenous for high growth rates. For low growth rates, the gel accumulates locally in the precipitates. Light gels are pushed ahead by the growing crystals and gel occlusion into the mineral is decreased; at low reagent solution concentrations slightly more gel gets occluded.

In conclusion, agar gel solid content determines the amount of gel occlusion and calcite orientation organization; reagent solution concentration influences the mode of gel distribution inside the mineral/gel composite aggregates.

2.2.2 Introduction

Hydrogels are popular platforms for biomimetic crystallization studies due to the numerous characteristics that these systems share with natural biomineralisation environments (Asenath-Smith et al. 2012). Carbonate biominerals are mineral-biopolymer composites with enhanced mechanical properties compared to those of their inorganic counterparts (Goetz et al. 2011). The occlusion of a biopolymer network in biogenic crystals is associated with microstrain fluctuations and decreased grain sizes to the presence of occluded biopolymer network and it has been argued that a connection exists between these features and the exceptional mechanical performance of these materials (Pokroy et al. 2006a, b). Synthetic calcite crystals containing a variety of occluded polymers, micelles and/or metal oxide nanoparticles have been produced (Munoz-Espi et al. 2005, Kim et al. 2010; 2011; 2014). Recent biomimetic investigations (Li & Estroff 2009, Li et al. 2011, Nindiyasari et al. 2014a, b; 2015) have shown that calcite crystals grown in a variety of gels, such as silica, agar, agarose, and gelatin incorporate the gel matrix during growth and, consequently, can be described as mineral-gel composites. Their microstructural characteristics bear similarities to those of carbonate biominerals (Li & Estroff 2007; 2009, Huang et al. 2008, Simon et al. 2011, Asenath-Smith et al. 2012, Nindiyasari et al. 2014a, b; 2015). More recently, a direct relationship between increasing biopolymer content and increasing calcite (composite) hardness, which derives from the reduced mobility of dislocations due to the high density of dislocations generated by the biopolymer occlusion-related lattice strain, has been demonstrated for synthetic calcite-amino acid composites (Kim et al. 2016).

It has been proposed that gel matrix incorporation within a growing crystal is mainly controlled by two parameters: gel strength and the growth rate of the composite. The strength of a given gel can be modified by changing its solid content (Li & Estroff 2009, Asenath-Smith et al. 2012). High values of both, gel strength and growth rate, result in occlusion of most of the gel within the crystal (Li & Estroff 2009, Asenath-Smith et al. 2012). In contrast, a weak gel and a low growth rate leads to the formation of crystals that contain only small amounts of gel or are virtually gel-free (Li & Estroff 2009, Asenath-Smith et al. 2012). The growth rate of a crystal depends on supersaturation (De Yoreo et al. 2003), which in a hydrogel system will vary as crystal growth proceeds according to the balance between mass transfer from the reagent deposits to the growing crystal location and the consumption of dissolved ions in the gel solution surrounding the growing crystal (Prieto et al. 1991, Sánchez-Pastor et al. 2011). In order to guarantee that a significant supersaturation is achieved and

maintained during growth, the concentration of the reagents needs to be high. However, as mass transfer through a gel almost exclusively occurs by diffusion (Henisch 1988), any condition (e.g. gel density) that affects the characteristics of the gel pore network and diffusion properties of the gel will also play a key role in defining degrees of supersaturation and growth rate evolution. It stands to reason that mass transfer through less porous, thicker gels will occur at a slower rate, preventing that crystal growth proceeds at high supersaturation (Sancho-Tomás et al. 2014).

In this study we discuss characteristics of gel occlusion into calcite together with calcite organization in agar gel-calcite composites grown in agar gels with two different solid contents and with two different reagent solution concentrations. We investigate four different growth scenarios defined by distinct gel strengths, supersaturation conditions and growth rate evolutions. We aim to understand (1) the combined influence of gel strength and growth rate on the amount of agar polymeric matrix occlusion into composite aggregates, (2) the characteristics of biopolymer distribution in the mineral component of the aggregate, (3) the influence of gel incorporation on internal microstructuring of the calcite, aggregate development and growth. We interpret our results considering observations obtained from other biomimetic systems as well as from carbonate biominerals.

2.2.3 Experimental Procedures

Table 2.2-1 summarizes experimental conditions in our four counter-diffusion crystal growth experiments. Crystallization experiments were carried out at 7 °C using a double-diffusion column system of 120 mm in length and 9 mm in diameter consisting of a horizontal and two vertical branches (Fig. 2.2-S1). The horizontal branch was filled with agar gel, while the vertical branches were filled with 5 ml of reagent aqueous solutions: calcium chloride (0.5 M or 0.1 M $CaCl_2$, Sigma Aldrich) and sodium carbonate (0.5 M or 0.1 M Na_2CO_3, Sigma Aldrich). Agar hydrogel was prepared by dissolving agar (Sigma Aldrich, plant cell culture tested) in water that was heated up to 80°C. The gel was poured into the horizontal branch, kept at 7 ºC for the gelation to take place and left for 24 hours to settle. We prepared gels with two different agar solid contents: 0.5 wt% and 2 wt%. Subsequently the reagent solutions were poured into the vertical branches of the column (Fig. 2.2-S1). All solutions were prepared by using high purity deionized (Milli-Q) water (18.2 MΩ).

Table 2.2-1. Experimental conditions of experiments A to D conducted in this study.

experiment	agar wt%	CaCl$_2$ (M)	Na$_2$CO$_3$ (M)	phases
A	0.5	0.5	0.5	calcite, vaterite ~ 9 wt%
B	0.5	0.1	0.1	calcite
C	2	0.5	0.5	calcite
D	2	0.1	0.1	calcite

Experiments A and C lasted for 11 weeks, while experiments B and D were conducted for 9 weeks. Aggregates were extracted by dissolving the gel in hot water. The precipitate was filtered through a 0.2 μm pore-sized membrane, the aggregates were washed 3 times with hot (60 °C) Milli-Q water and air-dried at room temperature.

Carbonate phase determination (Table 2.2-1) was performed with powder X-ray diffraction using a Bragg-Brentano type X-ray diffractometer (GE: XRD 3003 TT). XRD data were collected with a Cu K$_{\alpha1}$- radiation and a 2θ angle range between 10°-110° with a step size of 0.013°. Powder patterns were analysed with the Rietveld method (Rietveld 1969) using the program FullProf (Rodríguez-Carvajal 1993). The background was corrected by a 6-coefficient polynomial function.

Refinements were conducted using the structural model of calcite published by Maslen et al. (1993) and that of vaterite published by Kamhi (1963).

All investigated aggregates are composites of calcite and agar hydrogel. For visualizing the gel and its fabric within the gel-mineral composites, microtome polished (Seidl & Ziegler 2012) gel-mineral surfaces were etched for 90 seconds with a solution containing 0.1 M HEPES buffer at a pH of 6.5 and 2.5% glutaraldehyde for fixation. Etching was stopped by washing the samples 3 times for 10 minutes with 100% isopropanol. The mineral-hydrogel interface was exposed by etching the composite surface for 1 hour using 0.25 M HEPES buffer and 0.05 M EDTA (pH= 7.8) containing 2.5 % glutaraldehyde and 8 % paraformaldehyde as fixation solution. Subsequently the samples were washed 3 times with double distilled water for 10 minutes, and then dehydrated with an isopropanol series (30 %, 50 %, 70 %, 90 %, 100 %). Both, etched and decalcified samples were critical point dried in a BAL-TEC CPD 030 (Liechtenstein) after the chemical treatments. Carbon coating was applied for SEM observation.

Electron backscattered diffraction (EBSD) measurements were performed on microtome cut and polished aggregate surfaces coated with 4-6 nm of carbon. Both, EBSD measurements as well as the visualization of aggregate morphologies and surfaces, were carried out with a field emission SEM, SU5000, equipped with a Nordlys II EBSD detector and AZTec and CHANNEL 5 HKL software.

In this study, diffraction data gained from EBSD measurements are processed for the visualization of:

(a) Crystal orientation patterns (shown with colour-coded orientation maps and corresponding pole figures). Contoured versions of the pole figures show the strength of the clustering of the poles. We use in this study the lowest possible degree for half width and cluster size parameters for contouring in the Oxford Instruments CHANNEL 5 EBSD software, a half width of five degrees and a cluster size of three degrees, respectively. The half width controls the extent of the spread of the poles over the surface of the project sphere. A cluster comprises data with the same orientation. Crystallographic axes co-orientation strength is derived from the maximum value of the pole density distribution and is expressed with the multiple of uniform (random) distribution (MUD) value, calculated with the Oxford Instruments CHANNEL 5 EBSD software. High MUD values indicate high crystal co-orientation, while low MUD values reflect a low to random co-orientation.

(b) Local kernel misorientation maps, which show the deviation in orientation between neighbouring measurement points, calculated for 11x11 pixel clusters. This deviation corresponds to local internal strain. We attribute this strain to gel occlusion within the composite as this feature is not observable on calcite single-crystals grown from solution.

(c) Misorientation maps, which show the angle of misorientation for all measurement points with respect to a chosen reference orientation. For a grain we choose the most frequent values of the three Euler angles among the data points within the grain. These maps depict information such as the deviation from the mean orientation of a grain.

(d) Point-to-origin misorientation profiles, which depict the angle of misorientation with respect to a chosen reference orientation for all measurements points along the trajectory of a line through a map. We use the orientation of the starting point of the line as reference orientation. Misorientation (in degrees) is plotted as a function of distance (in μm) from the reference point.

Figure 2.2-S2 shows processed EBSD data measured on a calcite single crystal grown from solution. We use this crystal as a reference to the investigated composite aggregates in this study, as this calcite single crystal does not contain any occluded gel. Figure 2.2-S2 visualizes local kernel misorientation calculated for a 3x3 (Fig. 2.2-S2a) and an 11x11 pixels cluster (Fig. 2.2-S2b), respectively. The misorientation map with the point-to-origin profile A to B is shown in Figure 2.2-S2c.

Thermal gravimetric analyses (TGA) of calcite-gel composites were conducted in a TA Instruments Q500 under a flowing-air atmosphere. The initial weight of composites used for TGA measurements varied between 9 and 17 mg and comprised all composites that were recovered from 6 gel columns used for each crystal growth experiment. A sample of optical quality calcite from Naica, Chihuahua (Mexico) was analysed under identical conditions and used as reference. All the samples were heated from ambient temperature to 850 °C at a rate of 5 °C per minute. The weight loss trend of chosen samples as a function of temperature is depicted in Figure 2.2-S3. The gel content of the calcite-agar composites formed in each experiment was estimated by measuring their weight loss between 150 and 380 ºC and comparing it to the weight loss undergone by the reference sample in the same temperature range. This temperature range was defined based on the width of an exothermic peak in the differential thermal analyses (DTA) of the synthetic samples.

2.2.4 Results and Discussion

Aggregate Morphologies and Mineral Organization in Agar Gel-mineral Composites
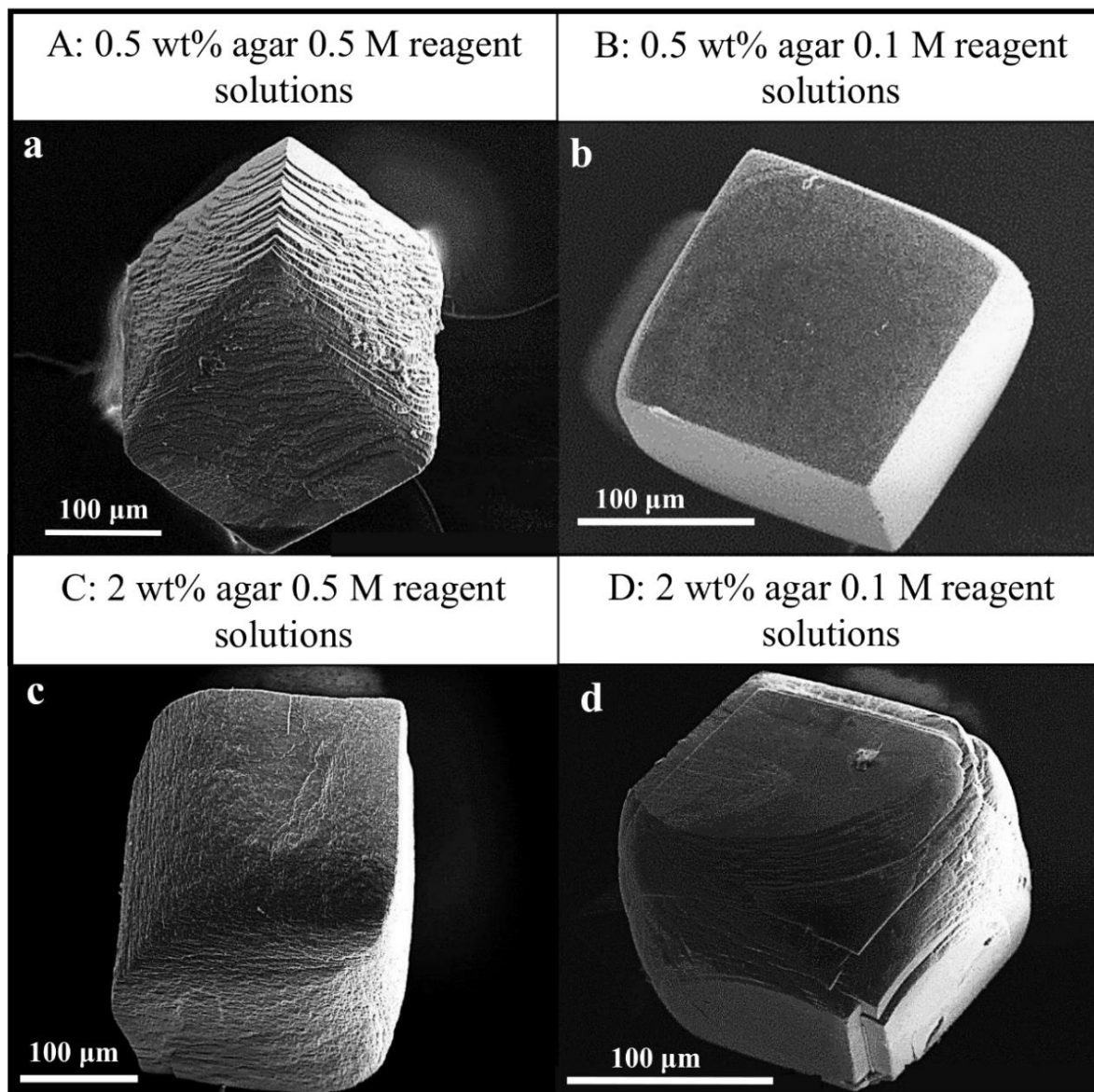
Figure 2.2-1. FE-SEM images showing the variety of morphologies of calcite−agar aggregates that were obtained from crystallization experiments by using experimental conditions A−D. A: 0.5 wt % agar, 0.5 M reagent solution concentration; B: 0.5 wt % agar, 0.1 M reagent solution concentration; C: 2 wt % agar, 0.5 M reagent solution concentration; D: 2 wt % agar, 0.1 M reagent solution concentration.

Figures 2.2-1, -2, -3 and appendix Figures 2.2-S4, -S5, -S6, -S7 visualize aggregate morphologies (Figs. 2.2-1, 2.2-S4), their surfaces (Figs. 2.2-2a, -2c, -S5, -3a, -3c, -S6) and patterns of mineral organization (Figs. 2.2-2b, -2d, -3b, -3d, -S7) in composites grown at experimental conditions A to D (Table 2.2-1). Calcite forms the major mineral in all precipitates.

However, for experimental setup A, Rietveld analyses document minor amounts of vaterite (which is spherically shaped, Fig. 2.2-S4a) in addition to calcite. Even though the majority of the calcite crystals show the typical, more or less distorted, rhombohedral habit (Fig. 2.2-1), at experimental conditions A, C, and D we also find radial aggregates of calcite.
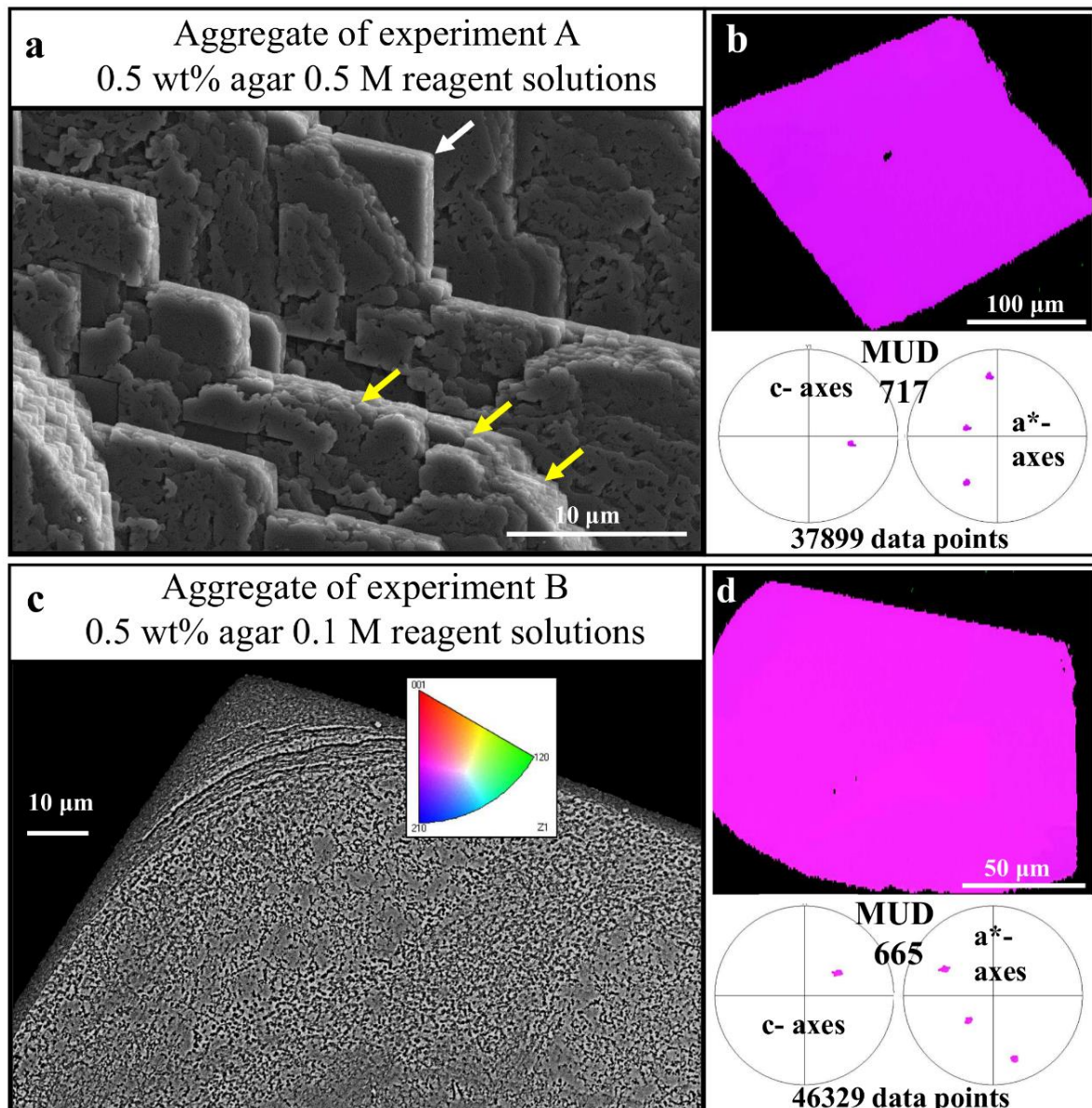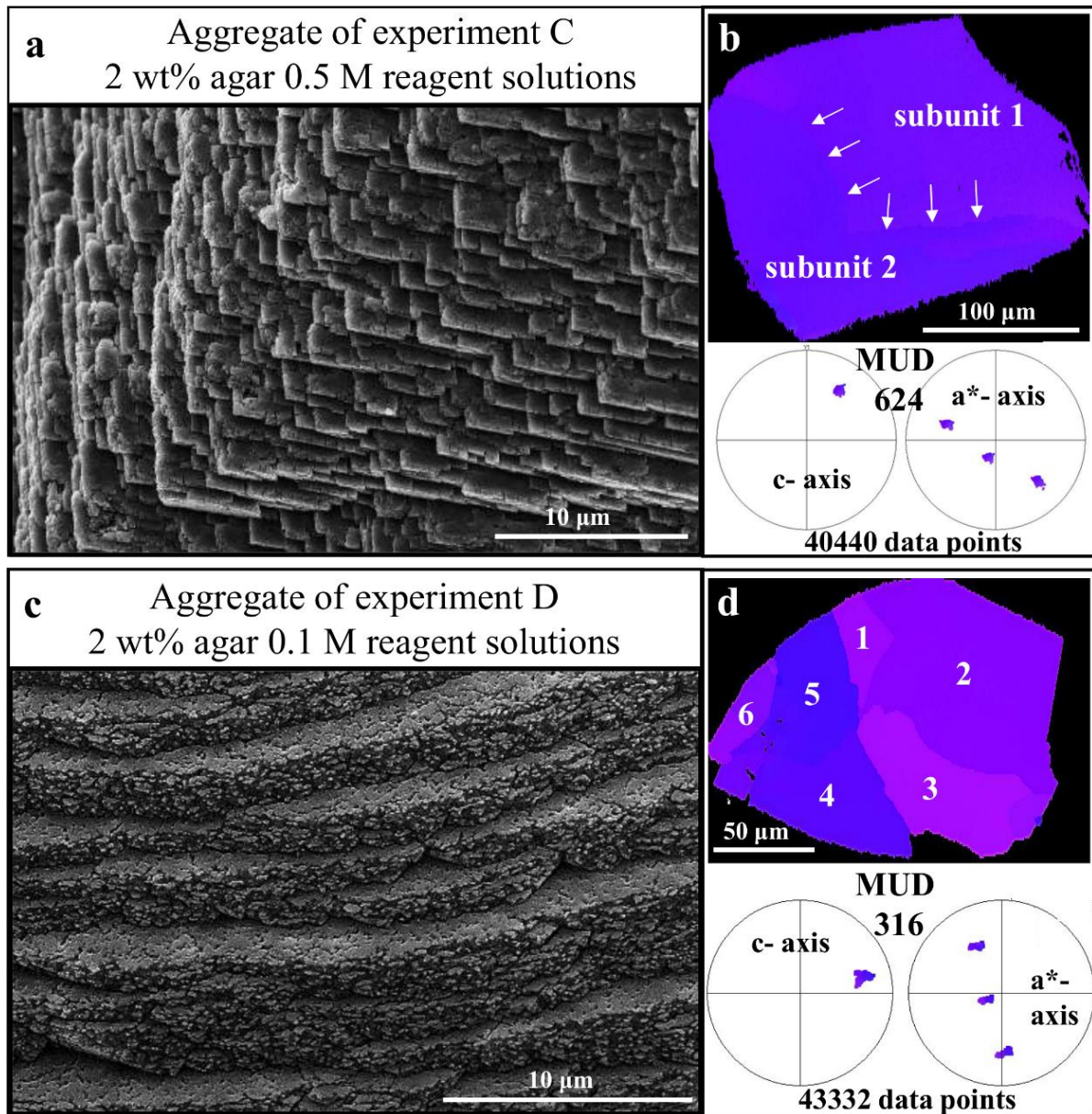

Figure 2.2-2. FE-SEM images of surfaces of calcite−agar aggregates obtained from experiments A and B (a,c). Two different edges are distinguishable on surfaces of aggregates grown at experimental condition A: slightly curved, roughly parallel to [010] (yellow arrows in a) and straight, parallel to the $[\bar{4}41]$ and $[48\bar{1}]$ directions (white arrow in a). (b,d) Calcite orientation with colour-coded EBSD maps and corresponding pole figures. In both, aggregate crystal coorientation is high as indicated by the high MUD (multiple of random uniform distribution) values.

These form predominantly at experimental conditions C and D and consist of a multitude of rhombohedral subunits (Figs. 2.2-S4b, -S4c).

The smoothness of calcite surfaces varies according to the used experimental conditions. Calcite surfaces that grew under experimental condition B are smooth (Fig. 2.2-2c), while surfaces of aggregates that formed at all other experimental conditions are rough, and are covered with growth steps (Figs. 2.2-2a, -3a, -3c, -S5, -S6). These steps are parallel to the $[\bar{4}41]$ and $[48\bar{1}]$ rhombohedral edges and to the [010] direction (Fig. 2.2-S5), thus, parallel to "periodic bond chains" (PBC) in the calcite structure (Heijnen 1985). For aggregates grown in experiment A (0.5 wt% agar, 0.5 M reagent solutions) steps bounded by straight $[\bar{4}41]$ and $[48\bar{1}]$ rhombohedral edges are clearly visible (white arrows in Figs. 2.2-2a, -S5a) next to rounded edges (yellow arrows in Figs. 2.2-2a, -S5a) that run roughly parallel to [010]. The surfaces of aggregates grown in experiment C show a much higher density of straight $[\bar{4}41]$ and $[48\bar{1}]$ rhombohedral edges which correlates with a significant increase in surface roughness (Fig. 2.2-3a). In aggregates formed in experiment D we observe particularly rough curved surfaces covered by a high density of rounded steps, where small straight sections oriented roughly parallel to $[\bar{4}41]$, $[48\bar{1}]$ and [010] can be distinguished (Fig. 2.2-3a). The surfaces of all aggregates contain pores. In aggregates of experiments A and B (Figs. 2.2-S6a, -S6b) pores are, however, less abundant and appear to be aligned to edges roughly parallel to crystallographic directions. A significantly higher density of pores, which have less regular shapes, is observed on the surface of aggregates grown in experiment C (Figs. 2.2-S6c). Surfaces of aggregates formed in experiment D have the highest porosity and are covered by numerous, homogeneously distributed, approximately spherical pores (Fig. 2.2-S6d).

Figures 2.2-2b, -2d, -3b, -3d and -S7 show patterns of calcite organization within the investigated aggregates in colour-coded EBSD maps and corresponding pole figures. The strength of crystal co-orientation is expressed with the MUD value for *c*-axes' pole density distributions. The MUD value of an EBSD scan is high when crystal co-orientation is high (e.g. in the case of single crystals), it is low when crystal co-orientation is low (e.g. in the case of polycrystals). For calcite single crystals grown from solution the MUD value is 725 (Nindiyasari et al. 2015).

Figure 2.2-3. FE-SEM images of surfaces of calcite−agar aggregates obtained from experiments B and C (a,c). Note the presence of numerous surface steps, which are rougher in the case of the composite obtained from experiments with 2 wt % agar and 0.1 M reagent solution concentration. (b,d) Calcite orientation with colour-coded EBSD maps and corresponding pole figures. When a strong gel (2 wt % agar) is used, subunit formation takes place. In the aggregate shown in (b), the homogeneity of colour indicates that the subunits are only minutely misoriented relative to each other; accordingly, the aggregate has a high MUD (multiple of random uniform distribution) value. In contrast, the aggregate depicted in (d) comprises several subunits. As the decreased uniformity in colour of the aggregate and the lower MUD values show, tilt between the subunits is increased in the aggregate.

All crystalline aggregates obtained in our experiments show an internal orientational spread (larger than that observed for the reference crystal, Fig. 2.2-S2), and in some of the aggregates this spread is related to clearly delimited slightly misoriented subunits. Such objects are referred to as mosaic crystals in the crystallographic literature (Darwin 1922, Hull 1975,

Wuttke 2014). Following Wuttke (2014) a mosaic crystal is an assembly of highly co-oriented crystalline blocks that are orientationally tilted relative to each other by a small angle. The individual subunits are separated by small angle grain boundaries (Hull 1975). These consist of an array of regularly spaced dislocations between which the lattice is coherently continuous across the small angle boundary. Increasing the "small" angle α the spacing D drops as D= B/tanα, where B is the length of the Burgers vector of the dislocations (Hull 1975). For the purpose of this article we arbitrarily define the upper limit of a "small" angle as the case when the spacing D drops below 10 times B (tanα= 0.1 → α= 5.7°), such that the disturbed structures around the dislocations overlap and the boundary becomes an incoherent large angle boundary (Hull 1975). Therefore, we consider boundaries with α > 5.7° as large angle boundaries.

The aggregates or crystals, respectively, that formed in experiments described in this article fall in three categories: (i) *single crystal composites* where small angle grain boundaries may be present but are insignificant within the experimental resolution. (ii) *mosaic crystal composites* with clear small angle boundaries (α < 5.7°). (iii) *Co-oriented polycrystal composites* which are aggregates consisting of co-oriented subunits with large angle boundaries between them (α > 5.7°).

Composites of experiment A show a high calcite crystal co-orientation (MUD value of 717, Fig. 2.2-2b) and no significant small or large angle grain boundaries. These are *single crystal composites* occluding minute amounts of biopolymers.

Aggregates obtained from experiment B have also high MUD values (MUD: 665, Fig. 2.2-2d). Relative to experimental condition A, a decrease in solution concentration from 0.5 to 0.1 M induces a slight decrease in calcite co-orientation strength. However, the aggregate can still be regarded as a *single crystal composite* as it does not seem to have any subunits (Fig. 2.2-2d). Thus, the concentration of reagent solutions does not influence the pattern and strength of calcite organization to a high degree.

Calcite organization within the aggregates is mainly influenced by the solid content of the gel (experiments C and D, Figs. 2.2-3b, -3d), such that an increase in gel solid content induces the formation of crystal subunits.

If the concentration of reagent solutions is high (experiment C, Figs. 2.2-3b, -S7), few subunits develop with misorientation angles well below 5.7°. Calcite co-orientation strength within the aggregate is still high (MUD: 624). This aggregate is a *mosaic crystal composite*.

A pronounced decrease in calcite co-orientation strength occurs when experiments are conducted with a high agar gel solid content and at low reagent solution concentrations (experiment D, Fig. 2.2-3d), as indicated by the low MUD value of 316 for the composite. Aggregates that form at these conditions are composed of several crystals or subunits which are misoriented relative to each other by more than 5.7°. These aggregates are *co-oriented polycrystal composites*.

Calcite co-orientation is highest for aggregates obtained at experiment A, thus, where the experiment was conducted with 0.5 wt% agar solid content and 0.5 M reagent solution concentrations (Fig. 2.2-2b). In contrast, the co-orientation of calcite is lowest for aggregates obtained from experiment D, thus, where agar solid content was 2 wt% and reagent solution concentrations were 0.1 M (Fig. 2.2-3d).

Characteristics of the Occluded Agar Polymeric Matrices

Figures 2.2-4 and 2.2-5 depict characteristics of gel occlusion within the aggregates, variations of the occluded hydrogel fabrics after composite formation, and hydrogel interlinkage with the mineral. Composites grown in light gels (0.5 wt % agar, experiments A and B) incorporate very low amounts of gel, more or less regardless of the concentration of the used counter-diffusing reagents (Fig. 2.2-S3). However, at close inspection, we find slight differences in the mode of gel occlusion, even in the case of light gels. The gel is more homogeneously distributed in composites that grow in the presence of highly concentrated (0.5 M) reagent solutions (experiment A, Fig. 2.2-4a). In calcite-gel composites that form from less concentrated (0.1 M) reagent solutions, we find that thin gel membranes develop (see Fig. 2.2-4b and red arrows in Fig. 2.2-5a and b) and compartmentalise space (experiment B). Calcite-gel composites formed in heavier hydrogels (2 wt % agar, experiments C and D) incorporate significantly higher amounts of gel polymeric matrices (Fig. 2.2-S3). Similar to the composites obtained in experiments A and B, the organization of the occluded matrix within the composite differs depending on the concentration of the counter-diffusing reagents when a strong gel is used. In composites that are obtained in experiments with highly concentrated (0.5 M) reagent solutions, the gel is more evenly distributed over the volume of the composite (experiment C, Fig. 2.2-4c) relative to aggregates that grow in the presence of low (0.1 M) reagent solution concentrations (experiment D, Fig. 2.2-4d). In the latter, in addition to gel membranes that encase the subunits, further membranous gel accumulations form and are distributed throughout the aggregate. Space in these aggregates is even more

compartmentalised. We further observed that in composites obtained in experiments B and D the distribution of the occluded gel matrix is also determined by differences in gel density.
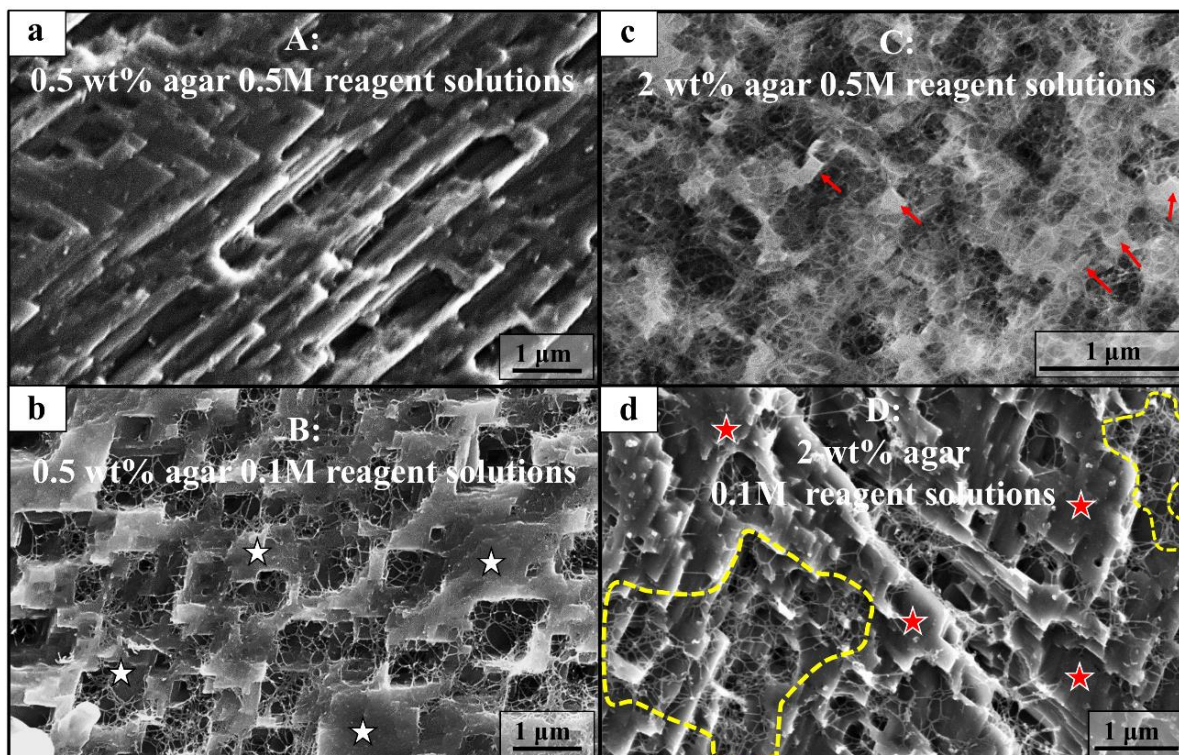
Figure 2.2-4. Cross sections of calcite−agar gel composites etched for 90 s with a solution containing 0.1 M HEPES buffer at a pH of 6.5 and 2.5% glutaraldehyde for fixation. (a) Composite formed in experiment A. This aggregate contains only minor amounts (0.3 wt % according to TG) of gel that appear homogeneously distributed within the mineral fraction of the composite. (b) Composite formed in experiment B. Gel occlusion (less than 0.1 wt % according to TG) is well observable, even though the gel network is thin and resides in a (most probably) 3D scaffold of mineral (white stars in b). (c) Composite formed in experiment C. A significant amount of occluded gel matrix (1.4 wt % according to TG) appears to be homogeneously distributed within the calcite. Undisturbed blocks of calcite (red arrows in c) extend over a few tens of nanometres. (d) Composite formed in experiment D. This composite contains a high amount of gel (0.9 wt % according to TG), partly inhomogeneously distributed within the aggregate: red stars in (c) point to regions where gel contents are decreased; higher accumulation of gel within the aggregate is indicated with yellow dashed lines.
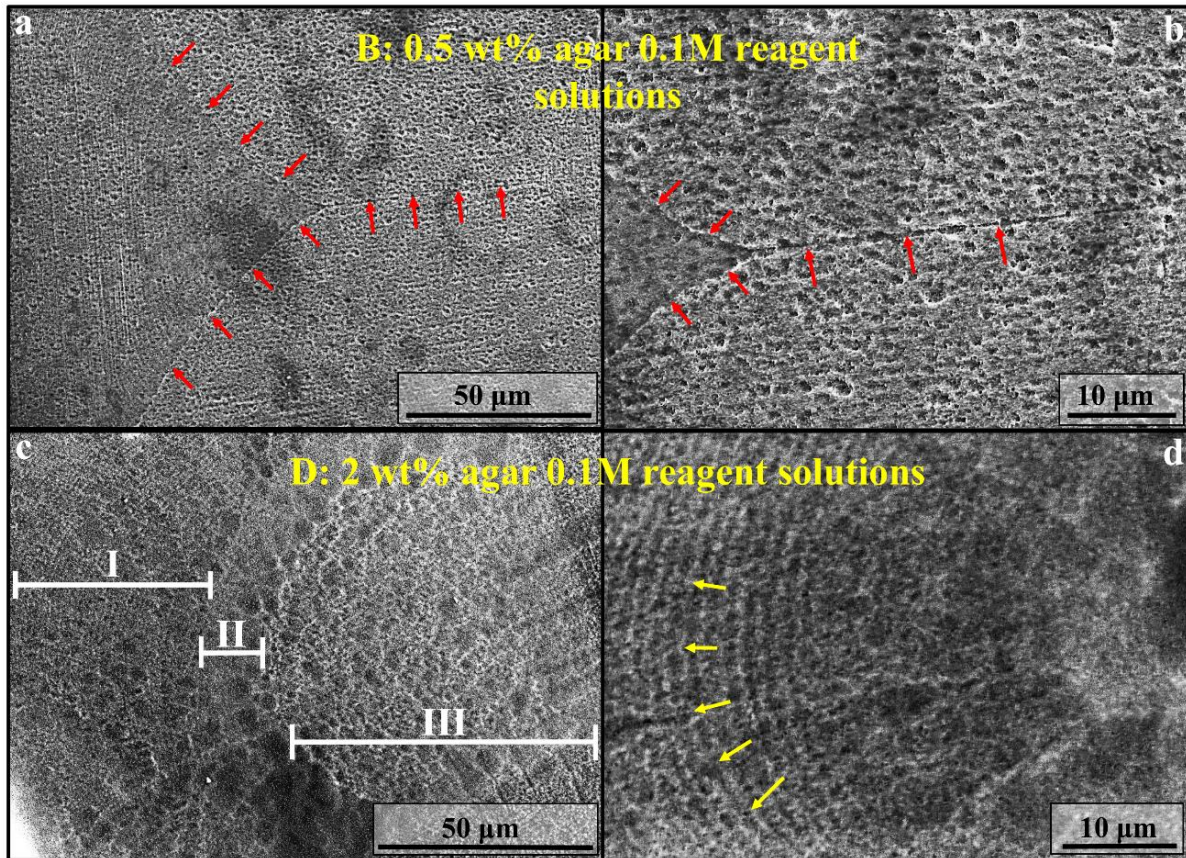
Figure 2.2-5. FE-SEM micrographs of cross sections of calcite−agar gel composites decalcified for 1 h with a solution containing 0.25 M HEPES buffer and 0.05 M EDTA at a pH of 7.8 and 2.5% glutaraldehyde and 8% paraformaldehyde for fixation. Patterns that show the differences in the amount of occluded gel throughout the calcite−gel composites arise after dissolution of the mineral component. (a,b) Composite formed in experiment B. (a) Fine boundary between sections of the composite with different amount of gel occluded is indicated by red arrows. (b) Close-up of the contact between sections (red arrows). (c,d) Composite formed in experiment B. (c) Composite contains concentric variations in the gel to mineral ratio according to which three large regions (I, II, and III; indicated with white segments) can be distinguished from rim to core. (d) Close-up of region II, where further variations in the amount of gel occluded are visible (yellow arrows). These variations are arranged as sequence of 1−2 μm wide "furrows", defining an oscillatory pattern.

Gel occlusion occurs to defined modes, e.g. sectorial patterns and concentric patterns, as evidenced by FE-SEM observations on cross sections of the decalcified calcite-gel composites shown in Figure 2.2-5. Details of a sectorial pattern of gel occlusion in composites formed in experiment B are depicted in Figures 2.2-5a and -5b, where red arrows highlight a fine boundary between sections of the composite that show different densities of occluded gel. A concentric pattern of gel distribution in a composite formed in experiment D is well visible in Figure 2.2-5c, where three regions, marked by the segments I, II and III, can be distinguished from the rim to the core of the composite. The boundaries between regions are defined as a combination of straight lines parallel to two of the external edges of the calcite

crystal, namely $[\overline{4}41]$ and $[48\overline{1}]$ directions, and a curved line. The latter is approximately parallel to the curved edge that, together with $[\overline{4}41]$ and $[48\overline{1}]$ edges, bounds faces in the aggregates grown in experiment D (Fig. 2.2-1d). This strongly suggests that the concentric pattern of gel distribution is growth-related. A closer observation of features of the cross-section of the decalcified composite reveals a sequence of ☐ 1-2 micrometre wide grooves (highlighted with yellow arrows in Fig. 2.2-5d) which reflect variations throughout the composite in the mineral to gel ratio. These variations clearly show an oscillatory nature at least in the region II of the composite (Figs. 2.2-5c and 5-d).

Gel-mineral interlinkage in aggregates of all four experiments is presented in Figure 2.2-4. As the SEM image of Figure 2.2-4a shows, very little gel is occluded into aggregates grown in experiment A. This low-density gel is homogenously distributed within the aggregate volume. In contrast, in aggregates obtained from experiments B, C and D the gel within the aggregate is prominently visible (Fig. 2.2-4b-d). Composites obtained from experiment B show a network of micron sized calcite entities (white stars in Fig. 2.2-4b) that appear gel-free. The occluded gel is interspersed in 1 μm sized pores inside a skeletal mineral growth structure. In contrast, as agar solid content of the gel used in experiments C and D is high, aggregates grown in latter experiments are characterized by dense gel occlusions with the mineral growing through the gel network (Figs. 2.2-4c and -4d). In the case of aggregates grown at experimental conditions C individual mineral unit dimensions are only a few hundred nanometres (red arrows in Fig. 2.2-4c) and are significantly smaller than those in aggregates grown in the weaker gel (Fig. 2.2-4b). In the latter (aggregate grown at experiment C, Fig. 2.2-4c) the density of mineral and gel seems to be homogeneous over the volume of calcite-gel composite. In contrast, in aggregates obtained from experiment D, formed from low concentrated reagents and strong gels, we find crystalline portions which appear to be almost devoid of gel (red stars in Fig. 2.2-4d), next to regions characterized by a high accumulation of gel (encircled with yellow dashed lines in Fig. 2.2-4d).

TG analyses of gel content correlate well with our SEM observations of gel occlusion (Fig. 2.2-S3). We find 1.4 wt% of occluded gel in aggregates obtained in experiment C, followed by 0.9 wt% in experiment D; in contrast, aggregates grown in experiments carried out with weak gels contain 0.3 wt% (experiment A) and less than 0.1 wt% (experiment B) gel in the aggregates, respectively.

From our observations on occluded gel organization and gel-mineral interlinkage we conclude that aggregates with an even distribution of gel form, when highly concentrated reagents are used, regardless of the concentration of the solid content of the gel. Furthermore, we conclude that the combination of highly concentrated reagents and gels with low solid content results in composites with the larger mineral portions devoid of gel. Finally, we observe that by combining thick gels and low concentrated reagents, composites with an inhomogeneous mineral-gel distribution are obtained.

Calcite Texture Triggered by Gel Occlusion

Figures 2.2-6 to -12 visualize the influence of gel occlusion on the mode of calcite organization within the aggregates with colour-coded local kernel misorientation maps, colour-coded misorientation maps and misorientation versus distance diagrams. We present all colour-coded maps enlarged in appendix Figures 2.2-S8 to -S10 and -S12 to -S13; subunits of the aggregate that grew at experiment D are also shown enlarged in Figs. 2.2-S14 and -S15.

Figures 2.2-6a to -9a show variations in local kernel misorientation (misorientation between a measurement point and its neighbouring points) on the EBSD map. In addition, these misorientation data are plotted in Figures 2.2-10 and -S11 as relative frequency vs. local kernel misorientation diagrams. Figures 2.2-6b to -9b show crystallite misorientation in the EBSD scanned field relative to the average orientation value of the scanned area. The degree of local kernel misorientation reflects aggregate regions with an increased local strain due to gel occlusion (Figs. 2.2-6a to -9a, Fig. 2.2-10), while misorientation relative to the average orientation of a scan field highlights aggregate regions where, as a consequence of gel occlusion, grain boundaries develop (Figs. 2.2-6b to -9b). The amount of occluded gel unambiguously influences the degree of crystal co- or misorientation in the aggregate. In the presence of a low amount of occluded gel the degree of misorientation between crystallites is low, while, when gel accumulation is increased, misorientation between crystallites also increases.
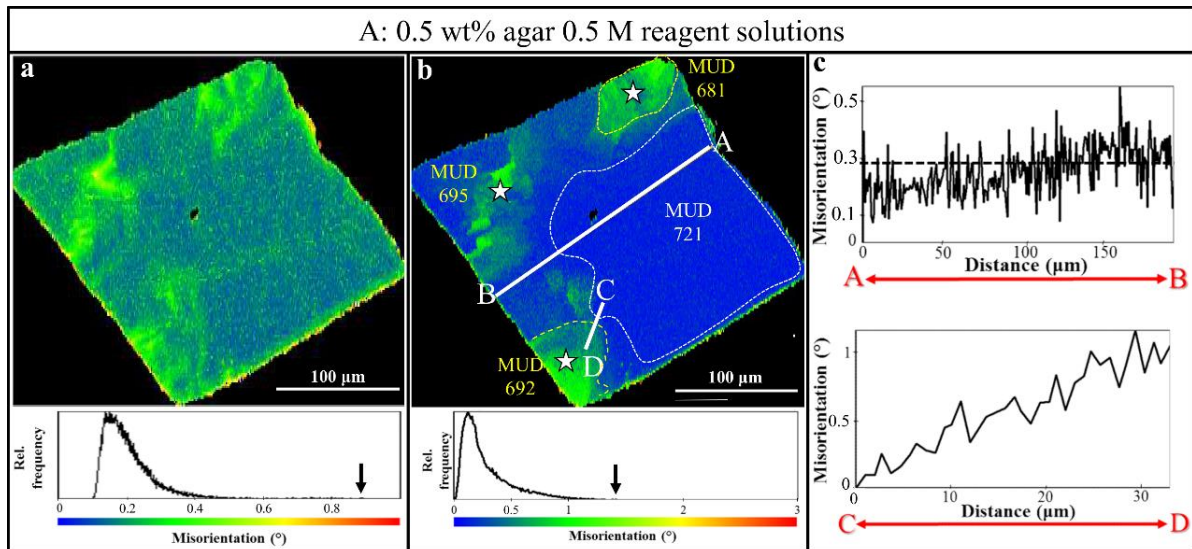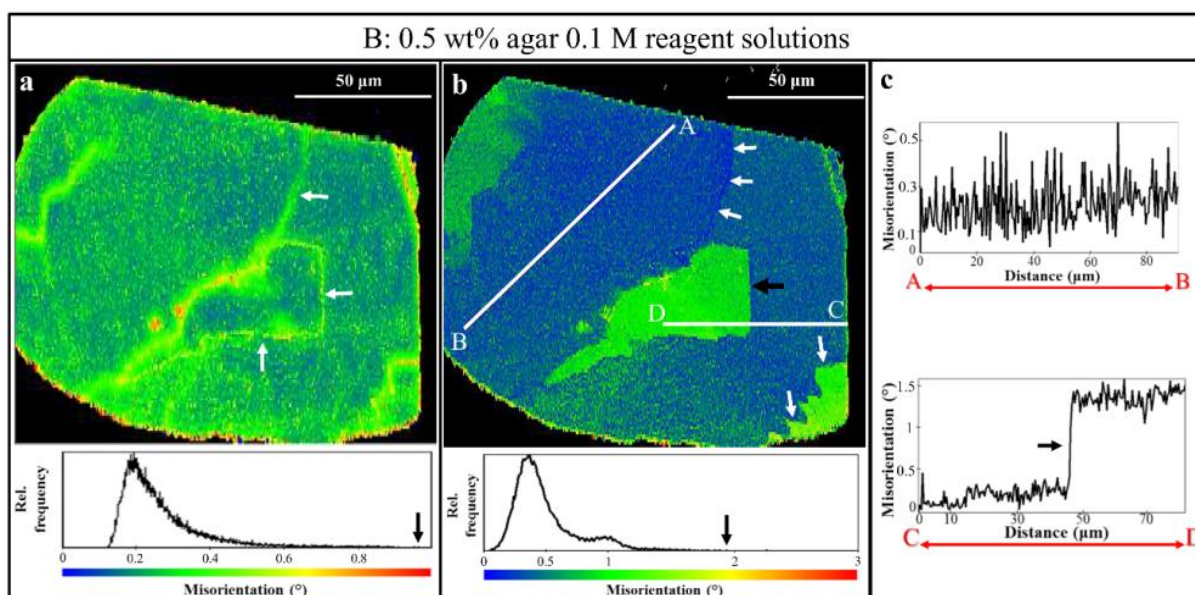
Figure 2.2-6. Colour-coded EBSD maps of (a) local kernel misorientation depicting increased local strain and therefore the distribution and amount of hydrogel occlusion into the composite, (b) misorientation in a scan field relative to the average orientation of that part of the aggregate, and (c) point-to-origin misorientation along profile lines. Corresponding legends are given below the misorientation maps. Gel incorporation into aggregates grown at experimental condition A is very minor. The gel is inhomogeneously distributed in the aggregate; the aggregate contains portions that are almost devoid of gel (deep blue colours in a, the region with a high MUD value in b) next to areas where a slightly increased amount of gel is present (yellow colours along the rim of the aggregate in a, green to yellow regions and white stars in b). In areas that are almost devoid of gel point-to-origin misorientation is low and scatters between 0.2 to 0.3 degrees (profile A to B in c), hardly exceeding the angular experimental resolution, while at aggregate portions with higher gel accumulations it reaches 1° (profile C to D in c).

Differences in Occluded Gel Concentrations

As it is well visible in Figures 2.2-6a and -S8a, even though the experiment was carried out with a weak gel, the gel network is present almost everywhere in the aggregate. A slight inhomogeneity in gel occlusion is observable as we find regions devoid (or almost devoid) of gel (deep blue areas in the map of Figs. 2.2-6a, -S8a) next to portions with some gel accumulation (green coloured regions at the aggregate's margins in the map of Figs. 2.2-6a, S8a). The distribution of green colours in the local kernel misorientation map of Figures 2.2-6a, -S8a is diffuse, thus, membrane formation has not taken place at experiment conditions A. As the legend in Figure 2.2-6a shows, maximum local kernel misorientation is 0.9 degrees (black arrow in the legend of Fig. 2.2-6a), thus, the degree of calcite co-orientation is almost undisturbed by gel occlusion. Slightly more gel is occluded in aggregates that grew in experiment B (Figs. 2.2-7a, -S8b) where we have a higher growth rate compared to experimental conditions A. In these aggregates, gel-free regions are rare (the base colour is green to yellow in the map in Figures 2.2-7a, -S8b). In addition, clear-cut gel accumulations

appear, indicated by light yellow colours in the local kernel misorientation map (white arrows in the map of Fig. 2.2-7a). These hint to the existence of thin gel membranes, separating minutely misoriented subregions from each other (see white arrows and black arrow pointing to low angle grain boundaries in Fig. 2.2-7b). Similar to the aggregate grown in experiment A, the maximum value of local misorientation is 0.9 degrees (black arrow in the legend to the local kernel misorientation map in Fig. 2.2-7a) in aggregate of experiment B. Gel occlusion is increased in the aggregate of experiment B relative to that in the aggregate of experiment A. This can be seen by comparing the relative frequency of local kernel misorientation as found for the aggregate grown in experiment A (black curve in Fig. 2.2-10a) - with that of the aggregate grown in experiment B (red curve in Fig. 2.2-10).

Figure 2.2-7. Colour-coded EBSD maps of (a) local kernel misorientation depicting increased local strain and therefore the distribution and amount of hydrogel occlusion into the composite, (b) misorientation in a scan field relative to the average orientation of that aggregate portion, and (c) point-to-origin misorientation along a profile line. Corresponding legends are given below the misorientation maps. Gel incorporation into aggregates grown at experimental conditions B is pervasive (see the uniformly distributed yellow to green colours in a). In these regions, point-to-origin misorientation along a profile line scatters between 0.2 to 0.4°. Membrane formation takes place at experimental conditions B (white and black arrows in a and b) causing the slight tilt of about 1° between neighbouring portions of the aggregate (black arrow in b and in the corresponding profile C to D in c).

Figures 2.2-8a and -9a, -S9, -S10 give local kernel misorientation maps for aggregates grown in dense gels and clearly highlight the occlusion of a high amount of gel (bright yellow and green colours in Figs. 2.2-8a, -9a, -S9a; local kernel misorientation going up to two degrees (see legends to Fig. 2.2-8a, Fig. 2.2-10b). Thus, a mosaic structure is induced. Thus, subunit

formation is induced (Fig. 2.2-9b) and occlusion of gel streaks within the aggregate (white arrows in Fig. 2.2-9a).
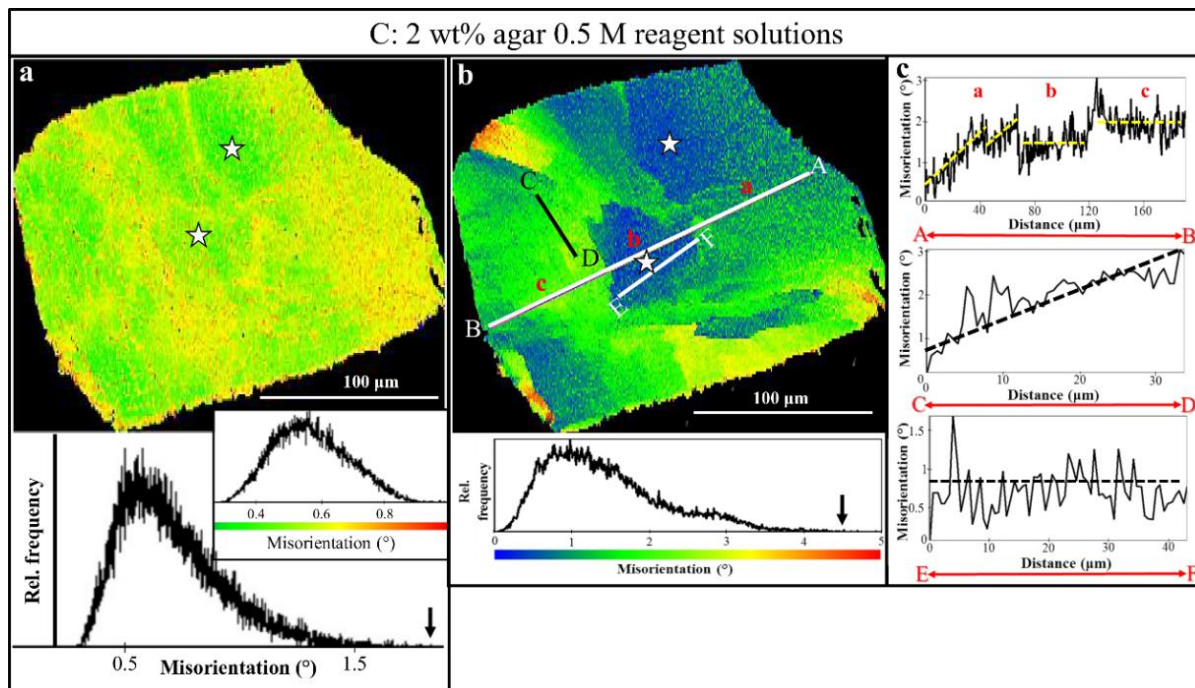
Figure 2.2-8. Colour-coded EBSD maps of (a) local kernel misorientation depicting increased local strain and therefore the distribution and amount of hydrogel occlusion into the composite, (b) misorientation in a scan field relative to the average orientation of that aggregate portion, and (c) point-to-origin misorientation along a profile line. Corresponding legends are given below the misorientation maps. Gel incorporation into aggregates grown at experimental conditions C is highest for all experimental conditions investigated in this study (well visible by the bright yellow to red colours in a). Accordingly, a higher amount of strain is present within the aggregate (see the green-yellow and red areas in b), maximum misorientation is increased to 5° (legend to b) as well as misorientation along selected profiles (c). However, the gel distribution is strongly inhomogeneous within the aggregate (note difference in colours in a and b, and variation in maximum misorientation values (c) in misorientation vs distance diagrams). White stars in (a,b) indicate the high correspondence of aggregate portions with increased local strain and distinct amounts of gel occlusions.

The distribution of green and yellow colours in Fig. 2.2-8a shows that gel occlusion is inhomogeneous in aggregates grown in experiment C, it appears that the formation of mosaic blocks takes place, and these are also characterized by different amounts of occluded gel. As gel occlusion is high in aggregate C, the maximum local kernel misorientation value is almost 2 degrees (Fig. 2.2-8, Fig. 2.2-10b) with a broad peak in local kernel misorientation at 0.6 degrees, ranging from 0.3 and 0.9 degrees (legend to Fig. 2.2-8a).

Experimental conditions D (dense gel connected to low reagent solution concentration) yield aggregates that are more like polycrystals with co-oriented subunits (Fig. 2.2-3d). At this

experimental setup, gel incorporation into the aggregate induces the following microstructural characteristics:

(a) With respect to gel incorporation we can distinguish two main parts of the aggregate (Figs. 2.2-9a, -S10), subunit I containing a high amount of incorporated gel (see black arrow in the legend of Fig. 2.2-S10a), and subunit II showing a smaller amount of gel occlusion (see black arrow in the legend of Fig. 2.2-S10b).

(b) Clear-cut gel membranes (black arrows in Fig. 2.2-9b) that separate subunits 1 to 6 (Figs. 2.2-3d) from each other.

(c) Very prominent are broad curved diffuse bands of gel within the entire aggregate (white arrows in Fig. 2.2-9a. These are structured into hierarchical subunits on at least 3 levels.

Thus, the use of a strong agar gel with low reagent solution concentration provokes the formation of a microstructural hierarchy.

Consequences of Gel Occlusion

Figures 2.2-6b to -9b, Fig. 2.2-11, Fig. 2.2-S12, 2.2-S13 show the deviation in orientation for each crystallite within the scanned area from the average orientation value of the scanned field. The non-uniformity in colours in all misorientation maps (Figs. 2.2-6b to 2.2-9b) visualizes low angle grain boundaries within all four aggregates. The aggregate shown in Fig. 2.2-6b represents, however, a special case, as large parts of the aggregate are undisturbed by gel occlusion. These regions are (almost) single-crystalline as they contain only insignificant amounts of gel (the dark blue region in the overall misorientation map encircled with a white dashed line in Fig. 2.2-6b). The MUD value of this portion of the aggregate is 721, a value very similar to that of calcite single crystals grown from solution (MUD of 725) (Nindiyasari et al. 2015). However, the corresponding legend to the misorientation map highlights that misorientation of the entire aggregate is slightly increased as it is above one degree.
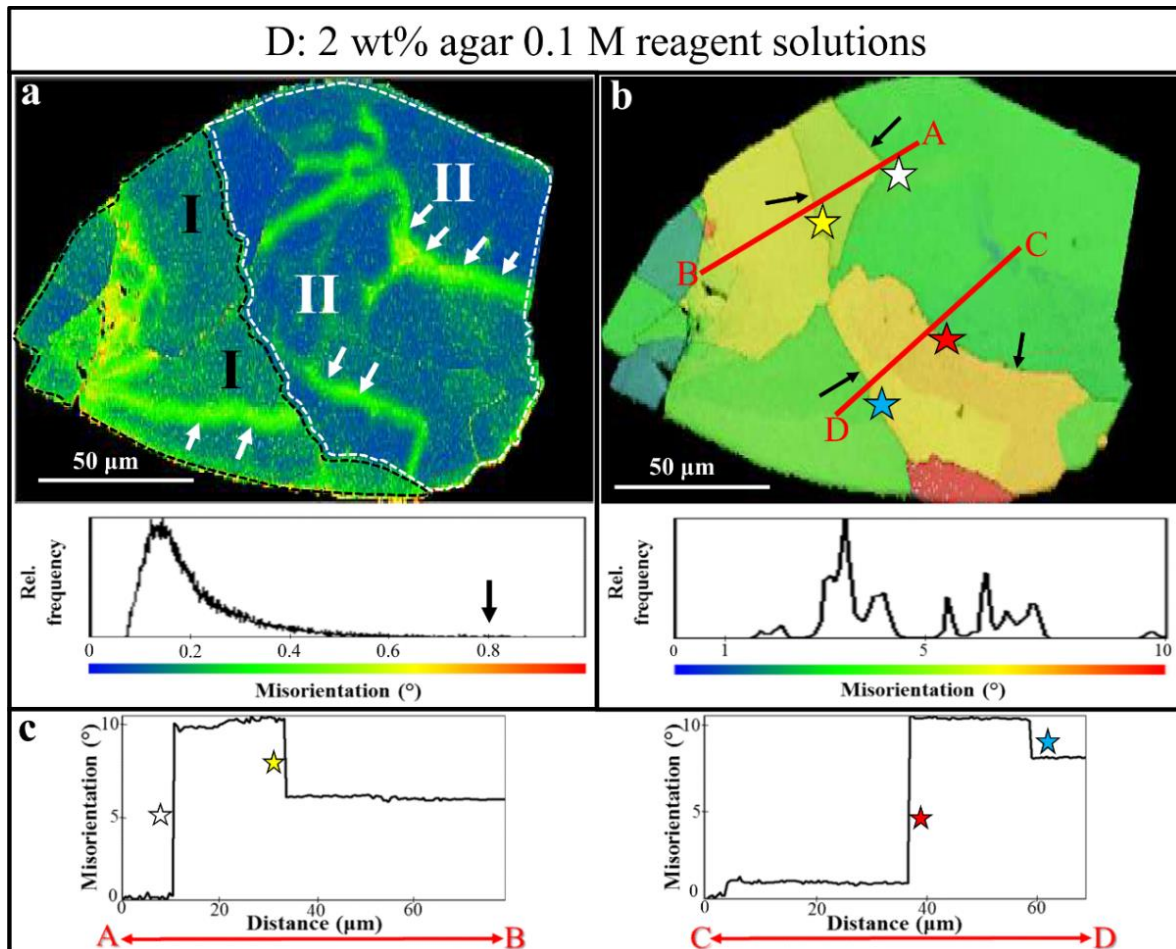
Figure 2.2-9. Colour-coded EBSD maps of (a) local kernel misorientation depicting increased local strain and therefore the distribution and amount of hydrogel occlusion into the composite, (b) misorientation in a scan field relative to the average orientation of that aggregate portion, and (c) point-to-origin misorientation along a profile line. Corresponding legends are given below the misorientation maps. The legend shown in (a) holds for the entire aggregate; see Figure 2.2-S14 for detailed information on individual subunits and the corresponding legends. Gel incorporation into aggregates grown at experimental conditions D is high (in comparison to that into aggregates grown at experimental conditions A and B); however, it is less than that of the composite formed at conditions C. The decrease in reagent solution concentration induces mainly a different mode (compared to conditions C) of gel occlusions: clear-cut gel membrane formation (black arrows in b) that induces subunit formation with distinct orientations (b,c) and hierarchy due to inhomogeneity in gel incorporation: the two major subunits I and II in (a) and diffuse gel streaks incorporated in most of the subunits (white arrows in a). The aggregate that grew at experimental conditions D is a polycrystal with co-oriented subunits (see the different peaks as an indication for subunits in the legend to b); note the similarity in colours depicting calcite orientation, and the legend for orientation is given in Figure 2.2-2c. The tilt at gel membranes and between two neighbouring subunits scatters between 2 and 10° (misorientation vs distance profiles A to B and C to D in c).

This is caused by those parts of the aggregate where slightly higher amounts of gel are occluded (white stars in Fig. 2.2-6b, regions encircled in yellow).

45

Accordingly, MUD values of these parts of the composite are below 700, point-to-origin misorientation along profile C to D reaches 1 degree (Figs. 2.2-6b, -6c) in contrast to the point-to-origin misorientation that scatters between 0.2 to 0.3 degrees (profile A to B in Figs. 2.2-6b, -6c) for those aggregate portions that are almost devoid of gel. Gel entrapment into aggregates that grew under experimental conditions B (0.5 wt% agar and 0.1 M reagent solutions concentration) is pervasive within the entire aggregate. Thus, compared to a single crystal grown from solution, local strain is present everywhere in the aggregate. Maximum misorientation reaches almost 2 degrees (see black arrow in the legend in Fig. 7b), point-to-origin misorientation along selected profiles scatters between 0.1 to 0.5 degrees (profile A to B in Fig. 7c) for those regions that contain a low amount of gel.
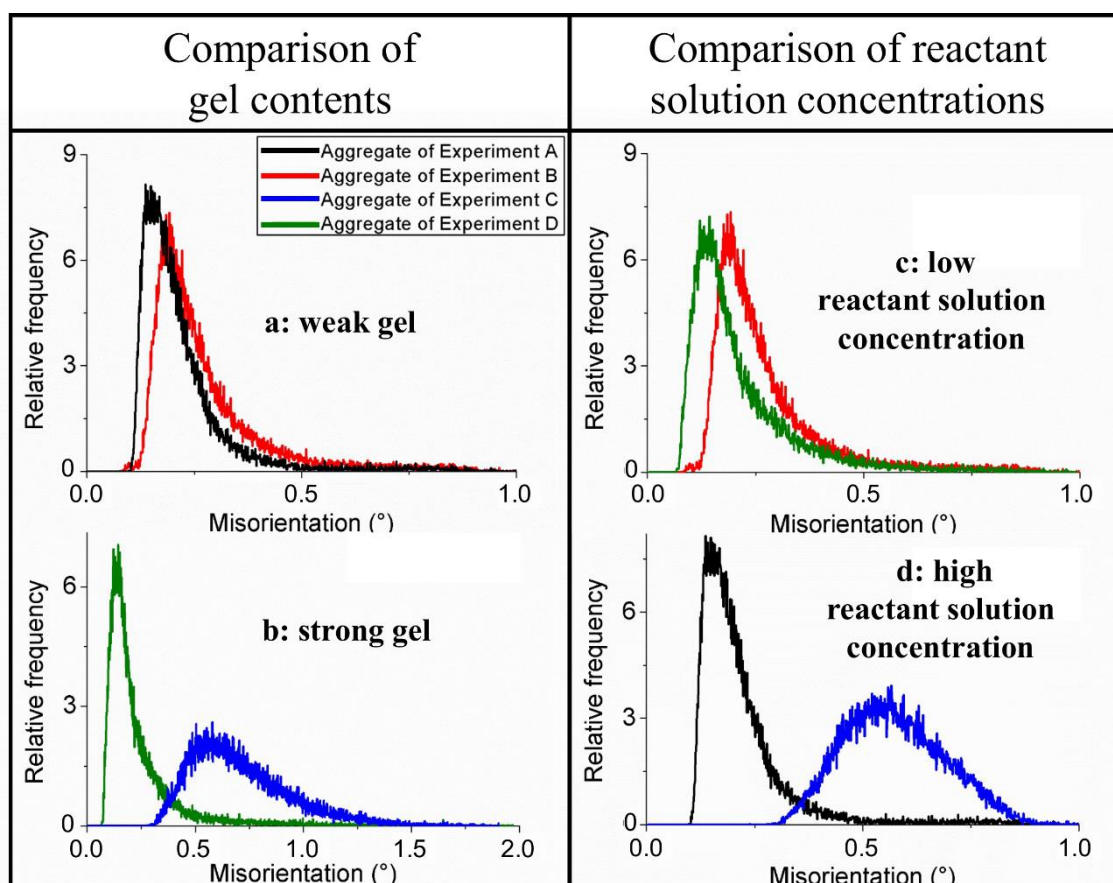
Figure 2.2-10. Relative frequency versus local kernel misorientation data for aggregates obtained at experiments A to D. (a) Comparison of aggregates obtained in the presence of weak gels, (b) comparison of aggregates obtained in the presence of strong gels, (c) comparison of aggregates obtained in the presence of low reagent solution concentrations, and (d) comparison of aggregates obtained in the presence of high reagent solution concentrations. Note that for strong gels local kernel misorientation reaches 2°. See also Figure 2.2-S11, where results for all aggregates are plotted into one diagram.

Few short-ranged gel membranes are present in this aggregate (white arrows in Fig. 2.2-7a and -7b) that induce a tilt between neighbouring aggregate portions of about 1 degree (black arrows indicating low angle grain boundaries in Fig. 2.2-7b and profile C to D in Fig. 2.2-7c).
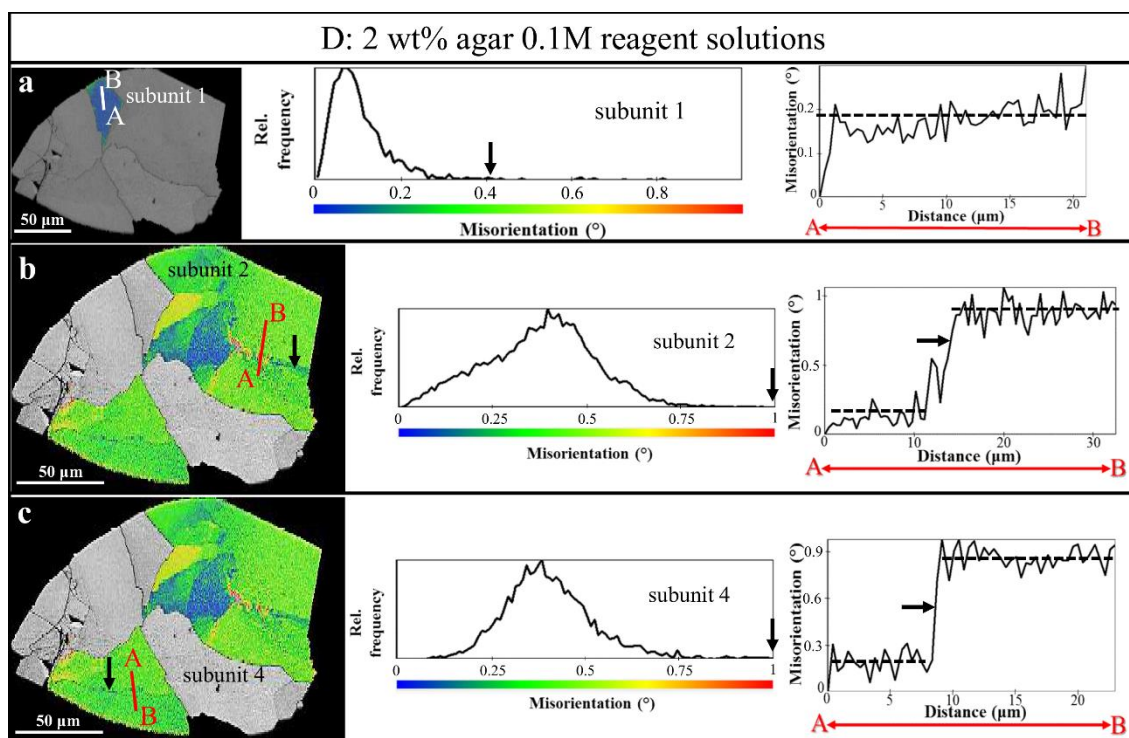
Figure 2.2-11. Misorientation maps with corresponding legends and point-to-origin misorientation vs distance diagrams for subunit 1 (a), subunit 2 (b), and subunit 4 (c) of the aggregate obtained at experimental condition D. Gel incorporation is strongly inhomogeneous within the aggregate. While it is low in subunit 1, it is significantly increased in subunits 2 and 4, where it is also quite inhomogeneously distributed. For subunits 2 and 4, we show a misorientation vs distance diagram within a subunit where gel is more homogeneously incorporated (profiles C to D, profiles shown in black in b,c). In both cases, point to point misorientation scatters between 0.15 and 0.3°. In addition, we show for both subunits (2 and 4) a misorientation vs distance diagram along a profile that crosses a boundary formed by a diffuse incorporation of gel (profiles A to B, profile lines shown in red in b,c). In both subunits, these boundaries are diffuse gel incorporations. As the corresponding legends show, for both subunits, tilt between neighbouring entities is about 0.5 to 0.6°, see black arrows in profiles A to B as well as in the misorientation maps in b,c.

Distribution patterns of local strain induced by gel occlusion at experimental conditions with a dense gel (experiments C and D) are shown in Figs. 2.2-8a, -9a, -S9, -S10, -S14. As higher amounts of gel are incorporated during growth, the aggregates become internally structured, and subunits, distinguished from each other by distinct tilts, develop. (in Figs. 2.2-8b, -9b, -11, -S7, -S13, -S15). At experimental conditions where agar solid content is 2 wt% and reagent solution concentrations are 0.5 M, misorientation of crystallites relative to the average orientation of the scanned area reaches almost 5 degrees (legend in Fig. 2.2-8b) as

gel incorporation is high and induces high local strains in the aggregate. Also, point-to-origin misorientation along selected profiles is often as high as 3 degrees (profiles A to B, C to D in Fig. 2.2-8c). Gel occlusion in these aggregates is inhomogeneous, we do find aggregate portions where a small amount of gel is incorporated during growth and where local strain induced by gel occlusion is almost negligible (see corresponding regions in Figs. 2.2-8a and -8b indicated by white stars). Here, the degree of misorientation between neighbouring points is low (profile E to F in Fig. 2.2-8c) and extends only up to 1.5 degrees.

At experimental conditions with an increased agar solid content (2 wt%) and low reagent solution concentrations (0.1 M, experiment D, Figs. 2.2-9b, -S13b, -S15), subunit formation starts as gel membranes form within the aggregate (Figs. 2.2-3d, -9a, -9b). Here, we find low and high angle grain boundaries with a tilt up to 10 degrees (misorientation versus distance diagrams along profiles A to B and C to D in Fig. 2.2-9c). Thus, the aggregate can be regarded as a polycrystal with co-oriented subunits.

However, the degree of gel occlusion and local strain within the aggregate varies from subunit to subunit. We observe almost single-crystalline subunits (subunit 1, Figs. 2.2-11a, -S15) with a degree of misorientation mainly up to 0.4 to 0.5 degrees and a point-to-origin misorientation between 0.1 and 0.2 degrees (profile A to B in Fig. 2.2-11a). In contrast, the aggregate also contains subunits where gel incorporation is not only increased but is also inhomogeneously distributed within the subunit (e.g. subunits 2 and 4, Fig. 2.2-S14). Accordingly, misorientation within these subunits reaches 1 degree (black arrows in legend to subunits 2 and 4 in Figs. 2.2-11b, -11c). In addition, these subunits are structured further and clearly show the presence of hierarchical subunits on at least 3 levels. Misorientation versus distance profiles A to B in Figures 2.2-11b, -11c demonstrate that tilt between these domains is between 0.5 and 0.8 degrees. Thus, high agar gel solid contents in combination with low reagent solution concentrations enable the growth of hierarchical composite agar gel-calcite aggregates.

What Exerts a More Profound Influence on Mineral Texture and Composite Aggregate Formation: Gel Strength or Reagent Concentration?

The occlusion of gel polymeric matrix within calcite crystals influences microstructural characteristics of the aggregate: the pattern and strength of crystal co-orientation as well as the presence or lack of subunits in the mineral–gel composite, as previous studies (Prieto et al. 1991, De Yoreo et al. 2003, Nindiyasari et al. 2015) showed. The magnitude of control is

given by mainly two factors: the amount of polymeric matrix that becomes incorporated into the mineral and the fabric and pattern of distribution of the gel matrix relative to the volume of crystal.
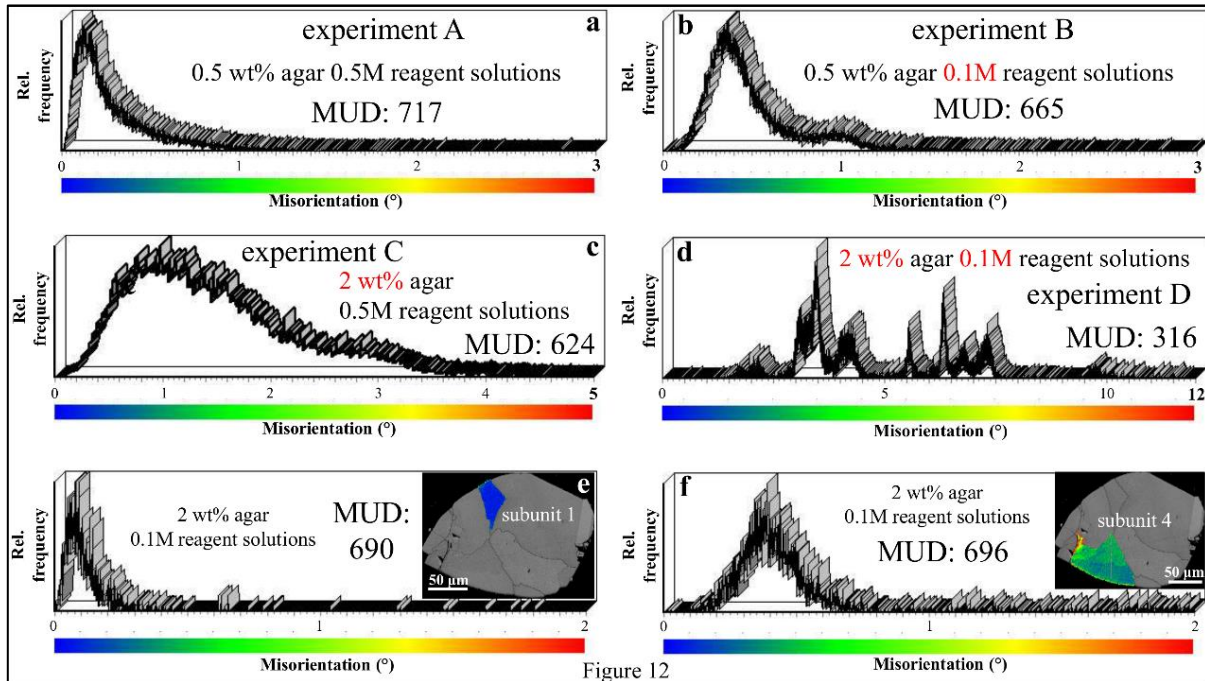
Figure 12. Relative frequency statistics for misorientation in aggregates grown from experimental conditions A−D (a−d), as well as for subunits 1 and 4 of the aggregate grown in experimental conditions D (e,f). MUD values give differences in the strength of calcite co-orientation related to differences in gel solid content and reagent solution concentrations. Well visible is the combined influence of agar gel solid content and the concentration of the counter-diffusing reagent solutions. The smallest amount of gel is included into aggregates that formed in the presence of weak gels and high reagent solution concentrations (a). The highest amount of gel gets incorporated into an agar gel calcite composite when a strong gel is used in the presence of high reagent solution concentrations (c). While gel solid content influences the amount of incorporated gel, the concentration of reagent solutions regulates the pattern of gel distribution within the aggregate. In the presence of a strong gel and a low reagent solution concentration, gel membranes form that divide differently oriented subunits from each other (see individual peaks in d). Furthermore, gel incorporation is highly inhomogeneous (e,f) and a further hierarchical level develops, as is the case in subunit 4 (f).

Work by Estroff's group (Simon et al. 2011, Asenath-Smith et al. 2012) demonstrated that the amount of gel that is occluded within mineral-gel-aggregates during growth is mainly determined by the two parameters: hydrogel strength and aggregate growth rate. In physical gels, like agar or gelatin gels, gel strength increases with their solid content (Asenath-Smith et al. 2012). Composite growth rate depends on the supersaturation, which in turn, is directly linked to the concentration of the reagent solutions. Thus, an increased gel strength connected to an increased growth rate induces that a high amount of gel is incorporated into the

aggregate, while the combination of a weak gel and slow growth rates leads to the formation of almost gel-free composites (Li & Estroff 2009, Asenath-Smith et al. 2012).

Calcite-agar gel composites that we obtained in our experiments correspond to four different growth scenarios (Table 2.2-1), defined by the combination of two different gel solid contents and two different concentrations of counter-diffusing reagents. A major focus of this study is to investigate and to assess which of the two parameters, gel strength or growth rate, exerts a more profound influence on gel occlusion into the composite and mineral organization in the aggregate. In a second step we address the feed-back signal of the mineral component in the composite to changes of gel strength and growth rate. Gel strength increases with the gel solid content and the reagent concentration determines the supersaturation that can be attained when crystallization starts and be maintained as growth proceeds. It can be expected that the amount of occluded gel and its distribution and organization in the composites formed at experimental conditions A-D will show distinct characteristics depending on the different weights that these two main parameters have in each case. A summary of observations and effects is given in Figure 2.2-12 and Table 2.2-2.

As expected, we find a high amount of occluded gel in calcite-gel composites that formed in experiment C (Table 2.2-1), where more concentrated (0.5 M) counter-diffusing reagents and a gel prepared with a higher solid content (2 wt% agar) were used (Figs. 2.2-4c, -8, -S9a, -S13a). This result supports the interpretation that high gel strengths and high growth rates promote the incorporation of a basically undisrupted gel network into calcite. Misorientation of calcite in composites that formed at these experimental conditions is 5 degrees (Fig. 2.2-8b), and is significantly higher than that in composites that grew under conditions with a low gel strength. Calcite-gel composites formed in lighter gels (experiments A and B, Table 2.2-1, Figs. 2.2-4a, -4b, -6, -7, -S8, -S12) incorporate smaller amounts of occluded gel. This is in agreement with the lower density of the gel network and, in the case of aggregates formed in experiment B, where less concentrated counter-diffusing reagents (0.1 M) were used, it is consistent with the effect of growth at slow rate under moderate to low supersaturation on gel occlusion, according to the model proposed by Estroff's group (Li & Estroff 2009, Asenath-Smith et al. 2012). The presence of gel accumulations in these composites (Fig. 2.2-7b) suggests that the fibres of the weak gel are pushed ahead by the growing crystal, or occasionally the fibres are even pushed together by abutting crystals, forming thin membranes (Fig. 2.2-7b) between them. This leads to local increases in gel density. As there is a correlation between gel density and gel strength, the gel would locally

become stiffer and, thus, it is more likely to become occluded. The direct consequence is a certain degree of inhomogeneity in the distribution of the occluded gel within the composite, which is higher in composites grown under lower supersaturation, from less concentrated reagents. Inhomogeneity in gel distribution connected to local gel accumulations could explain the relatively large maximum misorientation of 2 degrees in composites grown in experiment B (Fig. 2.2-8) compared to those formed in experiment A (maximum misorientation around 1°) as well as their slightly higher local kernel misorientation (Fig. 2.2-10), even though both types of composites formed in the weak gel.

Our TG (Fig. 2.2-S3) and SEM (Fig. 2.2-4) results demonstrate that the amount of occluded gel in composites formed in experiment A (Fig. 2.2-4a), conducted with a light gel (0.5 wt% agar) and a high concentration of counter-diffusing reagents (0.5 M), is lowest compared to gel contents of all other aggregates (Fig. 2.2-4b to -4d). Maximum misorientation in composites formed in experiment A is slightly above 1 degree, the lowest compared to maximum misorientation in all other composites. A lower incorporation of gel in composites from experiment A (light gel, high reagent concentration) compared to those from experiment B (light gel, low reagent concentration), is in clear contradiction with expectations from Estroff's model (Li & Estroff 2009, Asenath-Smith et al. 2012). Indeed, the significantly higher concentration of the reagents used in experiment A should guarantee that crystal growth occurred under higher supersaturation and, consequently, at a faster rate than in experiment B, thereby, promoting the occlusion of a higher amount of gel. This appears to be supported by our TG analyses, which yield a higher gel content for composites grown in experiment A. But the expectations are not corroborated by our SEM observations. A possible explanation for this discrepancy is the inhomogeneous distribution of the gel within the aggregate. Indeed, misorientation analyses in composites formed in experiment A indicate a remarkably inhomogeneous distribution of gel, with a large central region almost devoid of gel and some regions at the rim containing some gel. This suggests that the high crystallization pressures associated with crystal growth under high supersaturations can break and push away the weak gel. This enables the formation of gel-free (or almost gel-free), highly co-oriented aggregates with very little gel in their central parts and a higher gel density as well as lower crystal co-orientation in their periphery (Fig. 2.2-6). Gel accumulations in the peripheral regions of an aggregate grown under experimental conditions A are highlighted by white stars in Figure 2.2-6b.

The similar amount of occluded gel, according to both, TG measurements and SEM image (Figs. 2.2-4c, -4d), into composites grown in experiment D, using a heavier gel and low concentrated counter-diffusing reagents, as well as in experiment C, carried out also with a heavier gel but highly concentrated reagents, indicates that gel strength exerts a higher influence on the incorporation of the total amount of gel into the aggregate compared to the influence of the growth rate. Thus, even though the low concentration of the reagents in experiment D prevents that the crystal growth process occurs at fast rates and at high supersaturation conditions (as in experiment C), the occlusion of a high amount of polymeric matrix will be facilitated by the high gel strength. The growth rate exerts control on the pattern of gel occlusion distribution within the composite, which will be more homogeneous when growth proceeds at a higher rate, leading to higher MUD values (MUD of 624 in aggregates grown in experiment C compared to 316 in aggregates formed in experiment D, Fig. 2.2-3). Thus, in aggregates grown in experiment D, where both, the low concentration of the reagents and the low porosity of the heavier gel prevents growth at high rates under high supersaturations, we find the highest inhomogeneity in occluded gel distribution. These aggregates show clear-cut subunits which are divided from each other by gel membranes; and the tilt at these membranes between neighbouring subunits reaches up to 10 degrees (Fig. 2.2-9c). Moreover, next to almost single-crystalline subunits with an internal misorientation of less than 1 degree (Fig. 2.2-11a), further subunits are present that contain more occluded gel and, thus, show a higher internal misorientation (up to 2 degrees, Figs. 2.2-11b, -11c). These are structured further and contain small angle boundaries. Furthermore, these aggregates show gel occlusions that define concentric oscillatory patterns (Figs. 2.2-5c, -5d). Growth-related concentric oscillatory patterns involving compositional changes are well known to form during the growth of different solid solution crystals in gels (Putnis et al. 1992, Prieto et al. 1997, Prieto et al. 2013). For example, concentric oscillatory compositional zoning was first observed in gel-grown crystals of the $(Ba,Sr)SO_4$ solid solution and has later been found in gel-grown crystals of a variety of calcite type $(Ca,M)CO_3$ crystals involving the substitution of Ca by divalent metals in solid solution (M= Cd, Mn, Co, Mg, etc.) (Putnis et al. 1992, Fernández-Díaz et al. 1996, Prieto et al. 1997, Fernández-González et al. 1999, Katsikopoulos et al. 2008; 2009, Prieto et al. 2013). Cellular automaton simulations have recently demonstrated that such concentric oscillatory compositional zoning resulted from the interplay between the difference of the solubilities of the $CaCO_3$-MCO_3 end-members and the threshold supersaturation for their nucleation (Gonçalves et al. 2014). A similar explanation could be proposed to explain the development of concentric oscillations in gel incorporation.

It has been demonstrated that the threshold supersaturation for nucleation is higher in less porous, heavier gels than in lighter gels (Nindiyasari et al. 2014a). This means that the very early stage of crystallization in experiment D will occur under higher supersaturation than in experiment B and, most likely, an initial period of fast growth will take place. However, this rapid growth will also lead to a fast depletion of ions in the gel around the growing crystal. This depletion cannot be balanced by mass transfer from the reagent deposits due to both, the low concentration of the reagents and the low porosity of the heavy gel. As a consequence, the crystal growth rate will drop eventually down to zero. This stop will, however, be temporary because, as mass transfer progresses, supersaturation will slowly build up. Once a supersaturation barrier is overcome, crystal growth will restart. The progressive growth rate decrease during a growth cycle appears to be recorded within the calcite-gel composite in the form of changes in the density of the incorporated gel polymer matrix, with sequences of growth cycles resulting in concentric oscillatory patterns of occluded gel.

2.2.5 Conclusions

With this work we extend our studies of carbonate crystallization in hydrogel matrices and discuss the combined influence of hydrogel strength and counter-diffusing reagent solution concentration on mineral formation and aggregate growth. Hydrogel incorporation into carbonate mineral highly influences the pattern of crystal growth and determines morphological, microstructural and material properties of the composite aggregates (Prieto et al. 1991, De Yoreo et al. 2003, Nindiyasari et al. 2015). Several characteristics play an important role: The amount of incorporated gel, its fabric when it is incorporated and its pattern of distribution within the mineral. From our study we deduce the following conclusions (Table 2.2-2):

Table 2.2-2. The combined effect of agar gel solid content and reagent solution concentrations on mineral organization and aggregate formation in agar gel–calcite composites.

		high reactant solution concentration	**low** reactant solution concentration
light gel	**supersaturation**	high	low
	growth rate	high	low
	amount of occluded gel	almost no gel occluded	low amount of gel occluded
	aggregate texture	single crystal composite	single crystal composite
	homogeneity of occluded gel	-	high
dense gel	**supersaturation**	high	low
	growth rate	high	low
	amount of occluded gel	highest of all four samples	high
	aggregate texture	mosaic crystal composite	co-oriented polycrystal composite
	homogeneity of occluded gel	high	local accumulations

1.   High reagent solution concentrations give rise to high supersaturation and high growth rates that, when combined with a light gel, cause the formation of *single crystal composites*, while, in the case of a dense gel, the aggregate is a *mosaic crystal composite*.

2.   Low reagent solution concentrations effect low supersaturation and low growth rates, that, in combination with a light gel, facilitate the growth of *single crystal composites*. When low reagent solution concentration is combined with a dense gel, the composite that forms is a *co-oriented polycrystal composite*.

3.   Agar gel solid content determines the pattern of crystal organization within the composite aggregate. Gel incorporation into the mineral is highest when a gel with a high solid content is used.

4.   The reagent solution concentration mainly determines the distribution pattern of gel within the aggregate. Gel distribution is homogenous for high reagent solution concentrations. For low reagent solution concentrations, the gel accumulates locally within the aggregates.

5.   Hydrogel accumulations often occur according to defined patterns, such as oscillations.

6.   Light gels can locally be pushed ahead during crystal growth, and resulting volumes of mineral can be devoid or almost devoid of gel. The occlusion of strong gels becomes increased when highly concentrated counter- diffusion solutions are used.

7.   A deeper understanding of the combined effect of gel strength and growth rate evolution, which is complex and influenced by both, the concentration of the reagent solutions and the diffusion within the gel, permits the synthesis of biomimetic composites with unique microstructures and enhanced, finely-tuned mechanical properties.

In our assessment of the influence of the counter- diffusing reagent solution concentration on gel occlusion and aggregate organization we followed the qualitative approach of Estroff and collaborators. Improving this assessment will require quantitative information on the supersaturation evolution in the system. The application of the mass transfer modelling to silica gel has proved useful to quantitatively estimate the supersaturation at early stages of the crystallization (Katsikopoulos et al. 2008; 2009, Sánchez-Pastor et al. 2011). Extending these calculations in future to other types of hydrogels, such as agar hydrogel, will require to determine the relationship between the solid content in the hydrogel and its transport properties.

2.2.6 Acknowledgements

2.2.7 Supporting Information

Supporting information is available (Figures 2.2-S1-S15): Sketch of experimental setup, local kernel misorientation and misorientation maps of a calcite single crystal grown from solution, TGA curves of calcite composites, additional morphologies of calcite aggregates obtained in the experiments, SEM images of calcite composite surfaces, enlarged images of colour-coded EBSD maps and corresponding pole figures, enlarged images of local kernel misorientation and misorientation maps for all aggregates and subunits of aggregate D, and the relative frequency of local kernel misorientations of all four aggregates plotted in one graph.
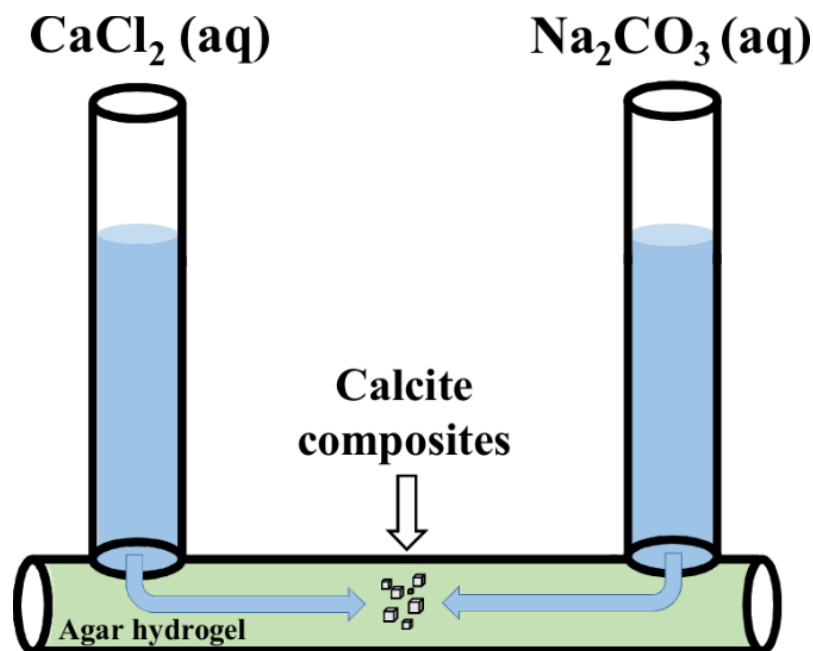
Figure 2.2-S1. Schematic sketch of the experimental setup (double-diffusion system).
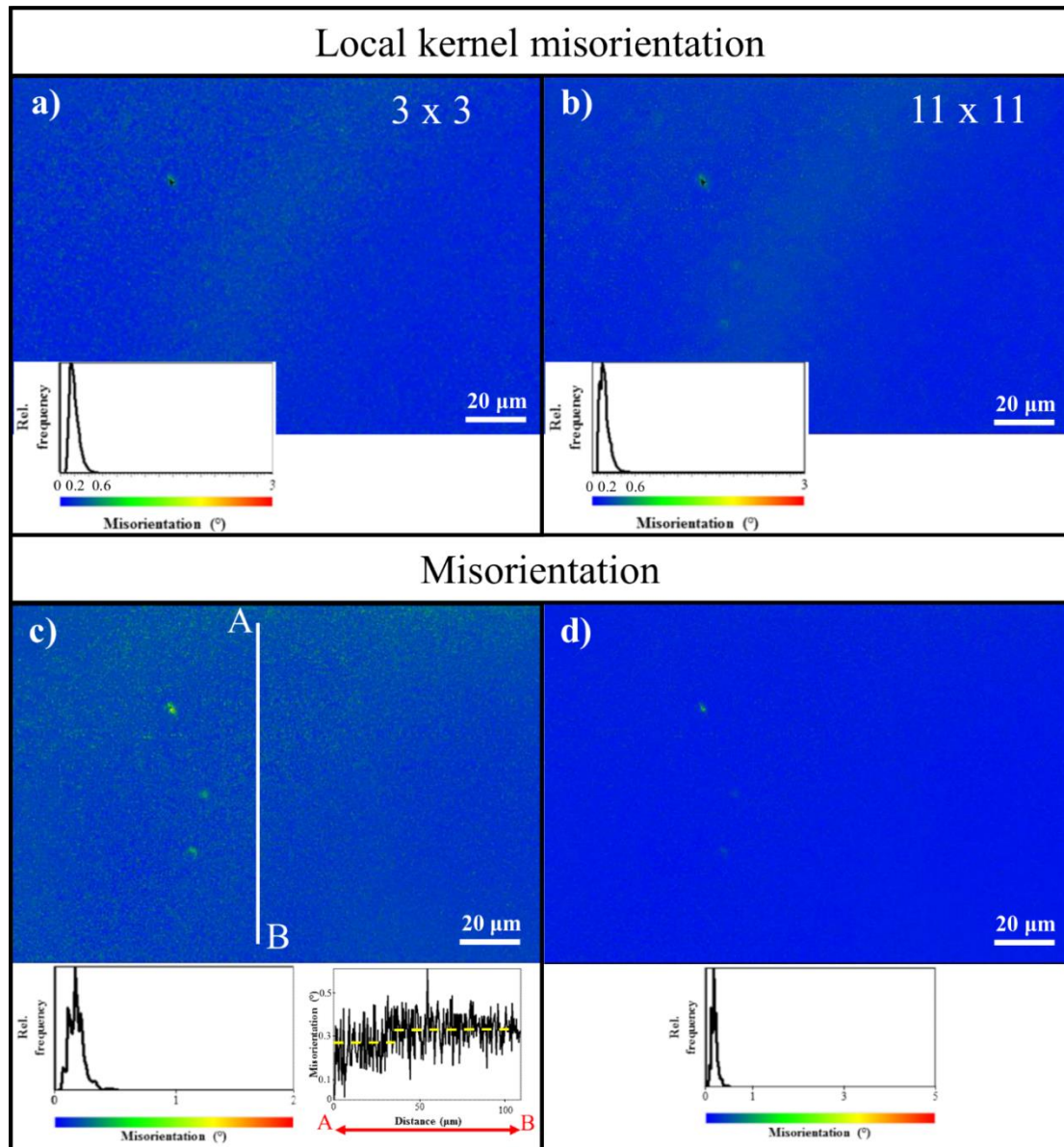
Figure 2.2-S2. (a) Local kernel misorientation maps of a calcite single crystal grown from solution calculated for 3x3 pixels cluster and (b) 11x11 pixels cluster. (c) Misorientation map with corresponding legend and point-to-origin misorientation vs. distance profiles for a calcite single crystal grown from solution. (d) Misorientation map with corresponding legend for a calcite single crystal grown from solution.
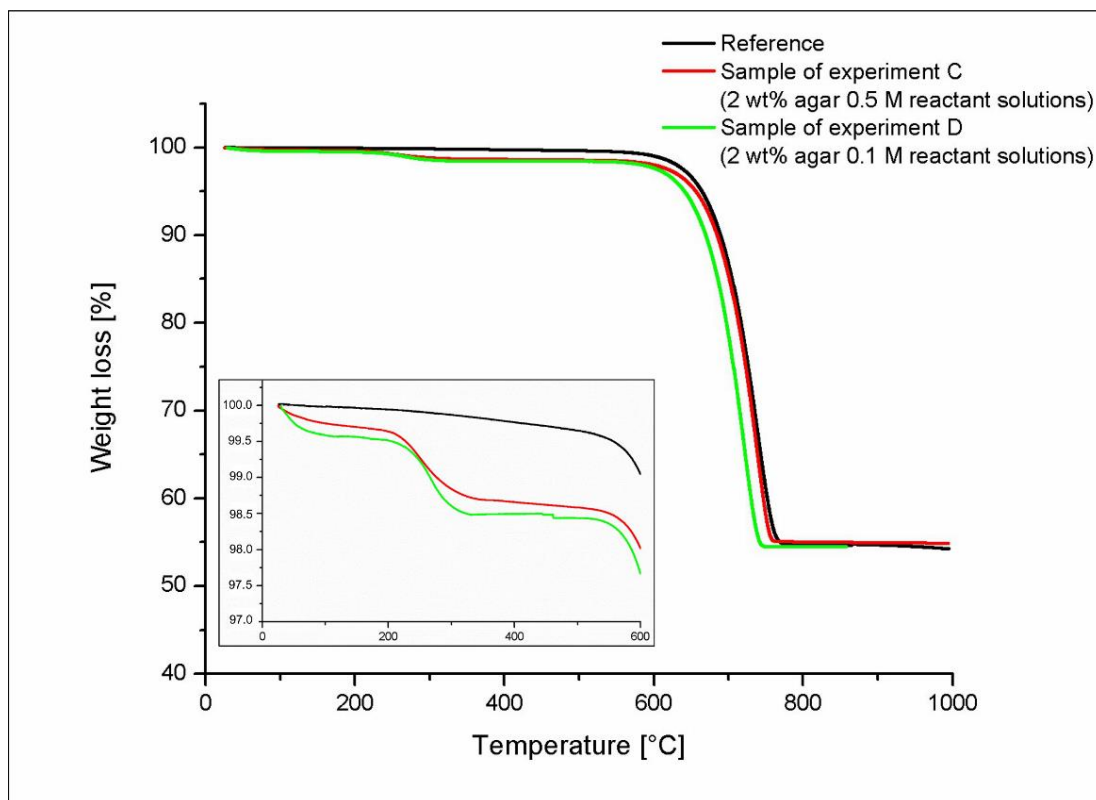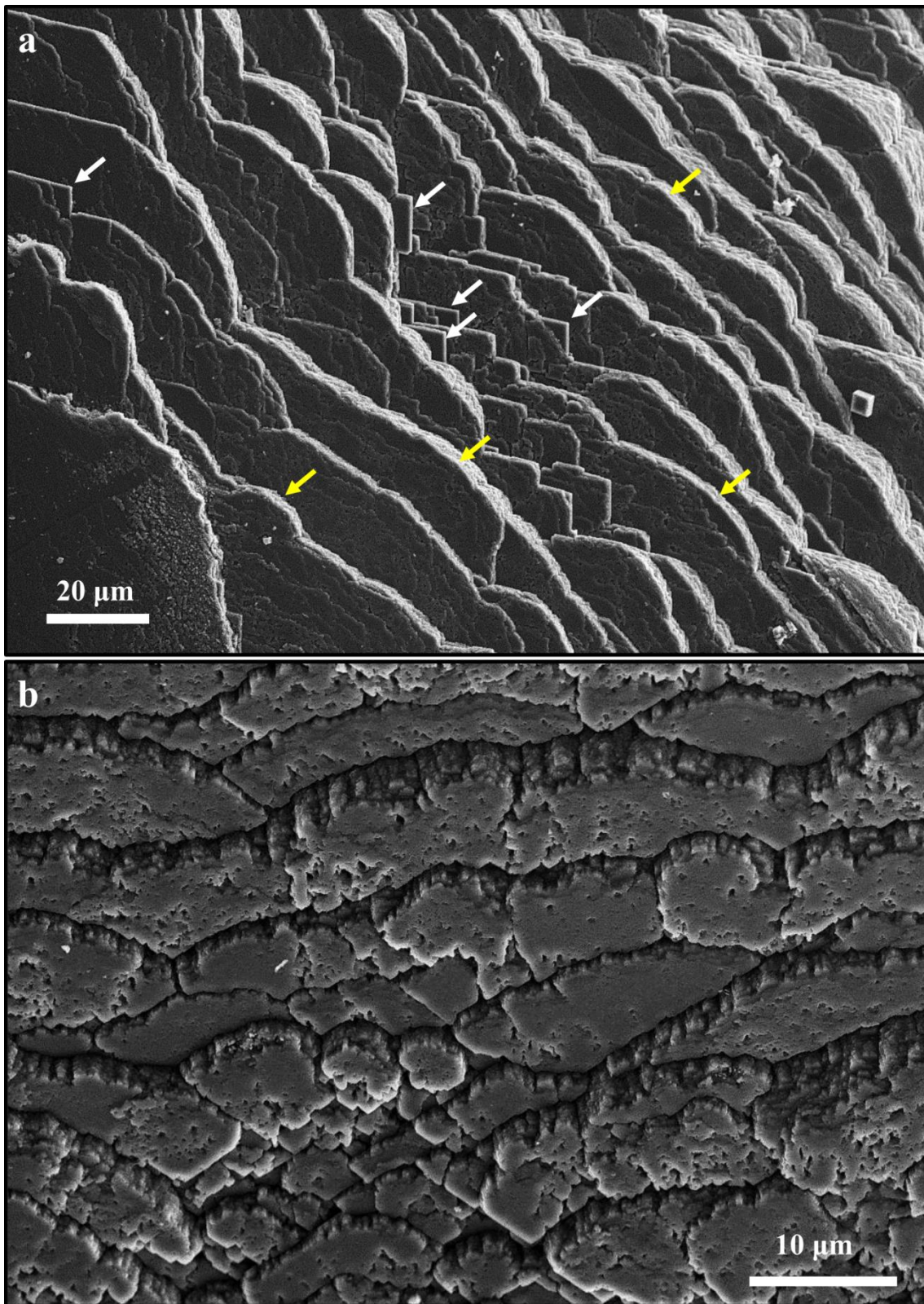
Figure 2.2-S3. TGA results for aggregates grown at experimental conditions C and D (the aggregates that incorporated the highest amount of gel) relative to a reference: calcite grown from solution.
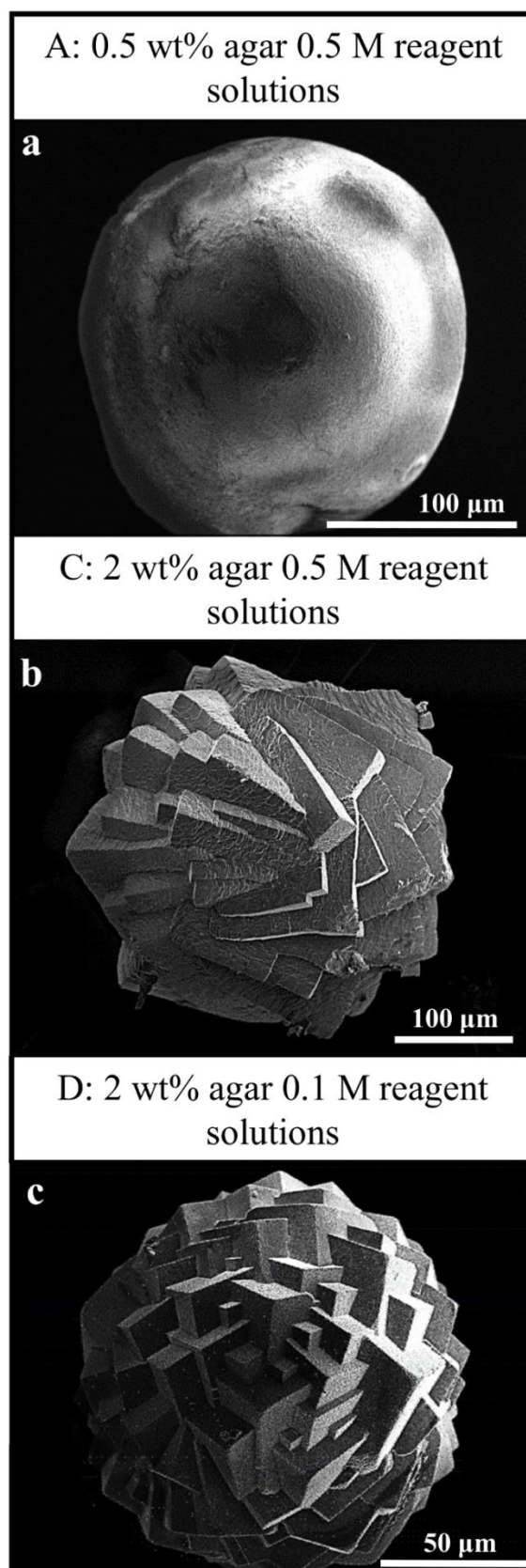
Figure 2.2-S4. Additional morphologies of aggregates obtained at experimental setups A, C and D.

Figure 2.2-S5. (a) Distribution pattern of rounded (yellow arrows) and rhombohedral (white arrows) edges bounding terraces in aggregates grown at experiment conditions A. (b) Rough curved edges bounding narrow terraces on the surface of an aggregate grown under experimental conditions A.
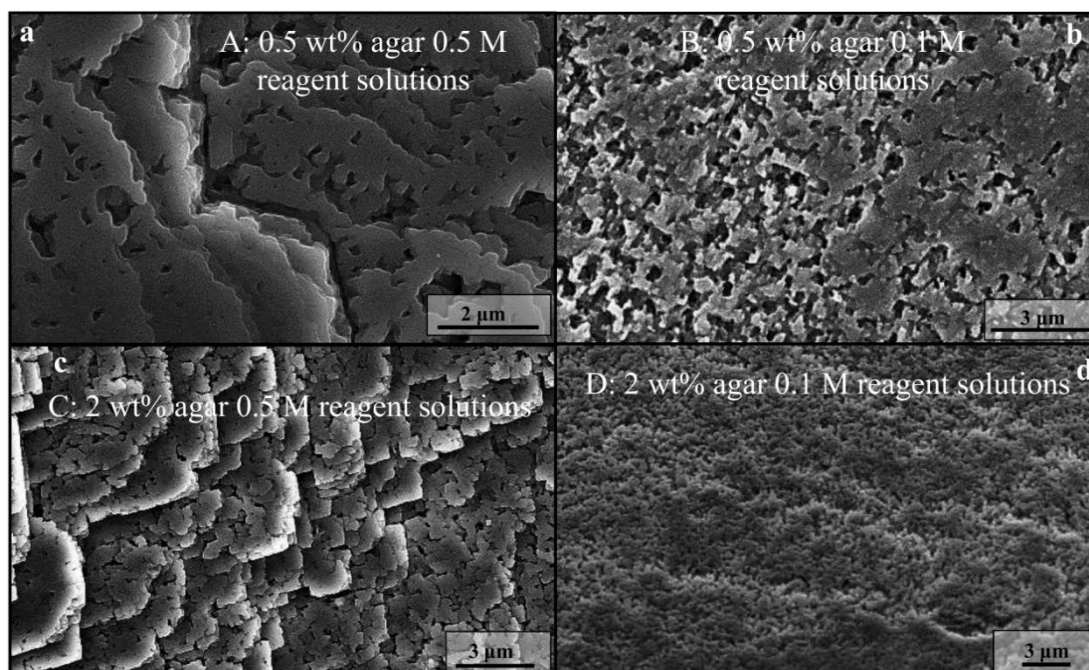
Figure 2.2-S6. Difference in surface roughness/smoothness of aggregates grown from experimental conditions A to D. Note the different characteristics of porosity on the surface of aggregates grown under different experimental conditions. More pores are visible in aggregates grown from less concentrated aqueous solutions (experimental conditions B and D; images b, d). Pores are bounded by straight lines parallel to crystallographic directions in aggregates grown in lighter gels (experimental conditions A and B; images a,b), while they show irregular morphologies to spherical morphologies in aggregates grown in heavier gels (experimental conditions C and D; images c,d).
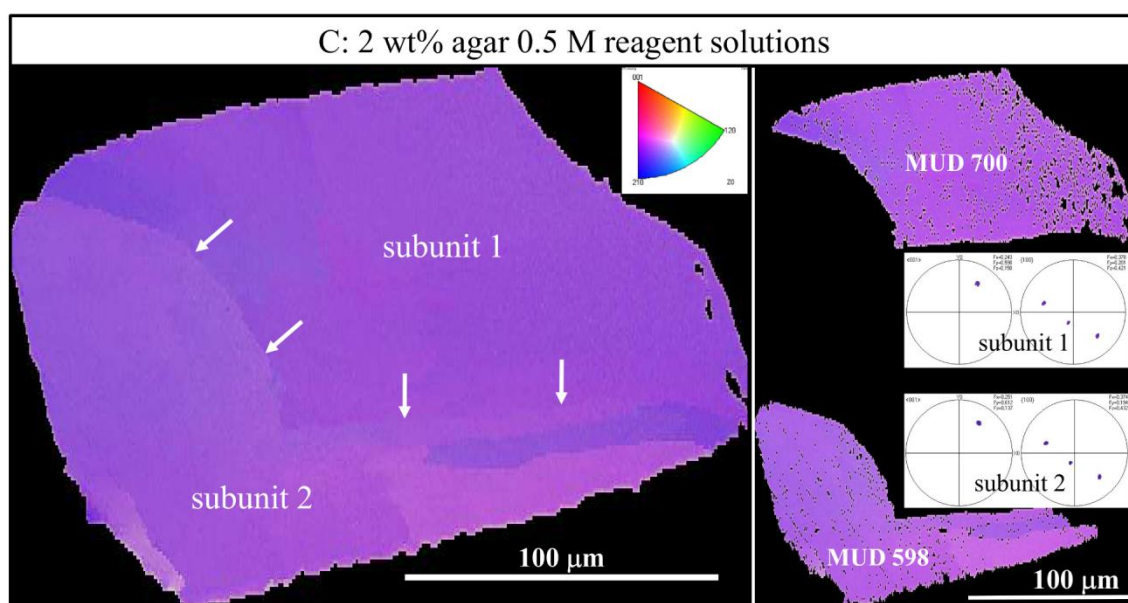

Figure 2.2-S7. Membrane formation (white arrows) that separates subunits (subunit 1 and subunit 2) from each other. The membrane is thin, very little visible and causes only a very minor tilt (below 1 degrees) between the neighbouring subunits.
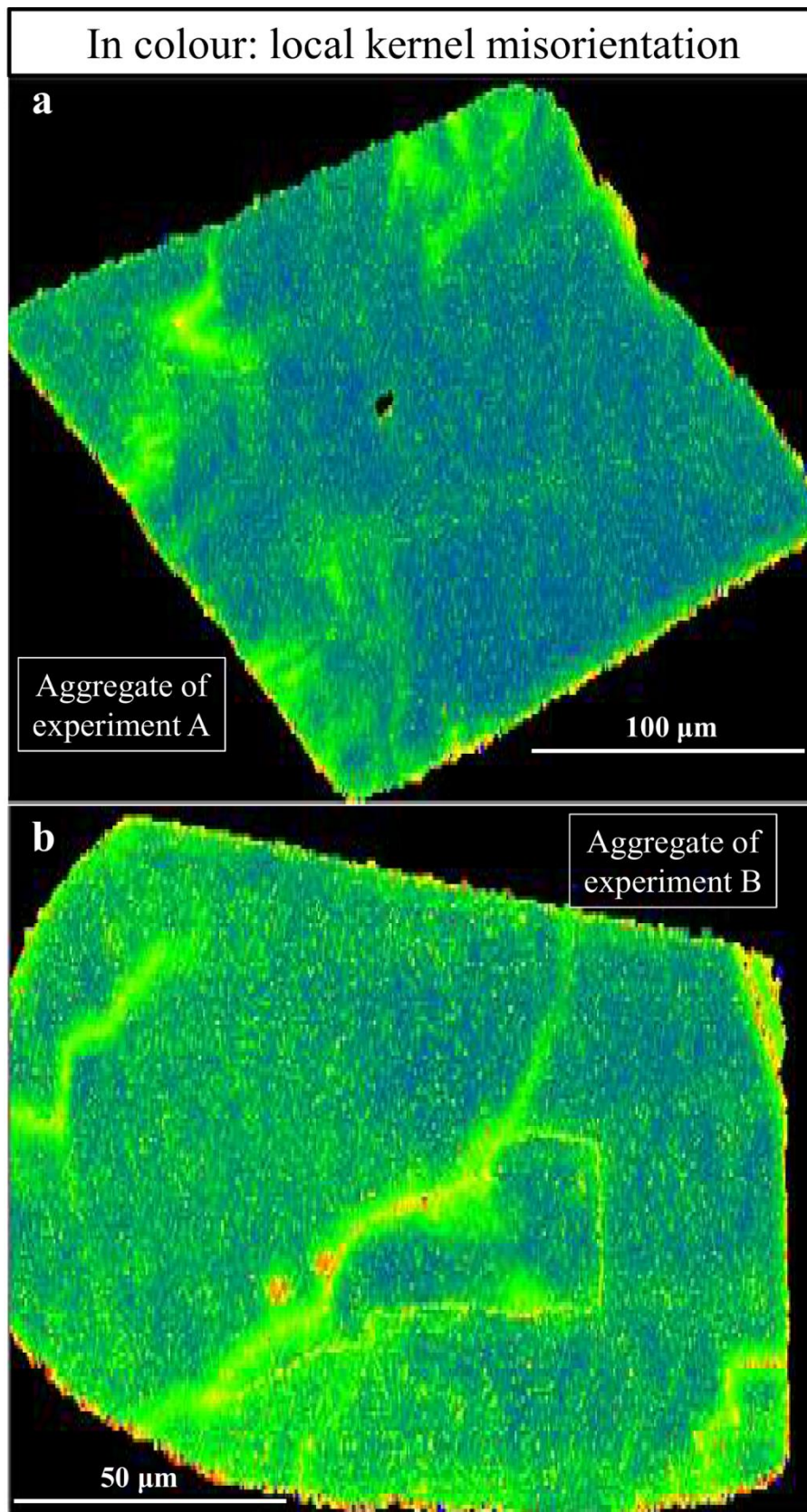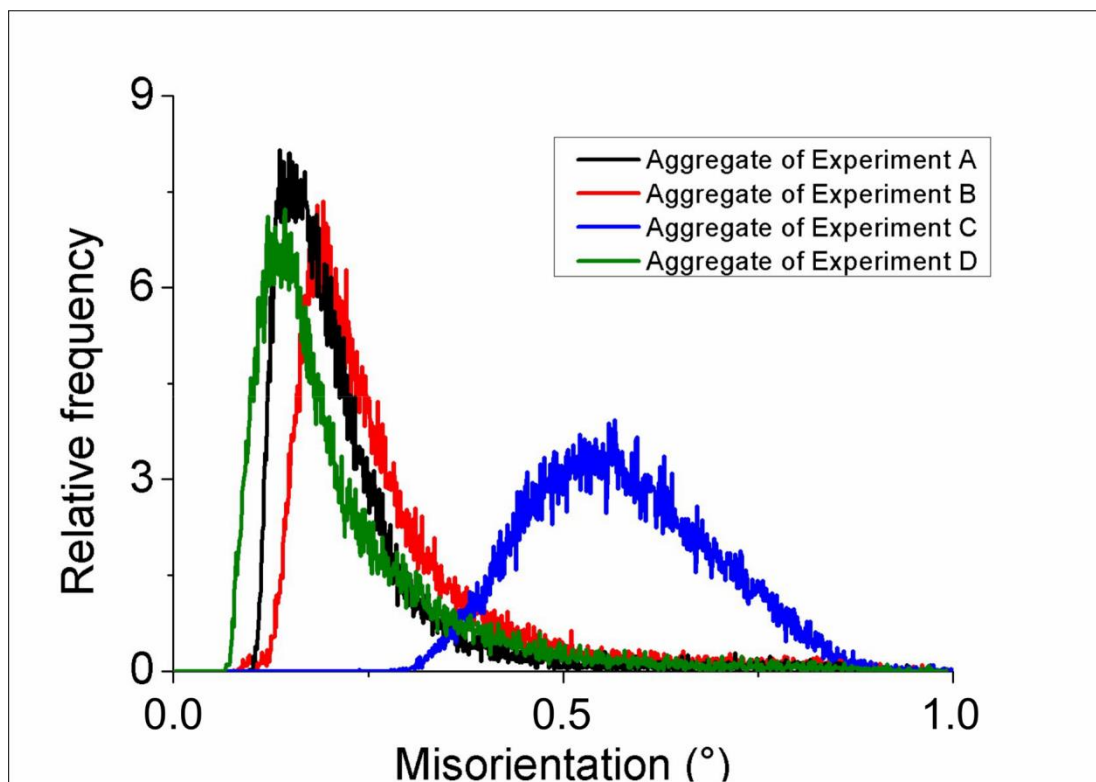
Figure 2.2-S8. Enlargement of local kernel misorientation maps shown in Figs. 2.2-6a and -7a for a better visualization of the distribution of blue, green and yellow colours.
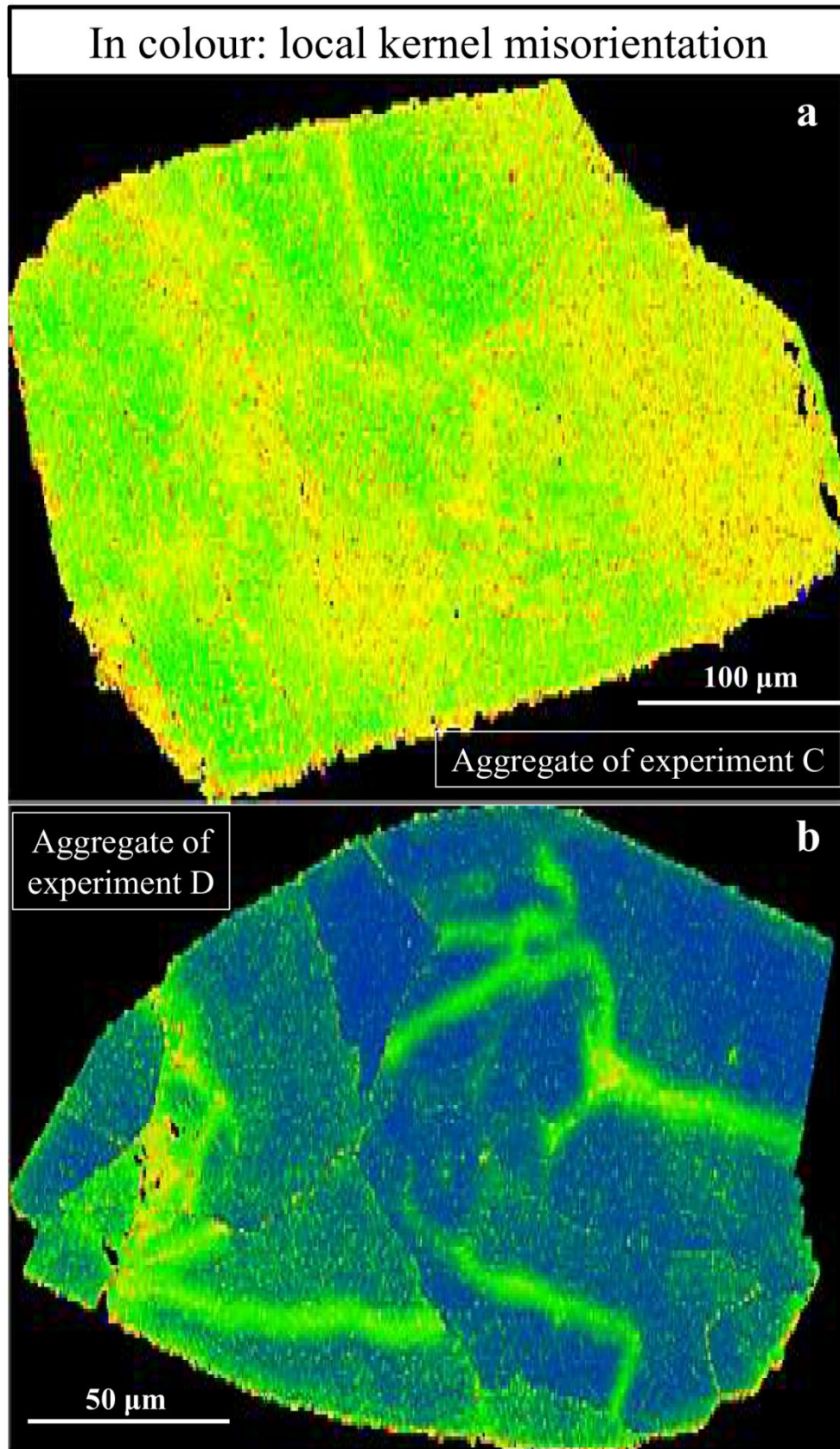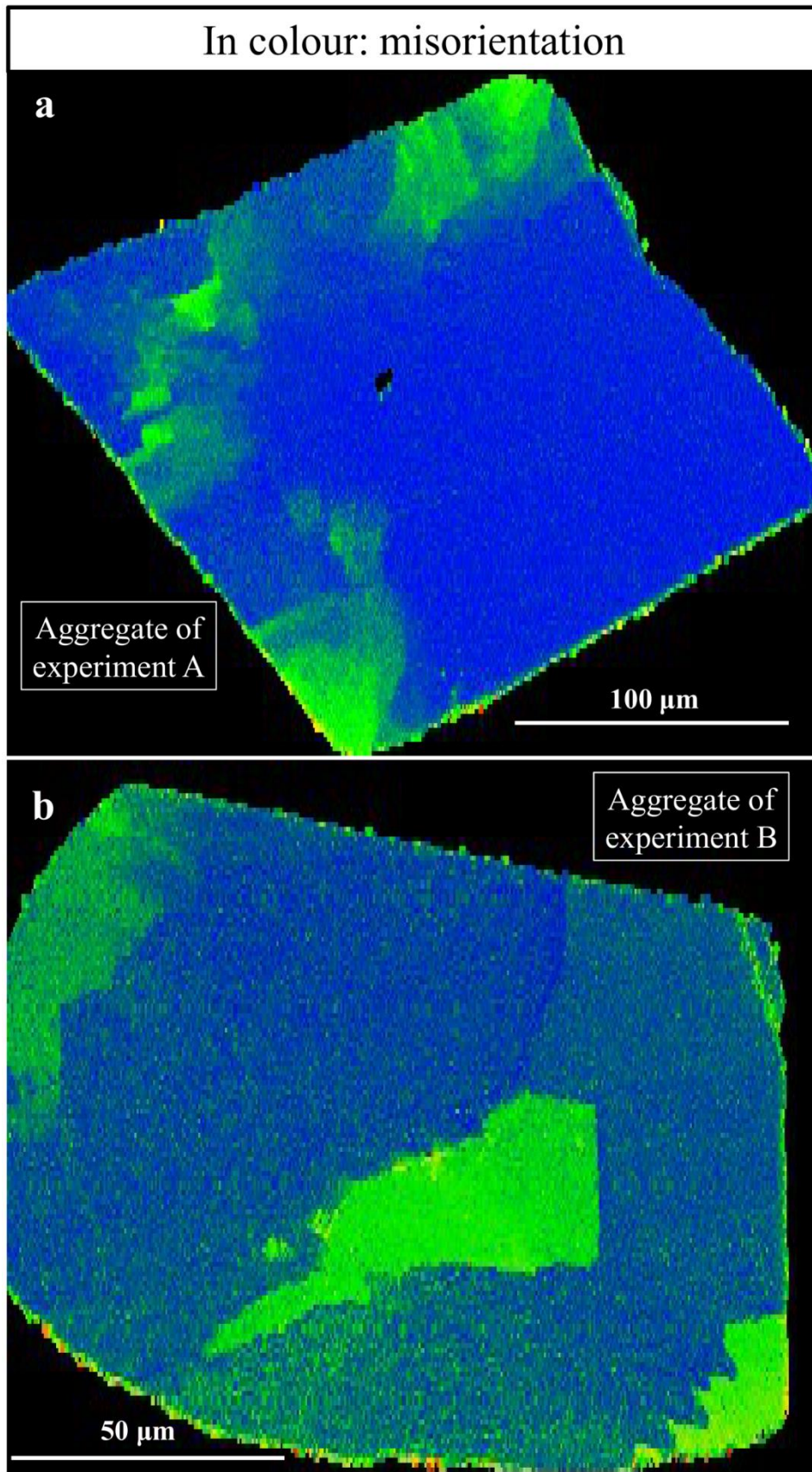
Figure 2.2-S9. Enlargement of local kernel misorientation maps shown in Figs. 2.2-8a and -9a for a better visualization of the distribution of blue, green and yellow colours.
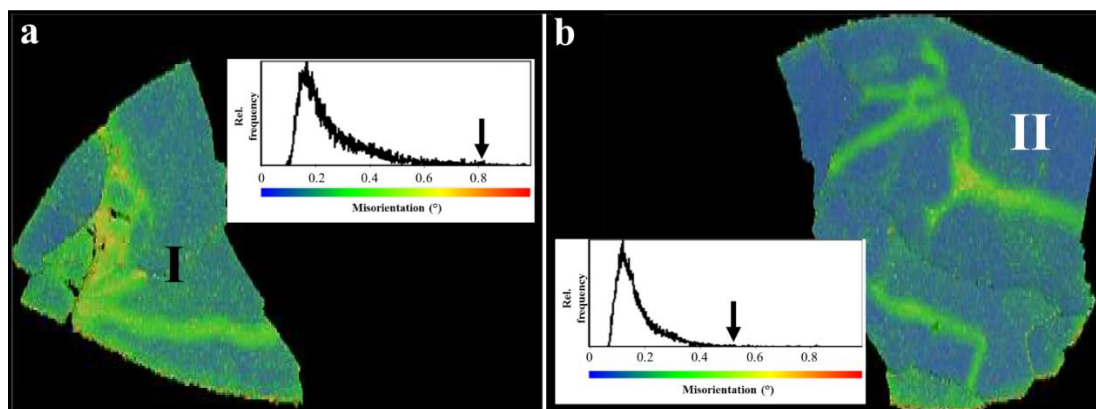
Figure 2.2-S10. Local kernel misorientation map and corresponding pole figures visualizing gel occlusion in the two major subunits I and II of the aggregate that grew at experiment conditions D. Note difference in maximum misorientation value (black arrows in the legends to S8a and S8b).

Figure 2.2-S11. Compilation of relative frequency vs. local kernel misorientation data for aggregates obtained at experiments A to D. For further details see Fig. 2.2-10.

Figure 2.2-S12. Enlargement of misorientation maps shown in Figs. 2.2-6b and -7b for a better visualization of the distribution of blue, green and yellow colours.

Figure 2.2-S13. Enlargement of misorientation maps shown in Figs. 2.2-8b and -9b for a better visualization of the distribution of blue, green and yellow colours.

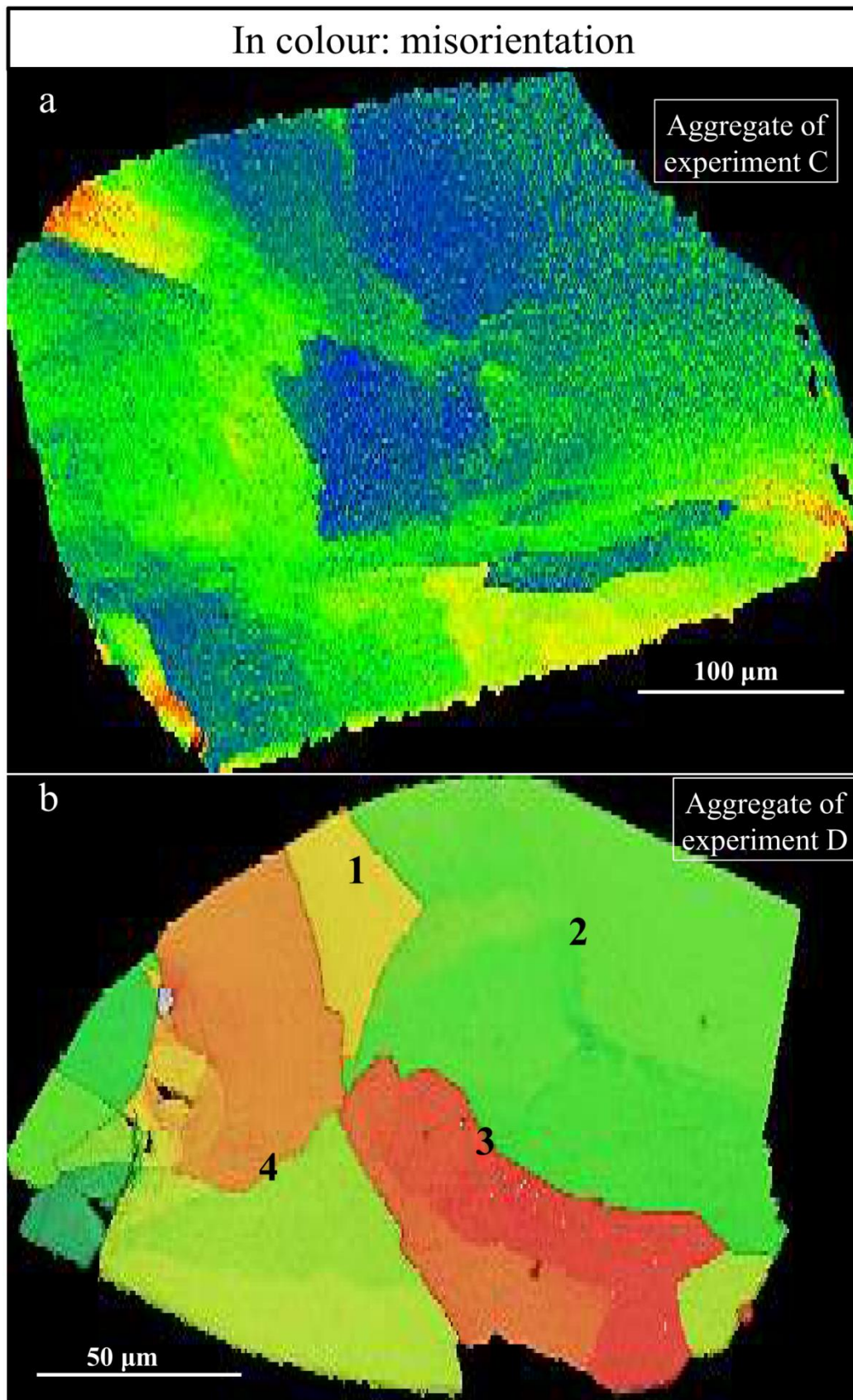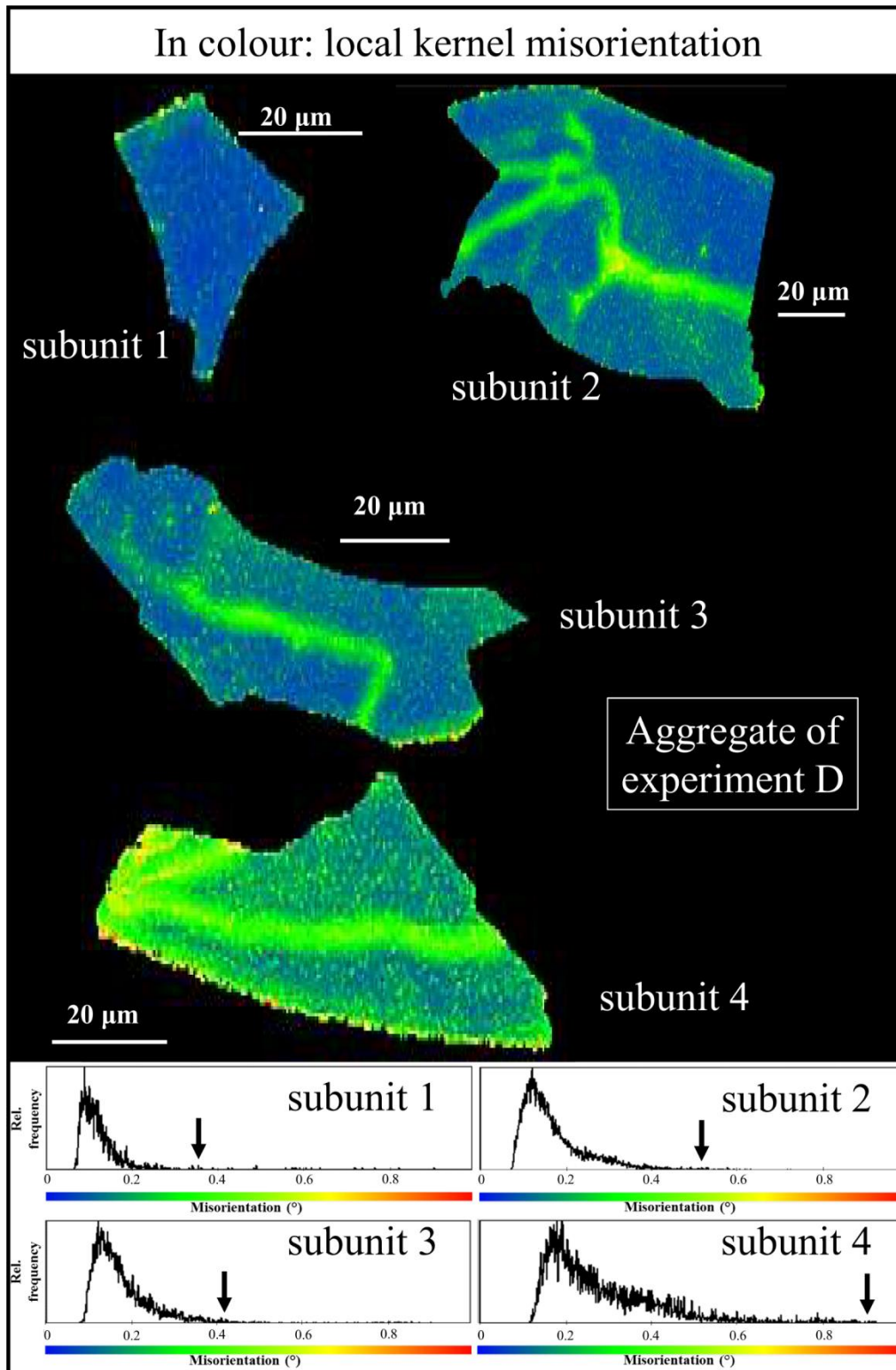**Figure 2.2-S14**. Enlargement of internal kernel misorientation maps and corresponding legends for sub-sub-subsets 1, 2, 3 and 4 of the aggregate that grew at experiment conditions D for visualization of differences in gel occlusion within the different aggregates.
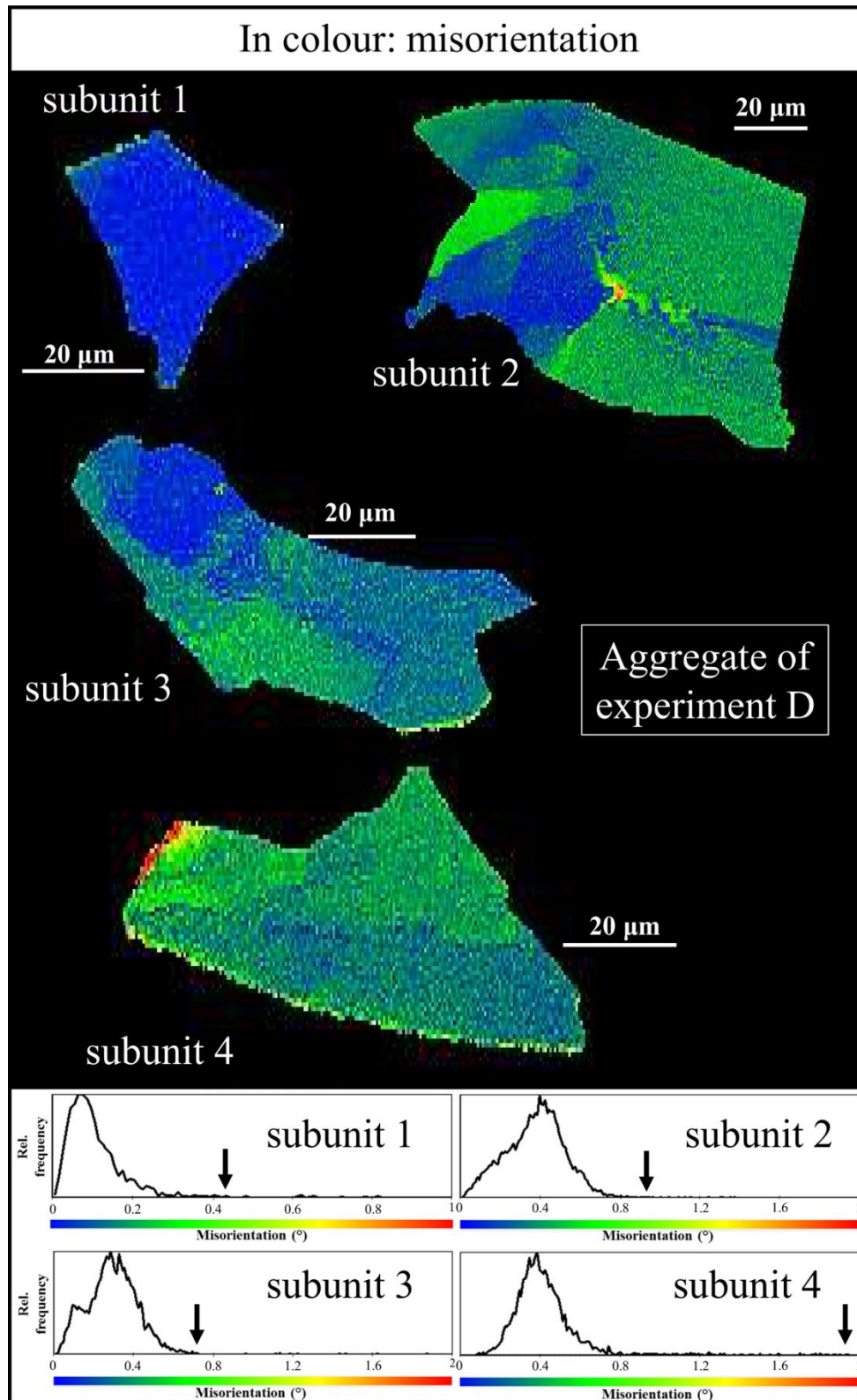
Figure 2.2-S15. Misorientation map and corresponding legends for sub-sub-subsets 1, 2, 3 and 4 of the aggregate that grew at experiment conditions D. Corresponding to the distribution pattern of the gel shown in Fig. 2.2-S12 internal strains develop, e.g. in subunits 2, 3 and 4.

2.3 Mineralogic Variations in Archaeological Bone Finds

Martina Greiner[1], Simon Trixl[2], Ferdinand M. Neuberger[2], Moritz N. Zenkert[1], Andrea Grigat, Anita Toncala[2], Joris Peters[2], Wolfgang W. Schmahl[1]

1 Department für Geo- und Umweltwissenschaften, Ludwig-Maximilians-Universität, 80333 Munich, Germany

2 Institut für Paläoanatomie und Geschichte der Tiermedizin, Ludwig-Maximilians-Universität, 80539 Munich, Germany

2.3.1 Introduction

Human migration, trade and culture transfer from pre-Roman times until the 1st century AD is subject of FOR 1670. This study on a particular subproject of FOR 1670 aims the creation of a map of isotope signatures of Celtic and Rhaetian archaeological bone finds excavated in the Rhaetian Alps and the alpine foreland – with focus on finds from the late Latène period (150 to 15 BC) and the Roman Imperial Age (15 BC to 450 AD). Both, cremated and non-cremated human remains and livestock bone finds are geochemically investigated and will contribute to the map of isotope signatures created in the context of FOR 1670.

Bone is a hierarchically structured composite with mineral and collagen being the main components. Mammal bone mineral is constituted of carbonated apatite (bioapatite) nanocrystals mineralizing mainly type I collagen microfibrils (Wagner & Weiner 1992, Glimcher 1998, Fratzl et al. 2004). If the composite structure remains intact, both the inorganic and organic compounds are protected from biochemical and chemical attack (Gernaey et al. 2001, Turner-Walker 2008).

Compared to the geologic mineral hydroxyapatite $Ca_5(PO_4)_3(OH)$, bioapatite is chemically more complex with carbonate (4-8 wt %) being an essential component. In general, the apatite (AP) structure is very accommodating to chemical substitutions which may provoke coupled ionic substitutions to maintain charge balance (Wopenka & Pasteris 2005). Chemically, the composition of bioapatite can be approximated as $(Ca,Mg,Na, vacancy)_5 (PO_4, HPO_4, CO_3)_3$ $(CO_3, H_2O, OH, F, Cl etc.)$ (Montel et al. 1981, Elliott 1994, Wilson et al. 1999, Elliott 2002, Pan & Fleet 2002). As well, trace elements such as Sr^{2+}, Pb^{2+} and Ba^{2+} can be substituted on

the Ca^{2+} cation position (Elliott 2002, Turner-Walker 2008). However, such substitutions can induce structural disorder within the AP crystal lattice (Elliott 2002). The decomposition of bone organic components which constitute about 20-28% (Lim 1975, LeGeros 1991, Elliott 2002), generates a high porosity and internal surface in the bone remains. Both, the structural misfits within the AP lattice and the newly created high surface area increase the free energy of the bioapatite which in consequence increases its solubility compared to stoichiometric hydroxyapatite (Epple 2003, Schmahl 2017). Thus, bone mineral in skeletal remains is prone to chemical and structural alterations. These diagenetically induced changes in bioapatite are likely to obscure the biological stable isotopic signatures of a bone find, therefore a careful validation of the samples conceived for the isotope map in the course of the DFG research group FOR 1670 is essential (Grupe et al. 2017).

To verify that the analysed material is original and uncontaminated (e.g. contamination with soil particles or chemical and structural alterations of the bioapatite after death), archaeological bones were investigated by X-ray Powder Diffraction (XRPD) as this method is highly suitable to identify extrinsic mineral phases and structural variations within the bone mineral itself. Selected samples (e.g. which showed further crystalline phases besides bioapatite or visibly bad preserved bones) were additionally analysed by Fourier-Transform-Spectroscopy (FTIR) as a complementary method to XRPD.

2.3.2 Materials and Methods

Among the archaeological animal bone samples considered for isotope studies in FOR 1670 (see Introduction), 65 random samples were selected for screening by X-ray Powder Diffraction. As already described in the Introduction, bone finds were dated to the Latène period (150 to 15 BC) and the Roman Imperial Age (15 BC to 450 AD). Among these, three samples with a bad state of conservation (based on their physical appearance) were analysed.

Surfaces of skeletal elements were mechanically removed with a scalpel to avoid contamination by soil. Finally, the bones were homogenized to a fine powder and passed through a sieve with a mesh size of 100 µm.

X-ray diffractograms were measured on a General Electric 3003 powder diffractometer in Bragg-Brentano reflection geometry. Cu-$K_{\alpha 1}$ radiation was selected with a focusing monochromator in the primary beam. An exposure time of 1000s on a 1D-Meteor detector was chosen, which resulted in a data collection time of 5 hours for a diffractogram from 10-110° 2θ.

The instrumental resolution function was experimentally determined with a NIST LaB_6 standard. For data evaluation and Rietveld refinement (Rietveld 1969) we applied the FULLPROF code (Rodríguez-Carvajal 1993, Rodríguez-Carvajal & Roisnel 2004) and chose a hexagonal symmetry model (Wilson et al. 2004) for refinement.

For full profile analysis, we applied the Thompson-Cox-Hastings method for convolution of instrumental resolution (as determined with a NIST LaB_6 standard) with anisotropic size and isotropic microstrain broadening (Thompson et al. 1987). However, crystallite size in *c*-direction was determined by a precise fit of the profile of the 002 reflection only, following the same Thompson-Cox-Hastings convolution procedures in FullProf as described for the full profile analysis.

Infrared spectra were measured on a Perkin-Elmer ATR-FTIR Spectrum two instrument with a resolution of 4 cm^{-1} with 128 scans.

2.3.3 Results and Discussion

X-ray Powder Diffraction

The majority of the analysed bone mineral samples exhibit similar or slightly larger lattice parameters to those of modern bovine bone (red and blue squares with black frame in Figure 2.3-1a). In comparison, mineralogical investigations on older archaeological bone finds dated to 5600-15 BC predominantly displayed bioapatite lattice parameters which are smaller than those of modern bovine bone and larger than those of hydroxyapatite (Schmahl et al 2017). However, we also observe a rather constant *c*-axis of the bioapatite while the *a*-axis varies across a broad range such that a pseudo-linear trend exists between unit cell volume and *a*-axis length (Figure 2.3-1a). As discussed by Schmahl et al. (2017) the unit cell volume V scales with the lattice parameters *a* and *c* as V = a²c sin 120°). Crystallite sizes in *a*-direction are between 59-140 Å; in *c*-direction, the crystallites are significantly larger (165-348 Å) (Figure 2.3-1b, -1c). There is only a vague correlation of crystallite sizes in *a*-direction slightly increasing with the crystallite size in *c*-direction
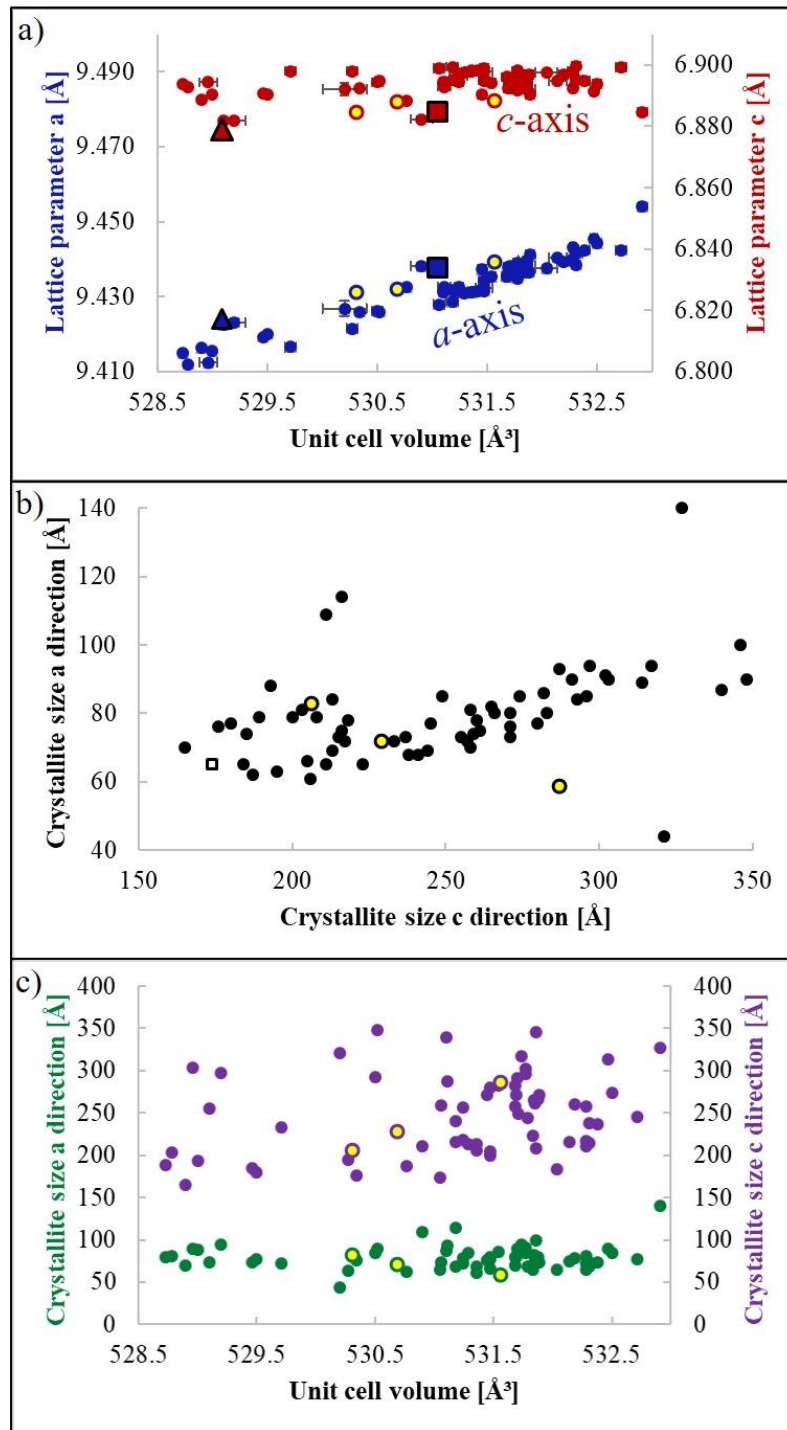
Figure 2.3-1. (a) Lattice parameters (unit cell axes) *a* (blue symbols) and *c* (red symbols) and unit cell volume of the 53 random archaeological samples according to Rietveld refinements. Triangles with black frame: Holly Springs Hydroxyapatite (Sudarsanan & Young 1969). Squares with black frame: Modern bovine femur. (b) Crystallite size in *a*-direction a vs. crystallite size in *c*-direction. The estimated standard deviation for crystallite sizes is 5 %. (c) Crystallite size in *a*- direction vs. unit cell volume (green circles) and crystallite size in *c*-direction vs. unit cell volume (purple circles). Yellow-filled circles are samples with a bad state of conservation (based on their physical appearance).

(Figure 2.3-1b), however there is only few data points diverging from the general trend. Crystallite sizes of two out of three badly preserved bones (yellow-filled circles in Figure 2.3-

1b) plot within the data cloud of the well preserved ones, the outlier displays a larger size in *c*-direction (287 Å) with respect to a relatively small size in *a*-direction (59 Å). However, also one of the well preserved samples shows this feature with 321 Å in *c*- and 44 Å in *a*-direction (Figure 2.3-1b).

We observe no correlation of crystallite size and unit cell volume regardless of conservation status (Figure 2.3-1c). As displayed in Figure 2.3-1a, hydroxyapatite lattice parameters (triangles with black frame in 2.3-1a) are smaller compared to those of bioapatite/ bone mineral. In former studies on bone cremation, it has been shown that there is a correlation between carbonate content and lattice parameters (and therefore the unit cell volume) as both decreased in consequence of thermal treatment (Greiner et al. 2018a). When bone mineral is treated at high temperatures it reacts to hydroxyapatite (Greiner et al. 2018a). Schmahl et al. (2017) inferred that bone mineral undergoes a chemical alteration while buried in the ground. Hereby, carbonate is exchanged with hydroxyl and fluorine which leads to the assumptions that i) carbonate content in younger archaeological bone finds is higher than in older archaeological bone finds and ii) unit cells are larger in younger bone finds than in older archaeological bone finds. This has to be investigated in further studies as this study only focuses on the mineralogical variety within archaeological bone finds of the same epoch.

It has been shown that crystallite size, inhomogeneity in chemical composition, and lattice defects (often summarized by the term "crystallinity") are primarily a function of "crystal age" which means that the characteristics of bone apatite crystals are mostly affected by the time between their formation and their resorption (bone turnover) from the tissue (Glimcher 2006). As we investigated non-cremated bone samples from the same age and same geographical area (therefore similar soil conditions), the variations we see in crystallographic parameters are most probable due to anatomical variations in bone mineral in general.

According to Rietveld refinements, nine out of 65 analysed archaeological samples exhibited a quartz mineral fraction of 0.1-3 wt%, whereas in only two samples more than 0.7 wt% quartz were detected. Only one sample displayed around 3 wt% calcite. Exemplary Rietveld refinement plots (10-60° 2 Theta) of bone samples containing calcite and quartz are shown in Figure 2.3-2. Quartz is a typical soil mineral and its detection
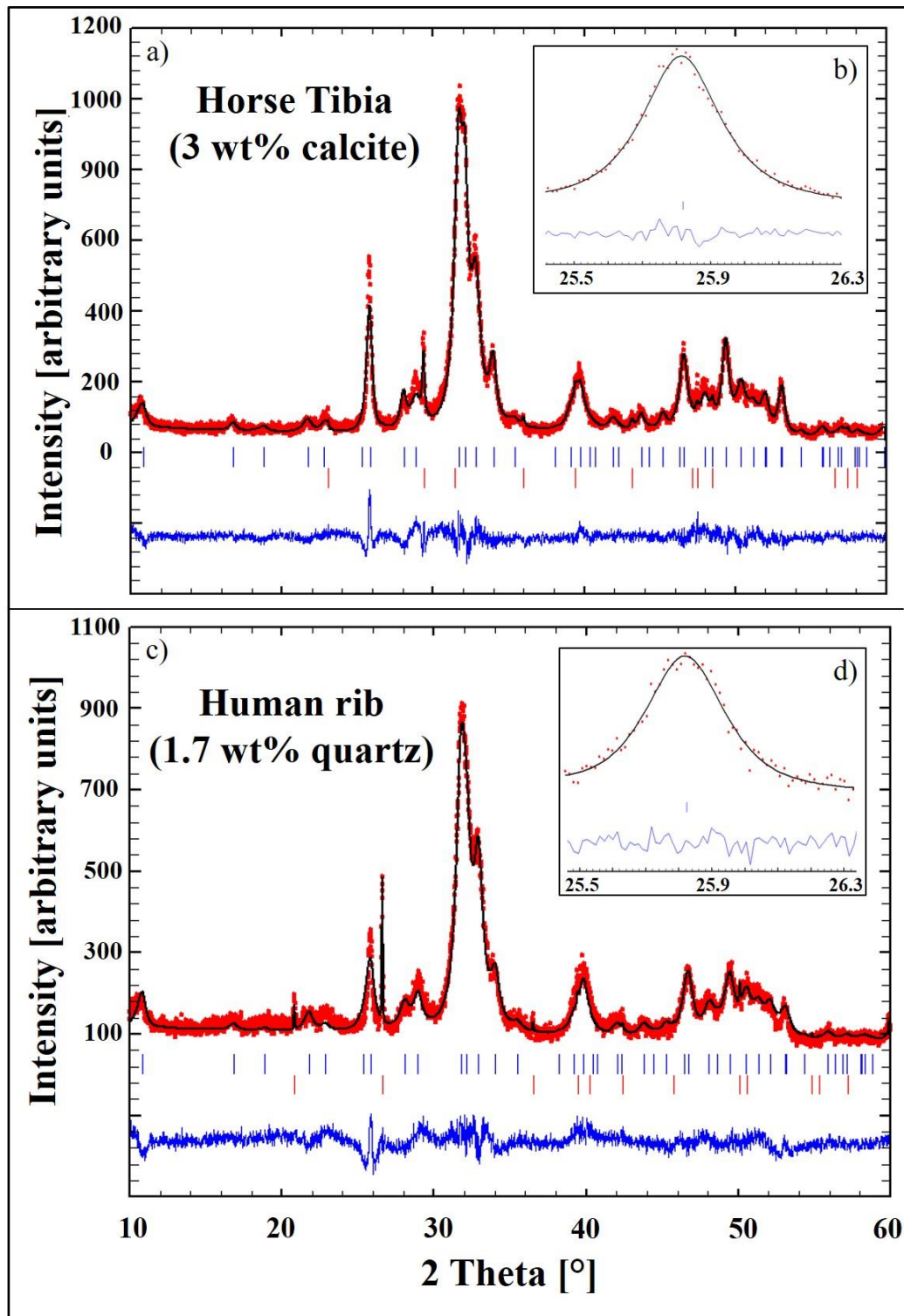
Figure 2.3-2. Rietveld refinement (10-60° 2θ) of archaeological bones **a)** horse Tibia, bioapatite with 3 wt% calcite. **b)** the 002 bioapatite reflection of the horse tibia (25.5-26.3° 2θ) **c)** human rib with 1.7 wt% calcite and **d)** the 002 bioapatite reflection of the human rib (25.5-26.3° 2θ)**.** Red dots: observed data points; black line: calculated XRD profile; bottom blue line: difference of observed and calculated data; blue vertical bars: positions of diffraction peaks of bone apatite; red vertical bars: positions of diffraction peaks of calcite (in **a**) or quartz (in **c**).

indicates that the sample cleaning procedure was not entirely effective. Soil mineral particles may have intruded into bone pores during burial and were not removed completely in the course of the cleaning process, most likely because the bones were not washed with distilled water and only the contaminated surface was removed. Contrary to expectations, the badly preserved samples displayed pure bioapatite and no foreign phases. Furthermore, their crystallographic parameters, such as unit cell volume and crystallite size (yellow-filled circles in Figure 2.3-1a) follow the same trend as the well preserved samples.

Fourier-Transform Infrared Spectroscopy

All archaeological bone spectra show characteristic phosphate group vibrational bands which can be attributed to AP at 470-480 cm^{-1} ($v_2PO_4^{3-}$), 500-750 cm^{-1} ($v_4PO_4^{3-}$), ~962 cm^{-1} ($v_1PO_4^{3-}$) and 980-1120 cm^{-1} ($v_3PO_4^{3-}$) identified according to Raynaud et al. (2002) and Destainville et al. (2003). Positions of the OH^- libration band at ~632 cm^{-1} (Destainville et al. 2003) and the OH^- stretch absorption band at 3570 cm^{-1} (González-Díaz & Hidalgo 1976, González-Díaz & Santos 1977, Vandecandelaere et al. 2012) are indicated in Figure 2.3-3a and b but are absent in all spectra. Moreover, characteristic absorption bands at 870-880 cm^{-1} and 1400-1458 cm^{-1} were attributed to $v_2CO_3^{2-}$ and $v_3CO_3^{2-}$ (Rey et al. 1989, Rey et al. 1990, Fleet 2009, Grunenwald et al. 2014). Thus, the archaeological bone mineral is not hydroxyapatite but carbonated apatite. Two distinguishable peaks can be observed for $v_2CO_3^{2-}$ which can be attributed to type B substitution (PO_4^{3-} site) at ~ 873 cm^{-1} and type A substitution (OH^- site) at 878 cm^{-1} (LeGeros et al. 1969, Rey et al. 1989). Organic compounds like amids (1250 cm^{-1} and ~1540-1750 cm^{-1}) show high peak intensities in all archaeological bone spectra (Figure 2.3-3). The modern bovine femur spectrum shows broad but more profound H_2O absorption bands from ~3000-3600 cm^{-1} (Brubach et al. 2005) compared to the archaeological bone spectra (Figure 2.3-3b). In addition, the modern bovine femur spectrum displays a broader shoulder than the archaeological bone spectra at ~1100 cm^{-1} which can be attributed to the antisymmetric stretching of HPO_4^{2-} and PO_4^{3-} (Frost et al. 2013).

Si-O-Si symmetrical stretching vibrations of quartz at 780 and 800 cm^{-1} (Simon & McMahon 1953) are observable in the IR spectra of the human rib (1.7 wt% quartz according to Rietveld refinements). Further characteristic quartz absorption bands at 1079 and 1057 cm^{-1} overlap with the $v_3PO_4^{3-}$ bands of apatite (Figure 2.3-2).
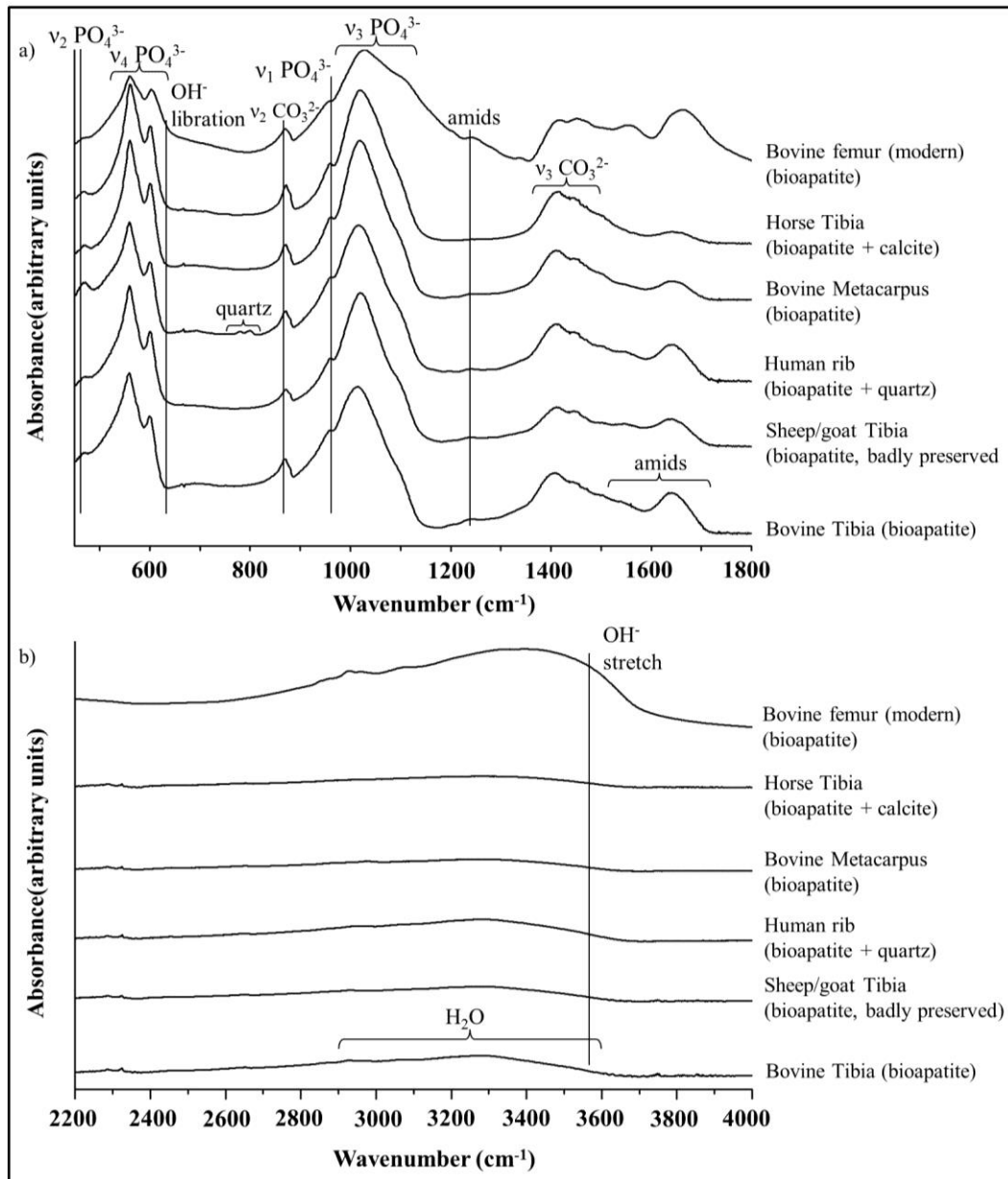
Figure 2.3-3. Infrared absorbance spectra from 450-1800 cm^{-1} of a modern bovine femur and archaeological animal and human bone finds dated to 15 BC - 450 AD (Roman Imperial Age) from **a)** 450-1800 cm^{-1} and **b)** from 2200-4000 cm^{-1}.

2.3.4 Concluding Summary

65 archaeological bone samples dated to 150 BC - 450 AD from the Rhaetian Alps and the alpine foreland were investigated by X-ray Powder Diffraction (XRPD) and in part by Fourier Transform Infrared Spectroscopy (FTIR). Additional mineral phases besides bioapatite were calcite (one sample) and quartz (nine samples). We attribute the presence of quartz to an insufficient cleaning procedure as quartz is a typical soil mineral, hence soil residuals were not removed entirely from the samples. Moreover, we ascribe deviations between crystallographic parameters among the analysed 65 specimens primarily to structural and chemical variations within the bone mineral itself ("crystal age", species and type of bone), possible secondary aspects are archaeological age (≙ burial time) and soil conditions (e.g. pH, acidity, humidity) during burial which requires further study.

2.4 pH-dependent Decomposition of Bone

2.4.1 Introduction

This chapter contains a short study on the decomposition of bone under acidic conditions. The mineral brushite ($CaHPO_4 \cdot 2H_2O$, a monoclinic calcium phosphate) has been found on archaeological bone samples and appeared as white crystallites on the bone surface (Herrmann & Newesely 1982, Verhoff et al. 2004). After Elliott (2002) and Epple (2003), the calcium phosphate phase brushite is stable at pH values below 5 (Figure 2.4-1). To study the influence of time and the kinetics of a possible apatite to brushite transformation in bone we characterized the calcium phosphate phases of bovine bone with XRPD after four and eight weeks in citric acid with pH values 4, 4.5 and 5.
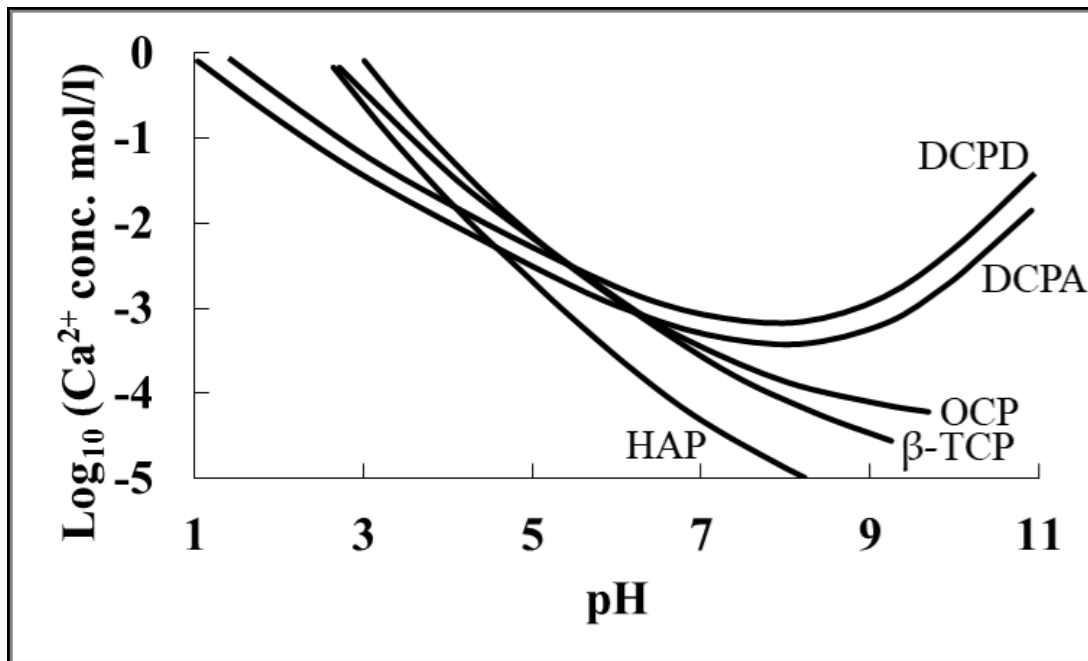
Figure 2.4-1. Solubility isotherms of calcium phosphate phases in the system $Ca(OH)_2 \cdot H_3PO_4 \cdot H_2O$ at 37 °C modified after Elliott (2002). Dicalcium phosphate dihydrate (DCPD) is brushite, dicalcium phosphate anhydrous (DCPA) is monetite, octacalcium phosphate (OCP), β-tricalcium phosphate (β-TCP) and hydroxyapatite (HAP).

2.4.2 Experimental

1 mM citric acid was prepared with Milli- Q water and the pH was adjusted with NaOH to 4, 4.5 and 5, respectively. 7x7x7 mm sized pieces of a bovine femur were cut and placed in vessels with 5 ml citric acid each, the solution was changed once a week. After four/eight weeks bone pieces were washed with Milli-Q water and powderized in a mortar and subsequently measured with XRPD.

X-ray diffractograms were measured on a General Electric 3003 powder diffractometer in Bragg-Brentano reflection geometry. Cu-K$_{\alpha 1}$ radiation was selected with a focusing monochromator in the primary beam. An exposure time of 1000s on a 1D-Meteor detector was chosen, which resulted in a data collection time of 5 hours for a diffractogram from 10-110° 2θ.

The instrumental resolution function was experimentally determined with a NIST LaB$_6$ standard. For data evaluation and Rietveld refinement (Rietveld 1969) we applied the FULLPROF code (Rodríguez-Carvajal 1993, Rodríguez-Carvajal & Roisnel 2004) and chose a hexagonal symmetry model (Wilson et al. 2004) for refinement.

For full profile analysis, we applied the Thompson-Cox-Hastings method for convolution of instrumental resolution (as determined with a NIST LaB$_6$ standard) with anisotropic size and isotropic microstrain broadening (Thompson et al. 1987). However, crystallite size in *c*-direction was determined by a precise fit of the profile of the 002 reflection only, following the same Thompson-Cox-Hastings convolution procedures in FullProf as described for the full profile analysis.

2.4.3 Results and Discussion

X-ray diffractograms of acid-treated bone do not show any reflections which can be assigned to other calcium phosphate phases beside apatite (Figure 2.4-2). Therefore, there has not been any phase transformation from apatite to a low pH acid stable calcium phosphate phase (e.g. monetite, brushite). Crystallographic parameters such as crystallite size and lattice defects are primarily a function of "crystal age" which means that the characteristics of bone apatite crystals are mostly affected by the time between their formation and their resorption (bone turnover) from the tissue (Glimcher 2006). Hence, the variations we see in crystallographic parameters (Table 2.4-1) are most probable due to anatomical variations in bone mineral in general and are not a consequence of the acid treatment. We could not observe any brushite formation within the experimental period of eight weeks. A possible reason for this is that the organic components of the bone might still be intact and protect the apatite crystallites from the acid solution.
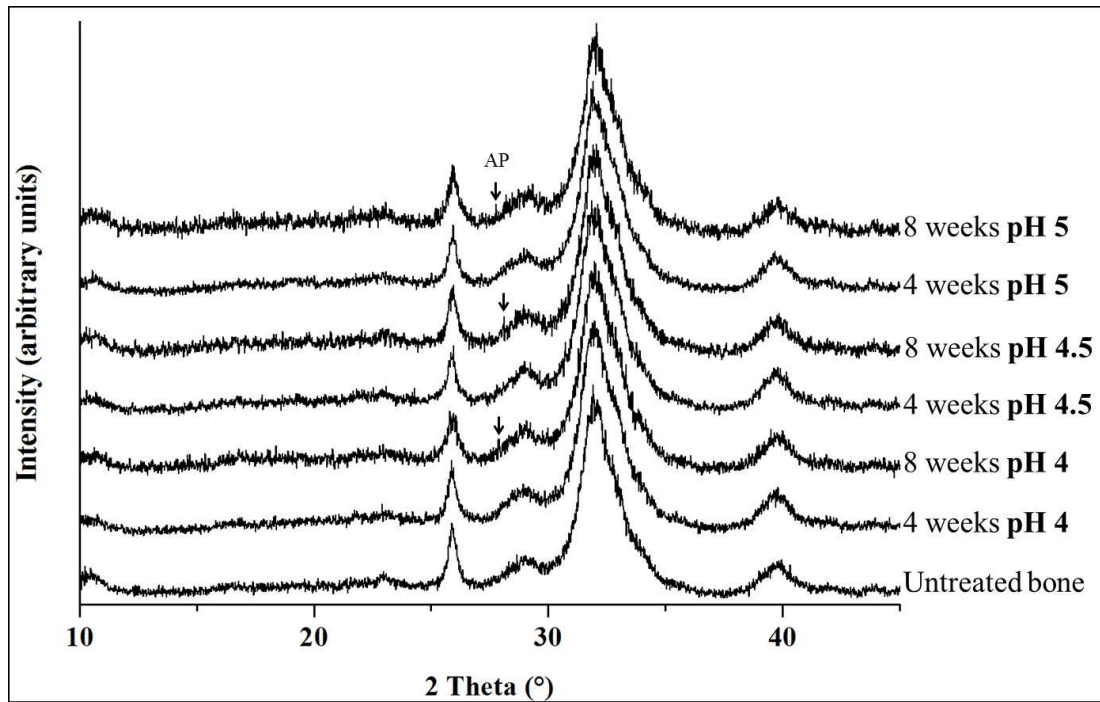
Figure 2.4-2. X-ray diffractograms (10-45° 2 Theta) of untreated bovine bone and bone after treatment with citric acid (pH 4, 4.5 and 5) for four or eight weeks, respectively. All peaks can be assigned to apatite (AP). Peaks which are not visible in the diffractogram of untreated bone but appear in acid-treated bone (black arrows) can also be assigned to AP.

Table 2.4-1. Crystallographic parameters according to Rietveld Refinements for bovine bone (untreated, for four or eight weeks treated with citric acid with pH 4, 4.5 and 5). The estimated standard deviation for crystallite sizes is 5 %.

	lattice parameter a [Å]	lattice parameter c [Å]	crystallite size in a direction [Å]	crystallite size in c direction [Å]
pristine bone	9.4376 (5)	6.8847(5)	65	174
4 weeks, pH 4	9.435(2)	6.890(1)	64	203
4 weeks, pH 4.5	9.437(2)	6.889(1)	63	216
4 weeks, pH 5	9.433(2)	6.896(1)	66	200
8 weeks, pH 4	9.436(1)	6.882(1)	70	217
8 weeks, pH 4.5	9.436(2)	6.894(2)	64	not determined
8 weeks, pH 5	9.439(2)	6.889(2)	72	177

2.5 Bone Incineration: An Experimental Study on Mineral Structure, Colour and Crystalline State

Martina Greiner[1], Alejandro Rodríguez-Navarro[2], Mario F. Heinig[1], Katrin Mayer[3], Balazs Kocsis[1], Andrea Göhring[3], Anita Toncala[3], Gisela Grupe[3], Wolfgang W. Schmahl[1]

1 Department für Geo- und Umweltwissenschaften, Ludwig-Maximilians-Universität, 80333 Munich, Germany

2 Departamento Mineralogía y Petrología, Facultad de Ciencias, Universidad de Granada, Campus Fuentenueva, 18071 Granada, Spain

3 Fakultät für Biologie, Anthropologie und Humangenomik, Ludwig-Maximilians-Universität, 82152 Planegg-Martinsried, Germany

2.5.1 Abstract

Unheated and heat-treated bovine bone material with differing heating times and heat-treated in increments from 100 °C to 1000 °C were analysed to study the crystallographic change of fresh biological bone mineral occurring during incineration. We combine several complementary analytical methods applied to the same unheated and heat treated material to ensure data consistency in order to establish a comprehensive study on heat-induced changes in bone. We applied quantitative powder X-ray diffraction, Fourier Transform Infrared Spectroscopy (FTIR), and Infrared-coupled Thermogravimetric Analysis (TGA-FTIR), and we correlated the analytical results with empirical indicators such as crystallinity indices (CI and IRSF) and bone colour changes after burning. At temperatures from 700 °C onwards after 30 minutes of heating, a considerable recrystallization reaction from bioapatite to hydroxyapatite occurred. FTIR revealed that there are no or only minor amounts of hydroxyl-ions in original bone mineral which in consequence should be referred to "carbonate-hydro-apatite" rather than hydroxyapatite. Thermal treatment induced a pronounced increase of crystallite size and an increase of hydroxyl groups in the apatite lattice accompanied by a depletion of water and reduction of carbonate contents during incineration. Thus, the heat treatment at temperatures $\geq$ 700 °C leads to the recrystallization of bioapatite to hydroxyapatite. Above 800 °C buchwaldite is formed from the Na component within the bone mineral. Moreover, we found that the transformation reaction involving crystallite growth mainly sets in after organic matrix compounds and their residues have been combusted and the apatite grains get into direct contact. The information in this work, obtained by a combination of analytical methods which are typically applied and approved to determine bone cremation temperatures, can help to better understand changes in complex biomaterials during heating. In particular, the knowledge from this study can be applied to assess the cremation conditions of archaeological bone finds. As changes in the bone mineral state are not only dependent on temperature but also on time, care must be taken to deduce a defined temperature which cremated bone finds were exposed to.

2.5.2 Introduction

From the late Bronze Age to Imperial Roman Times, the preferred manner of human burial in some parts of Europe was to cremate the bodies (Grupe et al. 2015). Structural and chemical analyses revealed that archaeological cremated bone remains from the Bronze Age (Urnfield Culture) in southern Bavaria were exposed to temperatures estimated from 700 °C to 1000 °C (Grupe et al. 2017). In archaeology, a first estimation of the heating temperature is usually based on the colour of the bone finds. Burn colour codes defined for example by Wahl (1982) or Stiner et al. (1995) are used to categorise heat exposure based on bone macroscopic appearance and colour. Since the colour of burnt bones is not only a consequence of temperature and the duration of heat-exposure (e.g. Herrmann 1977, Shipman et al. 1984, Von Endt and Ortner 1984, Nicholson 1993, Sillen and Hoering 1993, Bennett 1999, Thompson 2005, Thompson et al. 2016) but also dependent on the availability of oxygen (Walker et al. 2008) or influenced by inclusions of exogenous elements within the bone mineral such as copper (Dunlop 1978), it takes additional analytical methods to define the temperature which bone finds were exposed to.

Over the last years there's been various research on quantitative analytical methods such as X-ray diffraction (XRD) and Fourier Transform Infrared Spectroscopy (FTIR, KBr-method) analysis to understand heat-induced changes in bone in forensic, archaeological and anthropological contexts (e.g. Shipman et al. 1984, Rogers & Daniels 2002, Hiller et al. 2003, Enzo et al. 2007, Thompson & Chudek 2007, Munro et al. 2007; 2008, Lebon et al. 2008, Piga et al. 2008; 2009, Thompson et al. 2009, Snoeck et al. 2014, Mamede et al. 2018, Piga et al. 2018). XRD and full pattern analysis like the Rietveld method (Rietveld 1969) are suitable methods for the calibration of the temperature bones were exposed to (Holden et al. 1995, Person et al. 1996, Harbeck et al. 2011, Galeano & García-Lorenzo 2014). FTIR provides complementary detailed information about the chemical composition and structure of the main components of the bone material and their changes in consequence of thermal treatment (e.g. Weiner et al. 1993, Thompson et al. 2009). The thermal decomposition behaviour of bone has been thoroughly studied by e.g. Bonucci & Graziani (1974) and Ellingham et al. (2015) by Thermogravimetric Analysis (TGA).

However, some incommensurabilities remain and a direct comparison of the results reported by the mentioned authors is not feasible as different starting materials were investigated. In order to gain a deeper understanding about bone alteration by cremation, we study the evolution of bovine bone structure and chemistry as a function of heating temperature and

time. Specifically, we apply all above mentioned analytical methods to the same unheated and heated bone material to allow a direct comparison of the obtained results. Furthermore, we analyse the gaseous reaction products during bone decomposition by combining Thermogravimetric Analysis with Fourier Transform Infrared Spectroscopy (TGA-FTIR).

Bone is a hierarchically structured composite material constituted of carbonated apatite nanocrystals mineralizing collagen (type I) microfibrils (Weiner et al. 1999, Fratzl et al. 2004). Secondary organic components are non-collagenous proteins such as phosphoproteins, which are considered to play an important role in bone mineralization (Rho et al. 1998, Olszta et al. 2007). Analyses on human bone revealed that it contains about 20-28% organics and about 8% water (bound to both, collagen and mineral) (Lim 1975, LeGeros 1991, Elliott 2002). Biological apatite composition is chemically more complex than stoichiometric hydroxyapatite $Ca_5(PO_4)_3(OH)$ and can be approximated as $(Ca,Mg,Na, vacancy)_5$ $(PO_4, HPO_4, CO_3)_3$ $(CO_3, H_2O, OH, F, Cl$ etc.$)$ (Montel et al. 1981, Elliott 1994, Wilson et al. 1999, Elliott 2002, Pan & Fleet 2002). Moreover, the chemical composition changes with both species and type of bone and is influenced by diet, physical activity and age (Biltz & Pellegrino 1983, Driessens & Verbeeck 1990, Rodríguez-Navarro et al. 2018). Carbonate content in bone mineral was determined between 5 and 8 wt% and either substitutes in the OH^- channel site (A-type substitution) or substitutes a tetrahedral PO_4^{3-} group (B-type substitution) of the apatite structure (LeGeros et al. 1969, Rey et al. 1990, Wopenka & Pasteris 2005, Yi et al. 2013). In bone apatite, most of the carbonate substitutes are located at the phosphate-site rather than in the c-axis channel-site (Elliott 2002). In this study we refer to bone mineral as "bioapatite".

As previous studies showed, heating at low temperatures from 100 °C already induces small changes of the bioapatite structure (Harbeck et al. 2011). After Piga et al. (2009), Schmahl et al. (2017), and Greiner et al. (2018a) recrystallization of the bioapatite and crystallite growth notably sets in from 600 °C onwards. In this study, we aim to narrow both, the temperature range and the role of heating time in order to specify the conditions where hydroxyapatite crystallization sets in. Moreover, we aim to gain a deeper knowledge on the decomposition process as well as structural and chemical changes in bone during thermal heat treatment.

2.5.3 Materials and Methods

Pieces of compact bone were cut from the diaphysis of a fresh bovine femur and residuals of flesh, bone marrow and cancellous bone were mechanically removed. Subsequently, the

bones were defatted for five days with diethylether in a Soxhlet extractor which facilitates the grinding process. Fat residues on the bone surface were mechanically removed afterwards.

All heating experiments were carried out in a muffle furnace under oxidising conditions. Ten bone pieces were heated at temperatures ranging from 100 °C to 1000 °C (steps of 100 °C) for 150 minutes. In addition, six bone pieces were incinerated at 650 °C and six bone pieces at 700 °C for 10, 20, 30, 40, 50 and 60 minutes each. After incineration, the samples were finally homogenized to a fine powder and passed through a sieve with a mesh size of 100 μm to obtain a smooth sample surface for X-ray measurements.

X-ray diffractograms were measured on a General Electric 3003 powder diffractometer in Bragg-Brentano reflection geometry. Cu-$K_{\alpha 1}$ radiation was selected with a focusing monochromator in the primary beam. An exposure time of 1000s on a 1D-Meteor detector was chosen, which resulted in a data collection time of 5 hours for a diffractogram from 10-110° 2θ.

All samples were mixed with NIST 660b LaB_6 as an internal standard between 2 and 5 wt% depending on the sample. The instrumental resolution function was experimentally determined using the internal standard. For data evaluation and Rietveld refinement (Rietveld 1969) the FULLPROF code (Rodríguez-Carvajal 1993, Rodríguez-Carvajal & Roisnel 2004) was applied and we chose a hexagonal symmetry model of carbonated apatite (Wilson et al. 2004) for refinement. In the literature bone apatite is frequently sketched as platelet-shaped (e.g. Etok et al. 2007, Landis & Jacquet 2013) due to the hexagonal or near-hexagonal (e.g. Ikoma & Yamazaki 1999, Enzo et al. 2007, Tonegawa et al. 2010) metrics of the unit cell. The *a*- and *b*-axis cannot be distinguished in powder diffraction as the corresponding peaks exactly overlap. Therefore, crystallite size analysis by X-ray diffraction obtains only an average size for the directions perpendicular to the *c*-axis.

We used the Thompson-Cox-Hastings method for convolution of instrumental resolution with anisotropic size and isotropic microstrain broadening (Thompson et al. 1987). The low-angle part (10-12°) was excluded due to difficulties in describing small angle scattering contributions, such that the 010 reflection was not included in the refinement. We encountered persistent problems in modelling anisotropic line broadening in full-profile Rietveld refinement. Therefore, we finally determined the crystallite size in *c*-direction independently by a precise fit of the profile of the 002 reflection only, following the same Thompson-Cox-Hastings convolution procedures in FullProf as described for the full profile analysis.

Infrared spectra of the original and heat-treated bone mineral were measured on a Bruker Equinox FTIR instrument with a resolution of 4 cm^{-1} and with 128 scans, resulting in a 2 minutes acquisition time per sample. 1.4 mg of sample powder were mixed with 200 mg of KBr in a mortar, pressed to a pellet and subsequently measured. An analysis of the spectral decomposition in the range from 450-750 cm^{-1} was performed that resulted in seven bands. Every bandshape was fitted with a combination of a Gaussian and a Lorentzian sum function for peak height and width, centre position and peak area.

To study its thermal decomposition, we heat-treated the bone material in air and nitrogen atmosphere, respectively, by using a Shimadzu TGA-50H thermogravimetric analyzer equipped with a Mettler-Toledo AX26 Delta Range microbalance. The temperature was raised from 25 up to 950 °C at a heating rate of 20°C/minute. FTIR data from the gaseous reaction products were collected at regular time intervals of one minute.

2.5.4 Results

Bone Colour

The colour of bone changes in the course of thermal exposition. It was monitored by eye for a comparison with previously published observations and with the XRD and FTIR data.

Unheated bone appears in a white-beige colour. At a temperature of about 300 °C bone colour changes to brown, appears grey-white at around 600 °C, and remains white at temperatures above 700 °C (Table 2.5-1).

Table 2.5-1. Bone colour observed for unheated bone and heat-treated bone for 150 minutes from 100-1000 °C under oxidising conditions.

temperature (°C)	untreated	100	200	300	400	500
colour	white-beige	white-beige	grey-brown	brown	grey-beige	light grey

temperature (°C)	600	700	800	900	1000	
colour	grey-white	white	white	white	white	

Bone colour also changed dependent on the heating time periods. At 650 °C, the colour remains e.g. black after 10 minutes, and grey after 60 minutes incineration. In comparison, at 700 °C bone colour appeared black after 10 minutes heating, whereas it appears light grey after 60 minutes (Table 2.5-2).

Table 2.5-2. Bone colour observed for heat-treated bone at 650 and 700 °C from 10-60 minutes under oxidising conditions.

	10 min	20 min	30 min	40 min	50 min	60 min
650 °C	black	black	black	black-grey	black-grey	grey
700 °C	black	black	black-grey	grey	light grey	light grey

X-ray Diffraction

Figure 2.5-1a shows a selected section of the X-ray powder diffraction patterns (24-36° 2θ range) of unheated bone and bones heated at different temperatures (100, 200, …. 1000 °C) for 150 minutes. The untreated bone mineral displays extremely broadened diffraction peaks due to its nanocrystalline nature. With increasing temperature up to 600 °C only a slight sharpening of the overlapping 121, 112 and 030 reflections can be observed while the 002 reflection, corresponding to the crystallographic *c*-axis of the crystallites, displays fairly the same broadening as for untreated bone or bone treated at lower temperatures. The diffraction pattern sharpens considerably from 700 °C upwards. The region of 31.5-33° 2θ showing overlapping peaks below 700 °C reveals clearly distinct 121, 112 and 030 reflections after treatment at temperatures of 700 °C or higher.
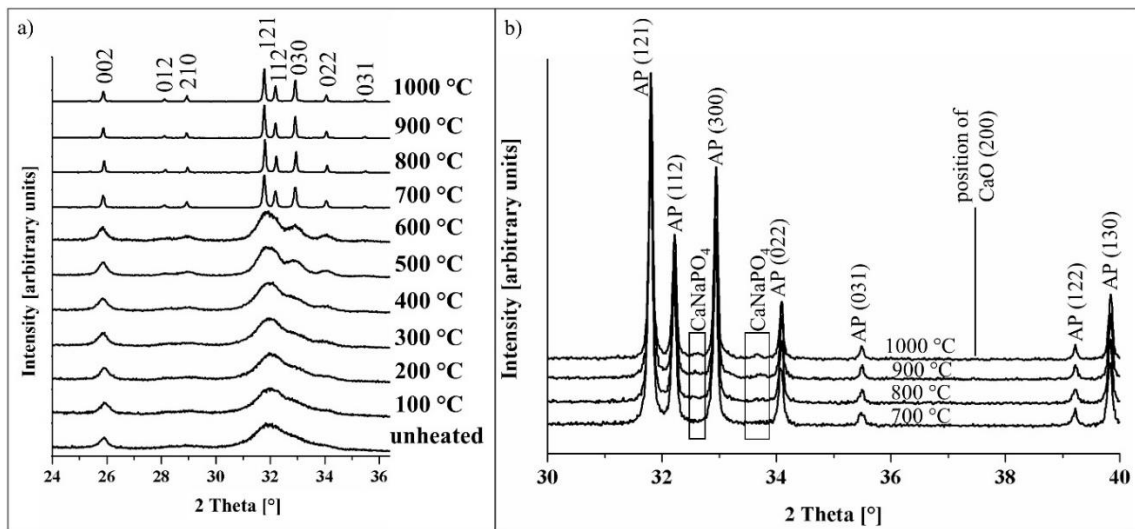
Figure 2.5-1. (a) Sections of X-ray diffraction patterns (24-36° 2θ) of unheated and heat-treated bone from 100-1000 °C; (b) XRD diffractograms (30-40° 2θ) of bone heat-treated at 700, 800, 900 and 1000 °C. Corresponding phases are indicated, the position expected for the most prominent peak of CaO (200) is also pointed out. Note the emerging buchwaldite peaks from 800 °C (indicated with black rectangels).

From 800 °C onwards, an additional mineral phase, which could be identified as buchwaldite, $CaNaPO_4$, (Ben Amara et al. 1983, Piga et al. 2018), appears (Figure 2.5-2b). According to the Rietveld refinement the bovine bone heat-treated at 1000 °C contains around 3 wt% of buchwaldite (Figure 2.5-2). No lime (CaO) (Smith & Leider 1968) could be detected in our analyses (Figure 2.5-1b).
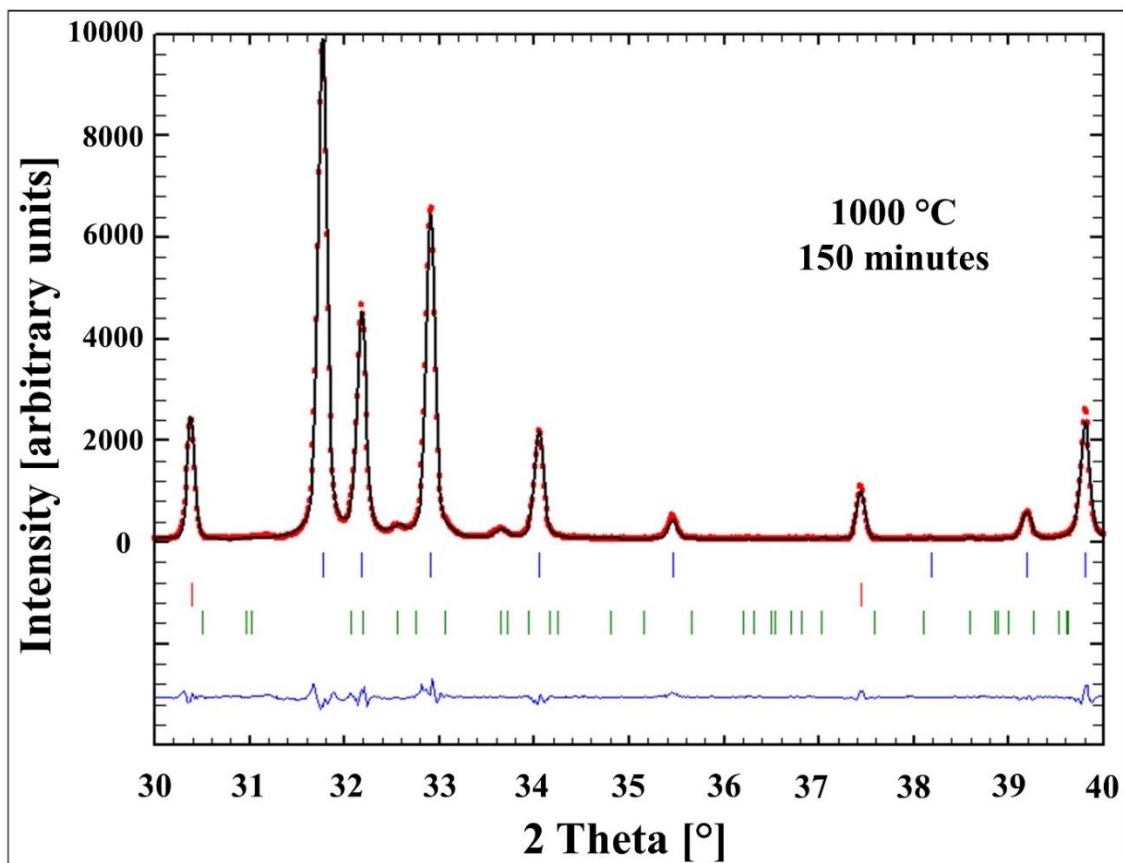
Figure 2.5-2. Rietveld refinement (30-40° 2θ) of bovine bone heat-treated at 1000 °C, 150 minutes heating. *Red dots*: observed data points; *black line*: calculated XRD profile; *bottom blue line*: difference of observed and calculated data; *green vertical bars*: positions of diffraction peaks of buchwaldite; *red vertical bars*: positions of diffraction peaks of LaB_6 standard, *blue vertical bars*: positions of diffraction peaks of bone apatite.

Our Rietveld refinements of unheated and heat-treated bone show a good agreement between observed and calculated diffraction profiles (see selected sections from 24-40° 2θ in Figure 2.5-3). Whole powder pattern refinements are shown in Figure 2.5-A1. The evolution of the lattice parameters *a* (=*b*) and *c* as measured at room temperature after thermal treatment for 2.5 h at each temperature is displayed in Figure 2.5-4a. The lattice parameter *c* considerably increases with treatment from 100-200 °C, then decreases when heat-treated at 300-700 °C. From 700 to 1000 °C lattice parameters slightly increase but vary by only six Rietveld refinement standard deviations. Crystallite size increases only slightly up to 600 °C and rises dramatically at 700 °C (Figure 2.5-4b).
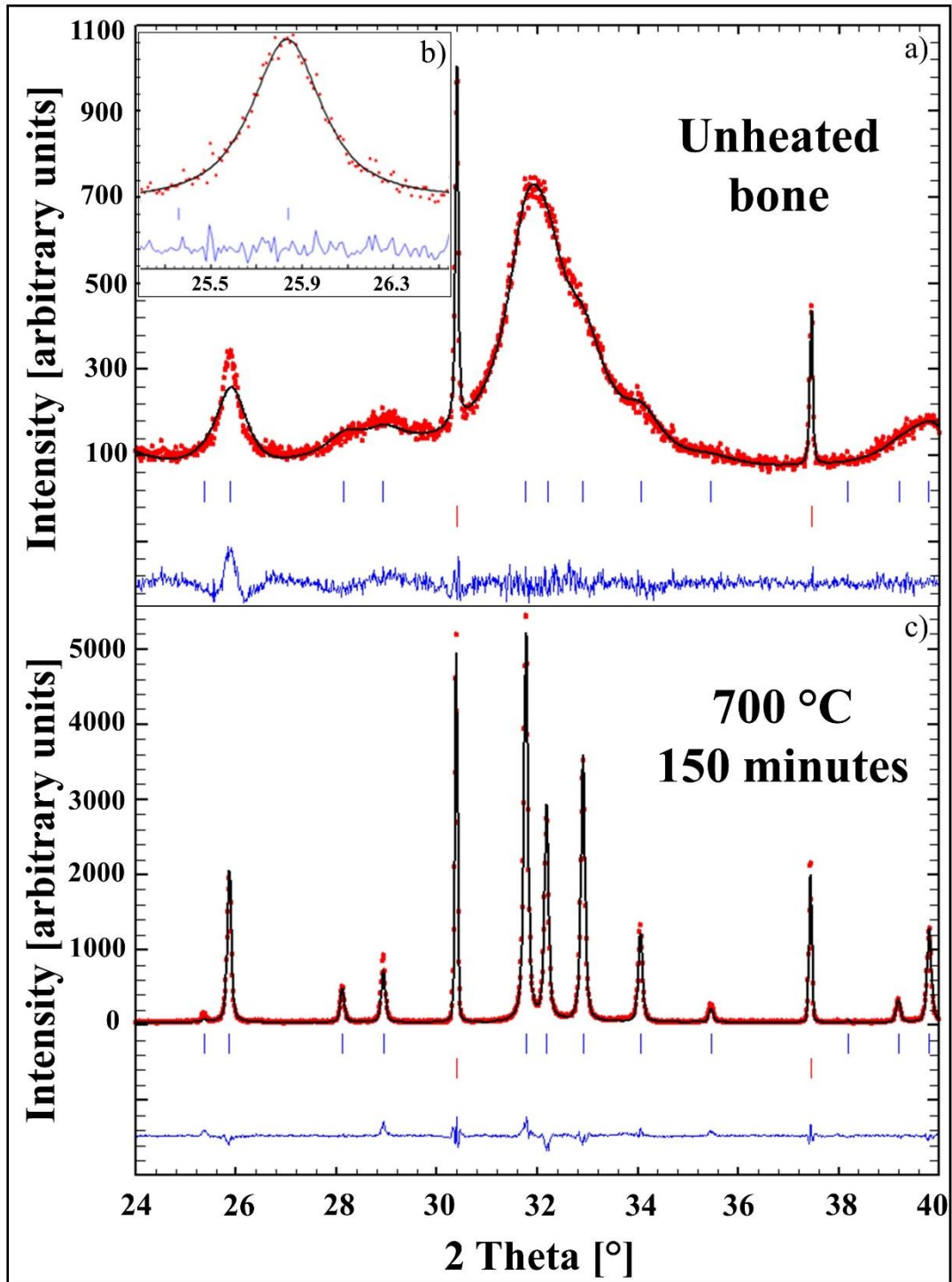
Figure 2.5-3. Rietveld refinement of (a) unheated bovine bone (24-40° 2θ), (b) the 002 reflection of unheated bovine bone (25.3-26.5° 2θ) and (c) bone heat-treated at 1000 °C for 150 minutes (24-40° 2θ). *Red dots*: observed data points; *black line*: calculated XRD profile; *bottom blue line*: difference of observed and calculated data; *red vertical bars*: positions of diffraction peaks of LaB$_6$ standard, *blue vertical bars*: positions of diffraction peaks of bone apatite.
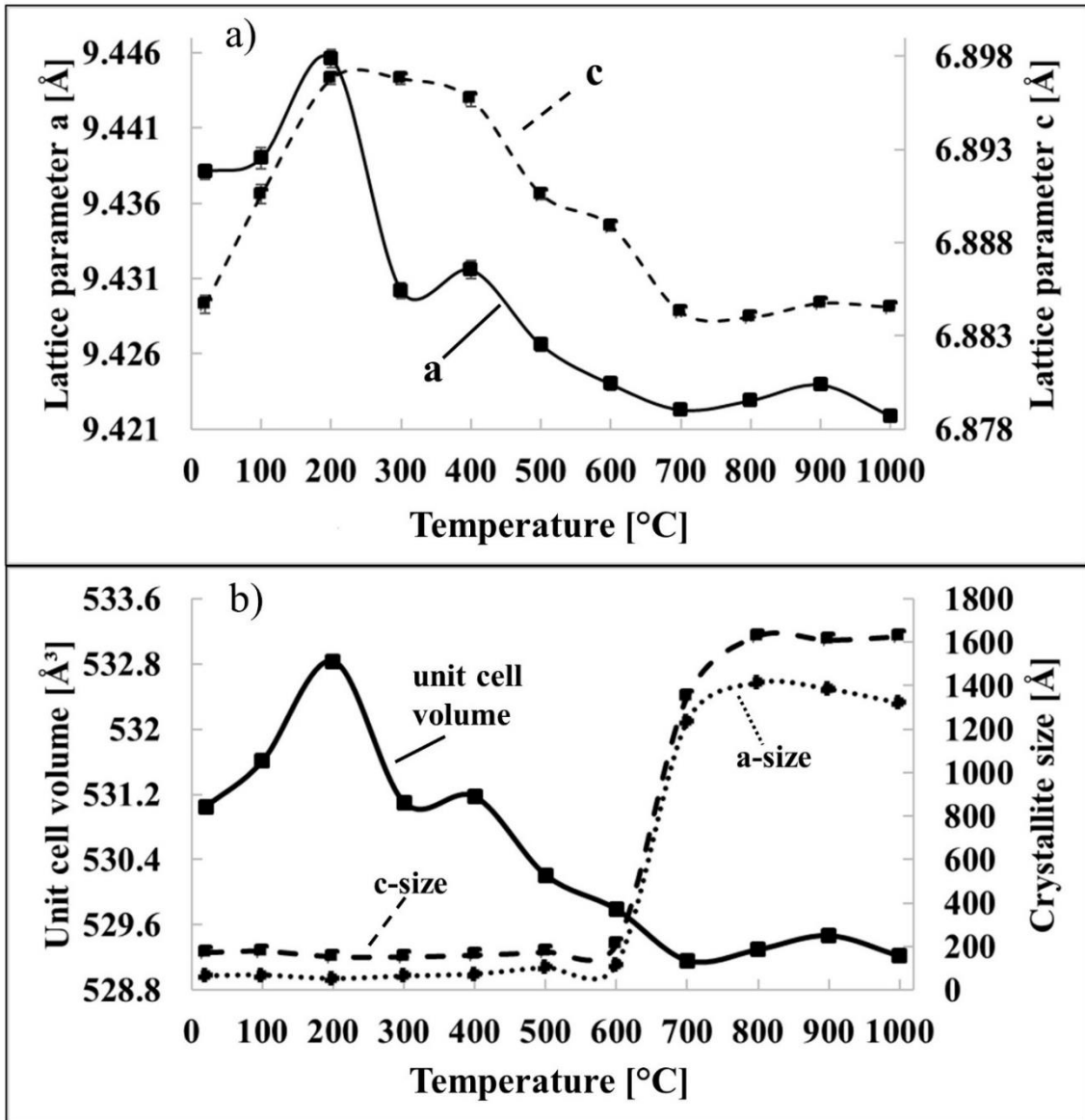
Figure 2.5-4. (a) Lattice parameters *a* (=*b*) (solid line) and *c* (dashed line) of bone mineral, untreated and heat-treated from 100-1000 °C for 150 minutes; (b) Crystallite sizes in *a*-direction (dotted line) and *c*-direction (dashed line) and unit cell volume (solid line) of bone mineral heat-treated from 100-1000 °C for 150 minutes. The standard deviation for crystallite sizes is estimated as 5 %.

Unit cell volume increases with heating at 200 °C, steadily decreases at 300-700 °C and slightly increases again from 700 °C along with the marked increase in crystallite size (Figure 2.5-4b).

Since we could observe a significant structural change in bone mineral between 600 and 700 °C we focussed on this temperature range and shortened the heating periods to study not only the temperature- but also the time-dependence of bone crystallinity during incineration.

The X-ray diffractograms (only 24-36° 2θ range shown in Fig. 2.5-5a) of bovine bone incinerated at 650 °C for 10-60 minutes depict a steady narrowing of the 121, 112, 030 and

022 reflections with increasing heating time; even though, a still broad peak shape is observed after 60 minutes heating (Figure 2.5-5a).

X-ray diffractograms of bovine bone heat-treated at 700 °C from 10-60 minutes show broad diffraction peaks from 10 to 30 min heating time, whereas reflections in the 31.5-33° 2θ range become considerably better defined after 30 minutes heating when compared to 650 °C (Figure 2.5-5a,b). Diffraction peaks of bone mineral after 40-60 minutes heating are dramatically sharper than peaks after 30 minutes heating at 700 °C (Figure 2.5-5b).
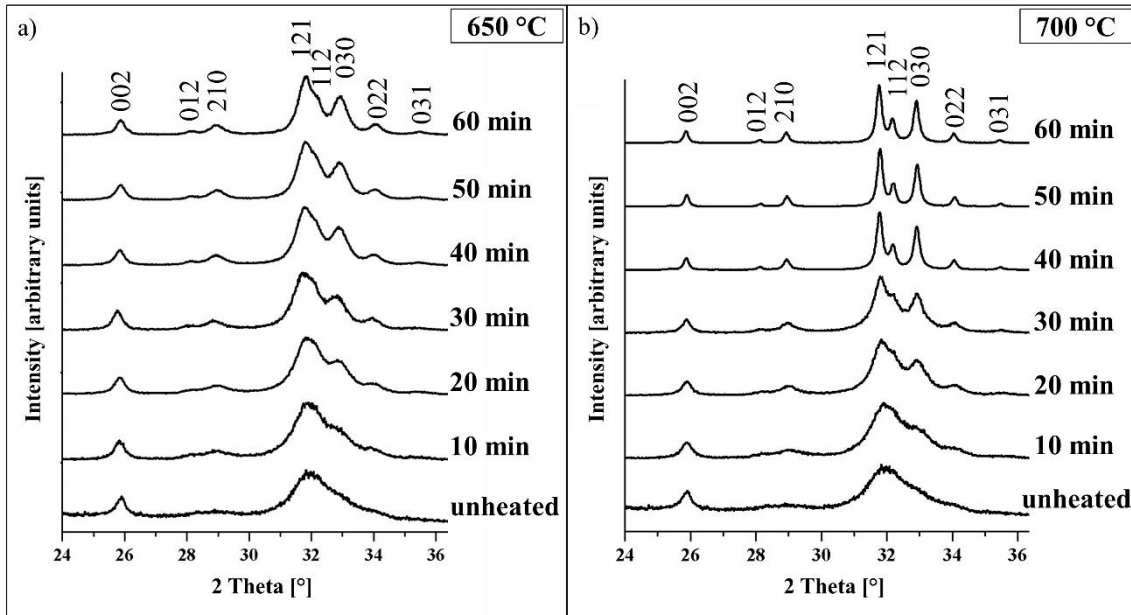
Figure 2.5-5. X-ray diffraction patterns from the 24-36° 2θ range of unheated and heat-treated bone from 10-60 minutes (a) at 650 °C and (b) at 700 °C.

Rietveld refinement results display more clearly the differences in crystallite size evolution when comparing 650 and 700 °C (Figure 2.5-6a,b). At 650 °C, lattice parameters *a* and *c* decrease steadily with progressing heating time, therefore the unit cell volume decreases as well (Figure 2.5-6a,b). Crystallite sizes in *a*- and *c*-direction increase steadily with elapsed heating time, after 60 minutes heating at 650 °C apatite crystallites display a size of 251 Å in *c*- and 187 Å in *a*-direction (Figure 2.5-6b). A standard deviation of 5 % for calculated crystallite sizes is generated according to multiple refinements with different initial values.

Bovine bone heat-treated at 700 °C shows a constant increase of the crystallite size in *a*- and *c*-direction up to 30 minutes incineration. With 40 minutes heating, we observe a relatively sudden and dramatic increase of crystallite size from 134 Å to 266 Å in *a*- and 205 Å to 392 Å in *c*-direction (Figure 2.5-6d). Furthermore, lattice parameters decrease (Figure 2.5-6c) with heating time up to 30 minutes (*a*-axis) and 40 minutes (*c*-axis) which in consequence leads to a shrinkage of the unit cell (Figure 2.5-6d). After 40 minutes heating the *c*-axis remains

constant, whereas the *a*-axis increases again from 30 to 40 minutes and remains stable until 60 minutes heating (Figure 2.5-6d). After 60 minutes heat-treated at 700 °C apatite crystallites have a size of 467 Å in *c*- and 389 Å in *a*-direction (Figure 2.5-6d).
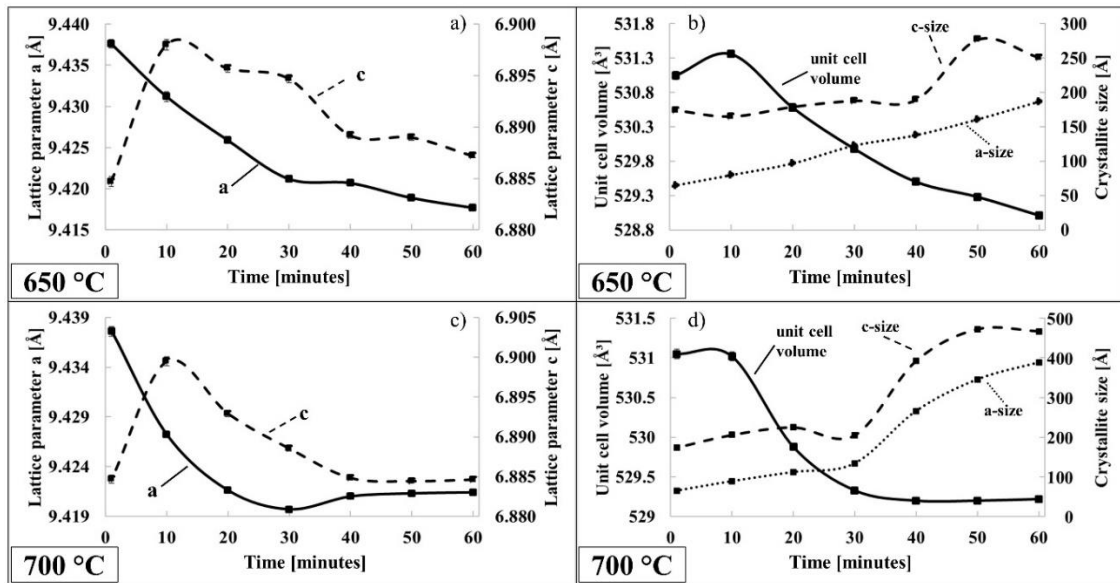
Figure 2.5-6. (a) Lattice parameters *a* (=*b*) (solid line), and *c* (dashed line) of bone mineral, unheated and heat-treated at 650 °C for 10-60 minutes; (b) Crystallite sizes in *a*-direction (dotted line), and *c*-direction (dashed line) as well as unit cell volume (solid line) of bone mineral heat-treated at 650 °C for 10-60 minutes; (c) Lattice parameters *a* (=*b*) (solid line), and *c* (dashed line) of bone mineral, unheated and heat-treated at 700 °C for 10-60 minutes; (d) Crystallite sizes in *a*-direction (dotted line) and *c*-direction (dashed line) and unit cell volume (solid line) of bone mineral heat-treated at 700 °C for 10-60 minutes. The estimated standard deviation for crystallite sizes is 5 %.

FTIR

A comparison of IR spectra of untreated bone and bone heat-treated at different temperatures is shown in Figure 2.5-7. Characteristic phosphate group vibrational bands at 470-480 cm^{-1} ($v_2PO_4^{3-}$), 500-750 cm^{-1} ($v_4PO_4^{3-}$), ~ 962 cm^{-1} ($v_1PO_4^{3-}$) and 980-1120 cm^{-1} ($v_3PO_4^{3-}$) could be identified according to Raynaud et al. (2002) and Destainville et al. (2003). Characteristic absorption bands at 873-879 cm^{-1} (shifting to higher wavenumbers with heat treatment) and 1400-1458 cm^{-1} were attributed to $v_2CO_3^{2-}$ and $v_3CO_3^{2-}$ (Rey et al. 1989, Rey et al. 1990, Fleet 2009, Grunenwald et al. 2014). Carbonate band intensity begins to decrease continuously from 400 °C with increasing temperatures, and the carbonate bands disappear almost completely when bone is incinerated at 1000 °C. The untreated bovine bone spectrum shows broad H_2O absorption bands from ~3000-3600 cm^{-1} (Brubach et al. 2005). With heat treatment, these peaks lose intensity and disappear in the spectra of bone treated at 700 °C and higher.

94
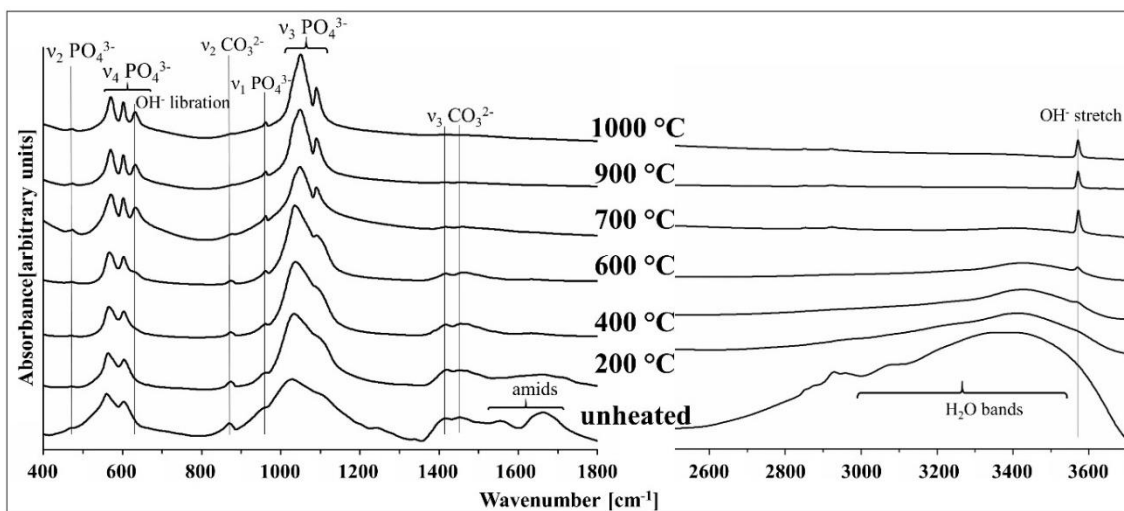
Figure 2.5-7. Infrared absorbance spectra from 400-1800 cm^{-1} (left side), and from 2500-3700 cm^{-1} (right side) of untreated bone as well as of bone heat-treated for 200, 400, 600, 700, 900 and 1000 °C.

At 200 °C heating, a subtle shoulder at 3570 cm^{-1} appears which can be attributed to the OH$^-$ stretching mode (González-Díaz & Hidalgo 1976, González-Díaz & Santos 1977, Vandecandelaere et al. 2012), whereas the OH$^-$ libration mode at ~632 cm^{-1} (Destainville et al. 2003) only becomes visible as a small shoulder at 400 °C heating (Figure 2.5-7). However, both OH$^-$ signals just emerge when bone gets heat-treated and they are absent in the spectra of unheated bone. For samples treated at 700 °C or higher the OH$^-$ signals increase pronouncedly and become well-differentiated. Organic compounds like amids (~1540-1750 cm^{-1}) show high peak intensities in the spectra of unheated bone and are barely visible in the sample treated at 400 °C; they diminish completely above 400 °C (Figure 2.5-7).

FTIR spectral decomposition in the 450-750 cm^{-1} range was based on seven peaks ($v_2PO_4^{3-}$, HPO_4^{2-}, PO_4^{3-}, PO_4^{3-}, PO_4^{3-}, OH$^-$, H_2O) (Vandecandelaere et al. 2012) for both, unheated and heat-treated bone (Figure 2.5-8a,b). The application of a protocol based on nine peaks for unheated bone to distinguish HPO_4^{2-} and PO_4^{3-} apatitic and non-apatitic evironments did not converge to a reliable fit.
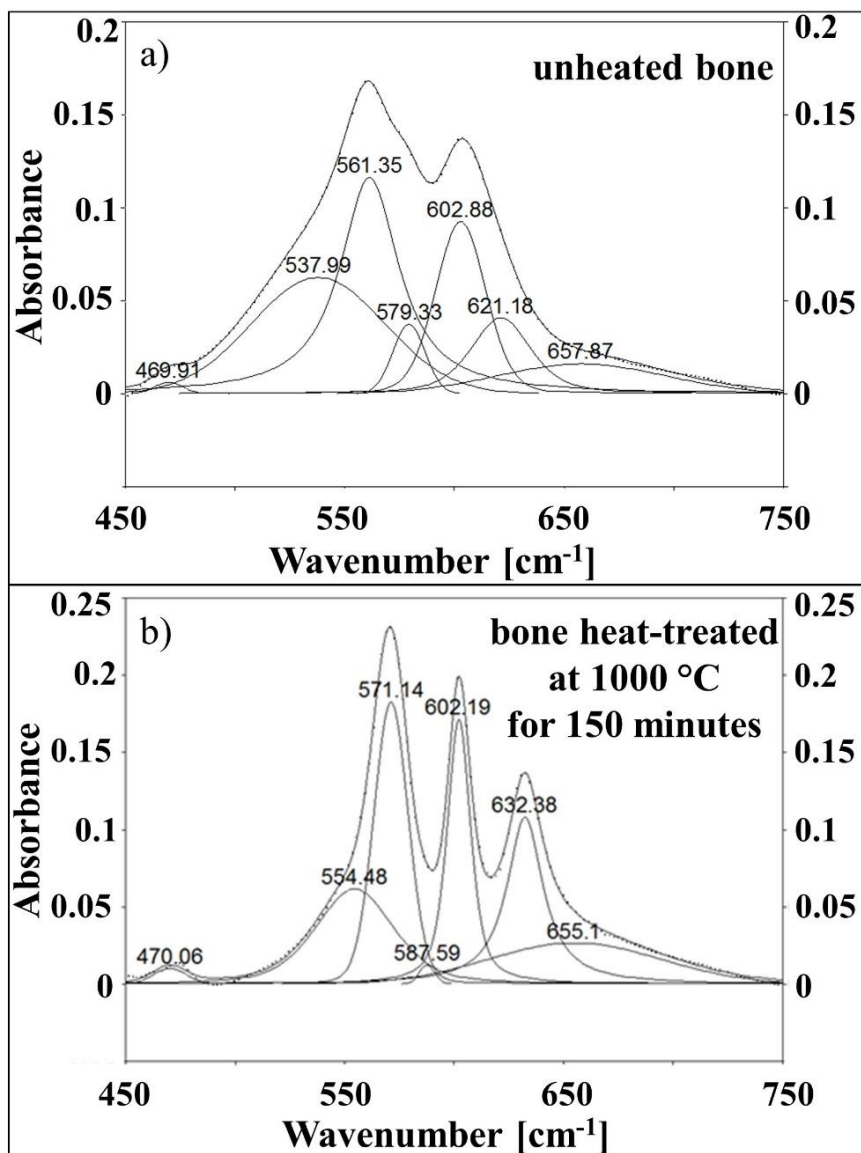
Figure 2.5-8. Spectral decomposition of the FTIR signal of the $\nu_2PO_4^{3-}$ and $\nu_4PO_4^{3-}$ vibration bands of (a) unheated bone, and (b) bone heat-treated at 1000 °C for 150 minutes.

The $\nu_2PO_4^{3-}$ and $\nu_4PO_4^{3-}$ bands of unheated bone mineral show poor development of their spectral features and a large peak overlap, they become narrower with increasing temperature (Figure 2.5-8a,b). The hydroxyl-libration peak at ~632 cm^{-1} appears well-differentiated in heat-treated bone at 1000 °C, whereas it only exhibits a faint band in the spectral decomposition of unheated bovine bone (~621 cm^{-1}). The HPO_4^{2-} band shifts to higher wavenumbers with heat treatment (538 to 554 cm^{-1}) and the peak area decreases (Figure 2.5-8a,b).

Empirical Crystallinity Indices from XRD and FTIR Data

For comparison with existing literature and to compare crystallinity indices obtained from different analytical methods, we provide popular empirical parameters such as the Crystallinity Index (CI) and the Infrared Splitting Factor (IRSF). The crystallinity index is a simple empirical measure of the degree of crystal organisation within bone mineral and involves a mathematical calculation using either XRD, Raman or FTIR data (e.g. Bonar et al. 1983, Shemesh 1990, Weiner & Bar-Yosef 1990, Person et al. 1995, Berna et al. 2004, Pucéat et al. 2004, Thompson et al. 2011). We calculated a CI (Table 2.5-3) from our XRD data according to Person et al. (1995): a baseline was taken between 24 and 38° 2θ (Cu-$K_{\alpha 1}$ radiation) and the height (H) was measured between the average value at the top of a peak and the value of the valley separating it from the following peak (Person et al. 1995). These values of the 202, the 300 and the 112 reflection are added and divided by the height of the highest peak 211:

$$CI = \sum \{H[202], H[300], H[112]\}/ H[211] \text{ (Eq. 2.5-1)}$$

We calculated the IRSF (Table 3) measure of crystallinity from our FTIR data according to Weiner & Bar-Yosef (1990) by adopting the following equation:

$$IRSF = \{A_{565} + A_{603}\}/ A_{595} \text{ (Eq. 2.5-2)}$$

with A_x being the absorbance corresponding to $\nu_4 PO_4$, the two anti-symmetric bending vibration bands of phosphate at 565 and 603 cm^{-1}, and the valley between them at 595 cm^{-1} (Lebon et al. 2010). A baseline was drawn between 495 and 750 cm^{-1} (Weiner & Bar-Yosef 1990).

Table 2.5-3. Incineration temperature (time = 150 minutes), Crystallinity index calculated from XRD (CI) and FTIR (IRSF) data, respectively, and crystallite size in *a*- and *c*-direction (estimated standard deviation 5 %.) according to Rietveld refinements (see also Figure 2.5-2b).

Temperature [°C]	CI	IRSF	*a*-size [Å]	*c*-size [Å]
unheated	0.11	2.43	65	174
100	0.14	2.67	68	180
200	0.16	2.81	52	155
300	0.17	2.97	64	154
400	0.19	3.12	73	162
500	0.24	3.56	103	177
600	0.35	4.26	114	211
700	1.23	6.17	1236	1351
800	1.31	6.32	1413	1630
900	1.28	6.29	1384	1612
1000	1.30	6.96	1320	1628

TGA-FTIR

The thermogram bovine bone heat-treated under air and its first derivative is shown in Figure 2.5-9a. We observe four distinct stages of weight loss for bovine bone heat-treated under oxidising conditions, the weight loss for different temperature ranges is: 7.27 % at 20-250 °C, 16.15 % at 250-375 °C, 7.67 % at 375-650 °C, and 2.01 % at 650-950 °C. The first derivative of the TGA curve ($\Delta_{mass}/\Delta_{temp}$) was calculated to determine the precise temperature ranges of bone weight loss. We found well-defined peaks for bovine bone heat-treated in air at around 113, 352, 466, 770 and 812 °C. The most prominent peak and therefore the largest weight loss occurs between 300 and 400 °C. Selected FTIR spectra of the gaseous reaction products of

bovine bone heat-treated under air atmosphere are shown in Figure 2.5-10. Distinct H_2O and CO_2 peaks emerge in the spectra at 122 °C and can still be observed in the spectra measured at 979 °C. CO bands at 2116 and 2177 cm^{-1} emerge from about 300 °C and disappear around 550 °C. N_2O bands appear around 490 °C, show less intensity at 653 °C and disappear completely at higher temperatures. NH_3 absorption bands appear first in the spectra measured at 367 °C, show highest intensity from 400-450 °C and show less intensity in the spectra taken at temperatures higher than 653 °C. These bands are produced by gases evolving from the thermal decomposition (pyrolysis) of the organic components of bone (mainly collagen and non-collagenous proteins).
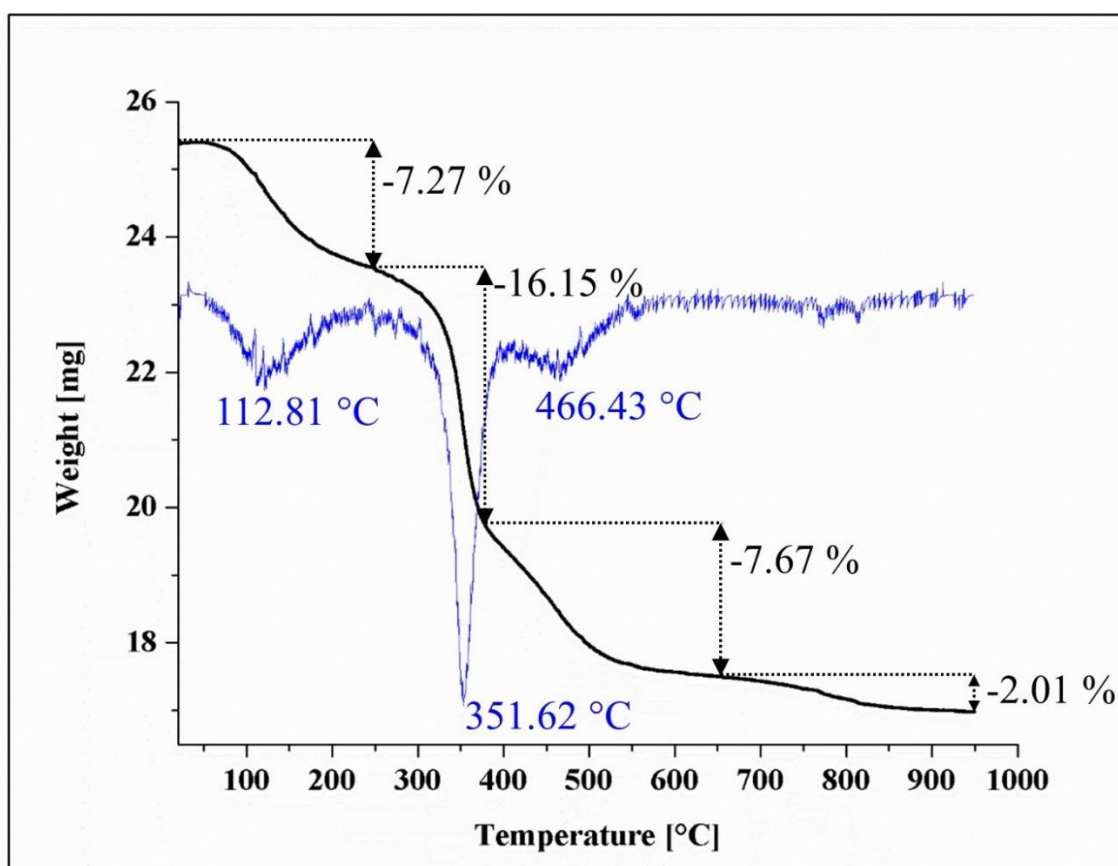
Figure 2.5-9. TGA thermogram of bone heat-treated in atmosphere (black line) and its first derivative (blue line).
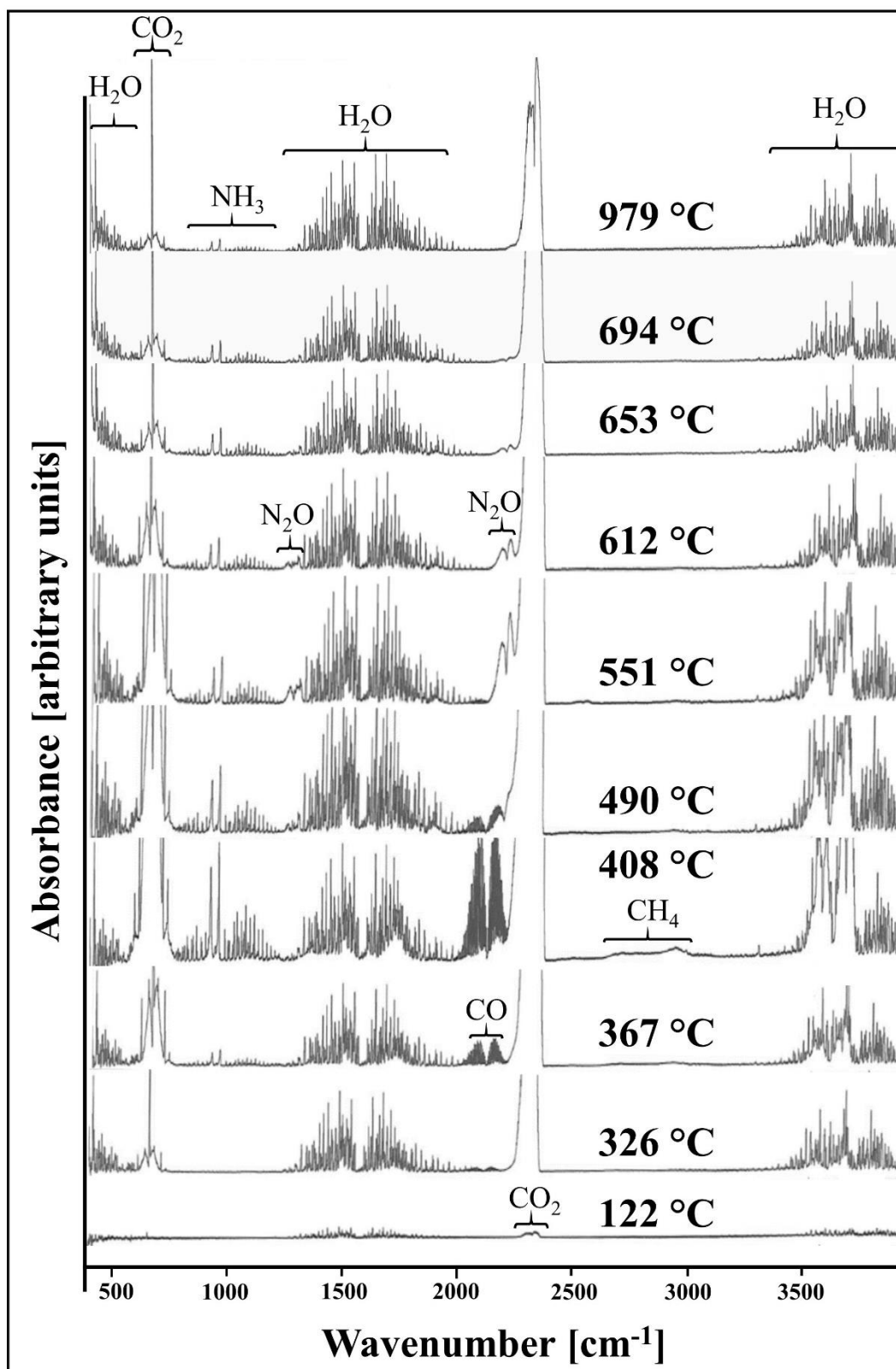
Figure 2.5-10. FTIR spectra of gaseous reaction products of bone during TGA measurements in air (oxidising conditions).

2.5.5 Discussion

Crystalline By-products During Heat Treatment

For heating at very high temperatures, lime (CaO) is a likely decomposition product of bioapatite, and it was indeed reported by Piga et al (2008, 2009). They detected around 3 wt% calcite in archaeological human bone finds and CaO after thermal treatment at 775 °C onwards (Piga et al. 2008), and explained it with the chemical reaction of carbonate thermal decomposition $CaCO_3 \rightarrow CaO + CO_2$ in consequence of thermal treatment. In our diffractograms we found *no evidence* for CaO. However, we identified another crystalline phase: Buchwaldite ($CaNaPO_4$), occurring from 800 °C and at higher temperatures as carbonate-free hydroxyapatite grows due to decomposition of the bioapatite. This can be explained with cortical bovine bone mineral containing about 1 wt% Na (Elliott 2002). $CaNaPO_4$ was also detected in a similar study by Etok et al. (2007) who investigated meat and bone meal (MBM), a product produced from wastes of the meat industry. In heat-treated MBM, however, $CaNaPO_4$ was already discernible at 500 °C. These authors also report the presence of KCl and NaCl from 500 °C and β-TCP occurring at 900 °C. These non-conformances may be due to differences in the materials (Na, K, and Cl contents, species, initial composition of the bioapatite) and/or the heating process.

Bone Mineral is not Hydroxyapatite

Original, untreated bone XRD patterns show broad diffraction peaks (Figure 2.5-1a) due to the nanometric size of the apatite crystallites. The original bone apatite is clearly no hydroxylapatite as proven by the lack of OH^- bands (Figures 2.5-7 and -8a). The high intensity of the carbonate and H_2O vibration bands clearly indicate that bone apatite instead is a carbonate-hydro-apatite (Figure 2.5-7). Similar conclusions were made by Pasteris et al. (2004) using raman spectroscopy, Rey et al. (1989, 1995) and Mkukuma et al. (2003) using infrared spectroscopy, Rey et al. (1995) using solid state NMR and Loong et al. (2000) using inelastic neutron scattering.

Following Fleet (2009) and Rey and co-workers (Rey et al. 1989, 1990; El Feki et al. 1991, Vandecandelaere et al. 2012), the position of the $v_2CO_3^{2-}$ peak at ~873 cm^{-1} of unheated and heat-treated bone samples up to 600 °C can be attributed to the B-type substitution, from 700 °C onwards we locate this peak at 878 cm^{-1} which is attributed to the A-type substitution. Following the previously mentioned authors, the shift of the HPO_4^{2-} band can be attributed to "non-apatitic HPO_4^{2-}" and "apatitic HPO_4^{2-}" at 538 cm^{-1} and 554 cm^{-1}, respectively.

With extended heating treatment (temperature and time) under oxidising conditions, the diffraction peaks of the bioapatite get sharper. At the same time, the intensity of the carbonate infrared signals decrease while the intensity of the OH^- infrared signals increase, most pronounced between 600 and 700 °C (Figure 2.5-7). As temperatures rise, the OH^- stretching occurs from 200 °C and increases with higher temperatures (Figure 2.5-7). This leads to the conclusion that the carbonate-hydro-apatite reacts to hydroxyapatite with heat treatment according to the formula $[CO_3]^{2-} + H_2O \rightarrow CO_2\uparrow + 2\ OH^-$. This was also observed by Cho et al. (2013) and Ooi et al. (2007) investigating bovine bone xenografts and Holcomb & Young (1980) studying the thermal decomposition of human tooth enamel. As the material approaches stoichiometric chemistry, the loss of carbonate and water and their replacement by OH^- in the structure lead to a decrease of unit cell parameters (Figures 2.5-4b, -6d). This reaction is correlated with a growth of the crystallites, which is even more pronounced at temperatures starting from 700 °C (Figure 2.5-4b). We attribute the weight loss at 650 °C and higher temperatures to the decomposition of the carbonate (Figure 2.5-9), which results in a carbonate content of around 4 wt% for the original bioapatite in a bovine femur.

Combustion of Organic Components in Bone Leads to Enhanced Crystallite Growth

If we assumed that the observed acceleration of crystallite growth at high temperatures is simply a thermally activated process, we would expect the crystallite growth rate r to follow a Boltzmann law as

$$r = r_0 \exp - \frac{E_A}{k_B T} \quad \text{(Eq. 2.5-3)}$$

where E_A is the activation energy, k_B is the Boltzmann constant and T is the temperature. Crystallite size K after time t is

$$K = r\ t = t\ r_0 \exp - \frac{E_A}{k_B T} \quad \text{(Eq. 2.5-4)}$$

Thus, for the isochronic experiment (t = 150 minutes) an Arrhenius law

$$\ln(K) = \ln(t) + \ln(r_0) - \left(\frac{E_A}{k_B}\right)\left(\frac{1}{T}\right) \quad \text{(Eq. 2.5-5)}$$

would result (if the heating and cooling periods can be neglected). Figure 2.5-11 plots $\ln(K)$ vs. $1/T$. In a simple thermally activated process a straight line would be expected. It can be clearly seen, that, instead, a large discontinuity occurs between 600 and 700 °C, i.e. the temperature where the combustion of the organic material is complete.
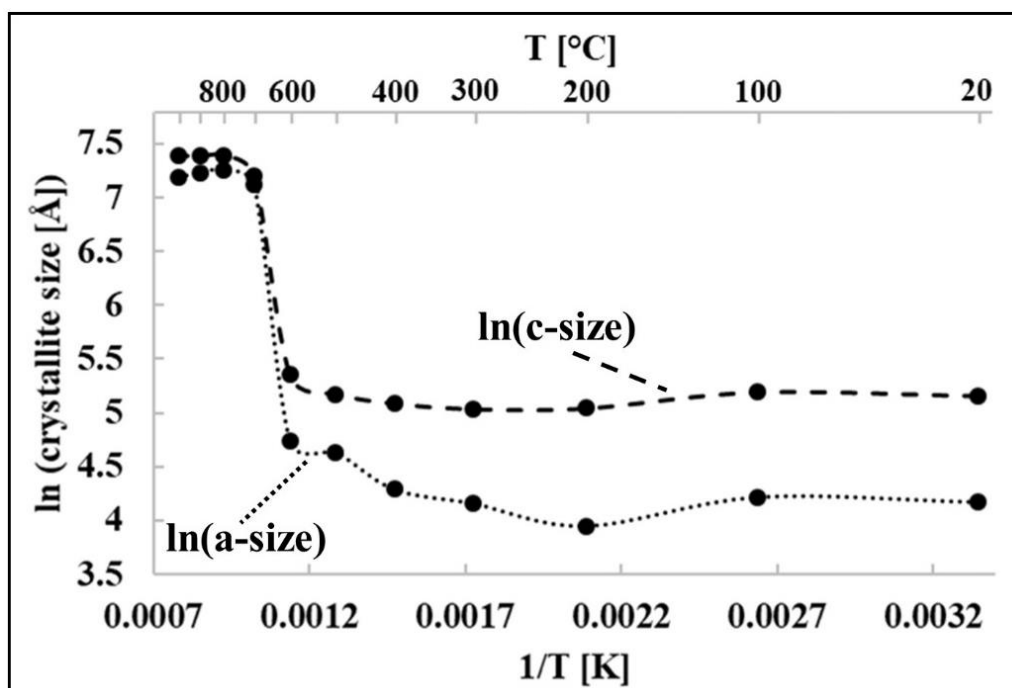
Figure 2.5-11. Arrhenius graph of the crystallite size in *a*- and *c*-direction.

Considering the stages of weight loss, we attribute the first stage from 20 to around 250 °C with the most prominent peak reaction rate at ~113 °C (Figure 2.5-9c) to the evaporation of water. Decomposition of the collagen molecules and non-collageneous proteins mainly occurs from about 300 °C (see considerable weight loss between 300-400 °C in Figure 2.5-9 and emerging CO_2, N_2O, and NH_3 absorption bands in the gaseous products spectra from 367 °C in Figure 2.5-10). HCN, HNCO and NH_3 are main pyrolysis products of proteins. CO, CO_2, H_2O and N_2O are their secondary reaction products due to combustion and reaction with air (Wargadalam et al. 2000, Hansson et al. 2004). For temperatures higher than about 650 °C, CO and N_2O signals disappear and NH_3 bands are less intense in the FTIR spectra (Figure 2.5-10). This leads to the conclusion that the majority of proteinous components (collagen and non-collageneous proteins) had been removed from the bone when this temperature was reached. Holden et al. (1995) investigating heat-treated human bones by electron microscopy imaging also reported the complete removal of organic compounds in the bone tissue at temperatures around 600 °C. If the enhanced crystallite growth was simply driven by T as a thermally-activated process, the Arrhenius graph of crystallite sizes and temperature would show a linear behaviour (Figure 2.5-11). Hence, we conclude that the noticeable acceleration of crystallite growth which we observed for samples heat-treated at 700 °C for 30 minutes and after (Figures 2.5-4b and -6d) takes place because the crystallites are no longer protected by organic residues coating so they can grow unhindered.

Concluding from Bone Colour and Crystallite Size to Cremation Temperature is not Trivial

The fact that the bone reaction process is not only temperature- but also time-dependent complicates the assignment of a cremation temperature to changes observed in bone characteristics (i.e. colour). There are visible changes of bone colour with progressing heating time: at 700 °C we observe black-coloured samples for 10 minutes, black-grey for 30, grey for 40 and light grey for 50 and 60 minutes. After 150 minutes heating at 700 °C, the bone material appears white. Samples heat-treated at 650 °C appear black from 10-30 minutes heating time, black-grey for 40 and 50 minutes, and remain grey after 60 minutes heating time. After Wahl (1982), bone remains grey at incineration temperatures around 550 °C, milky-white from 650-700 °C and white above 800 °C. After Harbeck et al. (2011), bones that were exposed to temperatures between 500-600 °C show a black-grey colour and remain white when burnt at 700 °C or higher. In conclusion, we show that an estimation of cremation temperature from the colour of archaeological incinerated bone finds is not straight forward at all, as bones incinerated at 700 °C for 30 minutes have quite the same colour as bones burnt for 40 and 50 minutes at 650 °C and as bones heat-treated between 500-600 °C.

In the same manner, one needs to be careful when estimating cremation temperature from bone crystallite size data. Our results show that bone heat-treated at 100 °C for 150 minutes displays similar crystallite sizes (68 Å in *a*- and 180 Å in *c*- direction) as bone treated at 650 °C for 10 minutes (80 Å in *a*- and 165 Å in *c*-size).

By comparing 650 °C and 700 °C, the same trend for lattice parameters and − in consequence - unit cell parameters is observable. Lattice parameters *a* and *c* decrease, therefore the unit cell shrinks which is coupled with an increase of the crystallite size (Figure 2.5-6). However, after 30 minutes heating the 50 °C temperature difference and the removal of the organic components or their residues, respectively, shows its impact as crystallites grow distinctively faster at 700 °C after 30 minutes heating which we ascribe to a progressive recrystallization reaction of bioapatite to hydroxyapatite.

After 30 minutes heating at 700 °C, decomposition products (essentially carbon, which is responsible for the black colour of samples incinerated for shorter times) of organics such as collagen, have almost disappeared and the apatite crystallites can grow without being hindered by organic compounds or their residues which separate and coat the crystallites.

In conclusion, there are well-defined changes in bone chemistry, structure and crystallinity during thermal treatment. The bone bioapatite unit cell shrinks with increasing temperature and the crystallite size increases dramatically after organic matter is lost. The original bone

mineral is carbonated apatite and it reacts/recrystallizes to hydroxyapatite in consequence of heat treatment. Moreover, an additional phase (buchwaldite, $NaCaPO_4$) forms from 800 °C onwards.

Our study assesses the results obtained from a combination of analytical methods which are typically applied and approved to determine bone cremation temperatures. This combination gives a more complete understanding of the complex processes taking place during bone cremation. The described changes in the state of the bone mineral are not only dependent of temperature but also on time. Thus, care must be taken when deducing the defined temperature cremated bone finds were exposed to.

2.5.6 Acknowledgements

2.5.7 Appendix
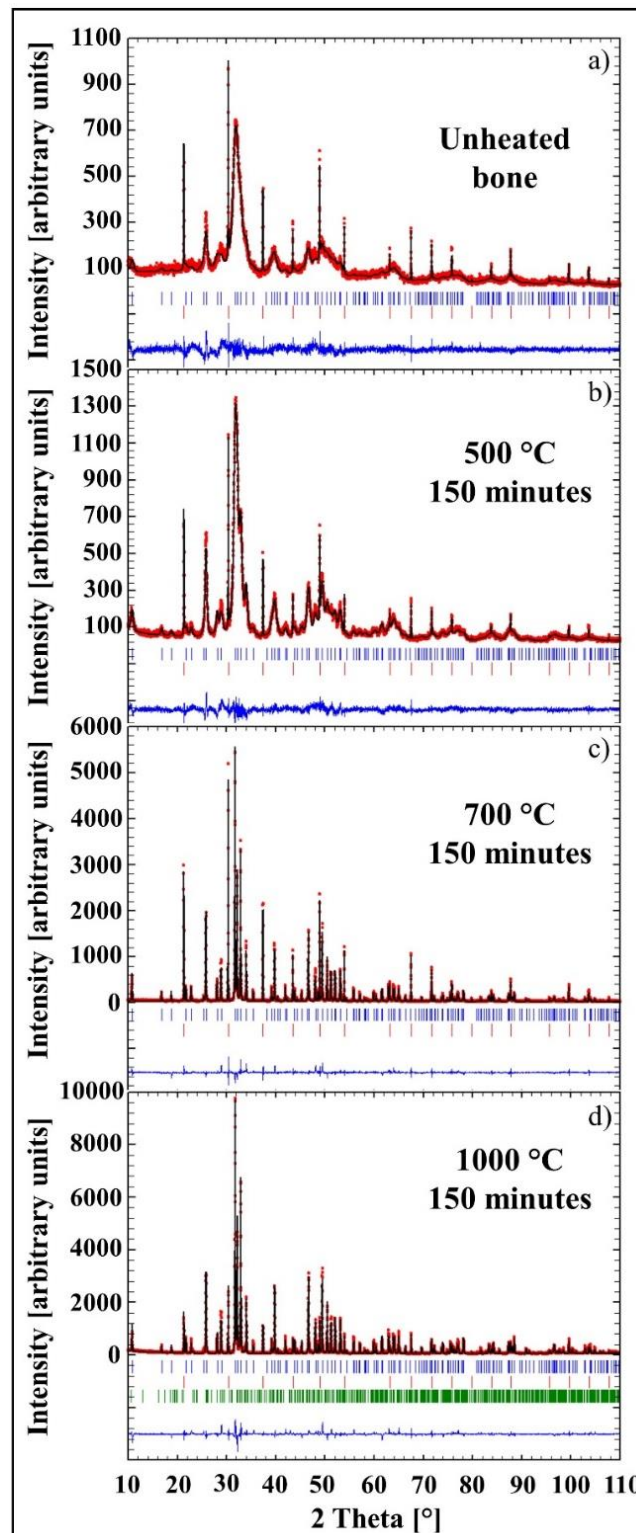
Figure 2.5-A1. Rietveld refinement (10-110° 2θ) of (a) untreated bovine bone; (b) bone heat-treated at 500 °C for 150 minutes; (c) bone heat-treated at 700 °C for 150 minutes; bone heat-treated at 1000 °C for 150 minutes. *Red dots*: observed data points; *black line*: calculated XRD profile; *bottom blue line*: difference of observed and calculated data; *green vertical bars*: positions of diffraction peaks of buchwaldite; *red vertical bars*: positions of diffraction peaks of LaB_6 standard, *blue vertical bars*: positions of diffraction peaks of bone apatite.

106

2.6 Biomineral Reactivity: The Kinetics of the Replacement Reaction of Biological Aragonite to Apatite

Martina Greiner[1], Lurdes Fernández-Díaz[2,3], Erika Griesshaber[1], Moritz N. Zenkert[1], Xiaofei Yin[1], Andreas Ziegler[4], Sabino Veintemillas-Verdaguer[5], and Wolfgang W. Schmahl[1]

1 Department für Geo-und Umweltwissenschaften, Ludwig-Maximilians-Universität, 80333 Munich, Germany

2 Departamento de Cristalografía y Mineralogía, Universidad Complutense de Madrid, 28040 Madrid, Spain

3 Instituto de Geociencias (UCM, CSIC), Ciudad Universitaria, 28040 Madrid, Spain

4 Central Facility for Electron Microscopy, University of Ulm, 89081 Ulm, Germany

5 Instituto de Ciencia de Materiales de Madrid, (ICMM, CSIC), Cantoblanco, 28049 Madrid, Spain

2.6.1 Abstract

We present results of bioaragonite to apatite conversion in bivalve, coral and cuttlebone skeletons, biological hard materials distinguished by specific microstructures, skeletal densities, original porosities and biopolymer contents. The most profound conversion occurs in the cuttlebone of the cephalopod *Sepia officinalis*; the least effect is observed for the nacreous shell portion of the bivalve *Hyriopsis cumingii*. The shell of the bivalve *Arctica islandica* consists of cross-lamellar aragonite, is dense at its innermost and porous at the seaward pointing shell layers. Increased porosity facilitates infiltration of the reaction fluid and renders large surface areas for the dissolution of aragonite and conversion to apatite. Skeletal microstructures of the coral *Porites* sp. and prismatic *H. cumingii* allow considerable conversion to apatite. Even though the surface area in *Porites* sp. is significantly larger in comparison to that of prismatic *H. cumingii*, the coral skeleton consists of clusters of dense, acicular aragonite. Conversion in the latter is sluggish at first as most apatite precipitates only onto its surface area. However, the process is accelerated when, in addition, fluids enter the hard tissue at centres of calcification. The prismatic shell portion of *H. cumingii* is readily transformed to apatite as we find here an increased porosity between prisms as well as within the membranes encasing the prisms. In conclusion, we observe distinct differences in bioaragonite to apatite conversion rates and kinetics depending on the feasibility of the reaction fluid to access aragonite crystallites. The latter is dependent on the content of biopolymers within the hard tissue, their feasibility to be decomposed, the extent of newly formed mineral surface area and the specific biogenic ultra- and microstructures.

2.6.2 Introduction

Research of the last decades has shown that carbonate biological hard tissues of marine and terrestrial organisms are highly valuable for their use in medical applications (e.g. Bohner 2010a, b; Zhang & Vecchio 2013, Clarke et al. 2016, Habraken et al. 2016, Rousseau 2018) e.g. as bone implant and bone graft materials. This is called forth not only by their biocompatibility, biodegradability and osteoconductive capabilities but also by their unique architectures: their specific shapes, varying porosities and thus compactness as well as pore size distributions. Many carbonate biological hard tissues were tested for their applicability for medical tasks (e.g. sponges, corals, coralline algae, cuttlefish bone, echinoderms, marine and terrestrial bivalves (e.g. Clarke et al. 2016). Two of these emerged as being highly valuable: bivalve shell nacreous and coral skeleton aragonite (White et al. 1972, Roy et al. 1974, Silve et al. 1992, Westbroek & Marin 1998, Berland et al. 2005, Fu et al. 2013, Clarke et al. 2016, Pountos & Giannoudis 2016, Green et al. 2017, Zhang et al. 2017). The ideal material for bone tissue engineering has to provide initial mechanical strength for support as well as the ability of gradual resorption for the replacement with newly synthesized tissue. The first materials that were used for bone graft substitutes were dense materials in granule or particulate form (e.g. Clarke et al. 2016). However, as these were only partially resorbable, replacement by new bone was often incomplete. The desire to mimic the natural structure of bone more closely led to the use of porous biological and biomimetic hard tissues, as these allow an improved interdigitation with the host bone and promote fluid exchange. This led to the search of naturally occurring scaffolds with bone like structures, e.g., coral skeletons. For this purpose, several colonial coral species were studied (e.g., *Porites* sp., *Goniopora* sp., *Acropora* sp., *Lophelia* sp., *Madropora* sp.) (Clarke et al. 2016), some having skeletal architectures (e.g. that of *Porites* sp.) resembling spongy cancellous bone and, others with a dense skeleton (e.g. *Acropora* sp., *Madropora* sp.), mimicking cortical bone. However, clinical tests showed that when too much stimulus is applied, pure coral scaffolds resorb too rapidly during the process of new bone formation. Hence, for use in medical applications, coral aragonite had to be functionalized into a, for the medical task, more appropriate material. Prior to use as a bone graft material, coral aragonite has to be transformed hydrothermally to apatite (AP). The conversion is performed only partially, such that an inner bioaragonite core is covered with an outer AP-coating. As aragonite is more soluble than apatite, the controlled conversion of bioaragonite to AP ensures a guided biodegradation rate that, if necessary, can be modified and tuned to local medical requirements (Zhang & Vecchio 2013, Green et al. 2017). The partial conversion of coral aragonite into AP ensures that the

obtained bone graft material retains its porous structure and remains biocompatible, but has also improved biodegradation properties that suit better bone remodelling and turnover. Conditioning of sepia cuttlebone and coral aragonite, echinoderm carapace and sea urchin spine calcite via hydrothermal conversion to AP has shown that in all cases porosity characteristics (pore abundance, size and distribution) of the AP product were ideal for their use in medical applications. However, conversion times to AP were highly variable and depended on both, the chosen experimental conditions and the specific biological hard tissue. In the present manuscript we investigate the impact of different biocarbonate hard materials on the rate and kinetics of bioaragonite to AP conversion. We use an open system set up, thus we allow under boiling conditions the continuous re-equilibration with atmosphere (see also Reinares-Fisac et al. 2017). We discuss major factors that lead to the differential reactivity of the biocarbonate hard tissue when transformed to AP, with the main focus being centred around the impact of distinct bioaragonite microstructures: that being present in the shell of the fresh water bivalve *Hyriopsis cumingii*, in the shell of the deep water, marine bivalve *Arctica islandica*, the microstructure that forms the skeleton of the warm water scleractinian coral *Porites* sp. and that, that comprises the lightweight structure of the cuttlebone of the cephalopod *Sepia officinalis*. We discuss results of conversion experiments that lasted up to 14 days and explore the role and effect of mineral organization, skeleton density, skeletal primary porosity and biopolymer content, fabric and distribution in the hard tissue for the kinetics of bioaragonite to AP conversion.

2.6.3 Materials and Methods

Test Materials

The warm-water coral *Porites* sp. was collected in Moorea, French Polynesia. *Arctica islandica* shell samples were collected in Loch Etive waters in Scotland. *Hyriopsis cumingii* samples were collected from Gaobao lake in China. *Sepia officinalis* cuttlebone was collected close to Elba in the Mediterranean Sea. The geological aragonite comes from Molina de Aragon in Spain.

Experimental Setup

Mineral conversion reactions were performed in a 2000 mL round flask filled with 1500 mL 1 M $(NH_4)_2HPO_4$ solution (Figure 2.6-A1a). The diammonium hydrogen phosphate (Sigma-Aldrich, St. Louis, MO, USA) solution was prepared with high purity deionized water (18.2 MΩ). The system was heated with a heating mantle and kept at a constant temperature of

about 99 °C that guaranteed that the aqueous solution was permanently boiling. A reflux condenser with constant flow of cold water was used to avoid water evaporation during the experiments. However, this reflux condenser did not prevent the escape of gases (e.g. CO_2) to the atmosphere. Similarly sized fragments of the hard tissues were immersed in the boiling solution. In the case of *Sepia officinalis* cuttlebone the investigated samples were 15 mm sided cubes, while in the case of *Porites* sp. we used cylindrically shaped sample pieces (12 x 8 mm). 20 x 10 mm thick fragments were used for *Arctica islandica* and *Hyriopsis cumingii*. Initial sample weights ranged between 0.3 and 1.2 g. As the aqueous solution volume to biomineral weight was very high, the small initial differences in sample weights are irrelevant. The samples were recovered from the solution after specific conversion reaction times (Figure 2.6-A1b), were washed with distilled water and were stored in isopropanol. $CaCO_3$ biominerals interacted with the phosphate-bearing boiling solution in an open system. Hence, our experimental setup, shown in Figure 2.6-A1a, allowed for a continuous re-equilibration with atmosphere.

Organic Matrix Preparation by Selective Etching

In order to image the organic matrix, sample pieces were mounted on 3 mm thick cylindrical aluminium rods using super glue. The samples were first cut using a Leica Ultracut ultramicrotome with glass knifes to obtain plane surfaces. The cut pieces were then polished with a diamond knife by stepwise removal of material in a series of 20 sections with successively decreasing thicknesses (90 nm, 70 nm, 50 nm). The polished samples were etched for 180 s using 0.1 M HEPES (pH = 6.5) containing 2.5% glutaraldehyde as a fixation solution. The etching procedure was followed by dehydration in 100% isopropanol three times for 10 min each, before specimens were critical point dried. The dried samples were rotary coated with 4 nm platinum and imaged using a Hitachi S5200 Field Emission-Scanning Electron Microscope (FE-SEM) at 4 kV.

Characterization Methods

X-ray patterns of all samples were collected on a Bragg-Brentano type X-ray diffractometer (XRD 3003 TT, GE Sensing & Inspection Technologies, Hürth, Germany) with Cu-$K_{\alpha1}$-radiation and a 2θ angle from 10°–110° with a step size of 0.013°. Rietveld refinement was performed with the program FullProf (Rodríguez-Carvajal & Roisnel 2004) on all samples containing more than 5 wt % AP. Refinements were conducted using the structural model of aragonite published by Jarosch and Heger (1986) and the model of AP published by Kay et al.

(1964). For samples with an AP content lower than 5 wt % a semi-quantitative percentage estimation was performed using the Reference Intensity Ratio (RIR) method (Dinnebier & Billinge 2008) using the structural phase models mentioned before. For the calculation of crystallite sizes, the pristine aragonitic sample was mixed with an internal standard (LaB_6, 10 wt %) to determine the instrumental resolution function. Thereafter the Thompson-Cox-Hastings method (Thompson et al. 1987) for convolution of instrumental resolution and isotropic microstrain broadening was applied on the XRD pattern of the pristine sample. Infrared spectra were measured on a Perkin–Elmer (Waltham, MA, USA) ATR-FTIR Spectrum two instrument with a resolution of 4 cm^{-1} with 128 scans. The samples were rotary-coated with 5 nm of platinum-palladium and imaged using a Hitachi SU5000 field emission-scanning electron microscope (Tokyo, Japan).

2.6.3 Results

X-Ray Diffraction Analysis

XRD measurements confirm that all investigated hard tissues consist of aragonite and evidence that their conversion into AP does not involve any intermediate calcium phosphate. All refinements give a good agreement between observed and calculated profile ($Chi^2 < 2.8$, an exemplary Rietveld fit is shown in Figure 2.6-A2). All obtained XRD patterns are shown in the Supplementary section of this manuscript. Table 2.6-1 and Figure 2.6-1 provide the percentage of aragonite to AP conversion as a function of conversion time, calculated from Rietveld analyses. We find a significant difference in newly formed AP between the studied biological hard tissues, not only between themselves but also between the biogenic samples and geological aragonite. The latter appears to be highly unreactive compared to most biogenic aragonites (Table 2.6-1).
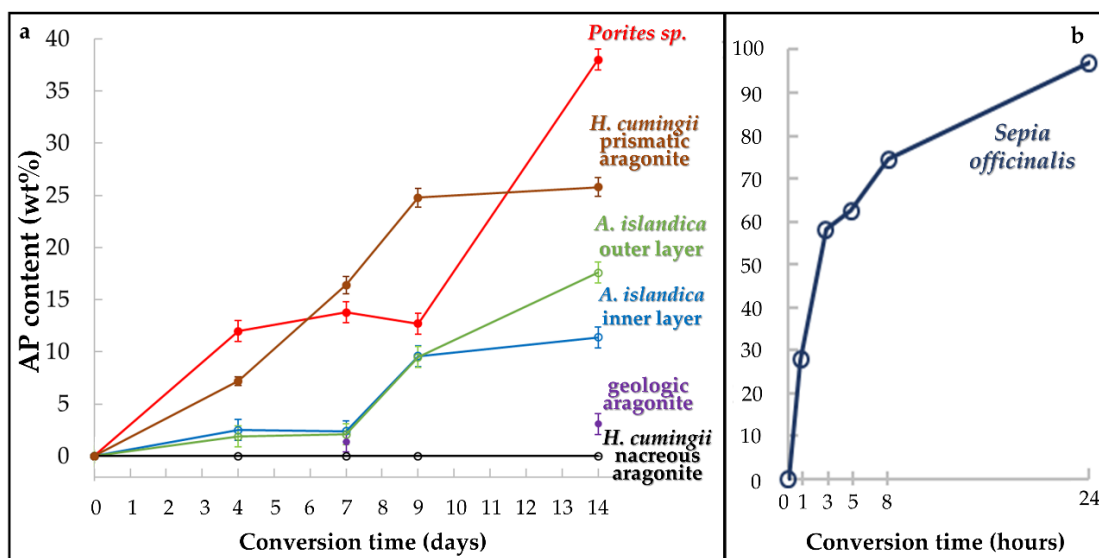
Figure 2.6-1. Newly formed apatite content of all samples relative to conversion time according to Rietveld analyses of the XRD measurements (a) 14 days *H. cumingii* nacre (brown line) and prismatic aragonite layer (black line), *A. islandica* outer (green line) and inner layer (blue line), geologic aragonite (violet data points) and *Porites* sp. (red line); (b) *Sepia officinalis*, conversion time 1–24 h. Error for *H. cumingii* nacre and *Sepia officinalis* is within the size of the corresponding data points.

Results of Rietveld refinements of XRD patterns of the aragonitic biogenic precursors versus time are shown in Figure 2.6-1. These as well highlight the striking differences in reactivity between the investigated samples. The highest reactivity is observed in *Sepia officinalis* cuttlebone, which consists of more than 60 wt % AP after only 5 h of conversion with the phosphate-bearing boiling solution. After 24 h, the conversion of the bioaragonite into AP is almost complete (Figure 2.6-1, Table 2.6-1). These results are in good agreement with those reported by Reinares-Fisac et al. (2017). All other investigated biological hard tissues transform at a much slower rate. Out of these we find the fastest conversion kinetics for the skeleton of *Porites* sp. The conversion trend is characterized by an initial rapid conversion speed, reaching 12 wt % AP after 4 days of reaction. With proceeding time, conversion does not progress further for the following 5 days. However, subsequently conversion kinetics accelerates again such that at 14 days of conversion 38 wt % AP is formed in the skeleton of *Porites* sp. (Figure 2.6-1). The shells of the bivalves, *Arctica islandica* and *Hyriopsis cumingii* react differently to conversion. Rietveld refinements of the XRD patterns of the shell of *Arctica islandica* show a similar conversion trend for both, the inner (shell portion next to the soft tissue of the animal) and the outer (seaward pointing) shell layer. Conversion starts first at a slow rate (~2 wt % of newly formed AP after 7 days of reaction), while after 9 days of reaction (~9.5 wt % of newly formed AP) it speeds up.

Alteration for the last five days is differently realized in the different shell portions of *Arctica islandica*. A fairly high conversion rate is observed for the seaward pointing shell part, while aragonite forming inner shell portions next to the soft tissue of the animal appears to be almost resistant to dissolution of aragonite and, hence, conversion to AP (Figure 2.6-1, Table 2.6-1).

Table 2.6-1. Samples used for conversion experiments, experiment time periods and apatite contents obtained for specific conversion times.

	AP content (wt%) after 4 days	AP content (wt%) after 7 days	AP content (wt%) after 9 days	AP content (wt%) after 14 days
Porites sp.	12.0(4)	13.8(3)	12.7(3)	38(1)
Hyriopsis cumingii (nacre)	< 1	< 1	< 1	< 1
Hyriopsis cumingii (prismatic aragonite)	7.2(4)	16.4(8)	24.8(9)	25.8(9)
Arctica islandica (shell layer next to seawater)	1.9	2.1	9.5(4)	17.6(5)
Arctica islandica (shell layer next to soft tissue)	2.5	2.4	9.6(7)	11.4(4)
geologic aragonite (single crystal)	not determined	1.4	not determined	3.1

	AP content (wt%) after 1 hour	AP content (wt%) after 3 hours	AP content (wt%) after 5 hours	AP content (wt%) after 8 hours	AP content (wt%) after 24 hours
Sepia officinalis	29.9(7)	58.2(8)	64.4(7)	74.5(8)	99(1)

Most striking is the very different conversion behaviour of nacreous aragonite (next to the soft tissue of the animal) and the prismatic shell portion (seawater pointing shell layer) of *Hyriopsis cumingii* (Figure 2.6-1, Table 2.6-1). All diffraction peaks in XRD patterns of the nacre sample can be assigned to aragonite, regardless the time of interaction with the phosphate-bearing aqueous solution. This evidences that the nacre did not undergo any conversion to AP during the time span of our experiments (Figure 2.6-A3). In contrast, the

prismatic shell portion of *Hyriopsis cumingii* is readily transformed to AP. We see a steady increase in conversion rate up to 9 days of alteration (Figure 2.6-1); about 25 wt % AP was found in the prismatic hard tissue of *Hyriopsis cumingii* after this alteration time. However, for the subsequent 5 days only minute amounts of bioaragonite transformed to AP in the prismatic shell portion of *Hyriopsis cumingii* (Figure 2.6-1, Table 2.6-1). In order to investigate the influence of the aragonite crystallite sizes on the reactivity, we calculated the crystallite size of *Sepia officinalis* cuttlebone and *Hyriopsis cumingii* nacreous aragonite by Rietveld refinement. The average size of nacreous aragonite crystals in *H. cumingii* is 504 Å; for *Sepia officinalis* the average granular aragonite crystallite size is 486 Å.

FTIR-Spectroscopy

IR-spectra of the four biological hard tissues being in contact with the phosphate-bearing solution for 14 days are shown in Figure 2.6-2. Absorption bands that can be assigned to the carbonate group vibrations in the structure of aragonite are present in all samples, with the exception of the completely reacted *Sepia officinalis* cuttlebone. The bands appear at 700 and 713 cm^{-1} ($v_4CO_3^{2-}$), 855–858 cm^{-1} ($v_2CO_3^{2-}$), 1083 ($v_1CO_3^{2-}$) and 1450–1475 cm^{-1} ($v_3CO_3^{2-}$) (Meejoo et al. 2006, Kannan et al. 2007, Kasioptas et al. 2010) and show variable intensities depending on the specific hard tissue. They are sharp in the spectrum of *Hyriopsis cumingii* nacre, are intense and clearly visible in the spectra of both, the outer and inner shell layers of *Arctica islandica*, are weaker and broader in the spectra gained from the skeleton of *Porites* sp. and for prismatic aragonite in the shell of the bivalve *H. cumingii*.
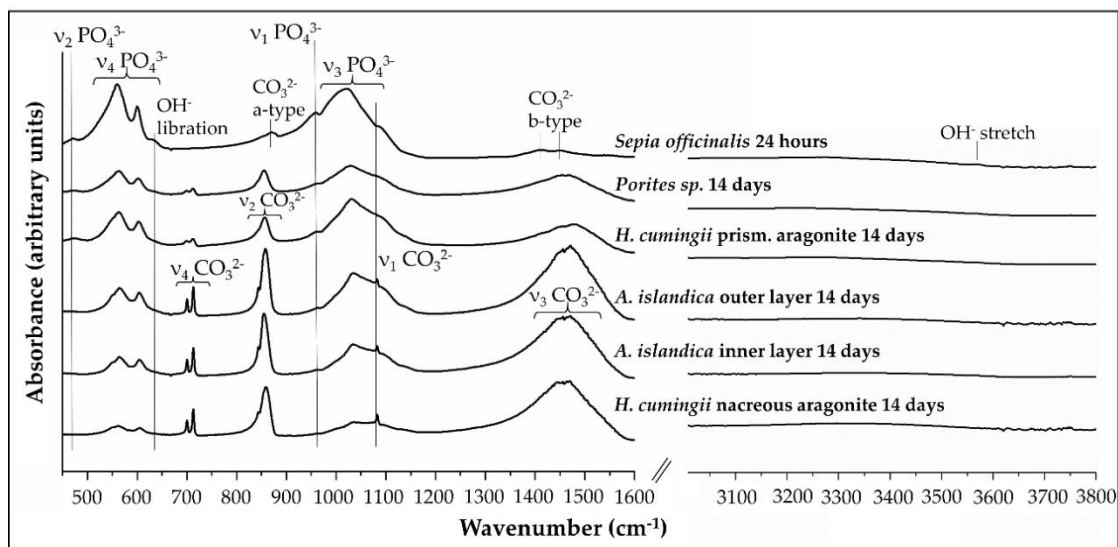
Figure 2.6-2. Infrared-spectra (450–1600 cm^{-1} and 3000–3800 cm^{-1}) for *Sepia officinalis* cuttlebone transformed for 24 h together with IR-spectra for *Porites* sp. coral aragonite, *H. cumingii* prismatic aragonite, *A. islandica* outer and inner shell layer aragonite and *H. cumingii* nacreous aragonite. Spectra are arranged according to AP content (wt %) determined with XRD and Rietveld analyses. AP content increases from bottom to top spectra.

Absorption bands that can be assigned to vibrations of the phosphate group in the structure of AP are clearly distinguishable at ~470 cm^{-1} ($v_2PO_4^{3-}$), 560–602 cm^{-1} ($v_4PO_4^{3-}$), ~960 cm^{-1} ($v_1PO_4^{3-}$) and at 1020–1100 cm^{-1} ($v_3PO_4^{3-}$) in the spectra of *Sepia officinalis* cuttlebone, *Porites* sp. skeleton, outer and inner shell layers of *Arctica islandica* and in prismatic aragonite in the shell of *H. cumingii* (Raynaud et al. 2002, Destainville et al. 2003, Han & Song 2006). The intensity and definition of these bands is highly variable depending on the hard tissue. Thus, the v_2 phosphate vibration is visible as a broad, weak band in the spectra of *H. cumingii* prismatic aragonite and the skeleton of *Porites* sp. This band is sharp and appears well-defined in the spectrum of *Sepia officinalis* cuttlebone. The *Sepia officinalis* spectrum also shows well-defined v_4 and v_1 phosphate bands. In contrast, the bands are broad and weak in the spectra of the *Porites* sp. skeleton, outer and inner shell layers of *Arctica islandica* and these prismatic aragonite of *H. cumingii*. Finally, a broad v_3 phosphate band is detectable in all spectra shown in Figure 2.6-2, including *H. cumingii* nacre.

The observed variation in intensity and definition of the absorption bands assigned to the carbonate and phosphate groups is in good agreement with the different degrees of conversion of the studied hard tissues as deduced from Rietveld refinements of XRD patterns. *H. cumingii* nacre constitutes an exception. According to XRD analysis *H. cumingii* nacre does not undergo any conversion to AP, even after 14 days of interaction with the phosphate-bearing solution. However, the presence of very weak and broad phosphate-bands (v_3 and v_4)

in the IR spectrum of *H. cumingii* nacre that was altered for 14 days supports that a minor amount of conversion to AP has taken place.

It is worthwhile to note that the IR spectrum of *Sepia officinalis* aragonite altered for 24 h shows bands that are not found in the spectra of the other altered samples. One of these bands appears at 873 cm^{-1} and can be assigned to vibrational frequencies of carbonate ions that substitute into OH$^-$ sites in the apatite structure (A-type substitution). Further two bands, those that appear at 1405 and 1450 cm^{-1}, can be interpreted as corresponding to carbonate ions substituted into the phosphate site in apatite structure (B-type substitution) (Ratner et al. 2004, Meejoo et al. 2006). Moreover, the spectrum of *Sepia officinalis* hard tissue transformed for 24 h also shows a broad band at ~633 cm^{-1} which can be interpreted as the OH$^-$ libration band (Raynaud et al. 2002), and a poorly developed shoulder appears at 3570 cm^{-1}. This can be attributed to the OH$^-$ stretching mode (González-Díaz & Hidalgo 1976, González-Díaz & Santos 1977, Vandecandelaere et al. 2012).

Scanning Electron Microscopy (SEM)

Figures 2.6-3–10 present FE-SEM images showing crystallite and mineral unit arrangement preservation together with the distribution pattern of newly formed apatite (AP) for the investigated altered biogenic skeletons. As reference materials we used pristine equivalents of the geologic aragonite (Figure 2.6-A4) and the altered skeletons (Figures 2.6-A5–A16). Figure 2.6-A4 shows structural features of a geologic aragonite single crystal that was altered for 14 days. We find that a thin layer of newly formed apatite has replaced the aragonite and covers the external surface of the crystal (Figure 2.6-A4b). The apatite layer shows a multitude of cracks (Figure 2.6-A4a) that most likely developed due to contraction when the sample was taken out of the boiling solution.
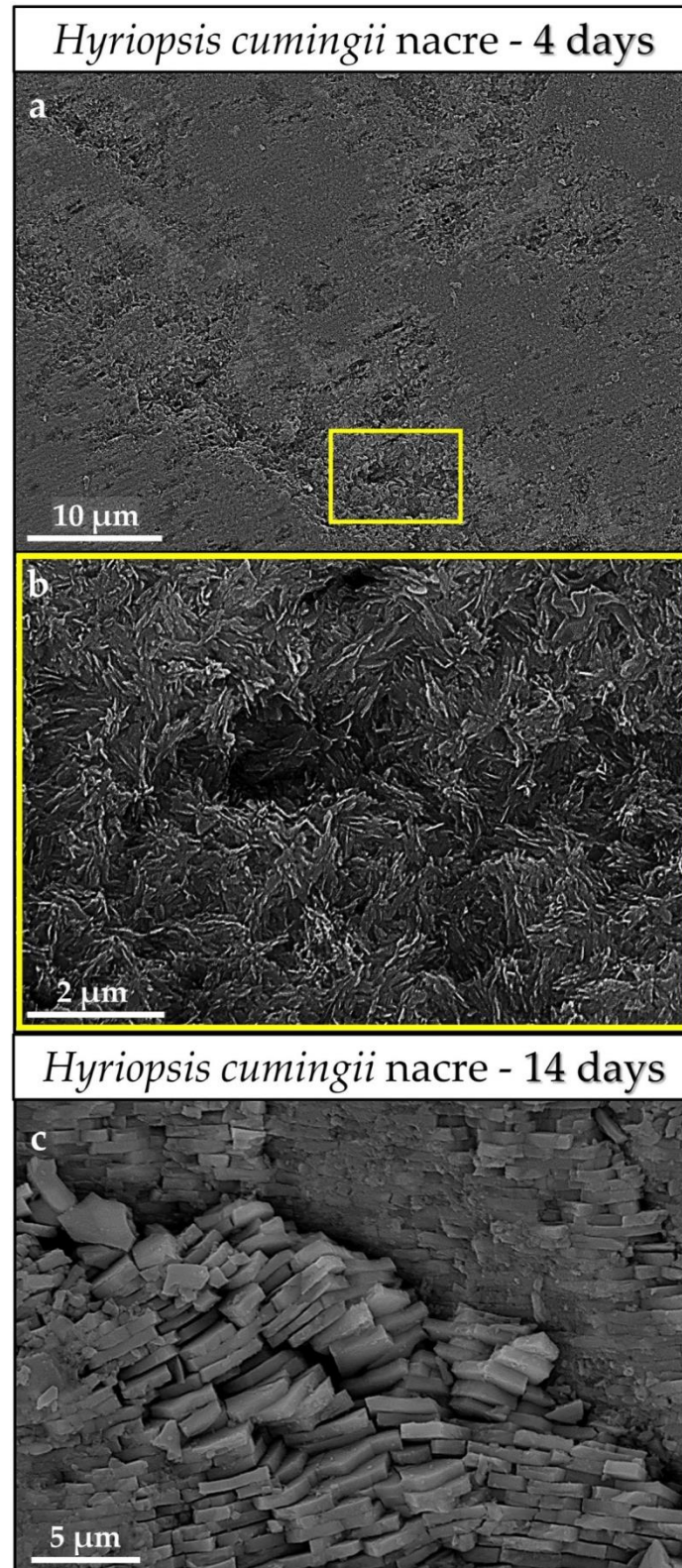
Figure 2.6-3. FE-SEM images of *Hyriopsis cumingii* nacre after (a,b) 4 days of conversion and (c) 14 days of conversion. Very little conversion to AP has taken place, the original arrangement of nacre tablets is well preserved (c). Even though, slight dissolution of aragonite induced that the surface of the nacreous shell layer became encrusted with a thin layer of newly formed AP crystals (a,b).

118

The shell of the bivalve *Hyriopsis cumingii* consists of aragonite that occurs in two distinct microstructures, nacreous aragonite next to the soft tissue of the animal and prismatic aragonite along the shell rim pointing to the seawater. The basic mineral units, prisms and tablets are encased by biopolymer membranes. Nacre tablets in the shell of the bivalve *H. cumingii* are arranged in a brick wall arrangement. As our XRD results (Figure 2.6-A3) and the comparison between the pristine (Figure 2.6-A5) and the 14 days altered (Figure 2.6-3c) shell portions show, the microstructure that was least transformed in the course of our experiments is nacreous aragonite. Nacre tablets as well as their microstructural arrangement remained well preserved even in the most altered sample (Figure 2.6-3). Even though, slight dissolution and reprecipitation has occurred as the surface of the 4 days altered and the nacre sample is covered with a layer of newly formed apatite crystals (Figure 2.6-3a,b). The weak and broad bands in the IR spectrum can be assigned to phosphate (v_3 and v_4). We identify them as AP, even though peaks that could be assigned to apatite were not found in the XRD pattern (Figure 2.6-A3).
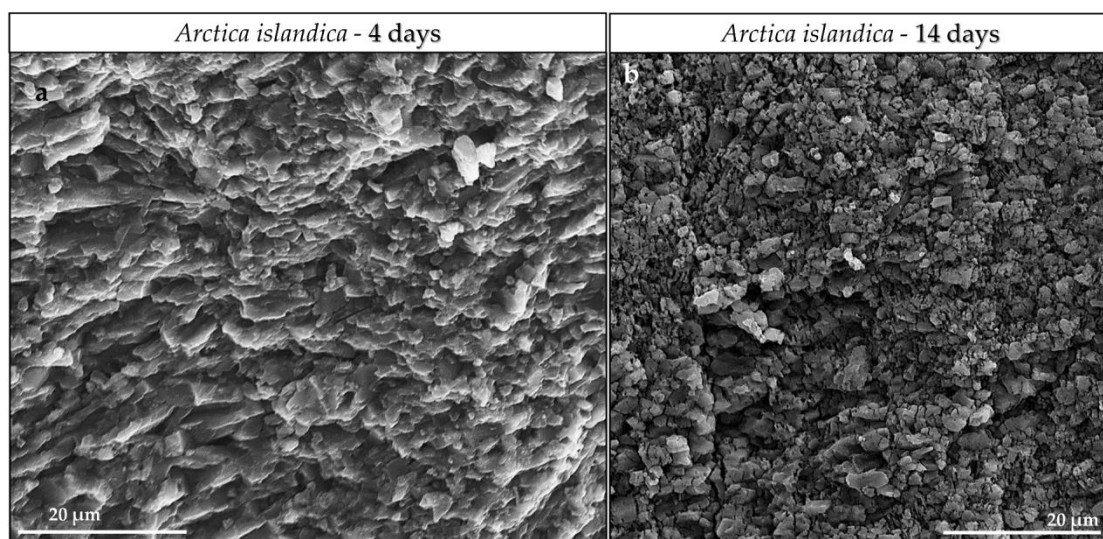
Figure 2.6-4. FE-SEM images of aragonite crystallite morphology and assembly after (a) 4 and (b) 14 days of conversion. We do not observe any major changes in crystallite morphology and size relative to that present in the pristine shell (compare Figure 2.6-4 to Figure 2.6-A6a).

The microstructure of the shell of the bivalve *Arctica islandica* is also highly resistant to the formation of new apatite (compare images in Figure 2.6-4a,b to Figure 2.6-A6a). The shell of pristine *Arctica islandica* (Figures 2.6-A6 and 2.6-A7) consists of densely packed and irregularly shaped mineral units (yellow stars in Figures 2.6-A6b,c and -A7) that are embedded into a network of biopolymer fibrils (Figure 2.6-A6b,c and Casella et al. 2017). Mineral unit size, porosity and density of aragonite crystal packing are unevenly distributed within the shell (Figures 2.6-A7 and -A8), such that, relative to inner shell portions, mineral

unit and pore sizes along the shell rim pointing to seawater, are increased. Mineral unit organization in the shell of *Arctica islandica* is little structured, especially in shell portions along the seawater pointing shell rim (Figure 2.6-A8b). However, aragonite that constitutes inner shell layers is present in a crossed-lamellar microstructural arrangement (Figure 2.6-A8a), especially that next to the soft tissue of the animal. Growth lines are frequent and are easily observable (white stars in Figure 2.6-A7a,c), as, at these, biopolymer contents and mineral unit sizes are increased. The shell of *Arctica islandica* can be addressed as consisting of densely packed aragonite. However, it shows primary porosity (Figure 2.6-A8), with the porosity being unevenly distributed. Along the seaward pointing shell portion, pores are abundant and large, while at shell parts that are inward and closer to the soft tissue of the animal, pores are small and significantly less frequent.

The shell of the bivalve *Hyriopsis cumingii* consists of aragonite that occurs in two distinct microstructures, nacreous aragonite next to the soft tissue of the animal and prismatic aragonite along the shell rim pointing to the seawater. The basic mineral units, prisms and tablets are encased by biopolymer membranes. Nacre tablets in the shell of the bivalve *H. cumingii* are arranged in a brick wall arrangement.

As our XRD results (Figure 2.6-A3) and the comparison between the pristine (Figure 2.6-A5) and the 14 days altered (Figures 2.6-3c) shell portions show, the microstructure that was least transformed in the course of our experiments is nacreous aragonite. Nacre tablets as well as their microstructural arrangement remained well preserved even in the most altered sample (Figure 2.6-3). Even though, slight dissolution and reprecipitation has occurred as the surface of the 4 days altered and the nacre sample is covered with a layer of newly formed apatite crystals (Figure 2.6-3a,b). The weak and broad bands in the IR spectrum can be assigned to phosphate (ν3 and ν4). We identify them as AP, even though peaks that could be assigned to apatite were not found in the XRD pattern (Figure 2.6-A3).

As Figure 2.6-1 highlights, up to 7 days of alteration the *Arctica islandica* microstructure is highly resistant to conversion of bioaragonite to apatite, the morphology of crystallites and mineral units remains well preserved and only a negligible amount of apatite formation takes place. Alteration becomes more marked from nine days onwards, when we find occasional occurrences of AP in pores and cavities that develop when the organic material within the shell becomes decomposed.

As the macroarchitecture of the skeleton of the scleractinian coral *Porites* sp. consists of a multitude of vertical and transverse elements (e.g., septa, columns, pali, theca, trabercular units), the bulk 2D appearance of the coral sample is characterized by many voids, gaps and recesses (Figure 2.6-A9a) and effects that the skeleton has a high surface area.

However, the basic mineral units of scleractinian coral skeletons are differently sized. Oriented clusters (white stars in Figure 2.6-A9b) of densely packed aragonitic needles and acicles nucleate at and grow outward from cavities within the coral skeleton, the centres of calcification (white arrows in Figure 2.6-A9c). The shape of basic mineral units in scleractinian coral skeletons can be addressed as partial or even as full spherulites. Already at 4 days of conversion a noticeable amount of AP forms and covers the surface of the coral skeleton (Figure 2.6-5a,b). At 14 days of conversion the AP cover increases in denseness (Figure 2.6-5c,d). In addition, we also observe some conversion to AP within the skeleton.
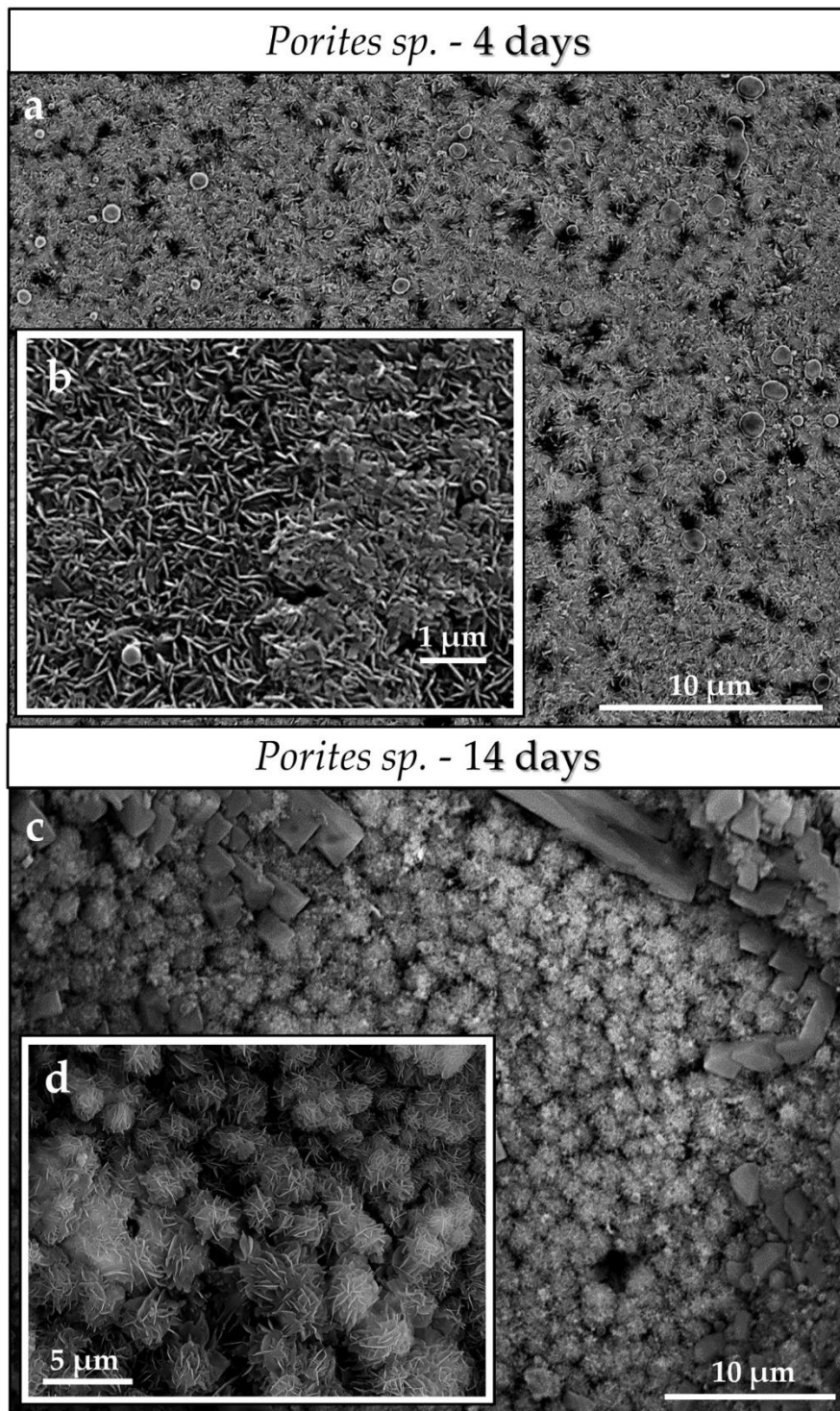
Figure 2.6-5. FE-SEM images depicting the coral skeleton *Porites* sp. after (a) 4 and (b) 14 days of conversion. Newly formed AP crystals cover the surface of the hard tissue already at 4 days of conversion. The compactness of the AP cover increases significantly with conversion time. SEM images shown in (b,d) depict AP crystal morphologies that form with different conversion times.

In contrast to the nacreous shell portion, prismatic aragonite in the shell of *Hyriopsis cumingii* is readily attacked. Aragonite prisms in modern *H. cumingii* (Figure 2.6-A10a) are large units

encased by thick biopolymer membranes (Figure 2.6-A10d,e) consisting of aragonite crystallites (Figure 2.6-A10b,c) placed within a network of organic fibrils (Figure 2.6-A10f). Conversion from biogenic aragonite to apatite starts instantly and increases steadily with alteration time. At 14 days of alteration more than 25 wt % of prismatic aragonite of *H. cumingii* is transformed to AP, while the nacreous aragonite within the shell remains almost totally unaffected (Figure 2.6-1). At 4 of days of conversion we find that a layer of AP covers the prisms. When altered for 14 days, conversion affects both, the surface of the prisms (the cover with AP becomes thicker) and the aragonite crystallites within the prisms (Figure 2.6-6b–d).
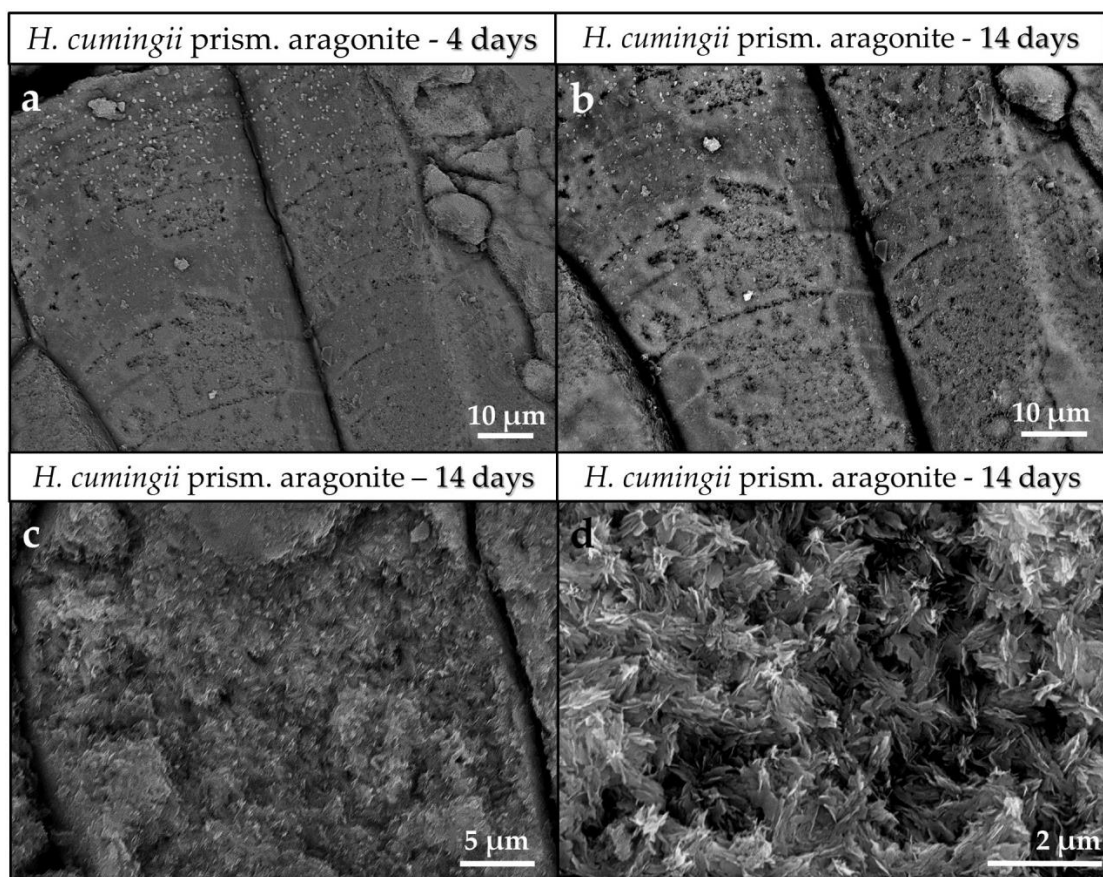
Figure 2.6-6. FE-SEM images showing *Hyriopsis cumingii* aragonite prisms altered for (a) 4 and (b–d) 14 days. Overall prism morphology does not change with alteration time. A layer of newly formed AP crystals covers the surface of the prisms already at 4 days of conversion. It increases in denseness with conversion time. Crystal morphologies in (d) clearly show that the aragonite within the prisms becomes converted to apatite at 14 days of alteration.

The most rapid and profound conversion takes place in the cuttlebone of the cephalopod *Sepia officinalis* (this study and Reinares-Fisac et al. 2017). The macrostructure of the cuttlebone resembles a carpark structure and consists of regularly spaced platforms that are interconnected by curved walls forming differently sized compartments within the cuttlebone

(Figure 2.6-A11). Nanoparticulate aragonite (Figure 2.6-A11a,b) with sizes between 400 to 600 nm constitute all skeletal elements, the platforms and the walls.
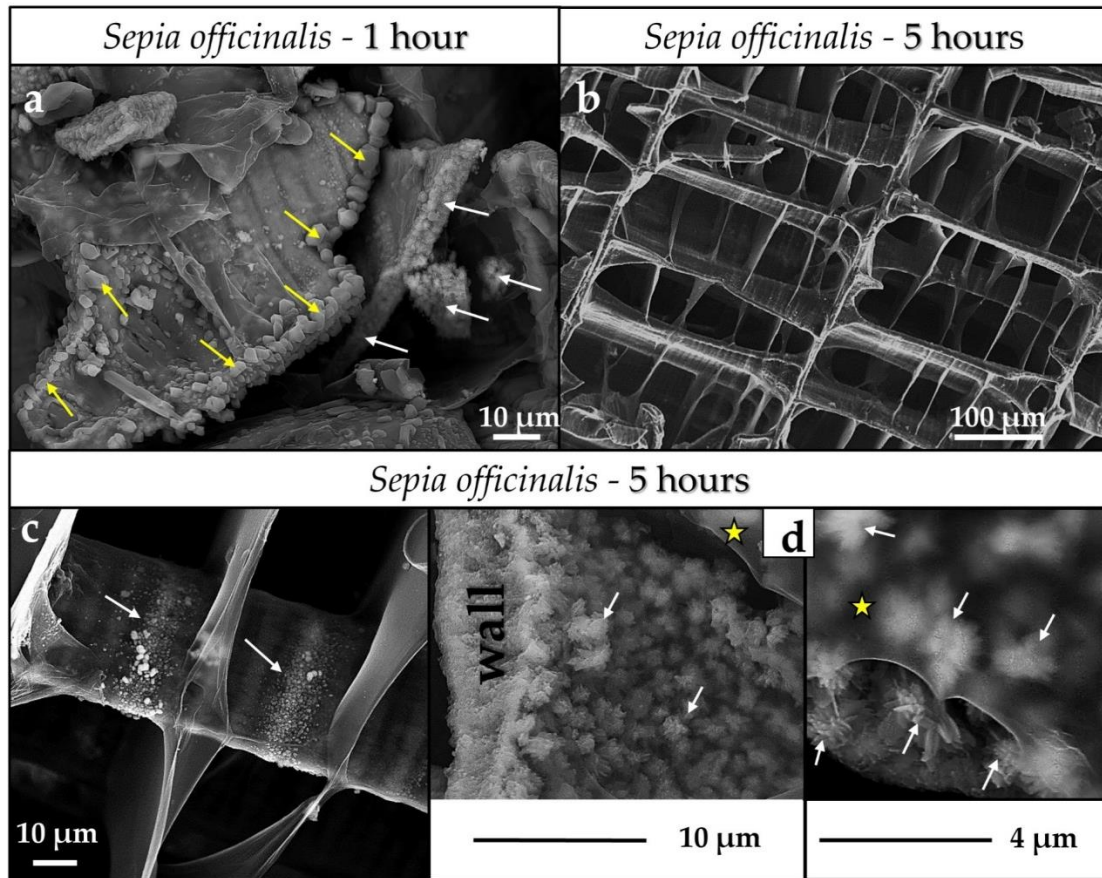
Figure 2.6-7. FE-SEM images showing *Sepia officinalis* cuttlebone altered for (a) 1 h and (b–d) 5 h. Even as early as 1 h of alteration of the cuttlebone, aragonite within skeletal elements starts to be converted to AP (white arrows in (a)), in addition to some newly formed crystals (black arrows in (a)) that precipitate onto skeletal element surfaces. At 5 h of conversion of aragonite to AP, AP formation within skeletal elements proceeds rapidly further (white arrows in (d)). In addition, newly formed AP starts to cover the surface of skeletal elements (white arrows in (c). Yellow stars in (d) point to the biopolymer lining that covers the surface of a skeletal element, in this case, a wall.

For the walls, we do not find a specific arrangement of the nanoparticulate aragonite, contrasting to the platforms that comprise different layers (white, yellow and blues stars in Figure 2.6-A1d), consisting of differently oriented stacks of aragonite rods (Figure 2.6-A12, white stars in Figure 2.6-A12a), with rods being composed of nanoparticulate aragonite embedded into a biopolymer matrix (Figure 2.6-A12b, yellow arrows in Figure 2.6-A12c). Etching of the cuttlebone for 180 s exhibits the biopolymer fraction within the skeleton (Figures 2.6-A15 and -A16). The high amount of biopolymers present in the cuttlebone is well observable as well as the large variety of organic fabrics. For all biological hard tissues

that we investigated in this study, the highest organic content is present in *Sepia officinalis* cuttlebone. This yields a huge interface area between the mineral and the biopolymer.
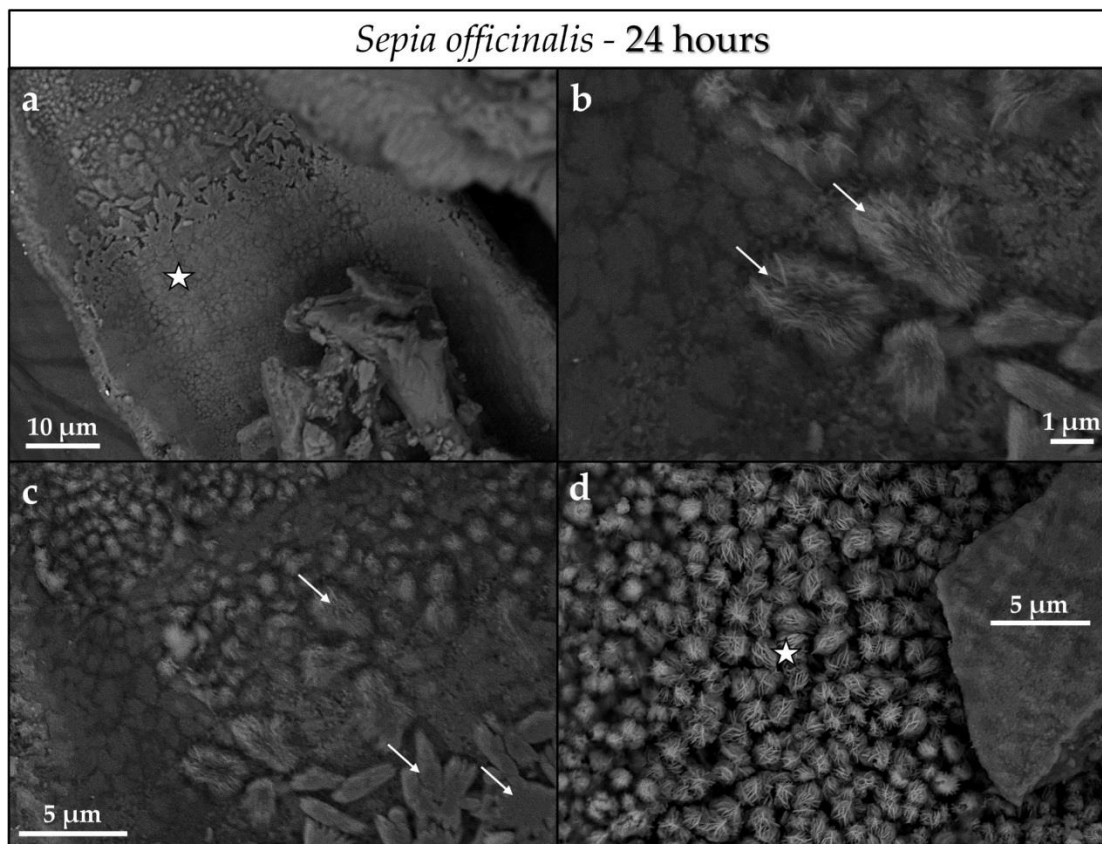
Figure 2.6-8. (a–d) FE-SEM images of *Sepia officinalis* cuttlebone after 24 h of conversion. Outer surfaces of skeletal elements (e.g., a chamber (a)) within the skeleton are covered with AP crystals. These become dense (white star in (d)), often fuse (white arrows in b,c) and finally encase the outer surface of the skeletal element (white star in (a)), conserving its outer morphology.

The aragonite within the cuttlebone is attacked instantly with the onset of the conversion process. Conversion for an hour already yields the formation of AP crystals within skeletal elements (white arrows in Figures 2.6-7a and -1b). At conversion for 5 h the original carpark structure of the cuttlebone is still preserved (Figures 2.6-7b), even though about 60 wt % of the aragonite is converted to AP. Up to this stage AP formation takes mainly place within skeletal elements (Figure 2.6-7d), while AP growth onto outer surfaces, e.g. the walls of compartments (white arrows in Figure 2.6-7c) occurs to a lesser degree.

We find that AP growth onto surfaces is highly increased during late stages of the reaction process (Figures 2.6-8 and 2.6-9): AP crystals merge (Figure 2.6-9) and form larger units (white arrows in Figure 2.6-8b,c). This creates a dense and solid layer of AP crystals that reproduces the external shape of cuttlebone elements (Figure 2.6-8a). Figure 2.6-10 shows the macrostructure of *Sepia officinalis* cuttlebone that was exposed to the reaction with the

phosphate-bearing solution for 3 days. Some ultrastructural features of the skeleton are still observable even though broken and deformed. The biopolymer membrane lining of the chambers is still present (yellow arrows in Figure 2.6-10d), however, now detached from the mineral.
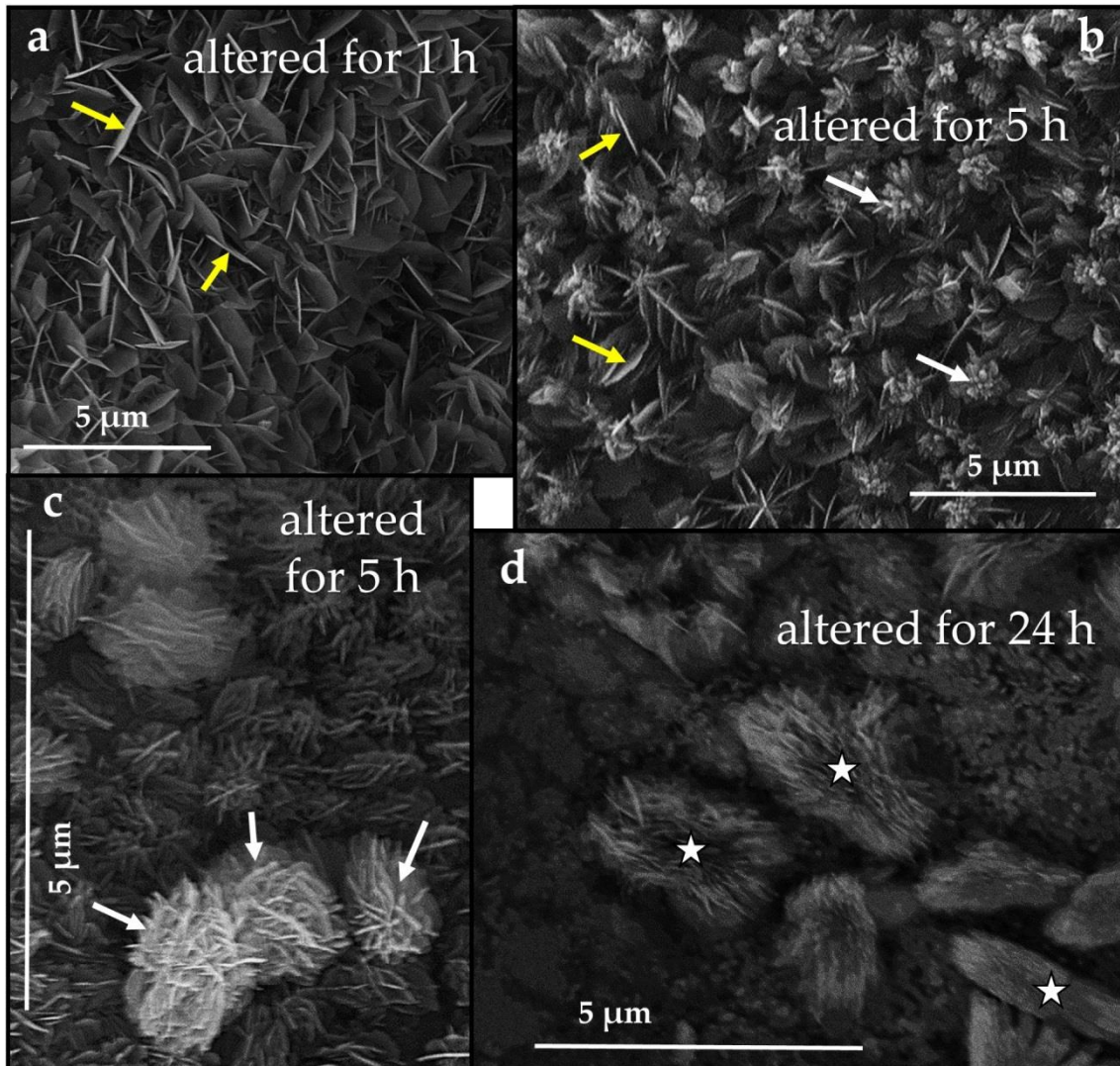
Figure 2.6-9. FE-SEM images showing the change in AP crystal morphology with progressive conversion of *Sepia officinalis* cuttlebone aragonite. (a) Conversion for 1 h; (b,c) conversion for 5 h and fusion of individual crystals; (d) fusion of some AP crystals and densification of the AP cover.

Even though the carpark structure of the skeleton is still preserved to some degree, the entire structure loses its cohesion as the walls detach from the platforms and the compartments become overgrown with newly formed precipitates.
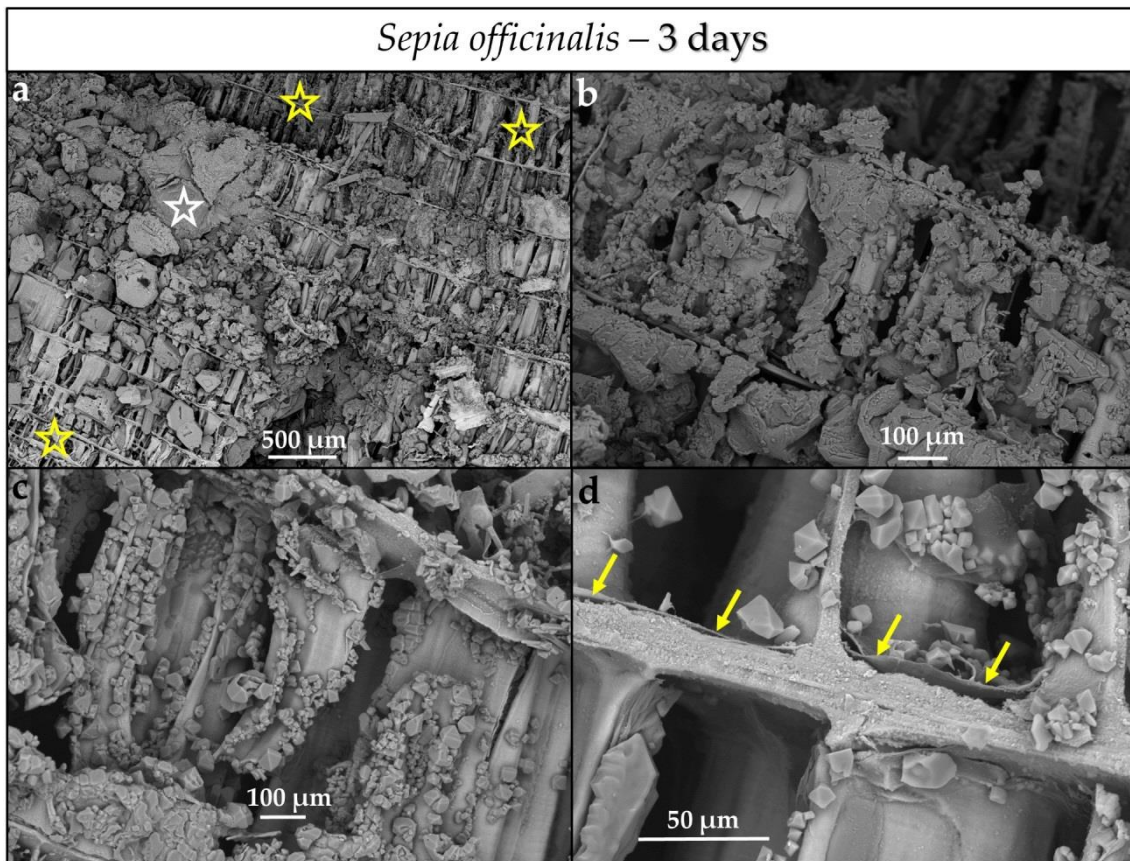
Figure 2.6-10. (a–d) FE-SEM images showing the *Sepia officinalis* cuttlebone ultrastucture when altered for 3 days. The original ultrastructure (yellow stars in (a)) is highly ruptured up to complete distortion (white star in (a)). Biopolymer membranes lining the chambers are not entirely decomposed yet (yellow arrows in (d)). However, they become detached from the surface of the skeletal element.

2.6.4 Discussion

The Phase Conversion Mechanism

The conversion of the studied aragonitic biominerals and that of geologic aragonite into AP occurs with the preservation of morphologies and some microstructural features. Pseudomorphic conversion of biocarbonate in contact with phosphate-bearing solutions takes place via interface coupled dissolution-recrystallization (Kasioptas et al. 2010; 2011, Schlosser et al. 2012, Reinares-Fisac et al. 2017). The conversion mechanism involves the dissolution of primary aragonite and the precipitation of secondary AP (Putnis 2002; 2009, Putnis & Putnis 2007, Pollok et al. 2011, Putnis & Fernández-Díaz 2011, Ruiz-Agudo et al. 2014). The preservation of external morphologies and microstructural features requires that the dissolution and the crystallization reactions are temporarily and spatially coupled (Putnis 2002; 2009, Putnis & Putnis 2007, Kasioptas et al. 2010, Pollok et al. 2011, Putnis & Fernández-Díaz 2011, Ruiz-Agudo et al. 2014) and that the dissolution of aragonite is the conversion rate-controlling step (Putnis 2002; 2009, Putnis & Putnis 2007, Fernández-Díaz et

al. 2009, Xia et al. 2009a, b; Kasioptas et al. 2010, Pollok et al. 2011, Putnis & Diaz 2011, Ruiz-Agudo et al. 2014, Putnis 2015).

The Conversion of Geologic Aragonite

At 14 days of reaction we observe only a thin cover and a thin rim (~ 100 microns) of AP that replaces the outer surface of the aragonite crystal (Figure 2.6-A4b). The transformed rim accurately reproduces the external shape of the aragonite crystal. The network of cracks within the newly formed AP layer covering the surface of the aragonite crystal (Figure 2.6-A4a) is due to rapid cooling-related shrinkage and is most likely generated when the crystal is extracted from the boiling solution. The very limited conversion of geologic aragonite to AP is most probably not due to early surface passivation.

Surface passivation during pseudomorphic mineral replacement occurs when (a) the structures of the parent and product phases show similarities that facilitate epitactic growth onto each other, and/or (b) the molar volume change associated with the conversion is positive (Putnis 2015). Previous studies of the conversion of aragonite to AP under hydrothermal conditions demonstrated that AP grows oriented onto the aragonite surface (Eysel & Roy 1975). Some authors interpreted this feature as evidence that the conversion is topotactic. However, strong arguments (Kasioptas et al. 2011) support the notion that AP oriented growth develops with the advancement of the replacement front due to competitive growth. Hence, in those cases where an epitactic layer of the product phase forms, it often consists of an aggregate of crystals where several epitactic orientations coexist (Roncal-Herrero et al. 2017, Cuesta Mayorga et al. 2018). Consequently, the newly formed product layer commonly contains a certain amount of intrinsic intergranular porosity and does not seal completely the parent phase from further interaction with the solution (Roncal-Herrero et al. 2017, Cuesta Mayorga et al. 2018). In addition, the molar volume change associated with the aragonite—AP conversion is negative (~6%) (Kasioptas et al. 2010, Schlosser et al. 2012, Reinares-Fisac et al. 2017). As the external shape of the sample is preserved during conversion, porosity has to be generated to compensate the molar volume loss (Putnis 2002; 2009, Putnis & Putnis 2007, Pollok et al. 2011, Putnis & Fernández-Díaz 2011, Ruiz-Agudo et al. 2014). In addition, further porosity is generated due to the difference in solubility between the original and the product phases, e.g., AP is many orders of magnitude more soluble than geologic aragonite (Putnis & Putnis 2007, Pollok et al. 2011). Hence, in the case of aragonite to apatite conversion, much porosity is generated, through which the fluid can communicate with the parent phase. In the case of geological aragonite, we must conclude that the negligible degree

of conversion is not a consequence of lack of communication between the interface and the reaction fluid, where the dissolution-recrystallization reaction takes place. It is the consequence of a very slow dissolution rate of geologic aragonite under the experimental conditions used in this study. The slow dissolution of the geologic aragonite sample can be attributed to its low reactivity, to which its single crystallinity and its low surface area extent only adds up.

The Conversion of Biologic Aragonites

With the exception of *H. cumingii* nacre, which undergoes almost no phase change up to 14 days of alteration, all other biological hard tissues that were investigated in this study transform to AP at a much faster rate than geologic aragonite (Figure 2.6-1, Table 2.6-1). One difference that explains the higher rates of conversion is given by the fact that the biologic hard materials consist of nanometre-to micrometre sized biocrystals, while the geologic aragonite is a macroscopic single crystal.

Hence, the surface area where the phosphate-bearing boiling solution can interact with the biogenic mineral is significantly higher in comparison to that of geologic aragonite. The direct consequence is a much faster dissolution of biogenic aragonite, and also a faster conversion to AP, as aragonite dissolution is the limiting step. In addition, the biogenic aragonite is more soluble than geological aragonite (Ortoleva 1982, Baig et al. 1999) since solubility is size-related and increases as the crystal size decreases—this also favours the faster conversion of biologic aragonite into AP. Another major factor that plays a role in accelerating the conversion of biogenic aragonite to apatite relates to the composite nature of the biologic hard material. All extracellularly formed biological hard tissues contain occluded biopolymers (Levi-Kalisman et al. 2001, Gaspard et al. 2008, Heinemann et al. 2011, Checa et al. 2016), these being developed as organic membranes, fibres or networks. The steadily advancing degradation of the organic component effects that the biologic aragonite becomes progressively more porous, thus channels are formed, through which the solution can reach inner sample regions. This creates an additional increase in mineral surface area that is exposed to the fluid, and herewith contributes to a faster conversion kinetics. However, it should be kept in mind that this porosity is inherent to biological hard tissues and is independent of that, that develops due to the aragonite to AP conversion process itself.

Sepia officinalis **Cuttlebone Aragonite**

Most interesting is the very different conversion kinetics of the investigated biogenic aragonite samples (a) from geologic aragonite and (b) between the biological materials themselves (Figure 2.6-1, Table 2.6-1). This is called forth by an interplay between specific microstructure, inherent (original) porosity, biopolymer content, fabric, pattern of organics distribution and the extent of mineral surface that can interact with the reaction fluid.

Sepia officinalis cuttlebone is the biomaterial that shows the highest reactivity. This highest reactivity compared to other biominerals cannot be attributed to differences in average crystallite size, since differences in this parameter are negligible (504 Å for *H. cumingii* and 486 Å for *Sepia officinalis*, the slowest and the fastest transforming biomaterial, respectively). Of the investigated hard tissues the cuttlebone has the most lightweight skeleton with the aragonite being well protected by various biopolymers: (a) a thick outer organic membrane shielding the outermost surface of the entire cuttlebone, (b) resistant biopolymer linings occluded within the cuttlebone covering the outer surfaces of all building elements (walls, platforms) (Figures 2.6-A13a, -A14a and -A16), and (c) biopolymer films and networks occluded within the building elements and in between the aragonite crystallites (Figures 2.6-A12b,c, -A13b and -A14, especially Figures 2.6-A15 and -A16). Reaction, especially at the very beginning of the conversion process (up to three hours of reaction), takes place at an extremely fast rate and is facilitated by the very large surface area of the mineral that becomes exposed to interaction with the aqueous solution. The large surface area exposure is given by (a) the highly permeable carpark structure of the cuttlebone (Figure 2.6-A11c), (b) the nanoparticulate nature of the biologic aragonite (Figure 2.6-A11a), (c) the very delicate fabric (Figures 2.6-A13b, -A15 and -A16) and (d) the rapid decomposition of organic material occluded within the building elements. Especially the latter contributes to an increase in porosity and escalates the conversion process.

The shape of the conversion curve for *Sepia officinalis* in our experiment very closely resemble that obtained by Kasioptas et al. (2010) at similar temperature under hydrothermal conditions. These authors found that their experimental data fitted well the Avrami function. The profile of a curve that is given by the Avrami equation for phase transformation at constant temperature indicates that, subsequent to nucleation and initial rapid reaction, the transformation to a new phase steadily slows down as little unreacted material is left for the production of a new phase (Avrami 1939; 1940; 1941). This is what we see for *Sepia officinalis* (Figure 2.6-1b). We find that two sections of the conversion curve can be

130

distinguished according to different conversion rates (Figure 2.6-1b). Up to three hours of reaction the conversion rate of bioaragonite to AP is incredibly high. This is the time period where the minute aragonite crystallites within the structural elements of the hard tissue are transformed to AP (white arrows in Figure 2.6-7d). The reaction is driven by the fast decomposition of occluded organics (characterized by their delicate fabric) within the major structural elements. However, as it is well visible in Figure 2.6-7c,d, the membrane linings that protect the outer surfaces of structural elements remain unaffected up to that point (yellow stars in Figure 2.6-7d). Conversion slows significantly down after three hours of reaction (Figure 2.6-1b). This is the time period where the protecting biopolymer membrane linings start to become attacked as well. This facilitates AP nucleation onto the outer surfaces of the walls and the platforms (Figure 2.6-7c); progressive conversion induces their complete coverage with AP (Figure 2.6-8). When altered for a few days the compartments of *Sepia officinalis* are not just filled up with AP, as the conversion of bioaragonite to AP is complete in 24 h, thus there is no parent aragonite left to be transformed to AP.

With ongoing conversion for a few days, we find that structural elements become highly deformed and the carpark structure becomes ruptured (Figure 2.6-10).

Porites sp. Acicular and *Hyriopsis cumingii* Prismatic Aragonite

Porites sp. and *Hyriopsis cumingii* prismatic aragonite are the biomaterials that reach the next highest degree of conversion to AP after *Sepia officinalis* cuttlebone (Figure 2.6-1, Table 2.6-1). Nonetheless, conversion kinetics is significantly different of that of the cephalopod cuttlebone. While in the cuttlebone replacement rates shoot up first and slow down at the end of the process, for *Porites* sp. aragonite and *Hyriopsis cumingii* prismatic aragonite we find at first (up to 4 days) a slow but steadily increasing dissolution of biological aragonite and precipitation of apatite (Figure 2.6-1a). Even though in *Porites* sp. and *Hyriopsis cumingii* prisms newly formed AP contents are high, the speed of conversion is not at all comparable to that of *Sepia officinalis* cuttlebone. In 14 days of alteration 25 and 38 wt % AP content is detected in *H. cumingii* prismatic shell layer and the *Porites* sp. skeleton, respectively.

With progressive reaction time, between 4 and 9 days of reaction, conversion to AP in the coral skeleton stops, in contrast to prismatic aragonite in *H. cumingii*, where it still increases steadily. For the time period between 9 and 14 days of reaction, AP formation rates change again: it increases significantly for *Porites* sp., while it stops for *H. cumingii* prisms (Figure 2.6-1a).

In comparison to the cuttlebone, significantly less organics are occluded in the bivalve shell and the coral skeleton. Hence, there is significantly less surface area where the reaction fluid can react with the mineral. The steady formation of AP in the coral and the bivalve shell within the first four days of reaction can be attributed to dissolution of bioaragonite along outer surfaces of the skeletons.

It is well visible (Figure 2.6-5) that already after 4 days of alteration the surface of *Porites* sp. Becomes covered with a thick layer of AP crystals. Exactly at this point we find that conversion of aragonite to AP in *Porites* sp. stops (Figure 2.6-1a). As the coral skeleton is dense and has very little occluded organics the conversion rate to AP is slow compared to that of the exceedingly more porous and highly organic rich cuttlebone. However, it is much faster than the conversion rate of geologic aragonite.

We know from previous work (Casella et al. 2018a) that the reaction fluid enters the skeleton of *Porites* sp. Through centres of calcification and that new mineral formation starts and extends from here into the skeleton. This characteristic is reflected in the conversion curve as well, with the sudden increase in AP content at later stages of reaction, between 9 and 14 days (Figure 2.6- 1a), when AP formation in *Porites* sp. shoots up significantly.

The prismatic aragonite shell portion of *Hyriopsis cumingii* is slightly porous. We find pores between the columns as well as within the membranes that encase the aragonite of the columns (Figure 2.6-A17). The reaction fluid enters the shell through these pores, infiltrates the entire prismatic shell portion and space between the columns as well as the inner parts of the columns. The network of biopolymer fibrils (Figure 2.6-A10d–f) within the columns becomes easily decomposed as their fabric is delicate. Accordingly, the surface area where reaction fluid can react with the mineral becomes highly increased; the aragonite crystallites constituting the prisms are minute to small in size, easily dissolved and reprecipitated as apatite (Figure 2.6-A10f). However, as Figure 2.6-1a shows, the conversion process for *H. cumingii* prisms stops abruptly at nine days of reaction. At this stage we find the surface of the columns to be covered with AP shielding the aragonite within the columns from reaction with the fluid. Even though more porosity is generated as the conversion progresses, an increase in tortuosity of the pathway that communicates the fluid with the remaining aragonite and a reduction in aragonite area exposed to the fluid might explain the slow-down of the reaction.

Arctica islandica **Cross-Lamellar and** *Hyriopsis cumingii* **Nacreous Aragonite**

The least conversion of bioaragonite to AP takes place in *Arctica islandica* cross-lamellar and *Hyriopsis cumingii* nacreous aragonite. In the latter we observe after 14 days of reaction less than 1 wt % of AP. In the shell of *Arctica islandica*, up to 7 days of conversion between 2 and 3 wt % and at 14 days of reaction only 11 wt % of AP formation, respectively (Figure 2.6-1, Table 2.6-1). As it is the case for *Porites* sp. and *Hyriopsis cumingii* prismatic aragonite, we find a slight increase in AP formation within the first 4 days of reaction for *Arctica islandica* aragonite as well. However, for *Arctica islandica* a time period follows (between 4 and 7 days) where AP formation ceases (Figure 2.6-1a). This is followed by a time span where we see a sudden increase in AP precipitation, especially along the seaward pointing rim of the shell (Figure 2.1-1a, Table 2.6-1). The shell of *Arctica islandica* is dense (especially shell parts next to the soft tissue of the animal) and consists of irregularly shaped mineral units that are embedded into a network of biopolymer fibrils (Figure 2.6-A7 and Casella et al. 2017). The shell is crossed by growth lines, where the organic matter content is slightly increased (Figure 2.6-A8). For the first 7 days of conversion treatment—where almost no AP formation occurs—most biopolymers within the shell become decomposed and, hence, the reaction fluid can permeate the entire hard tissue, not just its outer and inner surfaces. Due to decomposition of the biopolymers, there is a slight increase in mineral surface area, the amount of dissolved aragonite and that of newly formed apatite. For the final stage of alteration, we see for *Arctica islandica* a slight difference in AP formation kinetics between outer and inner shell layers. Along the seaward pointing shell part, conversion of bioaragonite to AP carries on (Figure 2.6-1a), while the aragonite that constitutes inward shell portions does not seem to transform further into apatite. In contrast to inner shell layers, the outer shell portion of *Arctica islandica* is porous (Figure 2.6-A9 and Casella et al. 2017). Hence in these regions, the reaction fluid can enter the shell through the growth lines as well as through voids, the primary pores. These pores are largely absent in more inward shell parts. The latter is compact, up to 14 days of conversion there is not much space present for fluid permeation, aragonite dissolution and new AP precipitation (this study and Casella et al. 2017).

As it is well observable in Figure 2.6-1 and Table 2.6-1, *Hyriopsis cumingii* nacre is the most resistant biological hard tissue to aragonite dissolution and AP formation. Two facts account for this: (i) each nacre tablet is encased into a biopolymer membrane sheath (Figure 2.6-A5c,d) that is obviously (ii) not affected by our conversion experiments due to: the used temperature, the chemical composition of our reaction fluid, and the time span of the experiment. Thus, the reaction fluid cannot infiltrate the shell except for the outer and inner

surfaces of the shell. Hence, the tablets and their arrangement to stacks remains intact (Figure 2.6-3d). The behaviour at conversion of this biogenic hard tissue resembles that of geologic aragonite most closely.

2.6.5 Conclusions

Biological hard tissues are hierarchical composites with unique microstructures. They interlink on many scales two distinct components: hard and brittle minerals with compliant biopolymers. Induced by evolutionary driven adaptation, modern skeletal microstructures and textures are highly diversified and are utilized as an additional means for the improvement of biomaterial functionality (Genin et al. 2009, Seidl et al. 2012, Huber et al. 2014; 2015, Checa 2018, Griesshaber et al. 2018).

We discuss in this manuscript the effect of the composite nature of biocarbonate hard tissues and biogenic microstructures on the rate and kinetics of bioaragonite to apatite conversion in an open experimental set up. We deduce the following conclusions for the different biologic and non-biologic hard materials (Tables 2.6-1 and 2.6-2, Figure 2.6-A11).

1. We find highly distinct rates and kinetics of conversion to apatite for the selected aragonitic biological hard tissues. This is dependent on the ability of the reaction fluid to access aragonite crystallites, which directly relates to the content and the extent of decomposition of biopolymers within the hard tissue, the extent of the newly formed surface area and the specific biological hard tissue macro- and microstructures.

2. When treated for up to, respectively, 1 and 14 days, a profound conversion of bioaragonite to apatite within mineral units and/or structural elements takes place in the cuttlebone of the cephalopod *Sepia officinalis* and in the prismatic columns of the bivalve *Hyriopsis cumingii*.

   a. Conversion of *Sepia officinalis* aragonite occurs almost instantly. It is highly accelerated at the beginning and slows down towards the end of the conversion process.

   b. Conversion to AP in *Hyriopsis cumigii* prisms is steadily increasing for almost the entire time span of the experiment. However, the process stagnates for the final stages of the experiment.

3. Even though having a large surface area given by the specific macrostructure, the acicular microstructure of the warm water coral *Porites* sp. gives a compact hard tissue. At the start of the conversion process only outer skeletal surfaces are subject to dissolution and conversion

to AP. With progressive conversion, apatite formation accelerates quickly when the fluid enters the skeleton through the centres of calcification.

4. The cross-lamellar microstructure in *Arctica islandica* is, at first, highly resistant to phase conversion. It speeds slightly up when the network of organic biopolymers becomes destroyed, and the reaction fluid can permeate the entire hard tissue. The presence of pores within outer shell layers facilitates fluid infiltration even further and accelerates even more the conversion process for this part of the shell.

5. Nacreous aragonite in *Hyriopsis cumingii* is most resistant to conversion. Even though nacre tablets are encased by organic membranes, the latter are not decomposed easily, thus the aragonite of the nacreous shell layer is not attacked and remains intact.

6. All aragonite biominerals transform into AP at a much faster rate than geological aragonite. *Hyriopsis cumingii* nacre is the biomaterial that shows a conversion kinetics that resembles that of geologic aragonite most closely. This is consistent with the resistance to degradation of organic membranes in the former.

2.6.6 Acknowledgements

2.6.8 Appendix
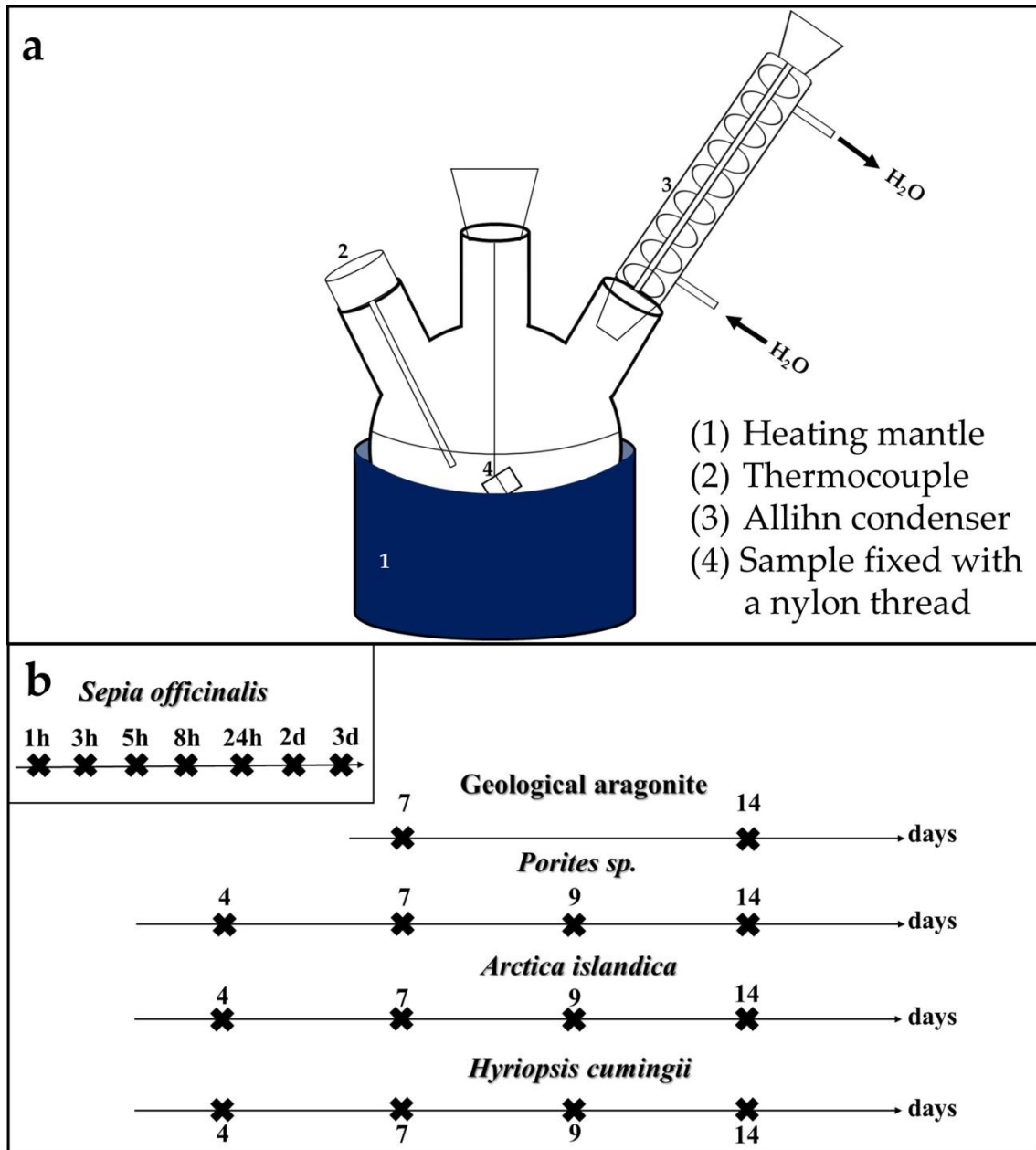
Figure 2.6-A1. (a) Experimental setup; (b) overview of conducted conversion experiments. *Sepia officinalis* cuttlebone was transformed for 1 to 24 h and 2 and 3 days. *Porites* sp., *Arctica islandica* and *Hyriopsis cumingii* aragonite were transformed up to 14 days. Geological aragonite was transformed for 7 and 14 days. In (a): (1) Heating mantle, (2) Thermocouple, (3) Allihn condenser, (4) Sample fixed with a nylon thread.
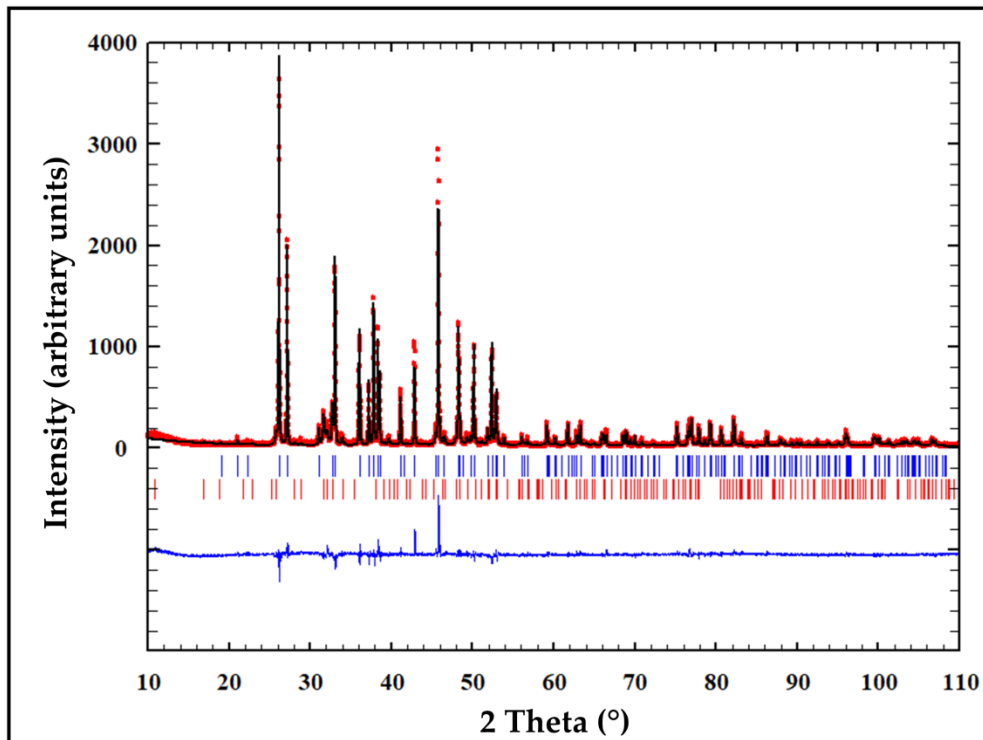
Figure 2.6-A2. Exemplary Rietveld refinement plot for *Porites* sp. after conversion for one week. Red dots: data points; black line: calculated XRD profile; bottom blue line: difference of observed and calculated data; blue vertical bars: positions of aragonite diffraction peaks; red vertical bars: position of apatite diffraction peaks.
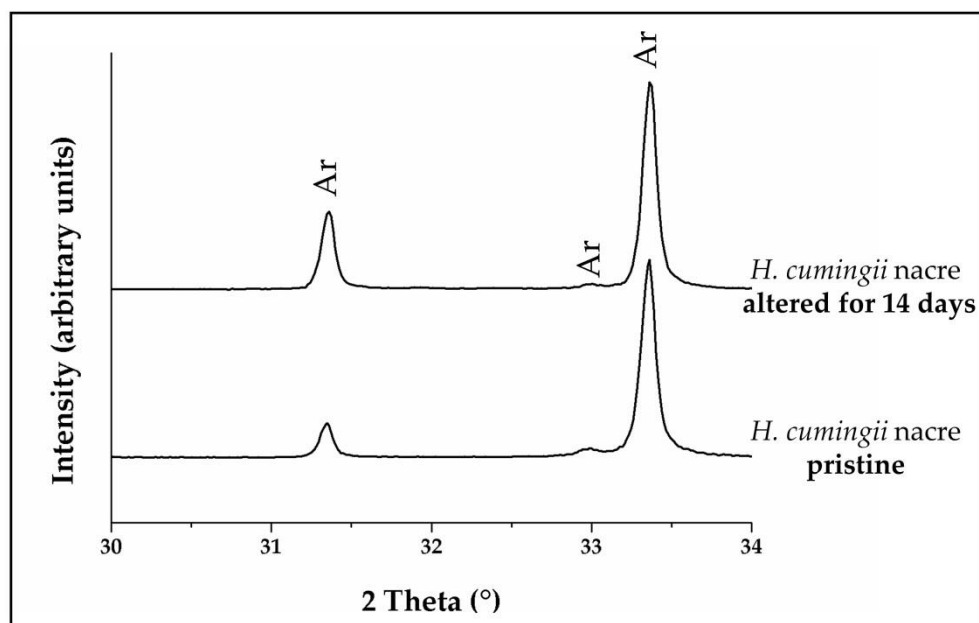
Figure 2.6-A3. XRD diffractograms (30–34° 2θ) of pristine and altered *Hyriopsis cumingii* nacre. Conversion was carried out for 14 days.
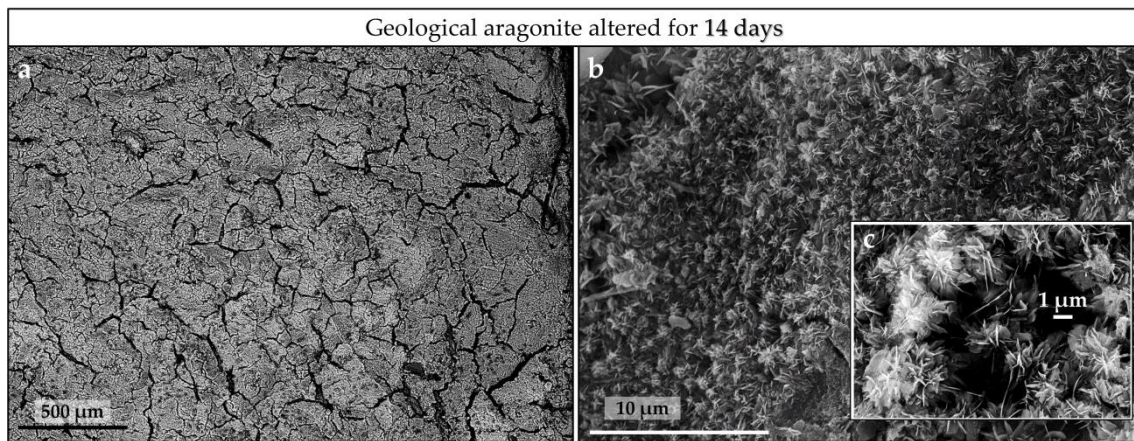
Figure 2.6-A4. FE-SEM images of geological aragonite transformed for 14 days.
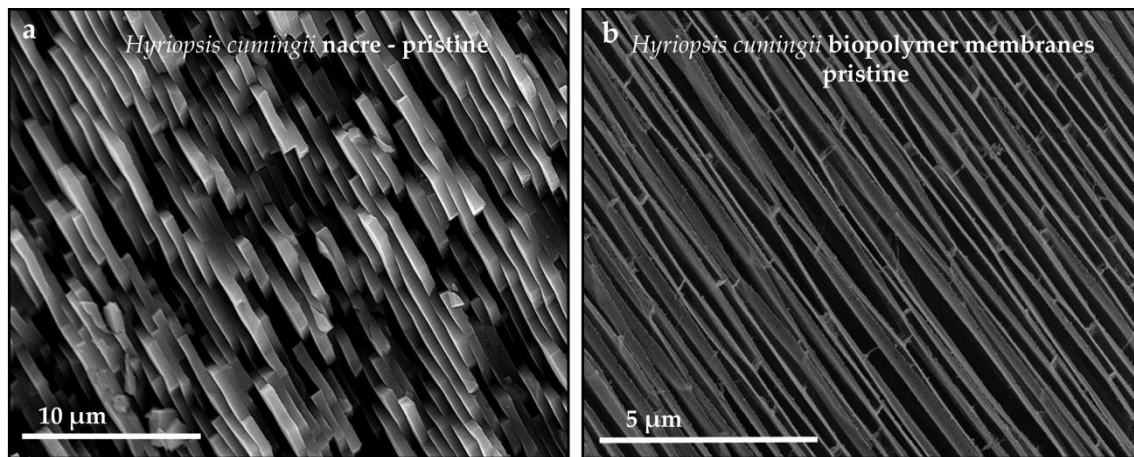
Figure 2.6-A5. FE-SEM images of nacre tablets (a) and biopolymer sheaths (b) encasing the tablets.
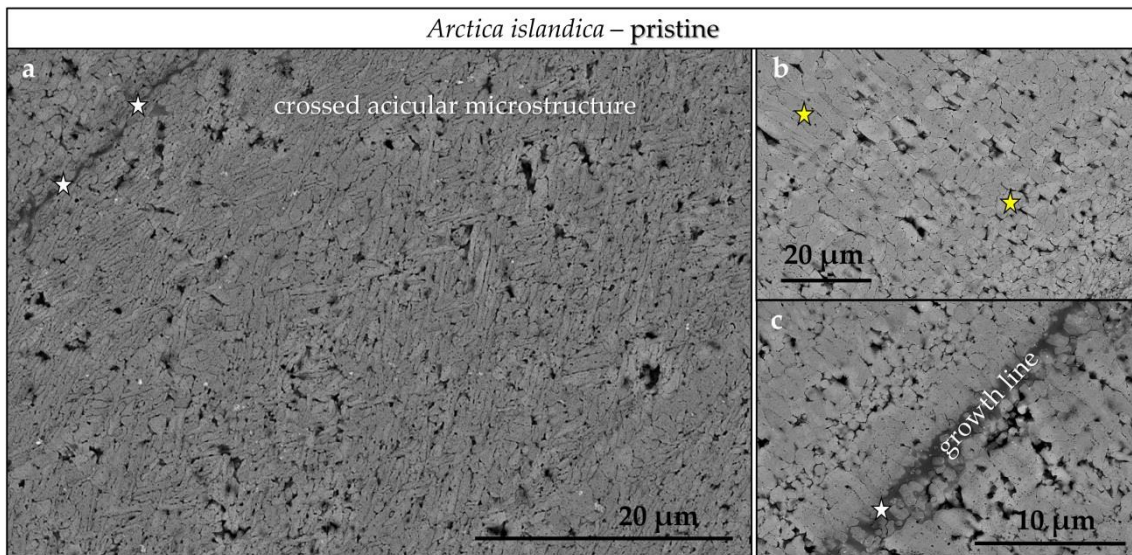
Figure 2.6-A6. FE-SEM images of (a) aragonite crystallites and (b,c) mineral unit morphologies in pristine *Arctica islandica*, where mineral units are embedded into a network of biopolymer fibrils. Aragonitic mineral units are larger in size in the shell portion facing seawater relative to that part of the shell that is next to the soft tissue of the animal.
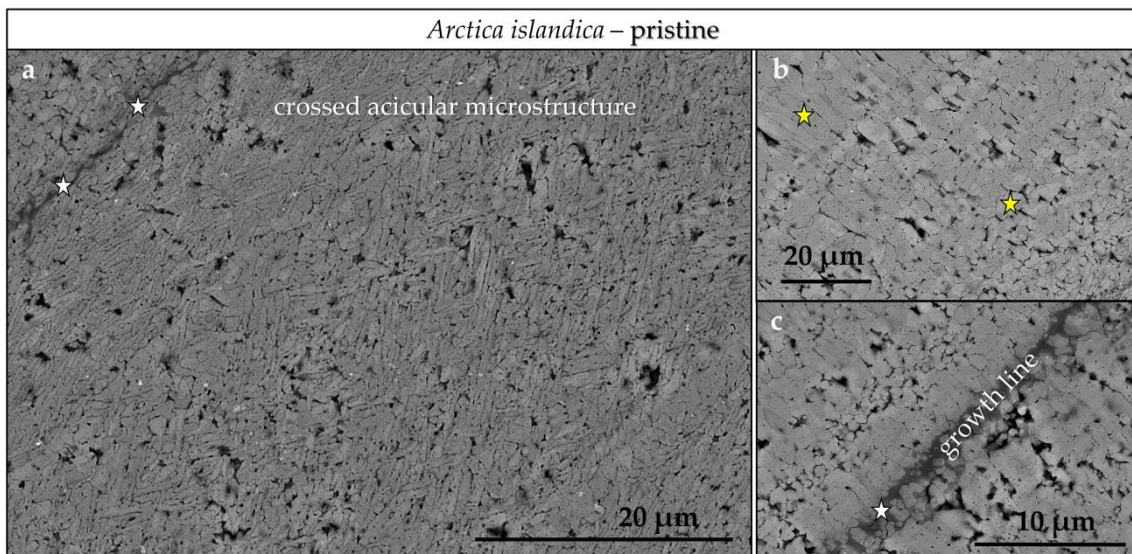
Figure 2.6-A7. FE-SEM images of (a) the shell microstructure of pristine *Arctica islandica*; (b,c) variation in size and morphology of constituting mineral units and presence of growth lines (white stars in (a,c) distinguished by an increased amount of biopolymer content.
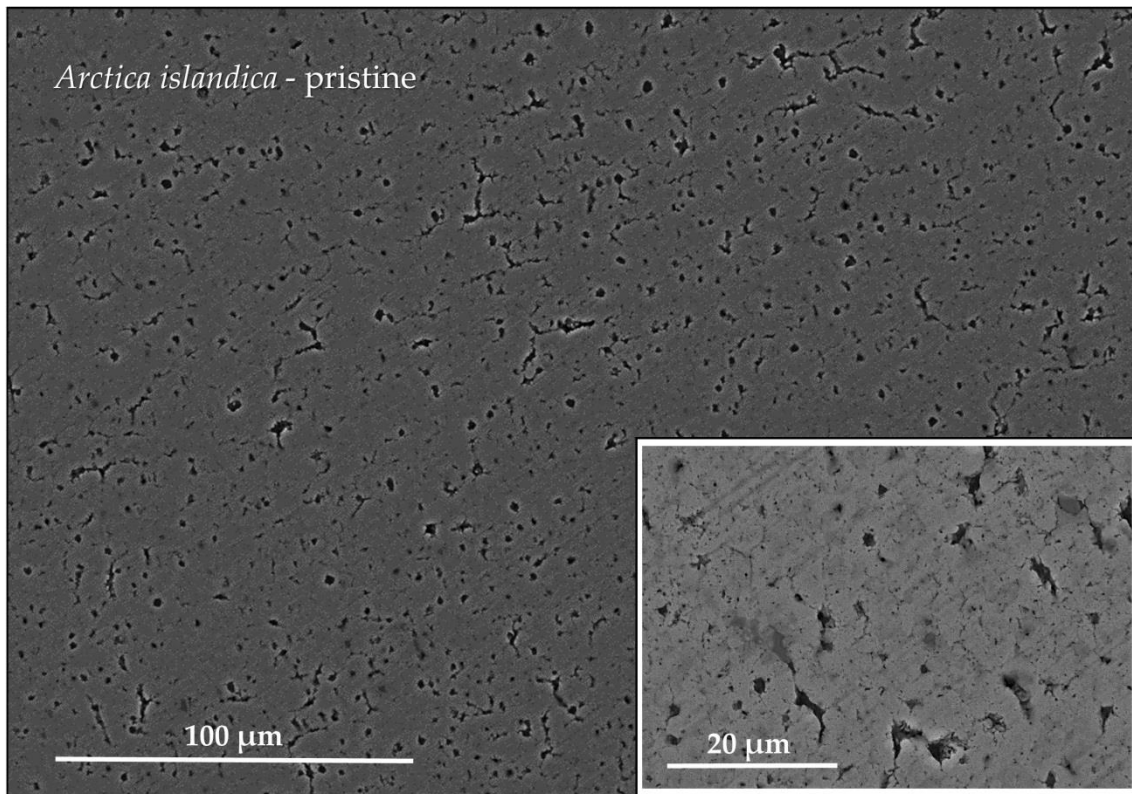
Figure 2.6-A8. FE-SEM images of the portion of *Arctica islandica* shell that is next to seawater. This part of the shell is characterized by high porosity and larger sized mineral units compared to inner shell portions next to the soft tissue of the animal.
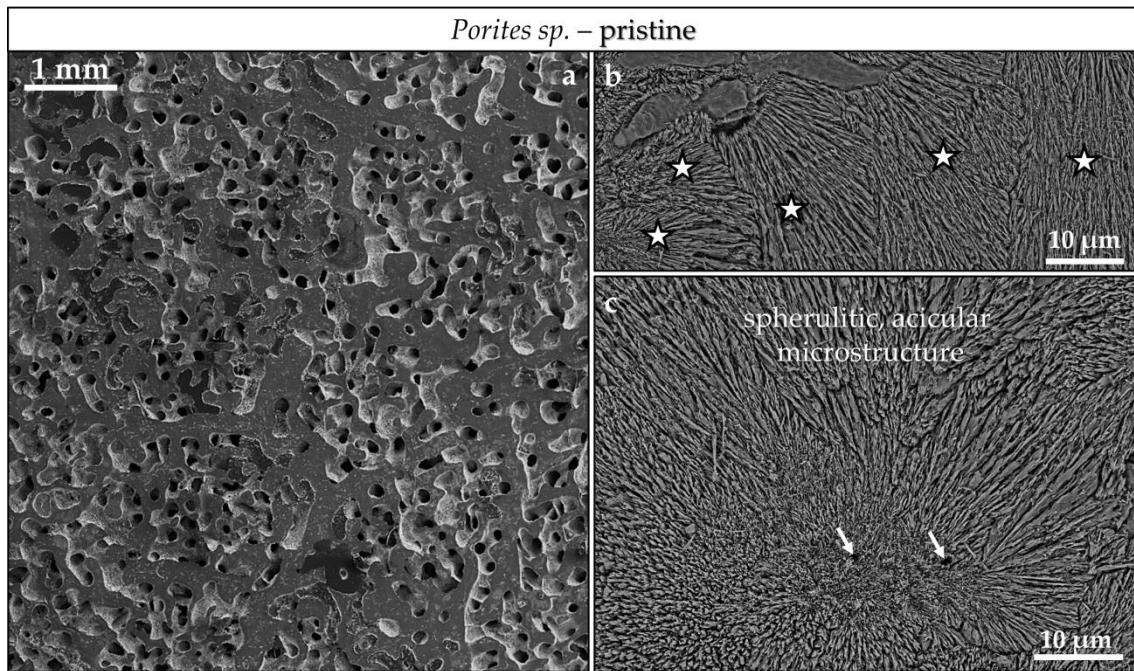
Figure 2.6-A9. FE-SEM images depicting the macro- and microstructure of the skeleton of the modern coral *Porites* sp. (a) Due to its specific architecture comprising many thin vertical and transverse elements, the skeleton of *Porites* sp. has an exceedingly high surface area. This does not imply that the skeleton is porous. The microstructure of *Porites* sp. (this study and Casella et al. 2018a) comprises a multitude of differently sized spherulites, mineral units consisting of radially arranged acicles and fibrils (b,c). These nucleate at centers of calcification (white arrows in c) and grow radially outward increasing in length until they abut the adjoining spherulite.
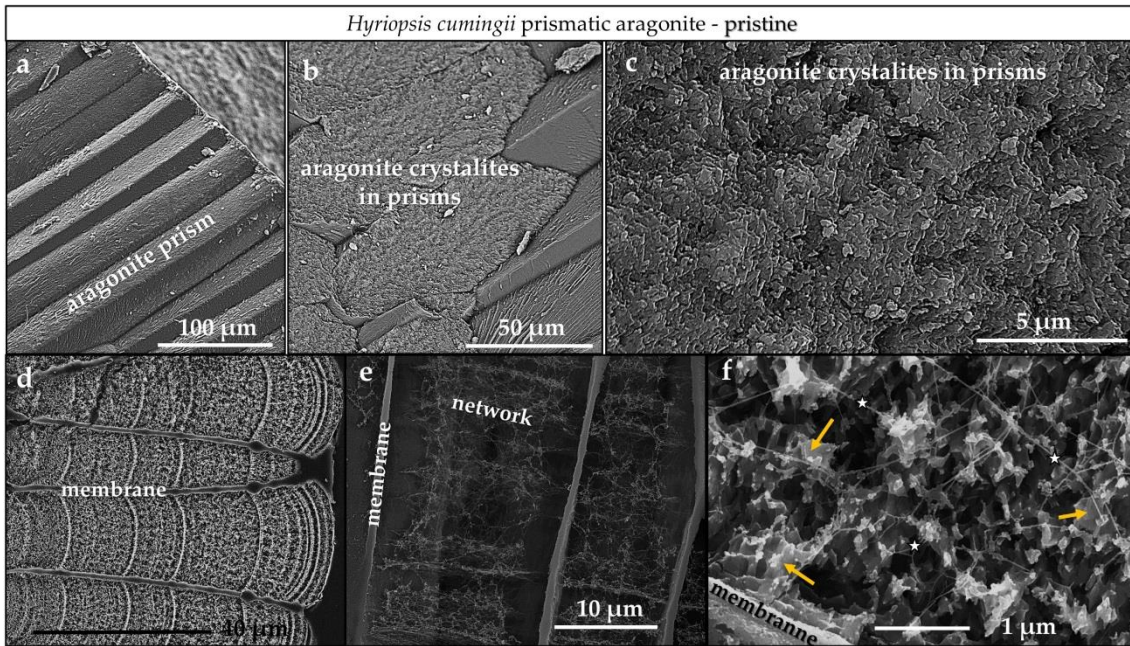
Figure 2.6-A10. FE-SEM images depicting microscale features of pristine *Hyriopsis cumingii* prismatic aragonite. (a) Aragonitic prisms comprise the outer shell layer adjacent to seawater, with all prisms being encased by organic membranes (d,e). Each prism consists of aragonite crystallites (b,c,f), embedded in an irregular network of thin biopolymer fibrils (e,f).

142
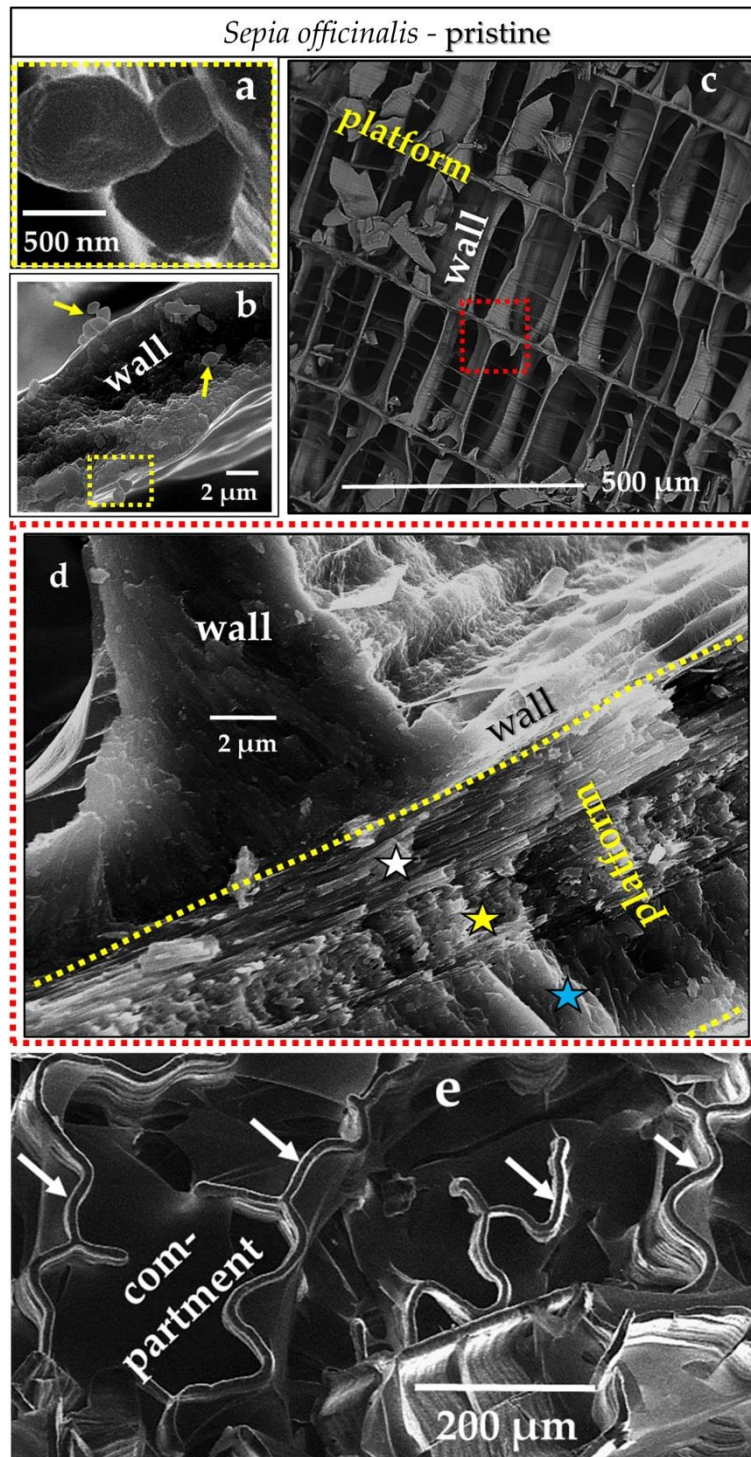
Figure 2.6-A11. FE-SEM images visualizing the macro-, micro- and nanostructure of pristine *Sepia officinalis* cuttlebone. (a) The cuttlebone is a lightweight structure comprising horizontal platforms and vertical walls, this arrangement of structural elements renders stability but also induces the formation of compartments; (b) the vertical walls (see view from above) are stabilized from implosion by vertical stop ridges consisting of thick biopolymer membranes (see (a)). Both, the walls and ridges consist of nanoparticulate aragonite (d,e). The platforms comprise arrays of aragonite rods (f), with the stacks of rods showing a well-defined twisted arrangement (white and yellow stars in (c)).
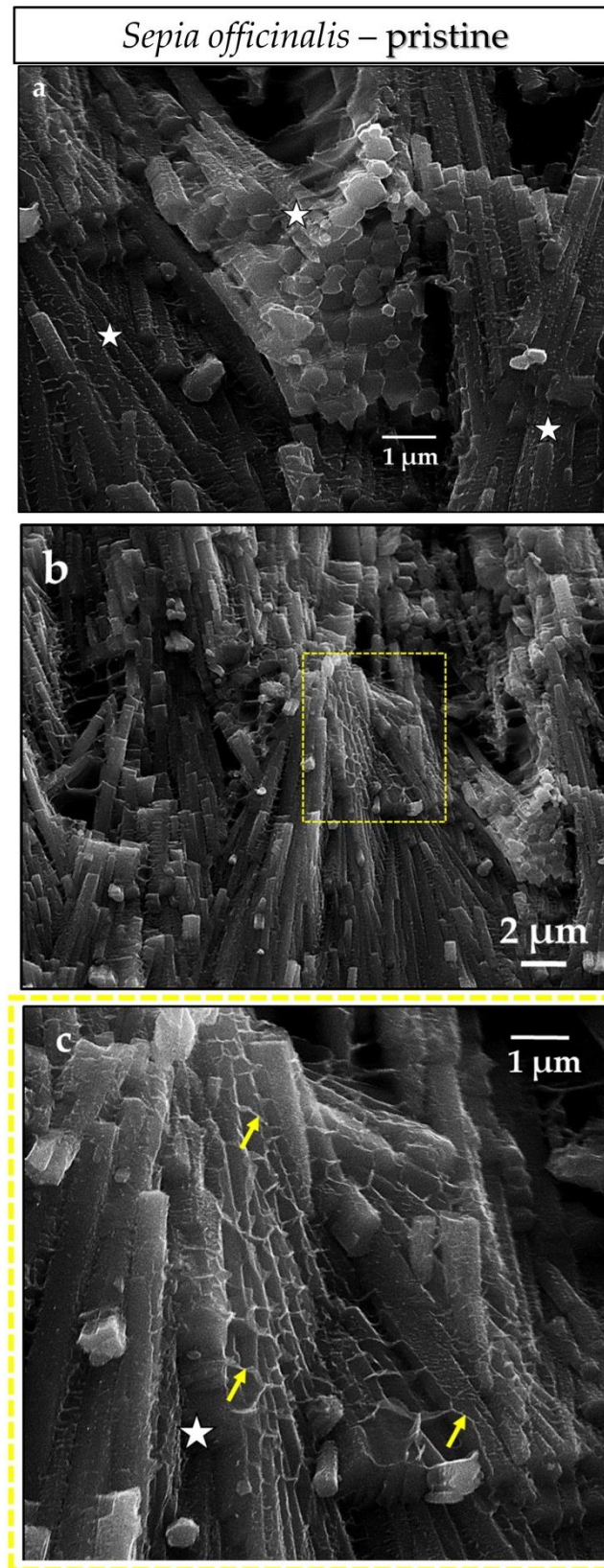
Figure 2.6-A12. FE-SEM images of arrays of aragonite rods (white stars in (a,b)) within pristine *Sepia officinalis* cuttlebone platforms. Each rod is a composite of a biopolymer matrix (or scaffold, yellow arrows in (b)) filled with aragonitic mineral.
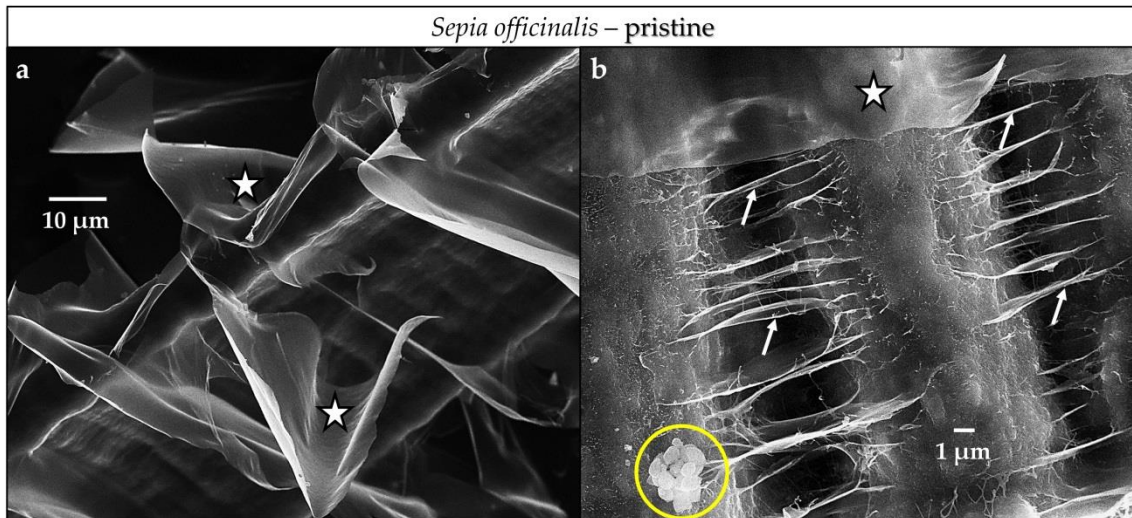
Figure 2.6-A13. FE-SEM images of biopolymers occluded within the cuttlebone of pristine *Sepia officinalis*. Thick membranes line the walls and platforms (white stars in (a,b)). A network of biopolymer films is occluded within the major structural elements of the cuttlebone, e.g., in a wall (b). An accumulation of aragonite nanoparticles constituting the skeleton appear encircled in (b).
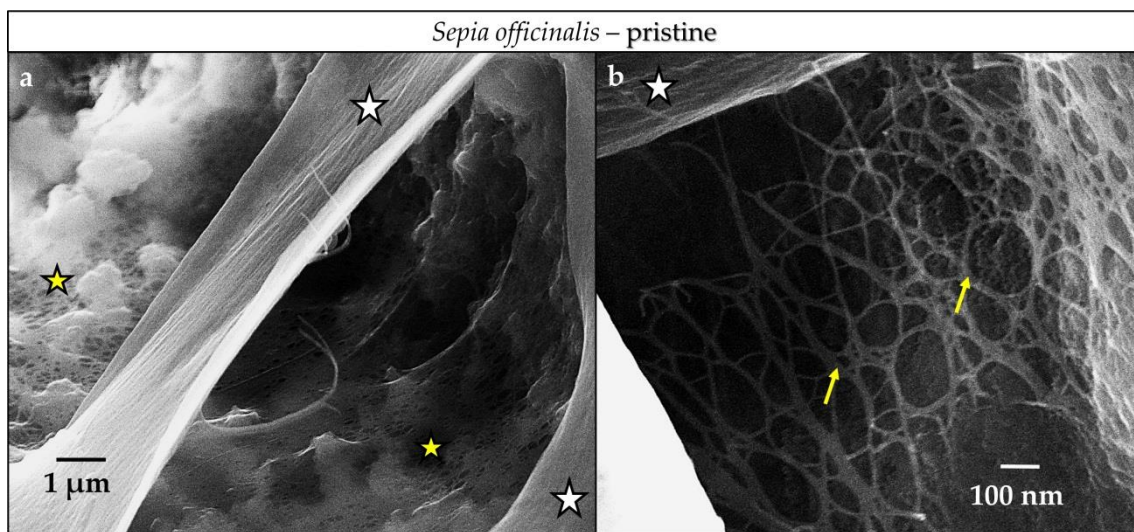
Figure 2.6-A14. FE-SEM images of biopolymer membranes (white stars in (a,b)), biopolymer networks (yellow arrows in (b)) and biopolymer foams containing nanoparticulate aragonite (yellow stars in (a)) in the cuttlebone of pristine *Sepia officinalis*.
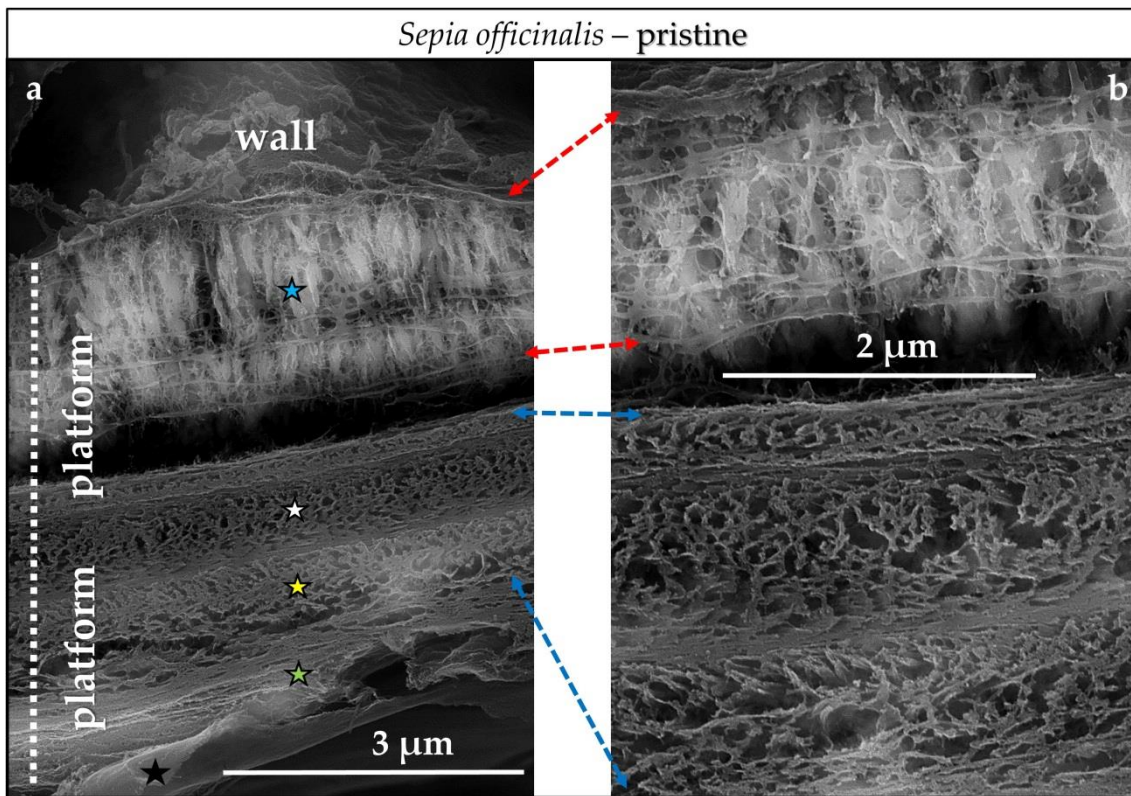
Figure 2.6-A15. FE-SEM images of demineralized *Sepia officinalis* cuttlebone showing the organic component within the skeleton that encases aragonite crystallites and individual mineral units, e.g., aragonite rods, stacks of rods. The differently coloured stars in (a) point to the different layers of a platform; see also Figure 2.6-A11d. The black star in (a) indicates the presence of the thick biopolymer membrane that lines all outer surfaces of all structural elements within the cuttlebone; (b) Organic content within a platform shown with a slightly higher magnification, relative to that given in (a).
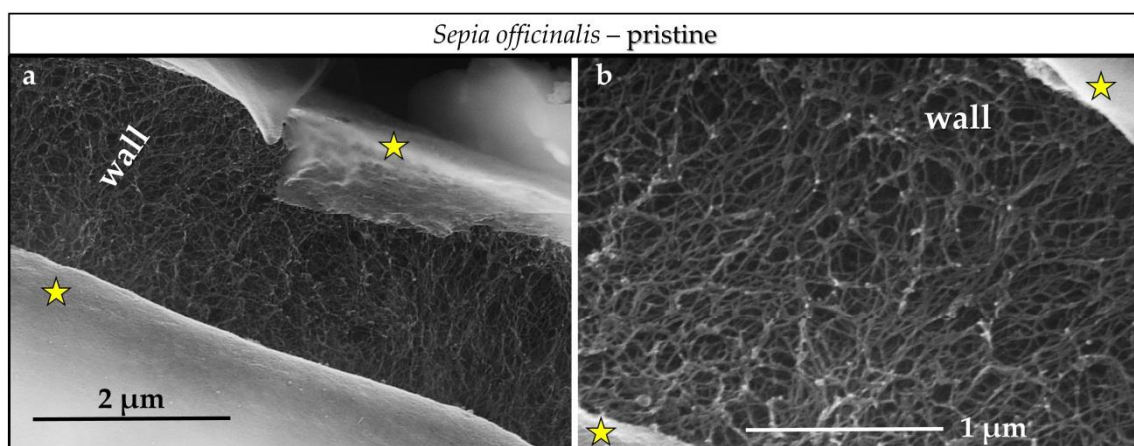
Figure 2.6-A16. FE-SEM images of the biopolymer network that is occluded within the walls of the cuttlebone of *Sepia officinalis*. Yellow stars in (a,b) point to the protruding biopolymer membranes that line all outer surfaces of all structural elements within the cuttlebone.
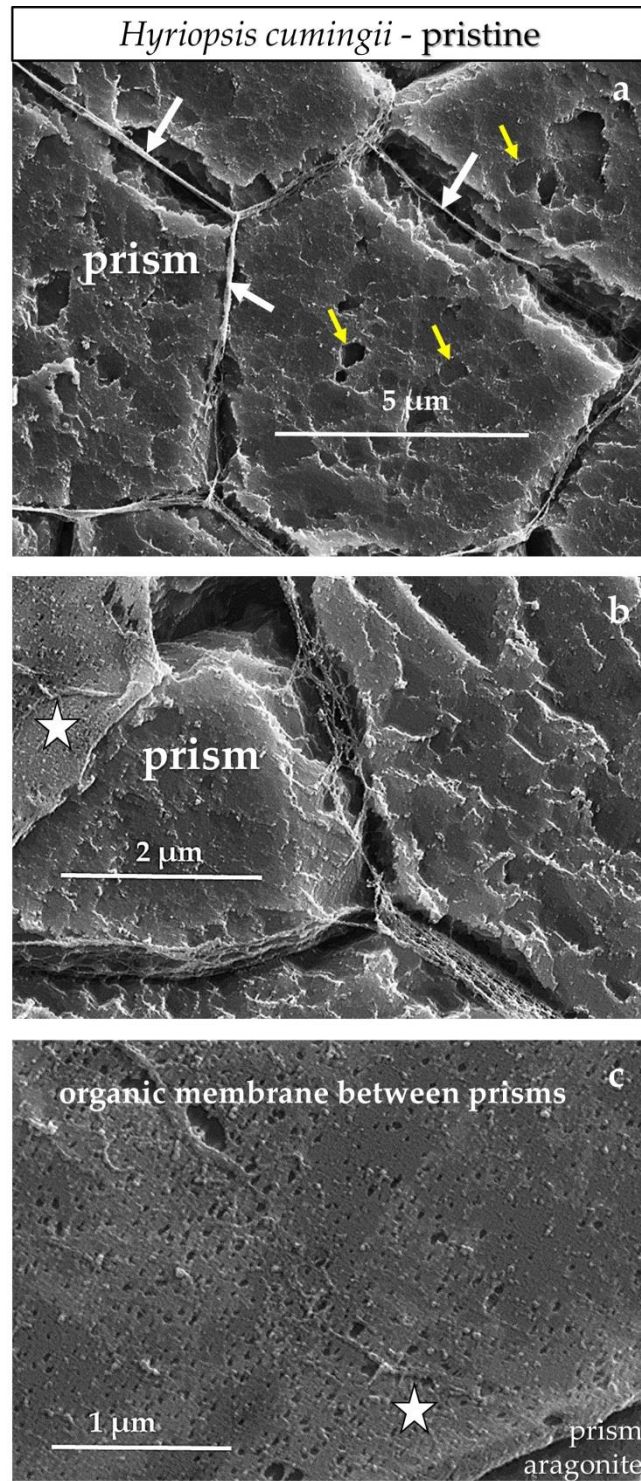
Figure 2.6-A17. FE-SEM images of etched sample surfaces showing in top view; (a,b) the assemblage of prisms with occluded biopolymer membranes (white arrows in (a), white stars in (b,c)) between them. Well visible is the porous nature of the membranes (b,c). Well visible is the internal structuring of prisms (e.g., (a)). Yellow arrows in (a) point to roundish mineral grains that are slightly misoriented relative to each other.

2.6.7 Supplementary Materials

The following are available online at http://www.mdpi.com/2075-163X/8/8/315/s1, X-ray diffractograms of all samples: *Sepia officinalis*, *H. cumingii* prismatic aragonite, *H. cumingii* nacreous aragonite, *Porites* sp., *A. islandica* inner layer, *A. islandica* outer layer, and Geologic aragonite.

3. Concluding Summary

The research presented in this thesis comprises investigations on carbonate and phosphate biominerals and biomineral mimicking synthetic composites.

Chapters 2.3-2.6 summarize studies on experimentally induced thermal reactions and both, experimentally induced and naturally occurring replacement reactions in biominerals. Chapter 2.3 focuses on the chemical and crystallographic variations in archaeological bone finds; the variations are possibly caused by substitution processes. During burial, the bone mineral is prone to diagenetic alterations caused by e.g. soil pH or humidity which can change the bioapatite lattice parameters. 65 archaeological bone finds from different species but the same archaeological site (similar burial time and soil conditions) were investigated and the deviations between their crystallographic parameters were ascribed to structural and chemical variations within the bone mineral itself which depends on crystal age, species and type of bone.

When bone finds are exposed to acidic conditions, the bioapatite is believed to dissolve and to be replaced by brushite, the more stable phase at acidic conditions. This was investigated in Chapter 2.4 by exposing fresh bovine bone to solutions with pH 4, 4.5 and 5. Within the experimental period of eight weeks, no brushite was formed.

Chapter 2.5 addresses the chemical and structural changes of bone in consequence of heat treatment. Fresh bovine bone was heated at different temperatures between 100 and 1000 °C for various periods of time. Original bone mineral is carbonated apatite with no or only minor amounts of hydroxyl ions. When heated, the carbonate content in bone mineral decreases and the hydroxyl content increases. After heating at 700 °C for 30 minutes, the bioapatite in bone reacts to hydroxylapatite which goes along with a significant crystallite growth. This process occurs mainly after all organic matter is combusted and the crystallites are in direct contact to each other. Above 800 °C the mineral buchwaldite is formed from the Na component within the bone mineral.

Chapter 2.6 covers the reaction kinetics of biological aragonite to apatite. Aragonitic biomineral samples exhibiting different microstructures were partially or fully converted into apatite in an open system. Even though all investigated specimens are composites with aragonite being the mineral component, the coral *Porites* sp., the cuttlebone *Sepia officinalis*, and the bivalves *Hyriopsis cumingii* and *Arctica islandica* showed highly distinct reaction rates. The reaction rates mainly depend on the ability of the reaction fluid to access the aragonite crystallites which directly relates to the specific biological hard tissue macro- and

microstructures. Cuttlebone *Sepia officinalis* displayed fastest conversion (almost fully converted after 24 hours) with its morphological features being preserved, whereas nacreous aragonite in *Hyriopsis cumingii* was most resistant to conversion.

Inspired by carbonate and phosphate biocomposites, biomimetic apatite and calcite composites were grown in hydrogels using the double-diffusion method and characterized (Chapters 2.1 and 2.2).

Hydrogel matrices are popular, widely used systems to mimic organic matrices in biominerals. During growth, the aggregates incorporate the hydrogel organic matrix. Parameters such as the solid content of the hydrogel and the concentration of the reagent solutions can be adjusted or protein components can be added to determine the characteristics of the biomimetic composite. Generally said, the higher the solid content the higher the hydrogel strength, whereas high reagent solution concentrations give rise to high supersaturation and therefore high growth rates. Both parameters have a strong and complex influence on mineral formation and aggregate growth.

Chapter 2.1 covers the crystallization of apatite aggregates in agarose and gelatin hydrogels with different solid contents (0.5 and 2 wt% agarose, 2.5 and 10 wt% gelatin). Compared to the counterpart experiment without protein, the protein amelotin (AMTN) promoted enhanced apatite crystallite sizes when added to the organic matrices except for agarose 2 wt%. Largest apatite crystals were obtained in gelatin 10 wt% with AMTN protein.

Chapter 2.2 handles the characterization of biomimetic calcite composites grown in agar hydrogels with different solid contents (0.5 and 2 wt%) and different reagent solution concentrations (0.1M and 0.5M). Gel distribution patterns within the aggregate are mainly determined by the reagent solution concentration, whereas the amount of incorporated hydrogel is mostly determined by the solid content of the gel. Gel incorporation into the aggregate is highest when a high gel solid content is used. Agar distribution is homogeneous when high reagent solution concentrations are used and accumulates locally at low concentrations. Aggregates grown in low solid contents show a high calcite co-orientation and are single crystal composites. At high gel solid contents, the calcite crystallites within the aggregates are less co-oriented: combined with a low reagent solution concentration, co-oriented polycrystal composites formed; combined with a high reagent solution concentration, mosaic crystal composites formed.

4. Outlook

The research presented in the course of this dissertation contributes to the understanding of biomineralisation processes and answered some questions on the thermal and replacement behaviour of biominerals with complex hierarchical structures. However, these experiments left open questions and provide new research perspectives which could cover following research topics:

1. It was shown that the balance between growth rate and hydrogel strength clearly plays a crucial role in the formation and development of calcite crystal aggregates (Chapter 2.2). The crystallization experiments on calcium carbonates in hydrogels followed a qualitative approach on the supersaturation in the double-diffusion system. In order to tune aggregate organization and to understand the factors controlling the internal micro-organization of biominerals, quantitative mass transfer modelling calculations can be conducted to determine the relationship between the solid content in the hydrogel and its transport properties. Understanding those parameters allows the fine-tuning and control of the material properties of biomimetic composites and might contribute to the design of future functional biomaterials.

2. From earlier studies (Nindiyasari et al. 2014b) it is known that the addition of Magnesium (Mg) to hydrogels can modify its strength and produces a wide variety of aggregate morphologies. Biologic calcite hard tissues can incorporate Mg up to concentrations of 45 mol% (Ma & Qi 2010). This research can be extended by using Mg-bearing hydrogels for calcite crystal growth in double-diffusion systems to mimic crystallization processes of Mg-containing calcium carbonate biominerals (Rudin 2018).

3. The influence of the amelotin (AMTN) protein on apatite (AP) crystallites in double-diffusion systems was studied by X-ray diffraction (Chapter 2.1). The next step will be to characterize the morphological features of the AP aggregates by transmission electron microscopy (TEM). Amelogenin protein self-assembly and its selective proteolytic enzyme digestion are presumed to direct the growth of apatite fibres and their organization in mammal enamel (Beniash et al. 2005). Amelogenin (AMGN) protein extracted from teeth has been proven to promote apatite formation and caused octacalcium phosphate (OCP) to grow with remarkably long crystal habits in gelatin hydrogel matrices (Taira et al. 1995, Wen et al. 2000). The combination of both, AMTN and AMGN serving as matrix molecules in hydrogel

systems and their influence on biomimetic calcium phosphate composites could be investigated in future experiments (Thümmler 2019).

4. Bone tissue shows large chemical and structural heterogeneity. The large amount of ionic substitutions and the small size of apatite crystallites facilitate the bone mineral dissolution (Wopenka & Pasteris 2005). An ongoing study shows that organic matrix and apatite crystallite characteristics strongly influence the bone mineral and dissolution behavior (Rodríguez-Navarro et al. 2019, unpublished). Further research on the dissolution and demineralization behavior of different types of bone tissues (e.g. cortical and medullary bone of various species) might provide knowledge needed to give a more complete picture of highly important processes such as bone formation and resorption during bone remodeling in vivo.

5. Structural and chemical variations within the bone mineral can be linked to crystal age, nutrition, species and type of bone (Boskey & Coleman 2010). Further specifications such as anatomical location, physical stress in vivo, and pathological conditions might influence bone mineral characteristics such as lattice parameters, crystallinity and ionic substitutions. Future research could include investigations of bones from several anatomical locations in individuals of one species with a different physical constitution (Foley 2019).

6. The skeletons of marine invertebrates exhibit unique architectures. Their special pore structures as well as their biocompatibility and biodegradability make them particularly suitable for medical tasks. To replicate their microstructures is of immediate interest e.g. in the fabrication of orthopedic prosthetic devices. Corals like *Porites* sp. or *Goniopora* sp. have a natural trabecular structure similar to that of bone. Their carbonate skeletons can be converted hydrothermally to apatite and can be used as a substitution biomaterial for bone (Damien & Revell 2004). This gives motivation to study the conversion of further coralline skeletons to AP in an open system.

Bibliography

Abbarin, N.; San Miguel, S.; Holcroft, J.; Iwasaki, K.; Ganss, B. (2015) The enamel protein amelotin is a promoter of hydroxyapatite mineralization. *J. Bone Miner. Res., 30,* 775-785.

Addadi, L.; Raz, S., Weiner, S. (2003) Taking Advantage of Disorder: Amorphous Calcium Carbonate and Its Roles in Biomineralization. *Adv. Mater., 15*, 959-970.

Altree-Williams, A.; Pring, A.; Ngothai, Y.; Brugger, J. (2015) Textural and compositional complexities resulting from coupled dissolution-reprecipitation reactions in geomaterials. *Earth-Sci. Rev., 150,* 628-651.

Asenath-Smith, E.; Li, H. Y.; Keene, E. C.; Seh, Z. W.; Estroff, L. (2012). Crystal Growth of Calcium Carbonate in Hydrogels as a Model of Biomineralization. *Adv. Funct. Mater., 22*, 2891-2914.

Avrami, M. (1939) Kinetics of Phase change. I General Theory. *J. Chem. Phys., 7,* 1103.

Avrami, M. (1940) Granulation, Phase Change, and Microstructure Kinetics of Phase Change. III. *J. Chem. Phys., 9,* 177.

Avrami, M. (1940) Kinetics of Phase change. II Transformation-Time Relations for Random Distribution of Nuclei. *J. Chem. Phys., 8,* 212.

Baig, A.A.; Fox, J.L.; Young, R.A.; Wang, Z.; Hsu, J.; Higuchi, W.I.; Chhettry, A.; Zhuang, H.; Otsuka, M. (1999) Relationships Among Carbonated Apatite Solubility, Crystallite Size, and Microstrain Parameters. *Calcif. Tissue Int., 64,* 437-449.

Ben Amara, M.; Vlasse, M.; le Flem, G.; Hagenmuller, P. (1983) Structure of the low-temperature variety of calcium sodium orthophosphate, $NaCaPO_4$. *Acta Cryst., 39,* 1483-1485.

Beniash, E.; Simmer, J.P.; Margolis, H.C. (2005) The effect of recombinant mouse amelogenins on the formation and organization of hydroxyapatite crystals in vitro. *J. Struct. Biol., 149,* 182-190.

Bennett, J.L. (1999) Thermal Alteration of Buried Bone. *J. Archaeol. Sci.,* 26, 1-8.

Berland, S.; Delattre, O.; Borzeix, S.; Catonne, Y.; Lopez, E. (2005) Nacre/bone interface changes in durable nacre endosseous implants in sheep. *Biomaterials, 26*, 2767-2773.

Berna, F.; Matthews, A.; Weiner, S. (2004) Solubilities of bone mineral from archaeological sites: the recrystallization window. *J. Archaeol. Sci., 31,* 867-882.

Bertinetti, L.; Drouet, C.; Combes, C.; Rey, C.; Tampieri, A.; Coluccia, S.; Martra, G. (2009) Surface characteristics of nanocrystalline apatites: effect of Mg surface enrichment on

morphology, surface hydration species, and cationic environments. *Langmuir, 25,* 5647-5654.

Biltz, R.M.; Pellegrino, E.D. (1983) The Composition of Recrystallized Bone Mineral. *J. Dent. Res., 62,* 1190-1195.

Bohner, M. (2010a) Design of ceramic-based cements and putties for bone graft substitution. *Eur. Cell Mater., 20,* 1-12.

Bohner, M. (2010b) Resorbable biomaterials as bone graft substitutes. *Mater. Today, 13,* 24-30.

Bonar, L.C.; Roufosse, A.H.; Sabine, W.K.; Grynpas, M.D.; Glimcher, M.J. (1983) X-ray Diffraction Studies of the Crystallinity of Bone Mineral in Newly Synthesized and Density Fractionated Bone. *Calcif. Tissue Int., 35,* 202-209.

Bonucci, E.; Graziani, G. (1975) Comparative thermogravimetric X-ray diffraction and electron microscope investigations of burnt bones from recent, ancient and prehistoric age. *Atti della accademia Nazionale dei Lincei, Rendiconti, classe die Scienze fisiche, matematiche e naturali, 59,* 517-532.

Boskey, A.; Coleman, R. (2010) Aging and Bone. *J. Dent. Res., 89,* 1333-1348.

Brubach, J.B.; Mermet, A.; Filabozzi, A.; Gerschel, A.; Roy, P. (2005) Signatures of the hydrogen bonding in the infrared bands of water. *J. Chem. Phys., 122,* 184509.

Burger, C.; Zhou, H.W.; Wang, H.; Sics, I.; Hsiao, B.S.; Chu, B.; Graham, L.; Glimcher, M.J. (2008) Lateral packing of mineral crystals in bone collagen fibrils. *Biophys. J., 95,* 1985-1992.

Busch, S.; Dolhaine, H.; DuChesne, A.; Heinz, S.; Hochrein, O.; Laeri, F.; Podebrad, O.; Vietze, U.; Weiland, T.; Kniep, R. (1999) Biomimetic Morphogenesis of Fluorapatite-Gelatin Composites: Fractal Growth, the Question of Intrinsic Electric Fields, Core/Shell Assemblies, Hollow Spheres and Reorganization of Denatured Collagen. *Eur. J. Inorg. Chem., 1999,* 1643-1653.

Cartwright, J.H.; Checa, A.G.; Gale, J.D.; Gebauer, D.; Sainz-Diaz, C.I. (2012) Calcium carbonate polyamorphism and its role in biomineralization: how many amorphous calcium carbonates are there? *Angew. Chem. Int. Ed. Engl., 51,* 11960-11970.

Casella, L.A.; Griesshaber, E.; Yin, X.; Ziegler, A.; Mavromatis, V.; Müller, D.; Ritter, A.C.; Hippler, D.; Harper, E.M.; Dietzel, M.; Immenhauser, A.; Schöne, B. R.; Angiolini, L.; Schmahl, W. W. (2017) Experimental diagenesis: Insights into aragonite to calcite conversion *arctica islandica* shells by hydrothermal treatment. *Biogeosciences, 14,* 1461-1492.

Casella, L.A.; He, S.; Griesshaber, E.; Fernández-Díaz, L.; Greiner, M.; Harper, E.M.; Jackson, D.J.; Ziegler, A.; Mavromatis, V.; Dietzel, M.; Eisenhauer, A.; Veintemillas-Verdaguer, S.; Brand, U.; Schmahl, W.W. (2018a) Hydrothermal alteration of aragonitic biocarbonates: assessment of micro- and nanostructural dissolution–reprecipitation and constraints of diagenetic overprint from quantitative statistical grain-area analysis. *Biogeosciences, 15,* 7451-7484.

Casella, L.A.; Griesshaber, E.; Simonet Roda, M. d. M; Ziegler, A.; Mavromatis, V.; Henkel, D.; Laudien, J.; Häussermann, V.; Neuser, R.D.; Angiolini, L.; Dietzel, M.; Eisenhauer, A.; Immenhauser, A.; Brand, U.; and Schmahl, W.W. (2018b) Micro- and nanostructures reflect the degree of diagenetic alteration in modern and fossil brachiopod shell calcite: a multi-analytical screening approach (CL, FE-SEM, AFM, EBSD). *Palaeogeogr. Palaeoclimat. Palaeoecol., 502,* 13-30.

Casella, L.A; Simonet Roda, M. d. M.; Angiolini, L.; Ziegler, A.; Schmahl, W.W.; Brand, U.; Griesshaber, E. (2018c) Archival biogenic micro- and nanostructure data analysis: signatures of diagenetic systems. *Data in Brief, 19,* 299-311.

Cazalbou, S.; Combes, C.; Eichert, D.; Rey, C.; Glimcher, M. (2004) Poorly crystalline apatites: evolution and maturation in vitro and in vivo. *J. Bone Miner. Metab., 22,* 310-317.

Cazalbou, S.; Eichert, D.; Ranz, X.; Drouet, C.; Combes, C.; Harmand, M.F.; Rey, C. (2005) Ion exchanges in apatites for biomedical applications. *J. Mater. Sci. Mater. Med., 16,* 405-409.

Checa, A.G.; Marcías-Sánchez, E.; Harper, E.M.; Cartwright, J.H. (2016) Organic membranes determine the pattern of the columnar prismatic layer of mollusk shells. *Proc. R. Soc. B, 283.*

Checa, A. (2018) Physical and Biological Determinants of the Fabrication of Molluscan Shell Microstructures. *Front. Mar. Sci., 5.*

Chernov, A.A. (1984) *Modern Crystallography III: Crystal Growth.* Springer: Berlin, Heidelberg, New York, Tokyo.

Cho, J.S.; Kim, H.S.; Um, S.H.; Rhee, S.H. (2013) Preparation of a novel anorganic bovine bone xenograft with enhanced bioactivity and osteoconductivity. *J. Biomed. Mater. Res. B 101B,* 855-869.

Clarke, S.A.; Choi, S.Y.; McKechnie, M.; Burke, G.; Dunne, N.; Walker, G.; Cunningham, E.; Buchanan, F. (2016) Osteogenic cell response to 3-D hydroxyapatite scaffolds

developed via replication of natural marine sponges. *J. Mater. Sci. Mater. Med., 27,* 1-11.

Cölfen, H.; Antonietti, M. (2008a) Mesocrystals and nonclassical crystallization. John Wiley & Sonst, Ltd: The Atrium, Southern Gate, Chichester, England.

Cölfen, H.; Antonietti, M. (2008b) Mesocrystals: Inorganic superstructures made by highly parallel crystallization and controlled alignment. *Angew. Chem. Int. Ed., 44,* 5576-5591.

Cuesta Mayorga, I.; Astilleros, J.M.; Fernández-Díaz, L.; Morales, J.; Prieto, M.; Roncal-Herrero, T.; Benning, L.G. (2018) Epitactic Overgrowths of Calcite ($CaCO_3$) on Anhydrite ($CaSO_4$) Cleavage Surfaces. *Cryst. Growth Des., 18,* 1666-1675.

Currey J.D.; Zioupos, P.; Davies, P.; Casino, A. (2001) Mechanical properties of nacre and highly mineralized bone. *Proc. R. Soc. Lond. B, 268,* 107-111.

Currey J.D. 2002. *Bones: Structure and Mechanics.* Princeton: Princeton University Press.

Damien, E.; Revell, P.A. (2004) Coralline hydroxyapatite bone graft substitute: A review of experimental studies and biomedical applications. *J. Appl. Biomater. Biomech., 2,* 65-73.

Darwin, C.G. (1922) XCII. The reflexion of X-rays from imperfect crystals. *Philos. Mag. 6, 43*, 800-829.

De Yoreo, J.J.; Vekilov, P.G. (2003) Principles of crystal nucleation and growth. *Rev. Mineral. Geochem., 54*, 57-93.

Destainville, A.; Champion, E.; Bernache-Assollant, D.; Laborde, E. (2003) Synthesis, characterization and thermal behavior of apatitic tricalcium phosphate. *Mater. Chem. Phys., 80,* 269-277.

Dinnebier, R.E.; Billinge, S.J.L. (2008) *Powder diffraction: Theory and practice*. Royal Society of Chemistry: Cambridge, pp. 300-303.

Dorozhkin, S.V. (2007) Calcium orthophosphates. *J. Mater. Sci., 42,* 1061-1095

Dorvee, J.R.; Boskey, A.L.; Estroff, L.A. (2012) Rediscovering Hydrogel-Based Double-Diffusion Systems for Studying Biomineralization. *Cryst. Eng. Comm.*, *14,* 5681-5700.

Driessens, F.C.M.; Verbeeck, R.M.H. (1990) *Biominerals*. CRC Press: Boca Raton, Florida.

Dunlop, J.M. (1978) Traffic light discoloration in cremated bones. *Med. Sci. Law, 18,* 163-173.

Eichert, D.; Sfihi, H.; Combes, C.; Rey, C. (2004) Specific characteristics of wet nanocrystalline apatites. Consequences on biomaterials and bone tissue. *Key Eng. Mater., 254-256,* 927-930.

Eichert, D.; Combes, C.; Drouet, C.; Rey, C. (2005) Formation and evolution of hydrated surface layers of apatites. *Key Eng. Mater., 284-286,* 3-6.

El Feki, H.; Rey, C.; Vignoles, M. (1991) Carbonate ions in apatites: Infrared investigations in the v_4 CO_3 domain. *Calcif. Tiss. Int., 49,* 269-274.

Ellingham, S.T.D.; Thompson, T.J.U.; Islam, M. (2015) Thermogravimetric analysis of porperty changes and weight loss in incinerated bone. *Palaeogeogr. Palaeoclimatol. Palaeoecol., 438,* 239-244.

Elliott, J.C. (1994) *Structure and Chemistry of the Apatites and Other Calcium Orthophosphates.* Elsevier: Amsterdam.

Elliott, J.C. (2002) Calcium Phosphate Biominerals. *Rev. Mineral. Geochem., 48,* 427-453.

Enzo, S.; Bazzoni, M.; Mazzarello, V.; Piga, G.; Bandiera, P.; Melis, P. (2007) A study by thermal treatment and X-ray powder diffraction on burnt fragmented bones from tombs II, IV and IX belonging to the hypogeic necropolis of "Sa Figu" near Ittiri, Sassari (Sardinia, Italy). *J. Archaeol. Sci., 34,* 1731-1737.

Eppell, S.W.; Tong, W.; Katz, J.L.; Kuhn, L.; Glimcher, M.J. (2001) Shape and size of isolated bone mineralites measured unding atomic force microscopy. *J. Orthop. Res., 19,* 1027-1034.

Epple, M. (2003) *Biomaterialien und Biomineralisation: eine Einführung für Naturwissenschaftler, Mediziner und Ingenieure.* Teubner: Stuttgart.

Estroff, L.A.; Addadi, L.; Weiner, S.; Hamilton, A.D. (2004) An organic hydrogel as a matrix for the growth of calcite crystals. *Org. Biomol. Chem., 2,* 137-141.

Etok, S.E.; Valsami-Jones, E.; Wess, T.J.; Hiller, J.C.; Maxwell, C.A.; Rogers, K.D.; Manning, D.A.C.; White, M.L.; Lopez-Capel, E.; Collins, M.J.; Buckley, M.; Penkman, K.E.H.; Woodgate, S.L. (2007) Structural and chemical changes of thermally treated bone apatite. *J. Mater. Sci., 42,* 9807-9816.

Eysel, W.; Roy, D.M. (1975) Topotactic reaction of aragonite to hydroxyapatite. *Z. Kristallogr. Cryst. Mater., 141,* 11-24.

Fernández-Díaz, L.; Pina, C. M.; Astilleros, J.M.; Sánchez-Pastor, N. (2009) The carbonatation of gypsum: Pathways and pseudomorph formation. *Am. Mineral., 94,* 1223-1234.

Fernández-Díaz, L.; Putnis, A.; Prieto, M.; Putnis, C.V. (1996) The role of magnesium in the crystallization of calcite and aragonite in a porous medium. *J. Sediment. Res.,66,* 482-491.

Fernández-González, A.; Prieto, M.; Putnis, A.; Lopez Andres, S. (1999) Concentric zoning patterns in crystallizing (Cd,Ca)CO$_3$ solid solutions from aqueous solutions. *Mineral. Mag., 63*, 331-343.

Fleet, M.-E. (2009) Infrared spectra of carbonate apatites: ν_2-Region bands. *Biomaterials, 30*, 1473-1481.

Fleet, M. (2015) *Carbonated Hydroxyapatite: Materials, Synthesis, and Applications.* Pan Stanford: New York.

Foley, B. (2019) Physical and anatomical variation of mammalian bone bioapatite structure and composition. Master Thesis, Ludwig-Maximilians-Universität München, to be submitted in September 2019.

Fratzl, P.; Gupta, H.S.; Paschalis, E.P.; Roschger, P. (2004) Structure and mechanical quality of the collagen-mineral nano-composite in bone. *J. Mater. Chem., 14,* 2115-2123.

Freyer, D. and Voigt, W. (2003) Crystallization and phase stability of CaSO$_4$ and CaSO$_4$-Based Salts. *Monatsh. Chem., 134,* 693-719.

Frost, R.L.; Xi, Y.; Scholz, R.; López, A.; Belotti, F.M. (2013) Vibrational spectroscopic characterization of the phosphate mineral hureaulite − (Mn, Fe)$_5$(PO$_4$)$_2$(HPO$_4$)$_2$ · 4(H$_2$O). *Vib. Spectrosc., 66,* 69-75.

Fu, K.; Xu, Q.; Czernuszka, J.; Triffitt, J.T.; Xia, Z. (2013) Characterization of a biodegradable coralline hydroxyapatite/calcium carbonate composite and its clinical implementation. *Biomed. Mater., 8,* 065007.

Galeano, S.; García-Lorenzo, M.L. (2014) Bone Mineral Change During Experimental Calcination: An X-ray Diffraction Study. *J. Forensic. Sci., 59,* 1602-1606.

Gaspard, M.; Marin, F.; Guichard, N.; Morel, S.; Alcaraz, G.; Luquet, G. (2008) Shell matrices of recent rhynchonelliform brachiopods: Microstructures and glycosylation studies. *Trans. R. Soc. Edinburgh, 98,* 415-424.

Genin, G.M.; Kent, A.; Birman, V.; Wopenka, B.; Pasteris, J.D.; Marquez, P.J.; Thomopoulos, S. (2009) Functional grading of mineral and collagen in the attachment of tendon to bone. *Biophys. J., 97,* 976-985.

Gernaey, A.M.; Waite, E.R.; Collins, M.F.; Craig, O.E.; Sokol, R.J. (2001) Survival and interpretation of archaeological proteins. In Brothwell, D.R.; Pollard, A.M. (Eds.) *Handbook of archaeological science.* Wiley: Chichester, pp. 323-329.

Gibbs, J.W.; Bumstead, H.A.; Longley, W.R. (1928) The collected works of J. Willard Gibbs. Vol. 1., Thermodynamics. Longmans, Green and Company: New York, London.

Glimcher, M.J. (1998) The nature of the mineral phase in bone: Biological and clinical implications. In Avioli, L.V.; Krane, S.M. (Eds.) *Metabolic Bone Disease and Clinically Related Disroders* (Third Edition). Academic Press: San Diego.

Glimcher, M.J. (2006) Bone: Nature of the Calcium Phosphate Crystals and Cellular, Structural, and Physical Chemical Mechanisms in Their Formation. *Rev. Mineral. Geochem., 64,* 223-282.

Goetz, A. J.; Steinmetz, D. R.; Griesshaber, E.; Zaefferer, S.; Raabe, D.; Kelm, K.; Irsen, S.; Sehrbrock, A.; Schmahl, W.W. (2011) Interdigitating biocalcite dendrites form a 3-D jigsaw structure in brachiopod shells. *Acta Biomater., 7,* 2237-2243.

Goldberg, M.; Septier, D.; Lécolle, S.; Chardin, H.; Quintana, M.A.; Acevedo, A.C.; Gafni, G.; Dillouya, D.; Vermelin, L.; Thonemann, B. (1995) Dental mineralization. *Int. J. Dev. Biol., 39,* 93-110.

Gonçalves, M.A.; Prieto, M. (2014) Development of Compositional Patterns during the Growth of Solid Solutions from Aqueous Solutions: A Cellular Automaton Simulation. *Cryst. Growth Des., 14*, 2782-2793.

González-Díaz, P.F.; Hidalgo, A. (1976) Infrared spectra of calcium apatites. *Spectrochim. Acta A, 32*, 631-635.

González-Díaz, P.F.; Santos, M. (1977) On the hydroxyl ions in apatites. *J. Solid State Chem., 22,* 193-199.

Green, D.W.; Ben-Nissan, B.; Yoon, K.S.; Milthorpe, B.; Jung, H.-S. (2017) Natural and Synthetic Coral Biomineralization for Human Bone Revitalization. *Trends. Biotechnol., 35,* 43-54.

Greiner, M.; Kocsis, B.; Heinig, M.F.; Mayer, K.; Toncala, A.; Grupe, G.; Schmahl, W.W. (2018a) Experimental Cremation of Bone: Crystallite Size and Lattice Parameter Evolution. In Endo, K.; Kogure, T.; Nagasawa, H. (Eds.); *Biomineralization: From Molecular and Nano-structural Analyses to Environmental Science.* Springer: Singapore.

Greiner, M.; Yin, X.; Fernández-Díaz, L.; Griesshaber, E.; Weitzel, F.; Ziegler, A.; Veintemillas-Verdaguer, S.; Schmahl, W.W. (2018b) Combined influence of reagent concentrations and agar hydrogel strength on the formation of biomimetic hydrogel-calcite composites. *Cryst. Growth Des., 18,* 1401-1414.

Greiner, M.; Rodríguez-Navarro, A.; Heinig, M.F.; Mayer, K.; Kocsis, B.; Göhring, A.; Toncala, A.; Grupe, G.; Schmahl, W.W. (2019) Bone Incineration: An Experimental

Study on Mineral Structure, Colour and Crystalline State. *J. Archaeol. Sci Rep., 25,* 507-518.

Griesshaber, E.; Schmahl, W.W.; Ubhi, H.S.; Huber, J.; Nindiyasari, F.; Maier, B.; Ziegler, A. (2013) Homoepitaxial meso- and microscale crystal co-orientation and organic matrix network structure in mytilus edulis nacre and calcite. *Acta Biomaterialia, 9,* 9492-9502.

Griesshaber, E.; Yin X.; Ziegler, A.; Kelm, K.; Checa, A.; Eisenhauer, A.; Schmahl, W.W. (2018) Patterns of mineral organization in carbonate biological hard materials. In: Heuss-Aßbichler, S.; Amthauer, G., John, M. (Eds.); *Highlights in Applied Mineralogy.* De Gruyter: Berlin, Boston, pp. 344.

Grunenwald, A.; Keyser, C.; Sautereau, A.M.; Crubezy, E.; Ludes, B.; Drouet, C. (2014) Revisiting carbonate quantification in apatite (bio)minerals: a validated FTIR methodology. *J. Archaeol. Sci., 49,* 134-141.

Grupe, G.; Harbeck, M.; McGlynn, G.C. (2015) *Prähistorische Anthropologie.* Springer: Berlin.

Grupe, G.; Grigat, A.; McGlynn, G.C. (2017) *Across the Alps in Prehistory.* Springer International Publishing, p. 75-104.

Habraken, W.; Habibovic, P.; Epple, M; Bohner, M. (2016) Calcium phosphates in biomedical applications: materials for the future? *Mater. Today, 19,* 69-87.

Han, J.K.; Song, H.Y. (2006) Synthesis of high purity nano-sized hydroxyapatite powder by microwave-hydrothermal method. *Mater. Chem. Phys., 99,* 235-239.

Hansson, K.M.; Samuelsson, J.; Tullin, C.; Åmand, L.E. (2004) Formation of HNCO, HCN and NH_3 from the pyrolysis of bark and nitrogen-containing model compounds. *Combust. Flame, 137,* 265-277.

Harbeck, M.; Schleuder, R.; Schneider, J.; Wiechmann, I.; Schmahl, W.W.; Grupe, G. (2011) Research potential and limitations of trace analyses of cremated remains. *Forensic Sci. Int., 204,* 191-200.

Hedges, R.E.M. (2002) Bone Diagenesis: An Overview of Processes. *Archaeometry, 44,* 319-328.

Heijnen, W.M.M. (1985) The morphology of gel grown calcite. *N. Jb. Miner. Mh., 8,* 357-371.

Heinemann, F.; Launspach, M.; Gries, K.; Fritz, M. (2011) Gastropod nacre: structure, properties and growth-biological, chemical and physical basics. *Biophys. Chem., 153,* 126-1253.

Henisch, H.K. (1988) *Crystals in Gels and Liesegang Rings*. Cambridge University Press: Cambridge.

Herrmann, B. (1977) On histological investigations of cremated human remains. *J. Hum. Evol., 6,* 101-103.

Herrmann, B.; Newesely, H. (1982) Dekompositionsvorgänge des Knochens unter langer Liegezeit 1. Die mineralische Phase. *Anthropol. Anz., 40,* 19-31.

Hiller, J.C.; Thompson, T.J.U.; Evison, M.P.; Chamberlain, A.T.; Wess, T.J. (2003) Bone mineral change during experimental heating: an X-ray scattering investigation. *Biomaterials, 24,* 5091-5097.

Holcomb, D.W.; Young, R.A. (1980) Thermal decomposition of human tooth enamel. *Calcif. Tissue Int., 31,* 189-201.

Holden, J.L.; Clement, J.G.; Phakey, P.P. (1995) Age and temperature related changes to the ultrastructure and composition of human bone mineral. *J. Bone Miner. Res., 10,* 1400-1409.

Huang, Y.X.; Buder, J.; Cardoso-Gil, R.; Prots, Y.; Carrillo-Cabrera, W.; Simon, P.; Kniep, R. (2008) Shape development and structure of a complex (otoconia-like?) calcite-gelatine composite. *Angew. Chem. Int. Ed., 47*, 8280-8284.

Huber, J.; Fabritius, H.O.; Griesshaber, E.; Ziegler, A. (2014) Function-related adaptations of ultrastructure, mineral phase distribution and mechanical properties in the incisive cuticle of mandibles of Porcellio scaber Latreille, 1804. *J. Struct. Biol., 188,* 1-15.

Huber, J.; Griesshaber, E.; Nindiyasari, F.; Schmahl, W.W.; Ziegler, A. (2015) Functionalization of biomineral reinforcement in crustacean cuticle: calcite orientation in the partes incisivae of the mandibles of Porcellio scaber and the supralittoral species Tylos europaeus (Oniscidea, Isopoda). *J. Struct. Biol., 190,* 173-191

Hull, D. (1975) *Introduction to Dislocations*. Pergamon Press GmbH: Kronberg-Taunus.

Ikoma, T.; Yamazaki, A. (1999) Preparation and Structure Refinement of Monoclinic Hydroxyapatite. *J. Solid State Chem., 144,* 272-276.

Jarosch, D.; Heger, G. (1986) Neutron diffraction refinement of the crystal structure of aragonite. *Tschermaks Mineral. Petrogr. Mitt., 35,* 127-131.

Kamhi, S.R. (1963) On the structure of vaterite, $CaCO_3$ Locality: Synthetic. *Acta Crystallogr., 16*, 770-772.

Kannan, S.; Rocha, J.H.G.; Agathopoulos, S.; Ferreira, J.M.F. (2007) Fluorine-substituted hydroxyapatite scaffolds hydrothermally grown from aragonitic cuttlefish bones. *Acta Biomater., 3,* 243-249.

Kashchiev, D. (2000) *Nucleation: Basic Theory with Applications.* Butterworth-Heinemann: Oxford, United Kingdom.

Kasioptas, A.; Geisler, T.; Putnis, C.V.; Perdikouri, C.; Putnis, A. (2010) Crystal growth of apatite by replacement of an aragonite precursor. *J. Cryst. Growth, 312,* 2431-2440.

Kasioptas, A.; Geisler, T. (2011) Polycrystalline apatite synthesized by hydrothermal replacement of calcium carbonate. *Geochim Cosmochim Acta, 75,* 3486-3500.

Katsikopoulos, D.; Fernández-González, Á.; Prieto, A.C.; Prieto, M. (2008) Co-crystallization of Co(II) with calcite: Implications for the mobility of cobalt in aqueous environments. *Chem. Geol., 254*, 87-100.

Katsikopoulos, D.; Fernández-González, Á.; Prieto, M. (2009) Precipitation and mixing properties of the "disordered" $(Mn,Ca)CO_3$ solid solution. *Geochim. Cosmochim. Acta, 73*, 6147-6161.

Kay, M.I.; Young, R.A.; Posner, A.S. (1964) Crystal Structure of Hydroxyapatite. *Nature, 204,* 1050-1052.

Kim, H.M.; Rey, C.; Glimcher, M.J. (1995) Isolation of calcium-phosphate crystals of bone by nonaqueous methods at low temperature. *J. Bone Miner. Res., 10,* 1589-1601.

Kim, Y.Y.; Ribeiro, L.; Maillot, F.; Ward, O.; Eichhorn, S.J.; Meldrum, F.C. (2010) Bio-Inspired Synthesis and Mechanical Properties of Calcite-Polymer Particle Composites. *Adv. Mater., 22*, 2082-2086.

Kim, Y.Y.; Ganesan, K.; Yang, P.; Kulak, A.N.; Borukhin, S.; Pechook, S.; Ribeiro, L.; Kroger, R.; Eichhorn, S.J.; Armes, S.P.; Pokroy, B.; Meldrum, F.C. (2011) An artificial biomineral formed by incorporation of copolymer micelles in calcite crystals. *Nat. Mater., 10*, 890-896.

Kim, Y.Y.; Schenk, A.S.; Walsh, D.; Kulak, A.N.; Cespedes, O.; Meldrum, F.C. (2014) Bio-inspired formation of functional calcite/metal oxide nanoparticle composites. *Nanoscale, 6*, 852-859.

Kim, Y.Y.; Carloni, J.D.; Demarchi, B.; Sparks, D.; Reid, D.G.; Kunitake, M.E.; Tang, C.C.; Duer, M.J.; Freeman, C.L.; Pokroy, B.; Penkman, K.; Harding, J.H.; Estroff, L.A.; Baker, S.P.; Meldrum, F.C. (2016) Tuning hardness in calcite by incorporation of amino acids. *Nat. Mater., 15*, 903-910.

Kniep, R.; Busch, S. (1996) Biomimetic Growth and Self-Assembly of Fluorapatite Aggregates by Diffusion into Denatured Collagen Matrices. *Angew. Chem. Int. Ed., 35,* 2624-2626.

Knoll, A.H. (2003) Biomineralization and Evolutionary History. *Rev. Mineral. Geochem., 54,* 329-356.

Kossel, W. (1927) Zur Theorie des Kristallwachstums. *Nachr. Ges. Wiss. Göttingen, 2,* 135-145.

Lalzawmliana, V.; Anand, A.; Mukherjee, P.; Chaudhuri, S.; Kundu, B.; Nandi, S.K.; Thakur, N.L. (2019) Marine organisms as a source of natural matrix for bone tissue engineering. *Ceram. Int., 45,* 1469-1481.

Landis, W.J.; Jacquet, R. (2013) Association of calcium and phosphate ions with collagen in the mineralization of vertebrate tissues. *Calcif. Tissue Int., 93,* 329-337.

Lebon, M.; Reiche, I.; Frohlich, F.; Bahain, J.J.; Falgueres, C. (2008) Characterization of archaeological burnt bones: contribution of a new analytical protocol based on derivative FTIR spectroscopy and curve fitting of the v_1v_3 PO_4 domain. *Anal. Bioanal. Chem., 392,* 1479-1488.

Lebon, M.; Reiche, I.; Bahain, J.J.; Chadefaux, C.; Moigne, A.M.; Fröhlich, F.; Sémah, F.; Schwarcz, H.P.; Falguères, C. (2010) New parameters for the characterization of diagenetic alterations and heat-induced chagnes of fossil bone mineral using Fourier transform infrared spectrometry. *J. Archaeol. Sci., 37,* 2265-2276.

LeGeros, R.Z. (1981) Apatites in biological systems. *Prog. Cryst. Growth & Charact., 4,* 1-45.

LeGeros, R.Z. (1991) *Calcium Phosphates in Oral Biology and Medicine*. Karger: Basel.

LeGeros, R.Z.; Trautz, O.R.; Klein, E.; LeGeros, J.P. (1969) Two types of carbonate substitution in the apatite structure. *Experientia, 25,* 5-7.

Levi-Kalisman, Y.; Falini, G.; Addadi, L.; Weiner, S. (2001) Structure of the nacreous organic matrix of a bivalve mollusk shell examined in the hydrated state using cryo-TEM. *J. Struct. Biol., 135,* 8-17.

Li, H.; Estroff, L.A. (2007) Porous calcite single crystals grown from a hydrogel medium. *Cryst. Eng. Comm., 9,* 1153-1155.

Li, H.; Estroff, L.A. (2009) Calcite Growth in Hydrogels: Assessing the Mechanism of Polymer-Network Incorporation into Single Crystals. *Adv. Mater., 21,* 470-473.

Li, H.; Fujiki, Y.; Sada, K.; Estroff, L.A. (2011) Gel incorporation inside of organic single crystals grown in agarose hydrogels. *Cryst. Eng. Comm., 13,* 1060-1062.

Lim, J.J. (1975) Thermogravimetric analysis of human femur bone. *J. Biol. Phys., 3,* 111-129.

Lippmann, F. (1973) Sedimentary Carbonate Minerals. Springer Verlag: Berlin Heidelberg.

Loong, C.K.; Rey, C.; Kuhn, L.T.; Combes, C.; Wu, Y.; Chen, S.H.; Glimcher, M.J. (2000) Evidence of hydroxyl-ion deficiency in bone apatites: an inelastic neutron-scattering study. *Bone, 26,* 599-602.

Lowenstam, H.A. (1981) Minerals formed by organisms. *Science, 211,* 1126-1131.

Lowenstam, H.A. and Weiner, S. (1989) On Biomineralization. Oxford University Press, Inc: New York.

Ma, Y.; Qi, L. (2010) Biomineralization of sea urchin teeth. *Front. Chem. China, 5,* 299-308.

Maier, B.J.; Griesshaber, E.; Alexa, P.; Ziegler, A.; Ubhi, H.S.; Schmahl, W.W. (2014) Biological control of crystalligraphic architecture: Hierarchy and co-alignment parameters. *Acta Biomaterialia, 10,* 3866-3874.

Mamede, A.P.; Vassalo, A.R.; Piga, G.; Cunha, E.; Parker, S.F.; Marques, M.P.M.; Batista de Carvalho, L.A.E.; Gonçalves, D. (2018) Potential of Bioapatite Hydroxyls for Research on Archaeological Burned Bone. *Anal. Chem., 90,* 11556-11563.

Mann, S. (1983) Mineralization in Biological System. *Struct. Bonding, 54,* 125-174.

Mann, S. (2001) *Biomineralization: Principles and Concepts in Bioinorganic Materials Chemistry.* Oxford University Press: New York.

Maslen, E.N.; Streltsov, V.A.; Streltsova, N.R. (1993) X-Ray Study of the Electron-Density in Calcite, $CaCO_3$. *Acta Crystallogr. B., 49,* 636-641.

Maxwell, S.; Ehrlich, H.; Speer, L.; Chandler, W. (2005) Medicines From the Deep: The Importance of Protecting the High Seas from Bottom Trawling. *Natural Resources Defense Council Issue Paper*,1-14.

Meejoo, S.; Maneeprakorn, W.; Winotai, P. (2006) Phase and thermal stability of nanocrystalline hydroxyapatite prepared via microwave heating. *Thermochim. Acta, 447,* 115-120.

Meldrum, F.C.; Cölfen, H. (2008) Controlling mineral morphologies and structures in biological and synthetic systems. *Chem. Rev., 108,* 4332-4432.

Mkukuma, L.D.; Skakle, J.M.S.; Gibson, I.R.; Imrie, C.T.; Aspden, R.-M.; Hukins, D.W.L. (2004) Effect of the Proportion of Organic Material in Bone on Thermal Decomposition of Bone Mineral: An Investigation of a Variety of Bones from Different Species Using Thermogravimetric Analysis Coupled to Mass Spectrometry, High-Temperature X-ray Diffraction, and Fourier Transform Infrared Spectroscopy. *Calcif. Tissue Int., 75,* 321-328.

Momma, K.; Izumi, F. (2011) VESTA 3 for three-dimensional visualization of crystal, volumetric and morphology data. *J. Appl. Crystallogr., 44,* 1272-1276.

Montel, G.; Bonel, G.; Heughebaert, J.C.; Trombe, J.C.; Rey, C. (1981) New concepts in the composition, crystallization and growth of the mineral component of calcified tissues. *J. Cryst. Growth, 53,* 74-99.

Mullin, J.W. (2001) Crystallization. Butterworth-Heinemann: Oxford, United Kingdom.

Munoz-Espi, R.; Qi, Y.; Lieberwirth, I.; Gomez, C. M.; Wegner, G. (2005) Surface-functionalized latex particles as controlling agents for the mineralization of zinc oxide in aqueous medium. *Chem. Eur. J., 12*, 118-129.

Munro, L.E.; Longstaffe, F.J.; White, C.D. (2007) Burning and boiling of modern deer bone: Effects on crystallinity and oxygen isotope composition of bioapatite phosphate. *Palaeogeogr. Palaeoclimatol. Palaeoecol., 249,* 90-102.

Munro, L.E.; Longstaffe, F.J.; White, C.D. (2008) Effects of heating on the carbon and oxygen-isotope compositions of structural carbonate in bioapatite from modern deer bone. *Palaeogeogr. Palaeoclimatol. Palaeoecol., 266,* 142-150.

Nicholson, R.A. (1993) A Morphological Investigation of Burnt Animal Bone and an Evaluation of its Utility in Archaeology. *J. Archaeol. Sci., 20,* 411-428.

Niederberger, M.; Cölfen, H. (2006) Oriented attachment and mesocrystals: non-classical crystallization mechanisms based on nanoparticle assembly. *Phys. Chem. Chem. Phys., 8,* 3271-3287.

Nielsen-Marsh, C.; Gernaey, A.; Turner-Walker, G.; Hedges, R.; Pike, A.; Collins, M. (2000) Chemical Degradation of Bone. In: Cox, M.; May, S. (Eds.); *Human Osteology: in Archaeology and Forensic Science*. Greenwich Medical Media: London, p. 439-454.

Nindiyasari, F.; Fernández-Díaz, L.; Griesshaber, E.; Astilleros, J.M.; Sánchez-Pastor, N.; Schmahl, W.W. (2014a) Influence of gelatin hydrogel porosity on the crystallization of $CaCO_3$. *Cryst. Growth Des., 14*, 1531-1542.

Nindiyasari, F.; Griesshaber, E.; Fernández-Díaz, L.; Astilleros, J.M.; Sánchez-Pastor, N.; Ziegler, A.; Schmahl, W.W. (2014b) Effects of Mg and Hydrogel Solid Content on the Crystallization of Calcium Carbonate in Biomimetic Counter-diffusion Systems. *Cryst. Growth Des., 14*, 4790-4802.

Nindiyasari, F.; Ziegler, A.; Griesshaber, E.; Fernández-Díaz, L.; Huber, J.; Walther, P.; Schmahl, W.W. (2015) Effect of Hydrogel Matrices on Calcite Crystal Growth Morphology, Aggregate Formation, and Co-Orientation in Biomimetic Experiments and Biomineralization Environments. *Cryst. Growth Des., 15*, 2667-2685.

Olszta, M.J.; Cheng, X.; Jee, S.S., Kumar, R.; Kim, Y.Y.; Kaufmann, M.J.; Douglas, E.P.; Gower, L. B. (2007) Bone structure and formation: A new perspective. *Mater. Sci. Eng. R Rep., 58,* 77-116.

Ooi, C.Y.; Hamdi, M.; Ramesh, S. (2007) Properties of hydroxyapatite produced by annealing of bovine bone. *Ceram. Int., 33,* 1171-1177.

Ortoleva, P. (1982) Solute reaction mediated precipitate patterns in cross gradient free systems. *Z. Phys. B, 49,* 149-156.

Palmer, L.C.; Newcomb, C.J.; Kalt, S.R.; Spoerke, E.D.; Stupp, S.I. (2008) Biomimetic systems for hydroxyapatite mineralization inspired by bone and enamel. *Chem. Rev., 108,* 4754-4783.

Pan, Y.; Fleet, M.E. (2002) Compositions of the apatite-group minerals: Substitution mechanisms and controlling factors. *Rev. Mineral. Geochem., 48,* 13-49.

Pasteris, J.D.; Wopenka, B.; Freeman, J.J.; Rogers, K.; Valsami-Jones, E.; van der Houwen, J.A.M.; Silva, M.J. (2004) Lack of OH in nanocrystalline apatite as a function of degree of atomic order: implications for bone and biomaterials. *Biomaterials, 25,* 229-238.

Pasteris, J.D.; Wopenka, B.; Valsami-Jones, E. (2008) Bone and Tooth Mineralization: Why Apatite? *Elements, 4,* 97-104.

Pasteris, J.D.; Yoder, C.H.; Sternlieb, M.P.; Liu, S. (2012) Effect of carbonate incorporation on the hydroxyl content of hydroxylapatite. *Mineral. Mag., 76,* 2741-2759.

Pauly, H. (1963) "Ikaite", a new mineral from Greenland. *Arctic, 16,* 263-264.

Pedrosa, E.T.; Putnis, C.V.; Putnis, A. (2016) The pseudomorphic replacement of marble by apatite: The role of fluid composition. *Chem. Geol., 425,* 1-11.

Person, A.; Bocherens, H.; Saliège, J.F.; Paris, F.; Zeitoun, V.; Gérard, M. (1995) Early Diagenetic Evolution of Bone Phosphate: An X-ray Diffractometry Analysis. *J. Archaeol. Sci., 22,* 211-221.

Person, A.; Bocherens, H.; Mariotti, A.; Renard, M. (1996) Diagenetic evolution and experimental heating of bone phosphate. *Palaeogeogr. Palaeoclimatol. Palaeoecol., 126,* 135-149.

Piga, G.; Malgosa, A.; Thompson, T.J.U.; Enzo, S. (2008) A new calibration of the XRD technique for the study of archaeological burned human remains. *J. Archaeol. Sci., 35,* 2171-2178.

Piga, G.; Thompson, T.J.U.; Malgosa, A.; Enzo, S. (2009) The potential of X-ray diffraction in the analysis of burned remains from forensic contexts. *J. Forensic. Sci., 54,* 534-539.

Piga, G.; Solinas, G.; Thompson, T.J.U.; Brunetti, A.; Malgosa, A.; Enzo, S. (2013) Is X-ray diffraction able to distinguish between animal and human bones? *J. Archaeol. Sci., 40,* 778-785.

Piga, G.; Amarante, A.; Makhoul, C.; Cunha, E.; Malgosa, A.; Enzo, S.; Gonçalves, D. (2018) β-Tricalcium Phosphate Interferes with the Assessment of Crystallinity in Burned Skeletal Remains. *J. Spectrosc., 2018,* 1-10.

Plummer, L.N. and Busenberg, E. (1982) The solubilities of calcite, aragonite and vaterite in CO_2-H_2O solutions between 0 and 90 °C, and an evaluation of the aqueous model for the system $CaCO_3$-CO_2-H_2O. *Geochim. Cosmochim. Acta, 46,* 1011-1040.

Pokroy, B.; Fitch, A.N.; Lee, P.L.; Quintana, J.P.; Caspi, E.a.N.; Zolotoyabko, E. (2006a) Anisotropic lattice distortions in the mollusk-made aragonite: A widespread phenomenon. *J. Struct. Biol., 153*, 145-150.

Pokroy, B.; Fitch, A.N.; Marin, F.; Kapon, M.; Adir, N.; Zolotoyabko, E. (2006b) Anisotropic lattice distortions in biogenic calcite induced by intra-crystalline organic molecules. *J. Struct. Biol., 155*, 96-103.

Pollok, K.; Putnis, C.V.; Putnis, A. (2011) Mineral replacement reactions in solid solution-aqueous solution systems: Volume changes, reactions paths and end-points using the example of model salt systems. *Am. J. Sci., 311,* 211-236.

Pountos, I.; Giannoudis, P.V. (2016) Is there a role of coral bone substitutes in bone repair? *Injury, 47,* 2606-2613.

Prieto, M.; Fernández-Diaz, L.; López-Andrés, S. (1991) Spatial and evolutionary aspects of nucleation in diffusing-reacting systems. *J. Cryst. Growth, 108*, 770-778.

Prieto, M.; Fernández-González, A.; Putnis, A.; Fernández-Díaz, L. (1997) Nucleation, growth, and zoning phenomena in crystallizing $(Ba,Sr)CO_3$, $Ba(SO_4,CrO_4)$, $(Ba,Sr)SO_4$, and $(Cd,Ca)CO_3$ solid solutions from aqueous solutions. *Geochim. Cosmochim. Acta, 61*, 3383-3397.

Prieto, M.; Astilleros, J.M.; Fernández-Díaz, L. (2013) Environmental Remediation by Crystallization of Solid Solutions. *Elements, 9*, 195- 201.

Pucéat, E.; Reynard, B.; Lécuyer, C. (2004) Can crystallinity be used to determine the degree of chemical alteration of biogenic apatites? *Chem. Geol., 205,* 83-97.

Putnis, A.; Fernández-Díaz, L.; Prieto, M. (1992) Experimentally produced oscillatory zoning in the $(Ba,Sr)SO_4$ solid solution. *Nature, 358*, 743-745.

Putnis, A. (2002) Mineral replacement reactions: From macroscopic observations to microscopic mechanisms. *Mineral. Mag., 66,* 689-708.

Putnis, A.; Putnis, C.V. (2007) The mechanism of reequilibration of solids in the presence of a fluid phase. *J. Solid State Chem., 180,* 1783-1786.

Putnis, A. (2009) Mineral Replacement Reactions. *Rev. Mineral. Geochem., 70,* 87-124.

Putnis, C.V.; Fernández-Díaz, L. (2011) Ion partitioning and element mobilization during mineral replacement reactions in natural and experimental systems. In: Prieto, M.; Stoll, H. (Eds.) *Ion partitioning in ambient-temperature aqueous systems*. Mineralogical Society of Great Britain & Ireland.

Putnis, A. (2015) Transient porosity resulting from fluid–mineral interaction and its consequences. *Rev. Mineral. Geochem., 80*, 1-23.

Ratner, B.; Hoffman, A.; Schoen, F.; Lemons, J. (2004) *Biomaterials science. An introduction to materials in medicine*, 3rd edition. Academic Press: Oxford, UK.

Raynaud, S.; Champion, E.; Bernache-Assollant, D.; Thomas, P. (2002) Calcium phosphate apatites with variable Ca/P atomic ratio I. Synthesis, characterisation and thermal stability of powders. *Biomaterials, 23,* 1065-1072.

Reinares-Fisac, D.; Veintemillas-Verdaguer, S.; Fernández-Díaz, L. (2017) Conversion of biogenic aragonite into hydroxyapatite scaffolds in boiling solutions. *Cryst. Eng. Comm.*, 19, 110-116.

Rey, C.; Collins, B.; Goehl, T.; Dickson, I.R.; Glimcher, M.J. (1989) The carbonate environment in bone mineral: a resolution-enhanced Fourier Transform Infrared Spectroscopy Study. *Calcif. Tissue Int., 45,* 157-164.

Rey, C.; Shimizu, M.; Collins, B.; Glimcher, M. (1990) Resolution-Enhanced Fourier Transform Infrared Spectroscopy Study of the Environment of Phosphate Ions in the Early Deposits of a Solid Phase of Calcium-Phosphate in Bone and Enamel, and their Evolution with Age. I: Investigations in the ν_4 PO$_4$ Domain. *Calcif. Tissue Int., 46,* 384-394.

Rey, C.; Miquel, J.L.; Facchini, L.; Legrand, A.-P.; Glimcher, M.J. (1995) Hydroxyl groups in bone mineral. *Bone, 16,* 583-586.

Rey, C.; Combes, C.; Drouet, C.; Cazalbou, S.; Grossin, D.; Brouillet, F.; Sarda, S. (2014) Surface properties of biomimetic nanocrystalline apatites; applications in biomaterials. *Prog. Cryst. Growth & Charact., 60,* 63-73.

Reznikov, N.; Shahar, R.; Weiner, S. (2014) Three-dimensional structure of human lamellar bone: the presence of two different materials and new insights into the hierarchical organization. *Bone, 59,* 93-104.

Rho, J.Y.; Kuhn-Spearing, L.; Zioupos, P. (1998) Mechanical properties and the hierarchical structure of bone. *Med. Eng. Phys., 20,* 92-102.

Rietveld, H.M. (1969) A Profile Refinement Method for Nuclear and Magnetic Structures. *J. Appl. Cryst., 2*, 65-71.

Rodríguez-Carvajal, J. (1993) Recent advances in magnetic structure determination by neutron powder diffraction. *Physica B, 192,* 55-69.

Rodríguez-Carvajal, J.; Roisnel, T. (2004) Line Broadening Analysis Using FullProf*: Determination of Microstructural Properties. *Mater. Sci. Forum, 443-444,* 123-126.

Rodríguez-Navarro, A.B.; McCormack, H.M.; Fleming, R.H.; Alvarez-Lloret, P.; Romero-Pastor, J.; Domínguez-Gasca, N.; Prozorov, T.; Dunn, I.C. (2018) Influence of physical activity on tibial bone material properties in laying hens. *J. Struct. Biol., 201*, 36-45.

Rodríguez-Navarro, A.B.; Domínguez-Gasca, N.; Benavides Reyes, C.; Sánchez Rodríguez, E.; Greiner, M.; Schmahl, W.W. (2019) Influence of mineral properties and organic matrix composition and structure on bone mineral dissolution. Unpublished.

Rogers, K.D.; Daniels, P. (2002) An X-ray diffraction study of the effects of heat treatment on bone mineral microstructure. *Biomaterials, 23,* 2577-2585.

Roncal-Herrero, T.; Astilleros, J.M.; Bots, P.; Rodríguez-Blanco, J.D.; Prieto, M.; Benning, L.G.; Fernández-Díaz, L. (2017) Reaction pathways and textural aspects of the replacement of anhydrite by calcite at 25 °C. *Am. Mineral., 102,* 1270-1278.

Rousseau M. (2018) Nacre: a biomineral, a natural biomaterial, and a source of bio-inspiration. In: Heuss-Aßbichler, S.; Amthauer, G., John, M. (Eds.); *Highlights in Applied Mineralogy*. De Gruyter: Berlin, Boston, pp. 285-300.

Roy, D.M.; Linnehan, S.K. (1974) Hydroxyapatite formed from Coral Skeletal Carbonate by Hydrothermal Exchange. *Nature, 247,* 220-222.

Rudin, S. (2018) The Combined Influence of Crystal Growth Rate and Agar Hydrogel Strength on the Formation of Biomimetic Hydrogel-Mg-Calcite and Sr-Calcite Composites. Master Thesis, Ludwig-Maximilians-Universität München.

Ruiz-Agudo, E.; Putnis, C.V.; Putnis, A. (2014) Coupled dissolution and precipitation at mineral–fluid interfaces. *Chem. Geol., 383,* 132-146.

Sánchez-Pastor, N.; Gigler, A.M.; Cruz, J.A.; Park, S.H.; Jordan, G.; Fernández-Díaz, L. (2011) Growth of Calcium Carbonate in the Presence of Cr(VI). *Cryst. Growth Des., 11*, 3081-3089.

Sancho-Tomás, M.; Fermani, S.; Gómez-Morales, J.; Falini, G.; García-Ruiz, J.M. (2014) Calcium carbonate bio-precipitation in counter-diffusion systems using the soluble organic matrix from nacre and sea-urchin spine. *Eur. J. Mineral., 26*, 523-535.

Sangwal K. (2007) *Additives and Crystallization Processes: From Fundamentals to Application.* John Wiley & Sons Ltd: The Atrium, Southern Gate, Chichester.

Schlosser, M.; Fröls, S.; Hauf, U.; Sethmann, I.; Schultheiss, S.; Pfeifer, F.; Kleebe, H.J.; Ferreira, J. (2012) Combined Hydrothermal Conversion and Vapor Transport Sintering of Ag-Modified Calcium Phosphate Scaffolds. *J. Am. Ceram. Soc., 96,* 412-419.

Schmahl, W.W.; Kocsis, B.; Toncala, A.; Wycisk, D.; Grupe, G. (2017) The Crystalline State of Archaeological Bone Material. In: Grupe, G.; Grigat, A.; McGlynn, G.C. (Eds.); *Across the Alps in Prehistory.* Springer International Publishing.

Schwarcz, H.P.; McNally, E.A.; Botton, G.A. (2014) Dark-field transmission electron microscopy of cortical bone reveals details of extrafibrillar crystals. *J. Struct. Biol., 188,* 240-248.

Seidl, B.H.; Ziegler, A. (2012) Electron microscopic and preparative methods for the analysis of isopod cuticle. *Zookeys, 176, 73-85.*

Seidl, B.H.M.; Reisecker, C.; Hild, S.; Griesshaber, E.; Ziegler, A. (2012) Calcite distribution and orientation in the tergite exocuticle of the isopods Porcellio scaber and Armadillidium vulgare (Oniscidea, Crustacea). *Z. Kristallogr., 227,* 777-792.

Sfihi, H. and Rey, C. (2002) 1-D and 2-D double heteronuclear magnetic resonance study of the local structure of type B carbonate fluoroapatite. In: Fraissard, J.; Lapina, B. (Eds.); *Magnetic Resonance in Colloid and Interface Science, Nato ASI Series II, Vol. 76.* Kluwer Academic Publishers. pp. 409-418

Shemesh, A. (1990) Crystallinity and diagenesis of sedimentary apatites. *Geochim. Cosmochim. Acta, 54,* 2433-2438.

Shimoda, S.; Aoba, T.; Moreno, E.C.; Miake, Y. (1990) Effect of Solution Composition on Morphological and Structural Features of Carbonated Calcium Apatites. *J. Dent. Res., 69,* 1731-1740.

Shipman, P.; Foster, G.; Schoeninger, M. (1984) Burnt Bones and Teeth: an Experimental Study of Color, Morphology, Crystal Structure and Shrinkage. *J. Archaeol. Sci., 11,* 307-325.

Sillen, A.; Hoering, T. (1993) Chemical characterization of burnt bones from Swartkrans. In: Brain C.K. (Ed.) *Swartkrans: A Cave's Chronicle of Early Man.* Transvaal Museum Monograph, Vol. 8 Transvaal Museum, Pretoria, p. 243-249.

Silve, C.; Lopez, E.; Vidal B.; Smith, D.C.; Camprasse, S.; Camprasse, G.; Couly, G. (1992) Nacre initiates biomineralization by human osteoblasts maintained in vitro. *Calcif. Tissue Int., 51*, 363-369.

Simon, I.; McMahon, H.O. (1953) Study of the Structure of Quartz, Cristobalite, and Vitreous Silica by Reflection in Infrared. *J. Chem. Phys., 21,* 23-30.

Simon, P.; Carrillo-Cabrera, W.; Huang, Y.X.; Buder, J.; Borrmann, H.; Cardoso-Gil, R.; Rosseeva, E.; Yarin, Y.; Zahnert, T.; Kniep, R. (2011) Structural Relationship between Calcite-Gelatine Composites and Biogenic (Human) Otoconia. *Eur. J. Inorg. Chem., 2011*, 5370-5377.

Simonet Roda, M.; Griesshaber, E.; Ziegler, A.; Rupp, U.; Yin, X.; Henkel, D.; Häussermann, V.; Laudien, J.; Brand, U.; Eisenhauer A.; Checa, A.G.; Schmahl, W.W. (2019) Calcite fibre formation in modern brachiopod shells. *Sci. Rep. 9,* 598.

Smith, D.K. jr.; Leider, H.R. (1968) Low-temperature thermal expansion of LiH, MgO and CaO. *J. Appl. Crystallogr., 1,* 246-249.

Snoeck, C.; Lee-Thorp, J.A.; Schulting, R.J. (2014) From bone to ash: Compositional and structural changes in burned modern and archaeological bone. *Palaeogeogr. Palaeoclimatol. Palaeoecol., 416,* 55-68.

Stiner, M.C.; Kuhn, S.L.; Weiner, S. Bar-Yosef, O. (1995) Differential Burning, Recrystallization, and Fragmentation of Archaeological Bone. *J. Archeol. Sci., 22,* 223-237.

Stranski, I.N. (1928) Zur Theorie des Kristallwachstums. *Z. Phys. Chem. 136,* 259-278.

Stuhler, R. (1938) *Fortschr. Gebiete Rontgenstrahlen, 57,* 231.

Sudarsanan, K.; Young, R.A. (1969) Significant precision in crystal structural detail. Holly Springs hydroxyapatite. *Acta Crystallogr. B, 25,* 1534-1543.

Sunagawa, I. (2005) *Crystals: Growth, Morphology and Perfection.* Cambridge University Press: Cambridge.

Taira, T.; Iijima, M.; Moriwaki, Y.; Kuboki, Y. (1995) A new method for in vitro calcification using acrylamide gel and bovine serum. *Connect. Tissue Res., 33,* 185–192.

Thompson, P.; Cox, D.E.; Hastings, J.B. (1987) Rietveld refinement of Debye–Scherrer synchrotron X-ray data from Al_2O_3. *J. Appl. Crystallogr., 20,* 79-83.

Thompson, T.J.U. (2005) Heat-induced dimensional changes in bone and their consequences for forensic anthropology. *J. Forensic Sci., 50,* 1008-1015.

Thompson, T.J.U.; Chudek, J.A. (2007) A novel approach to the visualisation of heat-induced structural change in bone. *Sci. Justice, 47,* 99-104.

Thompson, T.J.U.; Gauthier, M.; Islam, M. (2009) The application of a new method of Fourier Transform Infrared Spectroscopy to the analysis of burned bone. *J. Aracheol. Sci., 36,* 910-914.

Thompson, T.J.U.; Islam, M.; Piduru, K.; Marcel, A. (2011) An investigation into the internal and external variables acting on crystallinity index using Fourier Transform Infrared Spectroscopy on unaltered and burned bone. *Palaeogeogr. Palaeoclimatol. Palaeoecol., 299,* 168-174.

Thompson, T.J.U.; Szigeti, J.; Gowland, R.L.; Witcher, R.E. (2016) Death on the frontier: Military cremation practices in the north of Roman Britain. *J. Archaeol. Sci. Rep., 10,* 828-836.

Thümmler, R. (2019) Crystallization of Carbonates and Phosphates via Biomimetic experiments. Master Thesis, Ludwig-Maximilians-Universität München, to be submitted in July 2019.

Tonegawa, T.; Ikoma, T.; Yoshioka, T.; Hanagata, N.; Tanaka, J. (2010) Crystal structure refinement of A-type carbonate apatite by X-ray powder diffraction. *J. Mater. Sci., 45,* 2419-2426.

Tong, W.; Glimcher, M.J.; Katz, J.L.; Kuhn, L.; Eppell, S.J. (2003) Size and shape of mineralites in young bovine bone measured by atomic force microscopy. *Calcif. Tissue Int., 72,* 592-598.

Tütken, T. (2003) Die Bedeutung der Knochenfrühdiagenese für die Erhaltungsfähigkeit in vivo erworbener Element- und Isotopenzusammensetzungen in fossilen Knochen. Phd thesis, Eberhard Karls Universität Tübingen.

Turner-Walker, G. (2008) The chemical and microbial degradation of bones and teeth. In Pinasi, R.; Mays, S. (Eds.); *Advances in human paleopathology.* Wiley: Chichester, pp. 3-29.

Vandecandelaere, N.; Rey, C.; Drouet, C. (2012) Biomimetic apatite-based biomaterials: on the critical impact of synthesis and post-synthesis parameters. *J. Mater. Sci. Mater. Med., 23,* 2593-2606.

Verhoff M.A.; Wiesbrock, U.O.; Kreutz, K. (2004) Macroscopic findings for the exclusion of a forensic relevant soil embedded resting period in skeletal remains - An approach based upon literature. *Arch. Kriminol., 213 (1-2),* 1-14.

Von Endt, D.W.; Ortner, D.J. (1984) Experimental effects of bone size and temperature on bone diagenesis. *J. Archaeol. Sci., 11,* 247-253.

Wagner, H.D.; Weiner, S. (1992) On the relationship between the microstructure of bone and its mechanical stiffness. *J. Biomech., 25,* 1311-1320.

Wahl, J. (1982) Leichenbranduntersuchungen. Ein Überblick über die Bearbeitungs- und Aussagemöglichkeiten von Brandgräbern. *Praehistorische Zeitschrift, 57,* 1-125.

Walker, P.L.; Miller, K.W.P.; Richman, R. (2008) Time, Temperature, and Oxygen Availability: an experimental study of the effects of environmental conditions on the color and organic content of cremated bone. In Schmidt, C.W.; Symes, S.A. (Eds.); *The analysis of burned human remains.* Academic Press: San Diego, pp. 129-135.

Wang, J.J.; Zhou, Z.M.; Zhang, Z.B.; Du, B.; Zhan, Z.; Wang, Q.; Yuan, P.; Liu, L.R.; Zhang, Q.P. (2015) Biomimetic synthesis of platelet-shaped hydroxyapatite mesocrystals in a collagen mimetic peptide-PED hybrid hydrogel. *Mater. Lett., 159,* 150-153.

Wang, Y.; Azaïs, T.; Robin, M.; Vallée, A.; Catania, C.; Legriel P.; Pehau-Arnaudet, G.; Babonneau, F.; Giraud-Guille, M.M.; Nassif, N. (2012) The predominant role of collagen in the nucleation growth, structure and orientation of bone apatite. *Nat. Mater., 11,* 724-733.

Wargadalam, V.J.; Löffler, G.; Winter, F.; Hofbauer, H. (2000) Homogeneous Formation of NO and N_2O from the Oxidation of HCN and NH_3 at 600-1000 °C. *Combust. Flame, 120,* 465-478.

Wegst, U.G.K.; Bai, H.; Saiz, E.; Tomsia, A.P.; Ritchie, R.O. (2014) Bioinspired structural materials. *Nat. Mater., 14,* 23-36.

Weiner, S.; Bar-Yosef, O. (1990) State of Preservation of Bones from Prehistoric Sites in the Near East: A Survey. *J. Archaeol. Sci., 17,* 187-196.

Weiner, S.; Goldberg, P.; Bar-Yosef, O. (1993) Bone preservation in Kebara cave, Israel using on-site Fourier transform infrared spectrometry. *J. Archaeol. Sci., 20,* 613–627.

Weiner, S.; Traub, W.; Wagner, H.D. (1999) Lamellar Bone: Structure-Function Relations. *J. Struct. Biol., 126,* 241-255.

Weiner, S. and Dove, P.M. (2003) An Overview of Biomineralization Processes and the Problem of the Vital Effect. *Rev. Mineral. Geochem., 54,* 1-29.

Weiner, S.; Addadi, L. (2011) Crystallization pathways in biomineralization. *Annu. Rev. Mater. Res., 4,* 21-40.

Wen, H.B.; Moradian-Oldak, J.; Fincham, A.G. (2000) Dose-dependent modulation of octacalcium phosphate crystal habit by ameloginins. *J. Dent. Res., 79,* 1902–1906.

Westbroek, P.; Marin, F. (1998) A marriage of bone and nacre. *Nature, 392,* 861-862.

White, R.A.; Weber, J.N.; White, E.W. (1972) Replamineform: a new process for preparing porous ceramic, metal, and polymer prosthetic materials. *Science, 176,* 992-994.

Wilson, R.M.; Elliot, J.C.; Dowker, S.E.P. (1999) Rietveld refinement of the crystallographic structure of human dental enamel apatites. *Am. Mineral., 84,* 1406-1414.

Wilson, R.M.; Elliott, J.C.; Dowker, S.E.P.; Smith, R.I. (2004) Rietveld structure refinement of precipitated carbonate apatite using neutron diffraction data. *Biomaterials, 25,* 2205-2213.

Wopenka, B.; Pasteris, J.D. (2005) A mineralogical perspective on the apatite in bone. *Mater. Sci. Eng. C, 25,* 131-143.

Wuttke, J. (2014) Multiple Bragg reflection by a thick mosaic crystal. *Acta Crystallogr., Sect. A: Found. Adv., 70*, 429-440.

Xia, F.; Brugger, J.; Chen, G.; Ngothai, Y.; O'Neill, B.; Putnis, A.; Pring, A. (2009a) Mechanism and kinetics of pseudomorphic mineral replacement reactions: A case study of the replacement of pentlandite by violarite. *Geochim. Cosmochim. Acta, 73,* 1945-1969.

Xia, F.; Brugger, J.; Ngothai, Y.; O'Neill, B.; Chen, G.; Pring, A. (2009b) Three-dimensional ordered arrays of zeolite nanocrystals with uniform size and orientation by a pseudomorphic coupled dissolution−reprecipitation replacement route. *Cryst. Growth Des., 9,* 4902-4906.

Yi, H.; Balan, E.; Gervais, C.; Segalen, L.; Fayon, F.; Roche, D.; Person, A.; Morin, G.; Guillaumet, M.; Blanchard, M.; Lazzeri, M.; Babonneau, F. (2013) A carbonate-fluoride defect model for carbonate-rich fluorapatite. *Am. Mineral., 98,* 1066-1069.

Zhang, G.; Brion, A.; Willemin, A.S.; Piet, M.H.; Moby, V.; Bianchi, A.; Mainard, D.; Galois, L.; Gillet, P.; Rousseau, M. (2017) Nacre, a natural, multi-use, and timely biomaterial for bone graft substitution. *J. Biomed. Mater. Res., Part A, 105,* 662-671.

Zhang, X.; Vecchio, K.S. (2013) Conversion of natural marine skeletons as scaffolds for bone tissue engineering. *Frontiers of Mater. Sci., 7,* 103-117.

Zou, Z.; Habraken, W.J.E.M.; Matveeva, G.; Jensen, A.C.S.; Bertinetti, L.; Hood, M.A.; Sun, C.; Gilbert, P.U.P.A.; Polishchuk, I.; Pokroy, B.; Mahamid, J.; Politi, A.; Weiner, S.; Werner, P.; Bette, S.; Dinnebier, R.; Kolb, U.; Zolotoyabko, E.; Fratzl, P. (2019) A hydrated crystalline calcium carbonate phase: Calcium carbonate hemihydrate. *Science 363,* 396-400.

Danksagung

An dieser Stelle möchte ich mich bei allen bedanken, die mich während meiner Promotion begleitet haben.

Zuerst natürlich bei meinem Doktorvater Herrn Prof. Dr. Wolfgang W. Schmahl für diese Möglichkeit und für die Unterstützung und das Vertrauen, die fruchtbaren Diskussionen und die zahlreichen, lustigen off-topic Gespräche.

Mein tiefster Dank gebührt Frau Dr. Erika Griesshaber für ihre Unterstützung, Engagement und Rat und Hilfe in allen Lebenslagen.

Des Weiteren möchte ich mich bei der Deutschen Forschungsgesellschaft (DFG) für die finanzielle Unterstützung dieser Dissertation im Rahmen der Forschergruppe FOR1670 bedanken. Allen Beteiligten der Forschergruppe FOR1670 − insbesondere Frau Prof. Dr. Grupe - möchte ich für ihre Unterstützung und wertvollen Diskussionsrunden danken.

Vielen Dank all denen, die an der Probenanalyse und Erstellung der Manuskripte mitgewirkt haben: Lurdes Fernández-Díaz, Andrea Göhring, Mario Heinig, Balazs Kocsis, Katrin Mayer, Alejandro Rodríguez-Navarro, Anita Toncala, Sabino Veintemillas-Verdaguer, Florian Weitzel, Xiaofei Yin, Moritz Zenkert und Andreas Ziegler. Großen Dank auch an Bernhard Ganss und Karina Carneiro für die Bereitstellung des Amelotins.

Besonderer Dank geht an alle weiteren Kolleginnen und Kollegen: Kristian Bader, Laura Casella, Brittany Foley, Sixin He, Filomena Gargione, Ulf Gattermann, Peter Gille, Max Häberle, Michael Hahne, Stefanie Hoser, Barbara Jaeger, Guntram Jordan, Melanie Kaliwoda, Detlef Körner, Michael Lindner, Viola Mages, Bernd Maier, Fitriana Nindiyasari, Sohyun Park, Mirtha Pillaca Quispe, Alexander Reul, Mar Simonet Roda - tú eres mi corazón, Benedikt Röska, Stefan Rudin, Korbinian Schiebel, Judith Schwerin, Ziwei Tang, Robert Thümmler, und an alle, die ich hier unbeabsichtigt vergessen habe.

Mein unschätzbarer Dank geht an meine Freunde, auf die ich immer zählen kann und die auch in schwierigen Zeiten stets ein offenes Ohr für mich haben.

Zu guter Letzt möchte ich meiner Familie − Mama, Papa, Katrin und Alex danken. Danke, dass ihr mich meinen Weg gehen habt lassen und immer hinter mir standet, ohne euch hätte ich das hier nicht geschafft.

List of Peer-Reviewed Publications

Greiner, M.; Yin, X.; Fernández-Díaz, L.; Griesshaber, E.; Weitzel, F.; Ziegler, A.; Veintemillas-Verdaguer, S.; Schmahl, W.W. (2018) Combined Influence of Reagent Concentrations and Agar Hydrogel Strength on the Formation of Biomimetic Hydrogel-Calcite Composite. *Cryst. Growth Des. 18,* 1401-1414, **DOI:** 10.1021/acs.cgd.7b01324.

https://pubs.acs.org/doi/10.1021/acs.cgd.7b01324

Greiner, M.; Fernández-Díaz, L.; Griesshaber, E.; Zenkert, M.N.; Yin, X.; Ziegler, A.; Veintemillas-Verdaguer, S.; Schmahl, W.W. (2018) Biomineral Reactivity: The Kinetics of the Replacement Reaction of Biological Aragonite to Apatite. *Minerals, 8,* 315, **DOI:** 10.3390/min8080315.

https://doi.org/10.3390/min8080315

Greiner, M.; Kocsis, B.; Heinig, M.F.; Mayer, K.; Toncala, A.; Grupe, G.; Schmahl, W.W. (2018) Experimental Cremation of Bone: Crystallite Size and Lattice Parameter Evolution. In: *Biomineralization, From Molecular and Nano-structural Analyses to Environmental Science.* Endo K., Kogure T., Nagasawa H. (Eds.); Springer Nature, Singapore. **DOI:** 10.1007/978-981-13-1002-7_3.

https://doi.org/10.1007/978-981-13-1002-7_3

Greiner, M.; Rodríguez-Navarro, A.; Heinig, M.F.; Mayer, K.; Kocsis, B.; Göhring, A.; Toncala, A.; Grupe, G.; Schmahl, W.W. (2019) Bone Incineration: An Experimental Study on Mineral Structure, Colour and Crystalline State. *Journal of Archaeological Science: Reports, 25,* 507-518. **DOI:** 10.1016/j.jasrep.2019.05.009.

https://doi.org/10.1016/j.jasrep.2019.05.009

Mayer, K.; **Greiner, M.**; Göhring, A.; Schmahl, W.W.; Grupe, G. Burning bones- thermal stability of $\delta^{18}O_{phosphate}$. Submitted to Conference Proceedings „Cremations Burials in Europe" Münchner Archäologische Forschungen.

Casella, L.-A.; He, S.; Griesshaber, E.; Fernández-Díaz, L.; **Greiner, M.**; Harper, E.-M.; Jackson, D.-J.; Ziegler, A.; Mavromatis, V.; Dietzel, M.; Eisenhauer, A.; Veintemillas-Verdaguer, S.; Brand, U.; Schmahl, W.W. (2018) Hydrothermal alteration of aragonitic biocarbonates: assessment of micro- and nanostructural dissolution–reprecipitation and constraints of diagenetic overprint from quantitative statistical grain-area analysis. *Biogeosciences, 15,* 7451-7484. **DOI:** 10.5194/bg-15-7451-2018.

https://doi.org/10.5194/bg-15-7451-2018

Nindiyasari, F.; Fernández-Díaz, L.; Yin, X.; **Greiner, M.**; Griesshaber, E.; Tsige, M.; Ziegler, A.; Schmahl, W.W. (2019) Influence of gel-strength and magnesium doping on the organization of calcite/hydrogel mesocrystal composites. *European Journal of Mineralogy* **DOI:** 10.1127/ejm/2019/0031-2840.

https://doi.org/10.1127/ejm/2019/0031-2840

Simonet Roda, M.; Ziegler, A.; Griesshaber, E.; Yin, X.; Rupp, U.; **Greiner, M.**; Henkel, D.; Häusermann, V.; Eisenhauer, A.; Laudien, J.; Schmahl, W.W. (2019) Terebratulide brachiopod shell biomineralization by mantle epithelial cells. *Journal of Structural Biology,* in press. **DOI:** 10.1016/j.jsb.2019.05.002.

https://doi.org/10.1016/j.jsb.2019.05.002

Conference Contributions

Presentations

"Influence of Agar polymeric matrices on the formation of carbonate hydrogel-mineral composites"

Greiner, M.; Yin, X.; Fernández-Díaz, L.; Griesshaber, E.; Nindiyasari, F.; Ziegler, A.; Schmahl, W.W.

Granada-Münster Discussion Meeting GMDM4, Münster, Germany, November 23 – 25 2016.

"The co-operative influence of gel solid content and reagent solution concentrations on gel occlusion and crystal micro-organization in biomimetic calcite-agar composites"

Greiner, M.; Yin, X.; Fernández-Díaz, L.; Griesshaber, E.; Nindiyasari, F.; Ziegler, A.; Schmahl, W.W.

Reunión Científica de la Sociedad Española de Mineralogía (SEM), Oviedo, Spain, July 4 – 7 2017.

"The co-operate influence of Agar polymeric matrices and reagent solution concentrations on gel incorporation and crystal organization in hydrogel-mineral composite aggregates"

Greiner, M.; Yin, X.; Fernández-Díaz, L.; Griesshaber, E.; Nindiyasari, F.; Ziegler, A.; Schmahl, W.W.

14th International Symposium on biomineralization (BIOMIN XIV), Tsukuba, Japan, October 9 – 13 2017.

"Mineralogical aspects of bone cremation"

Greiner, M.; Rodríguez-Navarro, A.; Heinig, M.F.; Mayer, K.; Kocsis, B.; Göhring, A.; Toncala, A.; Grupe, G.; Schmahl, W.W.

APPA-Workshop "Möglichkeiten und Grenzen der anthropologischen Leichenbranduntersuchung", Weimar, Germany, April 12 – 13 2019

Poster

"Experimental cremation of bone."

Greiner, M.; Kocsis, B.; Mayer, K.; Toncala, A.; Gruppe, G.; Schmahl, W.W.

14th International Symposium on biomineralization (BIOMIN XIV), Tsukuba, Japan, October 9 – 13 2017.